On Kinetic Transport in Small System Collectivity and a Measurement of Separated Open Heavy Flavor Production in $p+p$ Collisions at $\sqrt{s_{NN}} = 200$ GeV

by

Javier Orjuela Koop

B.S., Universidad de los Andes, 2010

M.S., University of Colorado Boulder, 2014

A thesis submitted to the

Faculty of the Graduate School of the

University of Colorado in partial fulfillment

of the requirements for the degree of

Doctor of Philosophy

Department of Physics

2018

This thesis entitled:
On Kinetic Transport in Small System Collectivity and a Measurement of Separated Open Heavy Flavor Production in $p+p$ Collisions at $\sqrt{s_{NN}} = 200$ GeV
written by Javier Orjuela Koop
has been approved for the Department of Physics

_____

Prof. James L. Nagle

_____

Prof. Dennis V. Perepelitsa

Date _____

The final copy of this thesis has been examined by the signatories, and we find that both the content and the form meet acceptable presentation standards of scholarly work in the above mentioned discipline.

Orjuela Koop, Javier (Ph.D., Physics)

On Kinetic Transport in Small System Collectivity and a Measurement of Separated Open Heavy Flavor Production in $p+p$ Collisions at $\sqrt{s_{NN}} = 200$ GeV

Thesis directed by Prof. James L. Nagle

The present dissertation consists of two distinct parts. The first one is a comprehensive study of collective behavior in small collision systems from the point of view of kinetic theory, in which the medium formed in heavy-ion collisions is modeled as a collection of interacting quasiparticles. We investigate how parton scattering, where individual partons undergo very few scatters, can translate the initial collision geometry to final-state azimuthal anisotropy, yielding results in agreement with experimental data in a variety of systems, from ^{3}He+Au to $p+p$ collisions, and over a wide range of collision energies, prompting the question of the minimal conditions for collective behavior to appear within this framework.

The second part consists of an experimental measurement of the charm and bottom decay electron cross section in $p+p$ collisions at $\sqrt{s_{NN}} = 200$ GeV using the PHENIX detector at the Relativistic Heavy Ion Collider. Unlike previous measurements of inclusive heavy flavor electrons, we present a measurement of each flavor separately. The measurement proceeds by identifying a candidate sample of electron tracks, constructing a simulated electron cocktail to isolate the electron candidates from heavy flavor decays, and using a Bayesian inference procedure to statistically determine the provenance of electrons based on precise displaced vertex measurements. The resulting electron cross sections are consistent with perturbative QCD calculations, exhibiting small uncertainties and large kinematic reach, making them valuable baseline measurements for the future study of in-medium heavy flavor modification in other collision systems, such as A+A and p+A.

Dedication

To my family.

Acknowledgements

As I conclude this thesis, I would like to express my sincere gratitude towards those without whom this endeavor would not have come to fruition. First and foremost, I would like to thank my advisor, Prof. Jamie Nagle, for his generous guidance, the many opportunities he has provided, and for his unwavering commitment to excellence. A special thank you goes to Prof. Dennis Perepelitsa for his support, and for his contagious intellectual curiosity and work ethic. In their lab I have found a friendly and supportive environment where I have been able to grow as a scientist. I truly could not have wished for a better research group.

I would like to thank Andrew Adare and Darren McGlinchey, for mentoring me as a young graduate student. In particular, I am indebted to Andrew for his work on the VTX alignment and Bayesian approach to unfolding, and to Darren for his heavy flavor separation work in Au+Au. Also, to Tim Rinn, for working alongside me on the heavy flavor analysis at every step of the way. A very special thank you goes to Takashi Hachiya and the rest of the PHENIX VTX group for their hard work on detector operation, software, and analysis.

I have been fortunate enough to carry out my work within the PHENIX collaboration, where I have found friendly, smart people from whom I have learned, and to whom I could reach out whenever I had questions. In no particular order, and among many others, I would like to thank Dave Morrison, Julia Velkovska, Bill Zajc, Chris Pinkenburg, Martin Purschke, Stefan Bathe, Paul Stankus, Marzia Rosati, Jin Huang, Shengli Huang, and Qiao Xu.

I would also like to thank the postdocs in the lab from whom I have learned so much—namely Ron Belmont, Qipeng Hu, Sanghoon Lim—as well as the fellow students with whom I

have worked: Theo Koblesky, Kurt Hill, Shawn Beckman, Sebastian Seeds, Bill Yin, and Sebastián Vázquez-Carson.

A special thank you goes to Profs. Ben Brown, John Cumalat, and Paul Romatschke for serving on my thesis examining committee.

And last, but certaintly not least, I would like to thank my family. My parents, for their love and many sacrifices that brought me to where I am now; my grandmother and my aunt, for instilling in me their *joie de vivre*. And to Dmitriy, who is like family, for his steadfast support through this ride called graduate school.

i thank You God for most this amazing
day:for the leaping greenly spirits of trees
and a blue true dream of sky; and for everything
which is natural which is infinite which is yes
—e.e. cummings

Contents

Chapter

Tables

Table

Figures

Figure

The future of the world no longer disturbs me; I do not try still to calculate, with anguish, how long or how short a time the Roman peace will endure; I leave that to the gods. Not that I have acquired more confidence in their justice, which is not our justice, or more faith in human wisdom; the contrary is true. Life is atrocious, we know. But precisely because I expect little of the human condition, man's periods of felicity, his partial progress, his efforts to begin over again and to continue, all seem to me like so many prodigies which nearly compensate for the monstrous mass of ills and defeats, of indifference and error. Catastrophe and ruin will come; disorder will triumph, but order will too, from time to time. Peace will again establish itself between two periods of war; the words humanity, liberty, and justice will here and there regain the meaning which we have tried to give them. Not all our books will perish, nor our statues, if broken, lie unrepaired; other domes and pediments will rise from our domes and pediments; some few men will think and work and feel as we have done, and I venture to count upon such continuators, placed irregularly throughout the centuries, and upon this kind of intermittent immortality.

– Marguerite Yourcenar, *Memoirs of Hadrian*

All shall be well, and all shall be well, and all manner of thing shall be well.

– Julian of Norwich, *Revelations of Divine Love*

Chapter 1

Motivation and Scope

State of the art cosmological measurements currently place the age of the universe at around 13.8 billion years [32]. By approximately 10^{-12} seconds after the Big Bang, the universe had rapidly expanded and cooled down sufficiently for the four fundamental interactions to have separated, appearing as the distinct forces we know today. However, with a temperature in excess of 100 MeV, the early universe at this stage was too hot for hadronic bound states to form, existing instead as a mixture of deconfined quarks and gluons until about 10^{-6} seconds when hadronization began to take place. The primordial state of matter that filled the universe in this stage of its evolution is known today as the quark-gluon plasma (QGP) [166].

The advent of quantum chromodynamics (QCD), the field-theoretical description of the strong interaction, lay down the foundation for the study of the nature of the QGP, since it predicts an asymptotic decrease in the interaction strength between quarks and gluons in the short length scale limit. Experimentally, the running of the QCD coupling constant has been verified in data from a variety of high-energy experiments. However, in order to recreate the conditions of the early universe, one must also supply a high enough density of quarks and gluons, as are present in the collisions of relativistic heavy nuclei. Hence, the field of heavy ion physics is born.

The first machine to collide nuclei at relativistic energies was the BEVALAC [187] at Lawrence Berkeley Laboratory, starting in the early 1970s, reaching energies of up to 2 GeV per nucleon. During the 1990s, fixed-target experiments at CERN's Super Proton Synchrotron (SPS) and at Brookhaven's Alternating Gradient Synchrotron (AGS) sought to identify signatures of the QGP.

However, it was not until the early 2000s that definitive evidence for the formation of QGP was found in high-energy Au+Au collisions at Brookhaven's Relativistic Heavy-Ion Collider (RHIC), the first dedicated machine for heavy-ion collisions, capable of colliding Au nuclei at center-of-mass energies of up to 200 GeV/nucleon. Following the early experimental success of the RHIC program, the 2004 Nobel Prize in Physics was awarded—coincidentally—to Gross, Politzer, and Wilczek for their theoretical work on deconfinement in QCD from thirty years before. More recently, over the past decade, the Large Hadron Collider (LHC) at CERN has delivered collisions of Pb nuclei at energies of up to 8 TeV.

Instead of the expected weakly coupled gas of quarks and gluons it was discovered that at the temperature and baryo-chemical potential achieved in Au+Au collisions at RHIC, the QGP actually exhibits a number of unique properties [204] stemming from a tight coupling between its constituent particles. While some of these properties are discussed at length in Chapters 2 and 4, here we succinctly describe those which provide the context for this dissertation.

The first of these properties is the extremely low shear viscocity to entropy density, η/s, of the QGP, manifested as collective response of the medium to pressure gradients defined by the orientation and geometric overlap of the colliding nuclei. This observation of collectivity prompted the identification of the QGP as a liquid, as opposed to a gas which expands isotropically. It was found that the azimuthal anisotropy profile of the expansion, among other observables, can be well described by relativistic hydrodynamic theory assuming a minimal value for η/s. In fact, this quantity, which can be identified as the kinematic viscosity, is the lowest of any known fluid and has led to the QGP being dubbed the *perfect liquid*[119].

Additionally, it was found that the QGP is an extremely dense medium, highly opaque to probes participating in the strong interaction. In other words, color-carrying partons (i.e., quarks and gluons) interact with the medium and lose energy through a combination of radiative (i.e., gluon radiation) and collisional (i.e., elastic scattering) processes, analogous to electromagnetic bremsstrahlung and collisional ionization in ordinary radiation-matter interactions. However, the complexity and unique features of QCD make energy loss in the QGP very hard to calculate, with

many open questions still remaining. Experimentally, a common observable stemming from the opacity of the QGP medium is the reduction of jet energy, a phenomenon known as jet quenching [200].

The present dissertation consists of two distinct parts, encompassing the author's work on various aspects of contemporary heavy-ion physics over the course of his graduate studies. The first part is a comprehensive phenomenological study of collectivity in small collision systems from the standpoint of kinetic transport theory. As stated earlier, the azimuthal anisotropy of final-state particle momentum is a hallmark signature of the formation of strongly interacting QGP in large nucleus-nucleus (A+A) collisions, traditionally understood in the context of hydrodynamic theory. However, starting in 2010, the same signals were discovered in *small* collision systems at RHIC (i.e., p, d, ^{3}He+Au) and at the LHC (i.e., p+p and p+Pb) where QGP formation had been thought to be impossible, prompting a variety of explanations with very different underlying physical motivations. This dissertation explores the idea that partonic scattering with a very small number of scatterings per parton can translate the initial geometry of the collision into final-state azimuthal anisotropy in these systems, providing predictions in quantitative agreement with flow observables measured in d+Au collisions at RHIC over a wide range of collision energies, from $\sqrt{s_{NN}}$ = 200 GeV to $\sqrt{s_{NN}}$ = 19.6 GeV. This success prompts an exploration of the minimal conditions within this kinetic transport framework required to produce collectivity signals.

The second part of the dissertation is a measurement of the differential production of heavy quarks (i.e., charm and bottom) in $p + p$ collisions at $\sqrt{s_{NN}}$ = 200 GeV, using the PHENIX detector at Brookhaven National Laboratory. Given the large mass of heavy quarks, their thermal production is precluded in heavy-ion collisions; instead, they originate in early-time hard processes between colliding partons and are thus present during the full time evolution of the QGP. As such, they make excellent probes of the hot nuclear medium and its microscopic dynamics, in contrast to lighter quark flavors which are better suited to probe the dynamics of the bulk. Given the coupling between heavy quarks and the QGP, they follow the hydrodynamic flow of the medium losing energy in the process. A common approach used to describe these dynamics has been to model the

quark as experiencing drag, which defines the average trajectory of the particle along the flow field, with short-range stochastic deviations from this path arising from diffusion, as encapsulated in the Langevin equation. Despite the success of this drag-diffusion approach, the details of the coupling and energy loss mechanisms of heavy quarks in the QGP remain a subject of active investigation. Insight can be gained by leveraging the mass difference between charm and bottom quarks, which should be intutive in the Langevin picture since both diffusion and drag are physical processes highly sensitive to particle mass.

Unlike previous measurements of the *inclusive* production of heavy quarks, the focus of this dissertation is to measure the production of each flavor separately by identifying the semileptonic decay electrons of mesons with open heavy quark content and statistically determining the provenance (i.e., from either a charm or bottom quark) of the electron sample based on precise displaced vertex measurements. This procedure has been previously used by the PHENIX collaboration to measure the differential heavy quark production in Au+Au collisions; however, to understand how these quarks are affected by the hot nuclear medium, one must compare against a corresponding baseline measurement in $p + p$ collisions and that is what this dissertation aims to provide. This analysis was carried out together with Timothy Rinn of the Iowa State University heavy-ion physics group between 2015-2018. All figures and tables in Chapters 7 and 8 are the result of our joint work.

This dissertation is organized as follows. Chapter 2 provides a general introduction to the physics of the quark-gluon plasma. Part I—dealing with small system collectivity—then begins with Chapter 3, as an introduction to collective behavior in small systems; Chapter 4 then presents the AMPT transport model, as well as the results of studies of small system collectivity from a transport theory perspective. Part II of the dissertation starts with Chapter 5, which provides an introduction to open heavy flavor measurements in heavy ion collisions; Chapter 6 describes the PHENIX experiment, and Chapter 7 describes the heavy flavor separation analysis, with the results discussed in Chapter 8.

Chapter 2

Introduction to the Physics of the Quark-Gluon Plasma

2.1 Quantum Chromodynamics

Quantum chromodynamics (QCD) is the non-Abelian gauge theory of the strong force, one of four fundamental forces of nature. As part of the standard model of particle physics, it describes the short-ranged interaction among particles carrying color charge, the quarks and gluons, where the latter is the gauge boson mediating the interaction. In this section, we provide a very brief overview of the theory, describing the quark model, the QCD Lagrangian, and two hallmark properties of QCD: asymptotic freedom and quark confinement. More details can be found in standard references, such as [163, 111, 87], on which this section is based.

2.1.1 The Quark Model

By the year 1960, particle physics had come a very long way since J.J. Thomson's discovery of the electron in the late 19^{th} century. Numerous new particles had been discovered, yet there was no systematic way to organize them, classify them, or account for their seemingly arbitrary properties. Thus, in 1961, Murray Gell-Mann proposed an organization scheme based on the electric charge and *strangeness* of subatomic particles, arranging them in a variety of geometrical shapes according to their common properties. This way of arranging particles received the exotic name of the *Eightfold Way* [109]. For example, Fig. 2.1 shows the hexagonal array of the lightest baryons and the lightest mesons, known as the baryon and hadron octets, where particles are grouped by strangeness across horizontals, and by charge along the diagonals. Heavier particles can be arranged into more complex

structures, such as the baryon decuplet and other multiplets and supermultiplets which will not be discussed here.

The important observation, however, is that the geometric patterns can be explained by positing that mesons and baryons are composites, made up of fundamental particles called *quarks*, existing in 6 flavors[1] , with properties as listed in Table A.1. If we impose the rule that (anti)baryons must comprise three (anti)quarks, and that mesons must comprise a quark and an anti-quark, then it is straightforward to verify that the allowed combinations of quarks naturally populate the multiplets of the Eightfold Way. However, since quarks are spin $\frac{1}{2}$ particles, and the total wavefunction of baryons must be antisymmetric, a new quantum number of *color* was introduced to allow for quark combinations which seemed to violate the exclusion principle. Combined with the requirement that naturally occurring particles have a total color charge of zero, the quark model is complete. The model, postulated by Zweig and Gell-Mann, was not only successful in describing known hadrons, but it was also able to predict the existence and properties of as-of-then undiscovered particles. Mathematically, Gell-Mann identified the multiplets of the Eightfold Way with an SU(3) symmetry of the hadron spectrum. That is, the u, d, and s quarks constitute a fundamental representation of the SU(3) group, with hadrons in the various multiplets forming irreducible N-dimensional representations.

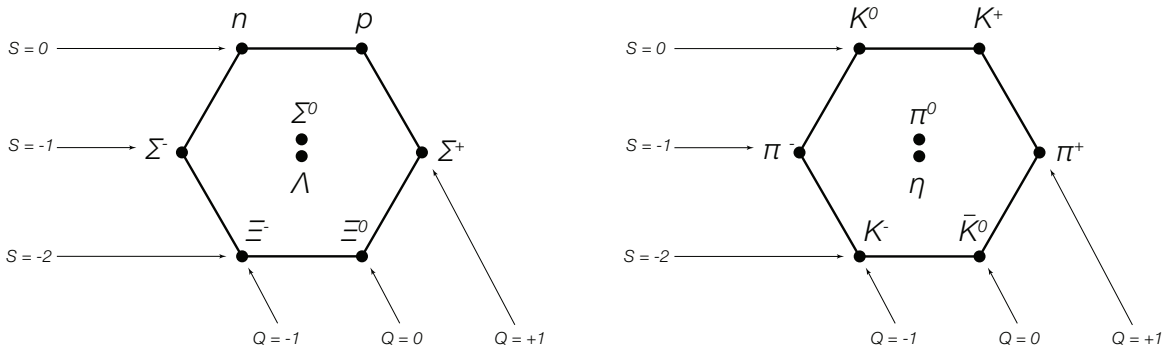

Figure 2.1: The baryon (left) and meson (right) octets of Murray Gell-Man's Eightfold Way.

[1] In the early 1960s, only thre quark flavors were posited: u, d, and s. The others were introduced as new hadronic states were discovered, and the quark model was extended to show how such states could also arise from the theory.

Table 2.1: The six flavors of quarks and their properties.

Flavor	Electric Charge	Mass	Isospin	Strangeness
u	$+\frac{2}{3}$	~ 4 MeV	$+\frac{1}{2}$	0
d	$-\frac{1}{3}$	~ 7 MeV	$-\frac{1}{2}$	0
c	$+\frac{2}{3}$	~ 1.5 GeV	0	0
s	$-\frac{1}{3}$	~ 135 MeV	0	-1
t	$+\frac{2}{3}$	~ 175 GeV	0	0
b	$-\frac{1}{3}$	~ 5 GeV	0	0

2.1.2 The QCD Lagrangian

The fundamental interactions between quarks and gluons can be written down succinctly with the following Lagrangian density [164],

$$\mathcal{L}_{\text{QCD}} = \mathcal{L}_{\text{classical}} + \mathcal{L}_{\text{gauge-fixing}} + \mathcal{L}_{\text{ghost}}. \tag{2.1}$$

The interaction term reads

$$\mathcal{L}_{\text{classical}} = -\frac{1}{4} F^A_{\alpha\beta} F^{\alpha\beta}_A + \sum \bar{q}_a (i\not{D} - m)_{ab} q_b \tag{2.2}$$

where $F_{\alpha\beta}$ is the field strength tensor from gluon fields A_α

$$F^\alpha_{\alpha\beta} = \partial^\alpha A^A_\beta - \partial^\beta A^A_\alpha - g f^{ABC} A^B_\alpha A^C_\beta, \tag{2.3}$$

where the indices A, B, and C run over eight colors of the gluon field (gluons carry both color and anti-color charge, giving rise to eight independent color configurations), g is the strong coupling constant, and f^{ABC} are the structure constants of the SU(3) group. The third term in the field strength tensor above is responsible for the three- and four-gluon self-interactions, characteristic of QCD, shown in the first two panels of Fig. 2.2. The second term $\mathcal{L}_{\text{classical}}$ encodes quark-gluon interactions, whose fundamental vertex is shown in the third panel of Fig. 2.2. The sum runs over all quark flavors, where D is the covariant derivative, and the q_a correspond to the quark fields in the triplet representation of SU(3).

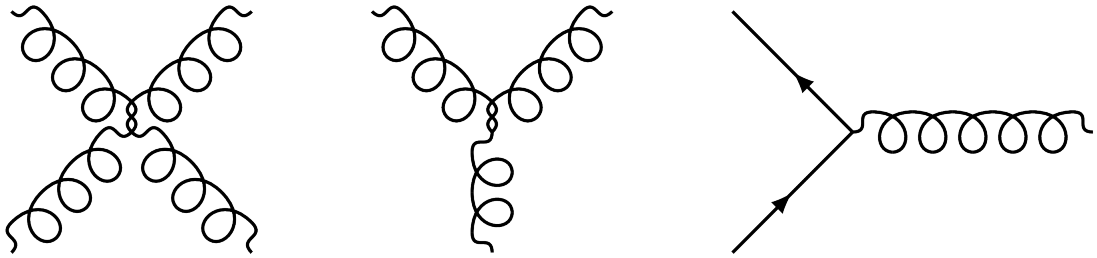

Figure 2.2: Feynman diagrams for the fundamental QCD interactions.

In order to define a propagator for the gluon fields, we make a choice of gauge, with

$$\mathcal{L}_{\text{gauge}} = -\frac{1}{2\lambda}(\partial^\alpha A^A_\alpha)^2, \tag{2.4}$$

where λ is the gauge parameter for the class of covariant gauges. While S-matrix elements do not depend on λ, the choice of gauge parameter changes certain calculational aspects of the theory. The choice of $\lambda = 0$ is called the *Landau* gauge, and $\lambda = 1$ is called the *Feynman* gauge. A Fadeev-Popov ghost field, which breaks gauge symmetry, must be added in order for the quantum field to yield unambiguous solutions. Thus

$$\mathcal{L}_{\text{ghost}} = \partial_\alpha \eta^{A\dagger}(D^\alpha_{AB}\eta^B), \tag{2.5}$$

where η is a scalar field following Fermi statistics.

2.1.3 Asymptotic Freedom and Confinement

An important feature of QCD, as an instance of a renormalizable field theory, is the 'running' of its coupling constant α_s. This means that the renormalized strength of the coupling depends on the distance (or, equivalently, the momentum transfer Q^2) scale at which the interaction is probed. Perhaps it is appropriate to first motivate this conceptually, before presenting a formal treatment. In QED, bare electric charges are screened by virtual e^+e^- pairs from vacuum fluctuations. As in a dielectric material, the virtual charges become polarized, effectively screening the bare charge, which becomes smaller with increasing distance. For instance, the commonly quoted value of the fine structure constant $\alpha = 1/137$ is actually its asymptotic value at low energies, which changes due to screening to $\alpha \approx 1/127$ at the scale of the Z boson mass.

Similarly, in QCD, fluctuations of the vacuum, as depicted to lowest order in Fig. 2.3, lead to the creation of virtual quark pairs and gluons which dress bare color charges. The effect of the $q\bar{q}$ pairs is analogous to that of e^+e^- pairs in QED vacuum polarization, such that the effective charge decreases with distance. However, the self-coupling of gluons leads effectively to an 'anti-screening' of the charge, which causes the effective charge to increase with distance. Of these competing effects, the gluon vacuum polarization dominates such that the β function for QCD is negative, and the theory exhibits color charge anti-screening, as can be demonstrated through a rigorous calculation.

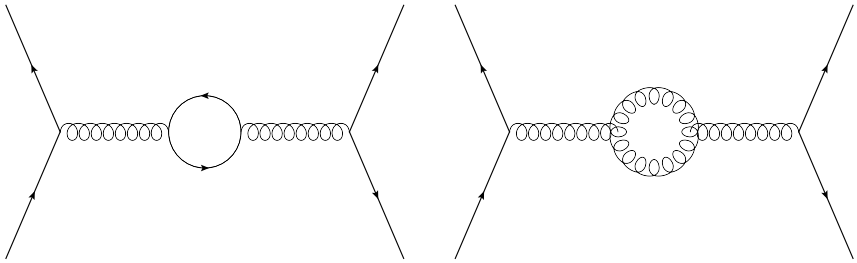

Figure 2.3: Feynman diagram for the polarization of the vacuum in QCD. The diagram on the left contributes to charge screening, and the one on the right, to anti-screening.

The anti-screening of color charges is directly related to the concept of a running coupling, which becomes small at large Q^2 (i.e, at short distances). Mathematically, the running coupling satisfies the renormalization group equation

$$\beta(\alpha_s) = \frac{\partial \alpha_s}{\partial \ln Q^2}, \tag{2.6}$$

where

$$\beta(\alpha_s) = -\alpha_s(b_o + b_1\alpha_s + b_2\alpha_s^2 + \cdots) \tag{2.7}$$

with coefficients b_i corresponding to diagrams with i number of loops. For instance, for three-color QCD and n_f almost-massless quarks, the β function becomes

$$\beta(g) = -\frac{b_0 g^3}{(4\pi)^2} \tag{2.8}$$

with $b_0 = 11 - \frac{2}{3}n_f$. In this case, the renormalization equation can be solved for the coupling constant, yielding

$$\alpha_s(Q) = \frac{\alpha_s^{(0)}}{1 + (b_0\alpha_s^{(0)}/2\pi)\ln(Q/M)}, \tag{2.9}$$

The arbitrary scale M can be eliminated by defining a characteristic mass scale Λ satisfying $g^2(b_0/8\pi^2)\ln(M/\Lambda)$, such that

$$\alpha_s(Q) = \frac{2\pi}{b_0 \ln(Q/\Lambda)}, \tag{2.10}$$

which clearly shows that the coupling becomes small with increasing Q^2. This running of the coupling constant has been verified experimentally through many measurements, with the world data summarized in [58], and shown in Fig 2.4. As a result, quarks approach the behavior of free particles when probed at a sufficiently short distances, which is known as asymptotic freedom. If, on the other hand, the distance between quarks is made very large, the coupling becomes very strong, with the consequence that no free color charges may exist in nature; instead, enough energy exists in the interaction to produce a new $q\bar{q}$ pair. This phenomenon is known as quark confinement.

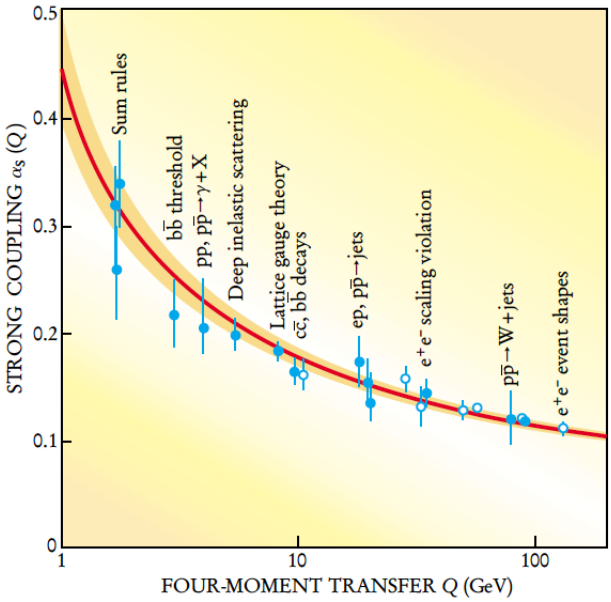

Figure 2.4: Running of the strong coupling constant with Q^2, from theory (curve with band), and experiment (points). Figure reproduced from [201].

2.2 QCD Matter Under Extreme Conditions: The Quark-Gluon Plasma

The previous section briefly outlined the theory of QCD, which provides a field-theoretical description of the interaction between quarks and gluons. However, despite its *fundamental* nature, there exist a wide range of phenomena arising from the many-body interaction of large numbers of quarks and gluons that cannot be readily identified as a direct consequence of the theory. Most notably among these emergent phenomena is the existence of bound states, such as the proton, the neutron, and atomic nuclei, which do not explicitly appear in the QCD Lagrangian.

Similarly, QCD does not unambiguously predict the properties of strongly interacting matter when subjected to high temperatures, in excess of $T \approx 100$ MeV, such as that produced in high-energy nuclear collisions. For instance, the initial expectation of finding a weakly interacting parton gas in relativistic nucleus-nucleus collisions quickly fell short when experimental evidence suggested the formation of an ultra-hot fluid medium characterized by a strong coupling between its constituent partons. Today we recognize this medium as a new state of matter called the *quark-gluon plasma* (QGP), noting that its name was coined before its experimental realization. In that sense, the "discovery" of the QGP was not merely the identification of a previously unknown form of QCD matter, but rather the charting of its novel properties, the development of new theoretical tools to describe them, and the arrival at a unified physical framework to understand the production of QGP in nuclear collisions and its subsequent time evolution.

The present section provides an overview of the physics of the QGP. We begin with a historical introduction to the problem of the highest possible temperature at which hadronic matter can exist, showing that the methods of statistical mechanics were applied to particle production in high-energy collisions long before the advent of the quark model or QCD. We then turn our attention to the thermodynamics of the QGP and the so-called "standard model" of ultrarelativistic heavy-ion collisions, which describes the various stages involved in the production, expansion, and hadronization of QGP in nuclear collisions.

2.2.1 Towards a Statistical Understanding of Particle Production in High Energy Particle Collisions

The driving force behind the development of particle physics was the search for the ultimate fundamental constituents of matter. Along these lines, matter was thought to be like a Russian matryoshka doll, where a particle could be broken up to reveal smaller particles within, which in turn could be further broken up, and so on until the final constituent was found. Moving along this chain required probing increasingly higher energy scales, from the molecular binding energies of a few eV, to atomic ionization potentials of tens of eV, to nuclear binding energies on the order of MeV. However, beyond this point, when hadrons were discovered, this simple picture broke down. In particle accelerators, collisions at the GeV scale resulted in the abundant production of even more hadronic states instead of the expected ultimate particle. This phenomenon of multi-particle production garnered significant attention, even before the quark model was proposed.

Already in 1950, Fermi [97] proposed a model where all of the energy of a nucleon-nucleon collision is deposited in a small volume of characteristic size $r \sim \hbar/m_\pi c$ (i.e., the Compton wavelength). He then argued that the system could be treated as being in equilibrium due to the strength of the interactions involved, such that the energy in the volume could be statistically distributed among the hadronic states accessible during the short lifetime of the system. Fifteen years later, around the time when the quark model was being developed, Hagedorn [114] presented the statistical bootstrap model of strong interactions, based on the assumption that hadrons are composite particles, made up of lighter hadrons, which in turn are made up of lighter hadrons, and so on. This simple requirement of self-consistency in the formation of hadron resonances actually allows the mass spectrum of emitted hadrons to be calculated. Here, as means of illustration, we present a toy model [98] that illustrates the main results of the statistical bootstrap model, asumming hadrons made up of resonances with vanishing kinetic energy. In such case, we can write the following recurrence relation for the mass spectrum $\rho(m)$—that is, $\rho(m)dm$ is the number of states

with mass between m and $m + dm$:

$$\rho(m) = \delta(m - m_0) + \sum_{n=2}^{\infty} \frac{1}{n!} \int \delta(m - \sum_{i=1}^{n} m_i) \prod_{i=1}^{n} \rho(m_i) dm_i. \tag{2.11}$$

Eqn. 2.11 can be solved for $\rho(m)$ by taking its Laplace transform

$$\int \rho(m) e^{-\beta m} dm = e^{-\beta m_0} + \sum_{n=2}^{\infty} \frac{1}{n!} \prod_{i=1}^{n} \int \rho(m_i) e^{-\beta m_i} dm_i, \tag{2.12}$$

and defining

$$z(\beta) = e^{-\beta m_0} \tag{2.13}$$

and

$$G(z) = \int e^{-\beta m} \rho(m) dm \tag{2.14}$$

such that 2.11 can be written as

$$z = 2G(z) - e^{G(z)} + 1, \tag{2.15}$$

which can be solved for $G(z)$ by differentiating and setting $G(z) = \sum_n c_n z^n$. In that case, the coefficients of the series can be shown to satisfy a recurrence relation

$$c_{n+1} = \frac{1}{n+1} \left(-n c_n + 2 \sum_{m=1}^{n} m c_m c_{n+1-m} \right), \tag{2.16}$$

such that the series solution for $G(z)$ has a radius of convergence $|z| \lessapprox 0.386$. This constraint on z can be used in Eqn. 2.13, which resembles a partition function, to derive a constraint on the maximum temperature for the hadrons. Let $z_H = 0.386$, such that

$$T_H = -\frac{m_0}{\log(z_H)}, \tag{2.17}$$

which, if we use $m_0 = m_{\pi^0}$, gives use a highest possible temperature of $T_H = 145$ MeV. This quantity is known as the *Hagedorn temperature*. If we finish solving the statistical bootstrap model equation for the mass spectrum, we find

$$\rho(m) \sim \exp(m/T_H). \tag{2.18}$$

Thus, this toy model demonstrates a central result of the statistical bootstrap model. Namely, high-energy hadronic collisions lead to the formation of a fireball, from which new hadrons are emitted following an exponential mass spectrum. However, this exponential increase implies the existence of a limiting temperature for hadronic matter, which can be interpreted in light of the equipartition theorem: if more energy is added to the system (say, by increasing the collision energy), it will lead to the excitation of new, heavier resonances, rather than increasing the energy per particle for existing states. Nowadays we associate the Hagedorn temperature with the point at which hadronic matter gives way to quark matter. If we were to treat the problem more formally, as did Hagedorn and others, we would find an exponential mass spectrum $\rho(m) \approx cm^a \exp(m/T_H)$ which can be fit to experimental data, to find $T_H \approx 160$ MeV. The implications of this limiting temperature were not fully understood in the mid 1960s. In fact, the understanding that the Hagedorn temperature is associated with the deconfinement transition of fundamental color charges within the hadrons would have to wait another decade for the development of QCD.

2.2.2 Thermodynamics of the QGP Transition

The derivation of the Hagedorn temperature in the previous section relied entirely on the concept of self-similarity of hadron structure, with no information on their quark content, or the properties of quarks. A full treatment of the transition between the hadronic and the deconfined phase would require solving the equations of QCD. We can begin to study the transition, however, using a simplified model of an ideal gas [175, 148] of massless pions. As bosons, the energy density is given by standard Bose-Einstein statistics

$$\epsilon = \frac{g}{(2\pi)^3} \int \frac{p}{\exp(p/T) - 1} d^3p, \tag{2.19}$$

where $E = p$ since we are working with massless particles. The integral can be evaluated, resulting in

$$\epsilon = \frac{3g}{\pi^2} T^4 \zeta(4) = g \frac{\pi^2}{30} T^4. \tag{2.20}$$

The pressure of the gas is one third of its energy density,

$$P = g\frac{\pi^2}{90}T^4. \tag{2.21}$$

For pions, the degeneracy $g = 3$ from their three charge states. Thus, the pressure of the pion gas is

$$P_\pi = \frac{\pi^2}{30}T^4. \tag{2.22}$$

At a high enough temperature, which we will later determine, the pion gas converts into a gas of quarks and gluons. The quarks being fermions, and the gluons being bosons, the pressure will be given by

$$\begin{aligned} P_{qgp} &= \frac{1}{3} \times \frac{1}{(2\pi)^3} \int \left(\frac{g_{\text{quark}}}{\exp(p/T)+1} + \frac{g_{\text{gluon}}}{\exp(p/T)-1} \right) p d^3p - B \\ &= \left(\frac{7}{8} g_{\text{quark}} + g_{\text{gluon}} \right) \frac{\pi^2}{90} T^4 - B. \end{aligned} \tag{2.23}$$

In the above equation, $g_{\text{quark}} = 3 \times 2 \times 2 \times 2 = 24$ to account for three colors, two flavors[2] , two spin projections, and two particle-antiparticle states; similarly, $g_{\text{gluon}} = 2 \times 8 = 16$ to account for two spin projections and eight colors. The constant B is the bag pressure from the bag model—a phenomenological model of quark confinement [83]—which is subtracted to account for the pressure from the vacuum on the quarks and gluons.

We have thus described the two phases of strongly interacting matter in our simplified model. The critical temperature at which the transition occurs can be found by solving $P_\pi(T_c) = P_{QGP}(T_c)$ for T_c, which yields

$$T_c = \left(\frac{45B}{17\pi^2} \right)^{1/4}, \tag{2.24}$$

which can be evaluated using $B \approx 0.0016$ (MeV)^4 to give $T_c \approx 150$ MeV.

Even though the simple pion gas model gives a remarkably good estimate of the transition temperature between hadronic and quark matter, a full understanding of the thermodynamics of strongly interacting matter requires solving QCD in the non-perturbative regime, using numerical

[2] Only two light flavors are considered, up and down, since the mass of the strange quarks is already ~ 100 MeV, and the other flavors are even heavier.

lattice methods. Lattice QCD allows for non-perturbative calculations since the discretization of spacetime regularizes the theory by introducing a momentum cutoff inversely proportional to the lattice spacing. Here we will present the main results of finite-temperature lattice QCD at vanishing baryo-chemical potential [175] regarding the thermodynamics of QCD matter. Given the Lagrangian of QCD in Eqn. 2.2, the partition function of strongly interacting matter reads

$$Z(V,T) = \int dA\ dq\ d\bar{q} \exp\left(- \int_V d^3x \int_0^{1/T} d\tau \mathcal{L}(A,q,\bar{q}) \right). \tag{2.25}$$

where the spatial integration is carried out over the entire volume of the system, and where the time integration is carried out (τ is the Wick-rotated time component) over a finite region of width dependent on the system temperature. Once the partition function has been calculated, the full thermodynamics of the system follows. Thus, from standard statistical mechanics, we can obtain the energy density and pressure $\epsilon = (T^2/V)(\partial \ln Z/\partial T)_V$ and $P = T(\partial \ln Z/\partial V)_T$.

Fig. 2.5 shows the energy density of strongly interacting matter, normalized by T^4, as a function of temperature using three different discretizations of the lattice in the temporal direction [65], for three-flavor QCD. The most salient feature of the plot is a very sudden change in ϵ/T^4 ocurring at around $T \sim 150$ MeV (the inset in Fig. 2.5 zooms in on this range). Far from this region, ϵ/T^4 is roughly constant. Since Eqn. 2.20 shows that $\epsilon/T^4 \propto g$, where g is the number of degrees of freedom, we identify $T \sim 150 - 200$ MeV as the point where a transition occurs from a hadronic state to a deconfined state of quarks and gluons. In fact, the high-temperature behavior of the plot is only about 10% below the value of the energy density for an ideal quark-gluon plasma.

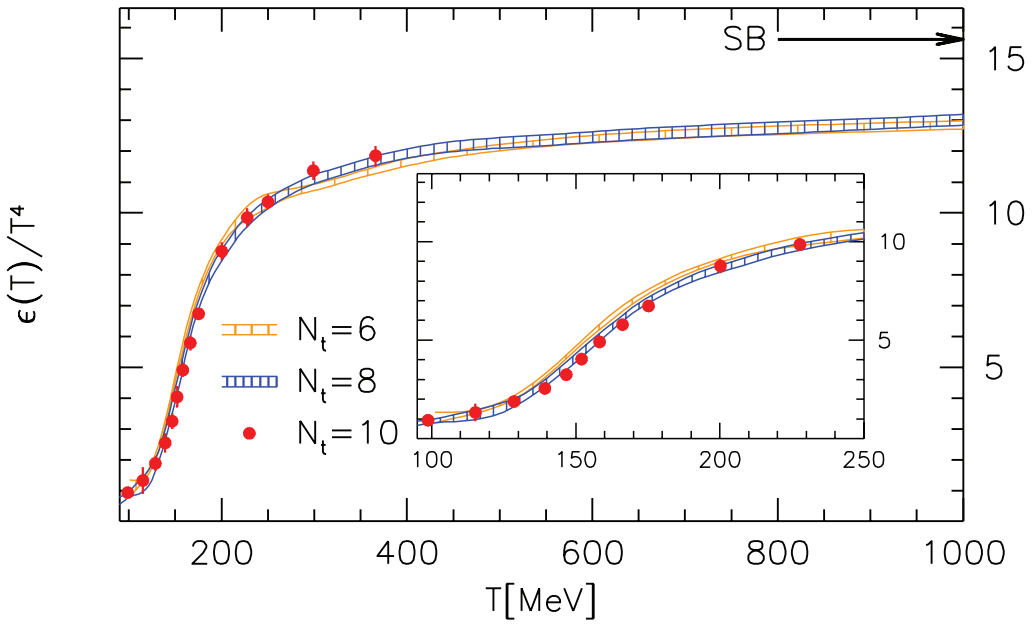

Figure 2.5: Energy density normalized by T^4 for QCD matter as a function of temperature, as calculated using lattice QCD with various discretizations in the temporal direction, $N_t = 6, 8, 10$. The arrow labeled 'SB' depicts the energy density in the Stefan-Boltzmann limit $\epsilon_{SB}/T^4 = 15.627$. Figure reproduced from [65].

Another important feature of this transition is related to the quark mass. Within hadrons, constituent quarks are dressed with gluons, which increases their mass substantially. However, as temperature increases, the quark masses approach that of bare quarks, which are very small. In the limit of vanishing bare quark mass, the Lagrangian in Eqn. 2.2 becomes chirally symmetric[3] . Thus, the transition of color deconfinement coincides with chiral symmetry restoration.

So far, we have discussed the existence of a transition around $T_c \approx 150$ MeV at vanishing baryo-chemical potential, but we have not discussed what kind of transition it is. Fig. 2.6 maps the nature of the transition for three-flavor QCD as a function of the quark masses. We will not discuss the lattice calulations resulting in the plot shown, but rather simply state the results. In the limit of infinite mass, regardless of quark flavor, the QCD Lagrangian reduces to that of a pure SU(3) gauge theory with a first-order phase transition. Similarly, in the vanishing mass limit where

[3] The dressing of the quarks within hadrons, and the breaking of chiral symmetry is responsible for the mass of hadronic matter, as opposed to the Higgs mechanism which gives *fundamental* particles their mass.

the chiral symmetry of the Lagrangian is restored, the transition is also first-order. Now, away from those limits ($0 < m < \infty$) there is no singular behavior on a line of first-order discontinuities. Instead, we speak of a smooth *cross-over* behavior, or a second-order phase transition. Given our current knowledge of the u, d and s quark masses, we locate the point in the diagram corresponding to physical reality, showing that the deconfinement transition we observe experimentally at $\mu_B = 0$ lies well within the cross-over region.

To conclude this section, we discuss the behavior of the deconfinement transition at non-vanishing baryo-chemical potential. In this region, conventional lattice QCD methods are no longer applicable, and recourse has to be made to alternative means of solving the QCD equations. Even though much work remains to be done to map the behavior of QCD matter, Fig. 2.7 shows our current best understanding of the phase diagram of this type of matter, as a function of temperature T and baryo-chemical potential μ_B. The most notable feature is that the cross-over region extends over a wide range in μ_B. Eventually, a critical point is reached, beyond which the smooth cross-over becomes a first order phase transition. Finally, at low enough temperatures and high enough μ_B, another phase transition is expected to occur in which the deconfined quarks in the QGP phase form bosonic pairs which then condense, thus giving rise to a hypothesized state of matter called a color superconductor [44]. This transition is the QCD analog of Cooper pair formation in QED.

The LHC, as the collider delivering the highest center-of-mass energies in the TeV scale, explores the cross-over region closest to $\mu_B = 0$. On the other hand, RHIC is capable of spanning a wide range in μ_B, making it possible to search for the critical point. In particular, the future phase II of the beam energy scan program (BES-II) will reach much lower energies, with increased luminosity and new instrumentation.

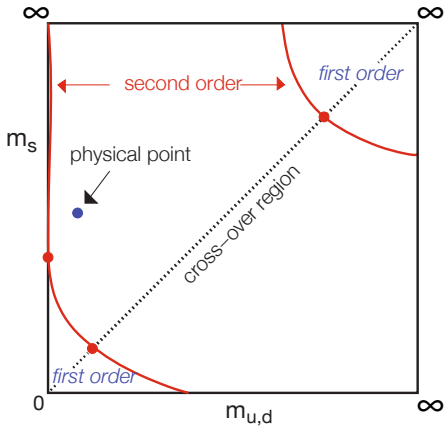

Figure 2.6: Character of the deconfinement transition in three-flavor QCD as a function of the quark masses. Figure reproduced from [175].

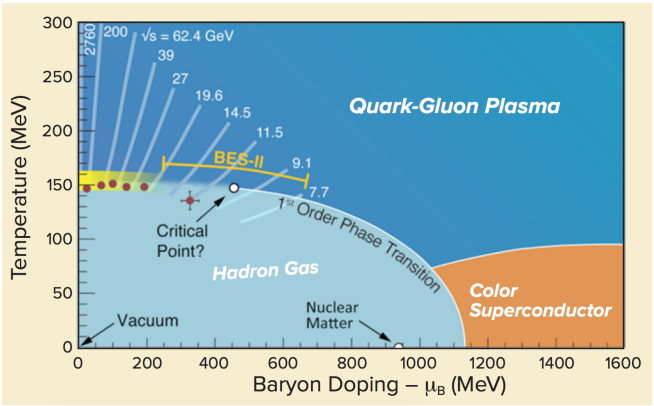

Figure 2.7: Phase diagram of QCD matter in temperature and baryo-chemical potential, with colored regions representing various phases. The boundary between the hadronic and QGP phases is blurred at low μ_B, indicating a smooth crossover. White lines are drawn to represent the trajectory followed by the QGP formed at a variety of collision energies, as it cools. The 'BES-II' label indicates the region explored by the RHIC Beam Energy Scan II program, in search of the critical point. Image credit: Shawn Beckman.

2.3 The Standard Model of Heavy Ion Collisions

In previous sections we discussed certain thermodynamic properties of QCD matter, focusing particularly on the deconfinement transition taking place at $T_c \approx 150 - 170$ MeV. However, no mention has been made of the means by which such hot QCD matter is actually produced and studied, which involves a wide range of physics and phenomenology beyond mere QCD. In modern particle colliders, particularly RHIC and the LHC, collisions of heavy ions at ultrarelativistic energies result in so-called fireballs of nuclear matter at very high densities and temperatures, which expand along directions defined by large pressure gradients. The hot matter cools down as it expands, eventually cooling down sufficiently to hadronize and give rise to final-state particles which are experimentally accessible to us. Thefore, if one wishes to study the QGP, it is imperative to develop an understanding of the entire lifecycle of heavy-ions collisions. Guided by a wealth of experimental data and advances in theoretical techniques, the framework describing the various stages in the evolution of the fireball has come to be known as the *standard model* of heavy ion collisions[4] .

We can break down the standard model into five distinct steps, depicted in Fig. 2.8: *(a) pre-collision*, in which the nuclei overlap right before the collision, and define a geometric region over which energy will be deposited; *(b) pre-equilibrium*, the process by which hadronic matter becomes deconfined and rapidly achieves thermal equilibrium; *(c) hydrodynamic expansion*, where the QGP expands according to hydrodynamics with minimal kinematical viscosity; *(d) hadronization*, in which the QGP cools down sufficiently for partons to form hadronic bound states once more; and *(e) hadronic scattering*, by which the hadrons interact and eventually free stream towards the detectors.

[4] The 'standard model' moniker, as applied to heavy-ion collisions, bears no relation to the standard model of particle physics. If parallels with other fields of physics are to be drawn, one can compare a heavy-ion collision with the Big Bang. In both cases, one deals with an expanding system in which initial-state quantum fluctuations persist and give rise to structure in the final-state. Hence, the standard model of nuclear collisions is analogous to the standard model of cosmology.

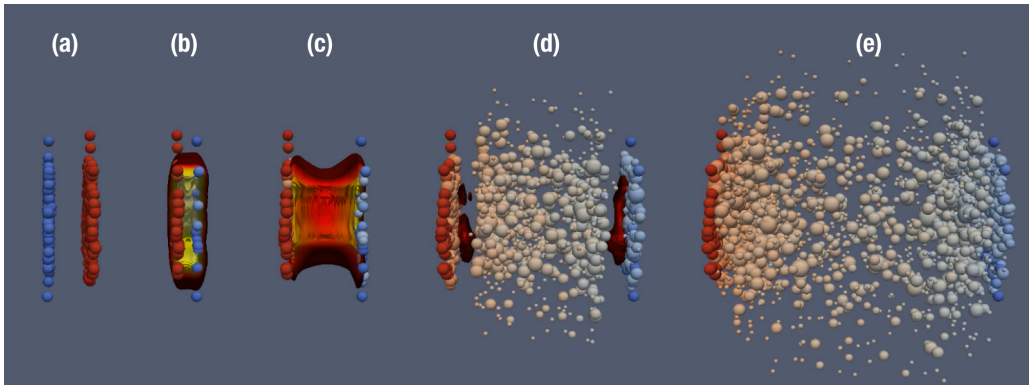

Figure 2.8: Time evolution of an ultrarelativistic heavy ion collision, with time increasing from left to right. Stage (a) represents relativistically contracted nuclei in the instants prior to the collision; (b) the pre-equlibrium stage, where quarks and gluons become unbound and approach thermal equilibration; (c) hydrodynamic expansion of the QGP formed in the collision; (d) hadronization, where previously unbound quarks and gluons recombine to form hadrons; (e) scattering and expansion of final-state hadrons. Image credit: Jonah Bernhard.

2.3.1 Collision Geometry

In the study of $p + p$ collisions, it is well known that not all events result in a full head-on collision; instead, many are just diffractive collisions. In nuclear collisions the situation is more complex since nuclei are large extended objects such that there is a wide range of possible overlap between them at the time of collision. When the impact parameter b is small (i.e., the overlap area is large), collisions are termed *central*, and when b is large (i.e., small overlap area), they are termed *peripheral*. Individual nucleons undergoing collisions with other nucleons are called participants, and those which do not are called spectators. Fig. 2.9 shows a semi-central A+A collison, where participants are shown in dark blue and red, and spectators in lighter hues. Since the event activity directly depends on the number of participants in a given collision, we see that a relation exists between particle production and the event geometry (i.e., the shape of the overlap area). Thus, the ability to characterize event geometry from experimentally accessible observables becomes a matter of central importance in heavy-ion collisions.

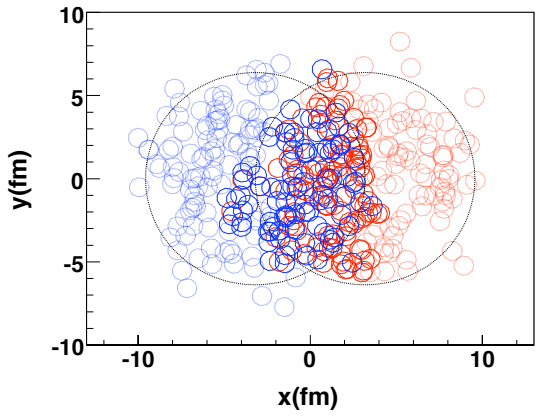

Figure 2.9: Initial geometry of a Au+Au event. The circles in light hues represent spectator nucleons; those in dark hues represent participant nucleons in the projectile and target nuclei. Figure reproduced from [45].

Even though Roy Glauber's name is more famously associated with the field of quantum optics, his work on quantum mechanical scattering in composite systems led to the development of the Glauber model [110], which is widely used in nuclear physics. In its various incarnations, the model provides a way of calculating otherwise inaccessible geometric quantities in heavy-ion collisions, such as the number of participants N_{part} and the number of binary collisions N_{coll} [146, 25]. It is instructive to first consider a variation of the model, called the optical Glauber model, which relies on two assumptions: namely that individual nucleons travel independently of each other in straight trajectories, remaining undeflected as they bore holes through the nuclear medium; and that nucleon-nucleon interactions occur inelastically with a cross section σ_{NN} which depends on the collision energy.

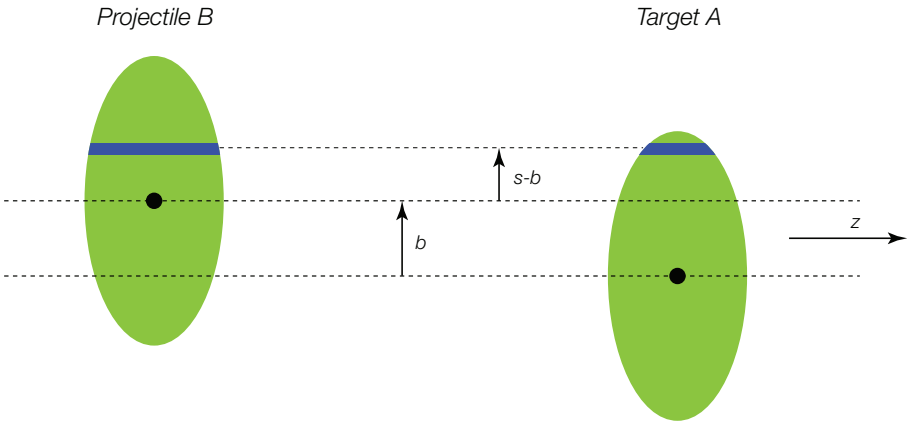

Figure 2.10: Side view of a nucleus-nucleus collision, indicating the geometry of the optical Glauber model. See text for details. Figure adapted from [146].

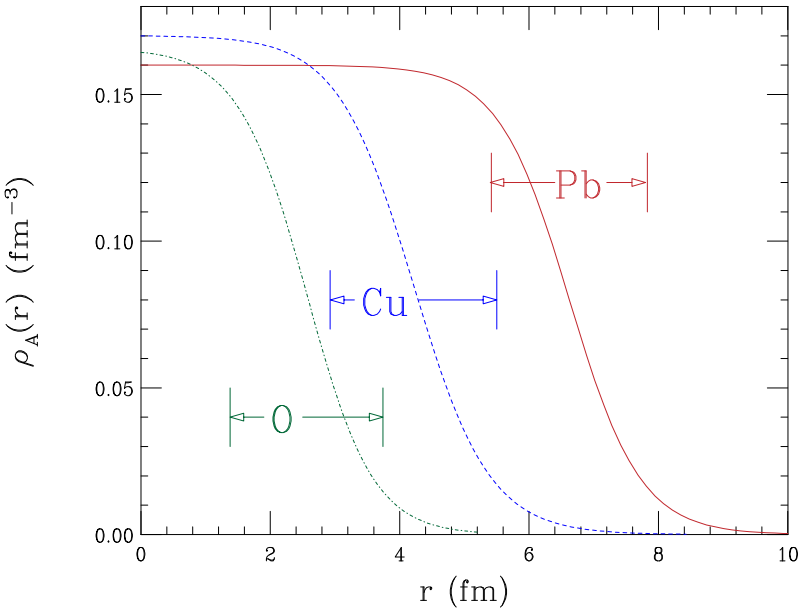

Figure 2.11: Nuclear density distributions for Pb, Cu, and O nuclei. Figure reproduced from [195].

Following the presentation in [146], Fig. 2.10 shows a schematic diagram of a nucleus-nucleus collision of impact parameter $\vec{b}$ (i.e., the separation between the center of the nuclei). The blue region within the nucleus indicates the "tunnel" that a pair of nucleons bore as they interact, a distance $\vec{s}$ away from the center of the nucleus A. If the nucleus is modeled with a continuous density

distribution—in an approach known as the optical limit—such as the Woods-Saxon distribution (shown for three different nuclear species in Fig. 2.11)

$$\rho_A(r) = \rho_0 \frac{1 + \omega(r/c)^2}{\exp[(r-c)/z] + 1}, \tag{2.26}$$

where ρ_0, ω, and c are parameters determined from electron-nucleus scattering experiments, we can write down the probability of a nucleon being found in the blue tube in nucleus A as

$$\hat{T}_A(\vec{s}) = \int \rho_A(\vec{s}, z) dz_A. \tag{2.27}$$

Therefore, the joint probability of finding a pair of nucleons, one from each nucleus, in the tube is $\hat{T}_A(\vec{s})\hat{T}_B(\vec{s}-\vec{b})d^2s$, which can be integrated to find the *nuclear thickness function*

$$\hat{T}_{A,B}(\vec{b}) = \int \hat{T}_A(\vec{s})\hat{T}_B(\vec{s}-\vec{b})d^2s. \tag{2.28}$$

The above expression corresponds physically to the area over which a nucleon in the projectile can interact with a nucleon in the target, such that the probability of n individual interactions taking place in an collision of impact parameter $\vec{b}$ between nuclei A and B is binomial:

$$P(n, \vec{b}) = \binom{N_A N_B}{n} [\hat{T}_{AB}(\vec{b})\sigma_{NN}]^n [1 - \hat{T}_{AB}(\vec{b})\sigma_{NN}]^{N_A N_B - n}, \tag{2.29}$$

where N_A and N_B are the number of nucleons in each nucleus, and the product $\hat{T}_{AB}(\vec{b})\sigma_{NN}$ is the probability of one nucleon-nucleon interaction. We can add up the above probability over all nucleon pair combinations $N_A \times N_B$ to obtain the differential cross section of interaction between nucleus A and nucleus B

$$\begin{aligned} \frac{d^2\sigma^{A+B}}{db^2} &= \sum_{n=1}^{N_A \times N_B} P(n, \vec{b}) \\ &= 1 - [1 - \hat{T}_{AB}(\vec{b})\sigma_{NN}]^{N_A N_B}. \end{aligned} \tag{2.30}$$

We thus arrive at our first geometric quantity, the number of binary collisions

$$\begin{aligned} N_{\mathrm{coll}(\vec{b})} &= \sum_{n=1}^{N_A \times N_B} n P(n, \vec{b}) \\ &= N_A N_B \hat{T}_{AB}(\vec{b})\sigma_{NN}. \end{aligned} \tag{2.31}$$

The number of participants is then given by

$$N_{\rm part}(\vec{b}) = N_A \int \hat{T}_A(\vec{s}) \left\{ 1 - \left[1 - \hat{T}_B(\vec{s} - \vec{b}) \sigma_{NN} \right]^{N_B} \right\} d^2 s + N_B \int \hat{T}_B(\vec{s} - \vec{b}) \left\{ 1 - \left[1 - \hat{T}_A(\vec{s}) \sigma_{NN} \right]^{N_A} \right\} d^2 s. \tag{2.32}$$

The above calculations are predicated on the use of continuous nuclear density distributions, when a closer description of reality would be achieved by modeling the nucleus as a discrete, or "lumpy" distribution of nucleons. Thus, in contraposition to the *optical Glauber model* stands the *Monte Carlo Glauber model*. In the Monte Carlo approach, a nucleus is modeled event-by-event by sampling individual nucleon coordinates from the nuclear density distribution, and assigning a random impact parameter to the collision, drawn from $d\sigma/db = 2\pi b$. Using the same nucleon-nucleon interaction cross section as in the optical Glauber calculation, a collision between a pair nucleons is said to occur if their separation satisfies $d < \sqrt{\sigma_{NN}/\pi}$. Instead of treating the nucleon as a black disk of area σ_{NN}, one can also model the nucleon as having a diffuse cross-sectional profile, also known as a gray-disk cross section, or experiencing event-by-event fluctuations in cross section, known as the Glauber-Gribov approach. Given this simple criterion to identify wounded nucleons, the number of participants and binary collisions follow by construction in the Monte Carlo approach.

It is of interest to compare the optical and Monte Carlo Glauber formalisms. The left panel of Fig. 2.12 shows the total cross section, as a function of σ_{NN}, as calculated with both models. For $\sigma_{NN} < 1$ mb, both yield the same total cross section, with optical Glauber resulting in a slightly higher value at $\sigma_{NN} > 1$ mb. The right panel shows $N_{\rm coll}$ and $N_{\rm part}$, which agree well between the two types of Glauber calculations. Even though the difference in total cross section may seem modest, the key difference between Monte Carlo Glauber and its optical counterpart is that the Monte Carlo approach allows us to model the local nucleon-level fluctuations in the density of the nuclear medium. The effects of such fluctuations are negligible in the limit of very weak nucleon-nucleon cross section, yet they are otherwise of substantial importance and have been

shown to account, for instance, for higher order azimuthal anisotropy in particle emission in A+A collisions, as will be discussed in a later section. State-of-the-art computer models treat the QGP as a continuous medium whose hydrodynamic expansion is highly sensitive to the initial collision geometry, such that even nucleon-level fluctuations are manifest in final-state observables. For the purposes of this dissertation, properly modeling such fluctuations in the initial geometry is critical to correctly interpreting experimental results, as will be discussed in Chapter 5 in the context of collective behavior in small collisions systems.

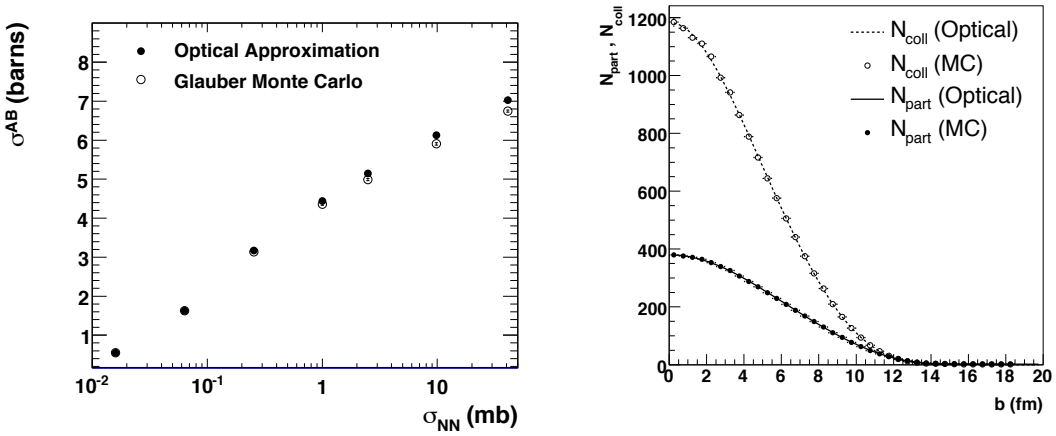

Figure 2.12: (left) inclusive cross section for identical nuclear collisions, and (right) number of participants and binary collisions as a function of impact parameter calculated in the Optical and Monte Carlo Glauber formalisms. Figure reproduced from [146].

So far we have seen that, in the Glauber model, we can posit that a monotonic direct relation exists between impact parameter and particle multiplicity, allowing us to characterize event geometry from experimental observables. Fig. 2.13 shows a cartoon of the *measured* distribution of the number of charged particles produced in A+A collisions, represented by the solid blue line. The distribution can be divided into quantiles, or *centrality classes*, as indicated by dashed lines. Each centrality class corresponds to a range of impact parameters as represented by the overlapping circles, with more central events being associated with smaller impact parameters. If one defines

a prescription to translate Monte Carlo Glauber $N_{\rm part}$ and $N_{\rm coll}$ values into particle production, one can generate a *simulated* multiplicity distribution. By matching the measured and simulated distribution, it is possible to determine the geometric quantities corresponding to each centrality class in data. This procedure, however, can be affected by a number of biases and uncertainties. For example, in small collision systems, correlations between particle production at central rapidity, and at forward rapidity where multiplicity is measured, can lead to the erroneous classification of event centrality. Given the focus of this thesis on small systems, Appendix B provides a full description of the PHENIX centrality categorization procedure in $(p)d$+Au—which is common also to large A+A collisions—as well as the above autocorrelation bias effect and how it is accounted for.

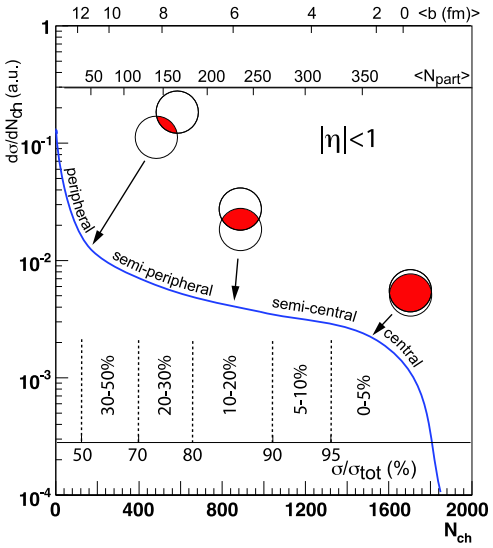

Figure 2.13: Relation between event multiplicity and event geometry. The blue line depicts the distribution of event multiplicity in A+A collisions, whose quantiles define centrality categories corresponding to the degree of overlap of the colliding nuclei, as determined by the impact parameter b. For each centrality, the Glauber model allows for the calculation of geometric quantities such as the number of nucleon participants $N_{\rm part}$ and impart parameter b. Figure reproduced from [146].

2.3.2 Hydrodynamic Expansion

Previous sections have described how, in the absence of theory of the strong interaction, statistical models were applied to the problem of hadron production in high-energy collisions. In great measure, the success of such models stemmed from their generality and emphasis on broad physical principles. Along these lines, Landau introduced the first hydrodynamic model of what we now call dense matter at high temperatures, as an improvement over Fermi's static 'fireball' description [97] . In Fermi's model, final-state particles are formed instantly and are emitted from the fireball without interacting. However, Landau [133] posited that the applicability of equilibrium thermodynamics to the description of the fireball implied that hydrodynamics should be equally applicable since it also depends on the mean free path being much smaller than the system size. Thus, in Landau's view, the fireball expands hydrodynamically, eventually reaching the point where the mean free path is no longer small and the system breaks up into final-state particles. The introduction of this expanding picture was a great success allowing, among other things, to explain why particle emission was not isotropic in momentum space as was the case in the static picture. However, interest in Landau's model eventually waned as the development of QCD took center stage. Yet, the wealth of experimental observations suggesting collective behavior in the collider era of heavy-ion physics has renewed the interest in relativistic hydrodynamics, spurring its development further.

Let's begin with the simplest case of *ideal* hydrodynamics, which is straightforward to set up, followed by the introduction of viscous corrections, based on [188, 204, 172, 158]. We begin by assuming a medium in *local* thermal equilibrium. The adjective 'local' indicates that while thermodynamic variables are allowed to vary in space and time, they do so very slowly such that their distribution is isotropic in the rest frame of a given fluid element. The energy-momentum tensor of such a fluid element of four-velocity u^μ is then

$$T^{\mu\nu} = \epsilon u^\mu u^\nu + P\Delta^{\mu\nu}, \tag{2.33}$$

where ϵ is the energy density, P is the pressure, and $\Delta^{\mu\nu} = g^{\mu\nu} + u^\mu u^\nu$ is the projection tensor.

Note that in the rest frame, $T^{\mu\nu}$ is a diagonal tensor. The equations of motion are then simply given by

$$\partial_\mu T^{\mu\nu} = 0. \tag{2.34}$$

It is informative to define $D = u^\mu \partial_\mu$ and $\nabla^\mu = \Delta^{\mu\nu}\partial_\nu$, to write the equations of motion as

$$D\epsilon = -(\epsilon + P)\nabla_\mu u^\mu \tag{2.35}$$

and

$$Du^\mu = -\frac{\nabla^\mu P}{\epsilon + P}. \tag{2.36}$$

As written, these equations are perfectly general, and certain assumptions are needed to solve them in the case of heavy ion collisions. Bjorken argued [63] that since the reaction volume is strongly stretched along the longitudinal direction, the transverse expansion can be ignored for a brief amount of time following the collision, reducing the problem to 1+1 dimensions. He assumed that the fluid is in uniform longitudinal motion with $v_z = z/t$, such that the system is boost-invariant along the longitudinal axis. This is called Bjorken scaling, since it implies that the system looks the same regardless of rapidity.[5] Under these assumptions, it is convenient to cast the problem in terms of the proper time $\tau = \sqrt{t^2 - z^2}$ and space-time rapidity $\eta_s = \operatorname{arctanh}(z/t)$ as follows

$$\epsilon(\vec{x}, t) = \epsilon(\tau), \tag{2.37}$$

$$u^\mu(\vec{x}, t) = (\cosh(\eta_s), 0, 0, \sinh(\eta_s)), \tag{2.38}$$

in curvilinear coordinate system where the fluid is at rest and space-time expands longitudinally. Using the above assumption yields a differential equation for the time evolution of the energy density

$$\frac{d\epsilon}{d\tau} = -\frac{\epsilon + P}{\tau}. \tag{2.39}$$

[5] Not to be confused with Bjorken's seminal contribution of the same name regarding the independence of the structure functions on Q^2 for fixed x in deep inelastic scattering experiments.

The above equation tells us that the internal energy in a fluid element is not conserved; rather, it is transformed into longitudinal flow under the action of pressure. The equation can be solved by making use of an equation of state (EoS) relating energy density and pressure. For an ideal relativistic gas, we have $P = c_s^2\epsilon$, where $c_s = \sqrt{\partial P/\partial\epsilon}$ is the speed of sound. Thus, we obtain the evolution of the energy density

$$\epsilon(\tau) = \epsilon_0 \left(\frac{\tau_0}{\tau}\right)^{1+c_s^2} \tag{2.40}$$

We know from thermodynamics that $Ts\epsilon + P$ and $s = dP/dT$. Thus, the solution of the hydrodynamic equations for the entropy density and temperature are

$$s(\tau) = s_0 \frac{\tau_0}{\tau}, \tag{2.41}$$

$$T(\tau) = T_0 \left(\frac{\tau_0}{\tau}\right)^{c_s^2}. \tag{2.42}$$

Notice from Eqn. 2.41 that the product $\tau s(\tau)$ is constant. Thus, the total entropy of the expanding fluid is also a constant, as expected in ideal hydrodynamics. On the other hand, Eq. 2.42 says that the fluid cools down slowly as a function of the proper time in longitudinal expansion.

Having discussed ideal hydrodynamics, let us turn now to *viscous* hydrodynamics. In this case, we decompose the energy-momentum tensor as follows

$$T^{\mu\nu} = T^{\mu\nu}_{\text{ideal}} + \pi^{\mu\nu} + \Pi\Delta^{\mu\nu}, \tag{2.43}$$

where $T^{\mu\nu}_{\text{ideal}}$ is the energy-momentum tensor of ideal hydrodynamics, $\pi^{\mu\nu}$ is the symmetric traceless shear tensor satisfying $\pi^{\mu\nu}u_\nu = 0$, and Π is the bulk stress tensor. This expression encodes corrections to ideal hydrodynamics from the gradient expansion of the energy-momentum tensor, which can be carried out to various orders. To first order, we have the so-called constituent equations

$$\pi^{\mu\nu} = -\eta\sigma^{\mu\nu} \qquad\qquad \Pi = -\zeta\nabla_\mu u^\mu, \tag{2.44}$$

where η and ζ are the shear and bulk viscosities, and

$$\sigma^{\mu\nu} = \nabla^\mu u^\nu + \nabla^\nu u^\mu - \frac{2}{3}\Delta^{\mu\nu}\nabla_\lambda u^\lambda. \tag{2.45}$$

The equation of motion arising from this first order correction is called the Navier-Stokes equation. If we take the Bjorken scaling model, the energy density is then found to obey

$$\frac{d\epsilon}{d\tau} = -\frac{\epsilon + P}{\tau} + \frac{1}{\tau^2}\left(\frac{4}{3}\eta + \zeta\right), \tag{2.46}$$

whose first term is identical to that of ideal hydrodynamics. The problem, however, with relativistic Navier-Stokes theory is that the dissipative perturbation propagates instantly, violating causality. This originates from the particular choice of the constituent equations. The situation can be remedied by taking into account second order gradient expansion corrections to the energy-momentum tensor. In that case, the theory is known as Israel-Stewart theory, which preserves causality because it incorporates relaxation terms for the dissipative currents. The interested reader is referred to [172] for further details.

To conclude this subsection, we briefly discuss some limitations regarding the applicability of hydrodynamics to heavy ion collisions. Firstly, notice that all derivations presented above relied on the gradient expansion of the energy-momentum tensor, which necessarily requires that the gradients be small, as is the case for systems near equilibrium. However, it has recently been proposed from holographic studies using the AdS/CFT correspondence that hydrodynamics may be applicable to out-of-equlibrium systems, long before thermodynamic variables isotropize in the rest frame of the fluid [77, 76]. Studies have suggested the existence of theories of out-of-equilibrium hydrodynamics with well-defined solutions even when large gradients are involved, for instance, based on the decay of non-hydrodynamic modes [170]. The implications of these developments for heavy-ion physics are significant, given the steep gradients involved and the very quick thermalization time involved in nuclear collisions, particularly those involving small nuclei.

2.3.3 Hadronic Freeze Out

As the hydrodynamic medium expands, it cools down and becomes less dense. The mean free path increases in the process, eventually becoming so large that hadrons decouple from the expanding QGP, entering a period of hadronic scattering prior to reaching the experimental apparatus.

This process is known as freezout, and properly modeling it is a key aspect of understanding the lifecycle of a heavy ion collision [98]. In modern hydrodynamic modeling there must be a prescription to interface the end of the break down of the hydrodynamic expansion and the production of hadrons. Here, we briefly discuss the so-called *Cooper-Frye* [79] approach in which a sharp cutoff (critical) temperature is imposed, below which all hydrodynamic processes stop. If this criterion is applied to all fluid elements, a hypersurface is defined and its energy density can be mapped onto hadrons, which then enter a hadronic scattering phase.

One may begin by considering the covariant expression for the number of particles with distribution $f(x,p)$, decoupling from the freezeout surface Σ:

$$N = \int \frac{d^3p}{E_p} \int d\Sigma_\mu(x) p^\mu f(x,p), \tag{2.47}$$

with

$$d\Sigma_\mu = \varepsilon_{\mu\alpha\beta\gamma} \frac{dx^\alpha}{d\alpha} \frac{dx^\beta}{d\beta} \frac{dx^\gamma}{d\gamma} d\alpha d\beta d\gamma, \tag{2.48}$$

where $\varepsilon_{\mu\alpha\beta\gamma}$ is the Levi-Civita symbol and α, β, γ parameterize the three-dimensional freezeout manifold in four-dimensional Minkowski space. The $d\Sigma_\mu$ can be explicitly calculated once a suitable set of coordinates has been defined. Now, from Eq. 2.47, we can write down the momentum distribution of emitted particles, also known as the Cooper-Frye formula:

$$E_p \frac{dN}{d^3p} = \frac{dN}{dyd^2p_T} = \int d\Sigma_\mu(x) p^\mu f(x,p), \tag{2.49}$$

where the distribution function is the appropriate Fermi-Dirac or Bose-Einstein distribution for particles in thermal equilibrium.

2.4 Collective Behavior and The Perfect Liquid

When discussing the standard model of heavy-ion collisons, we motivated the inclusion of a hydrodynamic stage by relating it to the observed collective behavior of the QGP. In this section, the details of this relation are discussed further, exploring the concept of *collective flow* as well as its experimental signatures [184, 186].

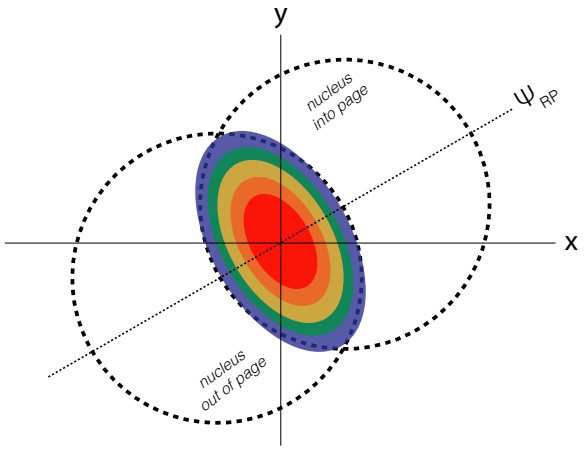

Figure 2.14: Schematic view of a semi-central Au+Au collision along the beam axis. The impact parameter makes an angle Ψ_{RP} with the $x-$axis, defining the reaction plane. The colored area in the overlap region depicts the pressure gradient created in the collision.

Fig. 2.14 shows a schematic representation of a semi-central A+A collision looking down along the beam axis (i.e., the $z-$axis). The impact parameter, that is the vector joining the center of both nuclei, forms an angle Ψ_{RP} with respect to the $x-$axis, which defines the so-called reaction plane, or plane of symmetry of the collision. The QGP will form in the almond-shaped overlap region. Due to the geometry of the region, the hot nuclear matter there will be subjected to an anisotropic pressure gradient, represented by the colored ovals. Notice that the pressure is greatest at the center of the region, and falls off towards the edge. However, the change in pressure is steeper along the minor axis than along the major axis of the ellipse. As a result, the QGP will expand hydrodynamically preferentially along the steepest gradient (that is, in the reaction plane). This anisotropic expansion results in the development of correlations between spatial coordinates and the direction of hydrodynamic expasion, which we call collective flow. Experimentally, collective flow appears as a modulation in the yield of final-state particles, which can be expressed with a Fourier series, as follows

$$E\frac{d^3N}{dp^3} = \frac{1}{2\pi p_T}\frac{d^2N}{dp_T dy}\left(1 + 2\sum_{n=0}^{\infty} v_n \cos[n(\phi - \Psi_{RP})]\right), \tag{2.50}$$

where ϕ is the azimuthal angle of individual particles. The odd terms in this expansion are iden-

tically zero due to the symmetry of the overlap region about the reaction plane. Individual terms in the series are associated with distinct azimuthal modulation shapes exhibiting $2\pi/n$ rotational symmetry; thus, $n = 2$ is associated with ellipticity, $n = 3$ is associated with triangularity, etc., as shown in Fig. 2.16. The strength of each term is given by the magnitude of the Fourier coefficients $v_n = \langle \cos[n(\phi - \Psi_{RP})] \rangle$, where the average is taken over all particles in a given event. Thus, v_1 is called directed flow, v_2 is called elliptic flow, and v_3, triangular flow.

It is important to notice that, in A+A collisions, non-vanishing v_n, with $n > 2$, only arise when fluctuating initial conditions are taken into account [46]. That is, if the initial conditions were given by a smooth distribution, then the azimuthal modulation of final-state particles could be described with just an elliptic component in the Fourier series. To illustrate this point, consider Fig. 2.15, depicting two semi-central A+A events with the same impact parameter. In principle, the spatial layout of participating nucleons (shown in red) should conform to the elliptical geometry of the interaction region, as shown in the left panel of the figure. However, nucleon-level fluctuations can impart non-elliptic contributions to the initial geometry of participants, as shown in the right panel.

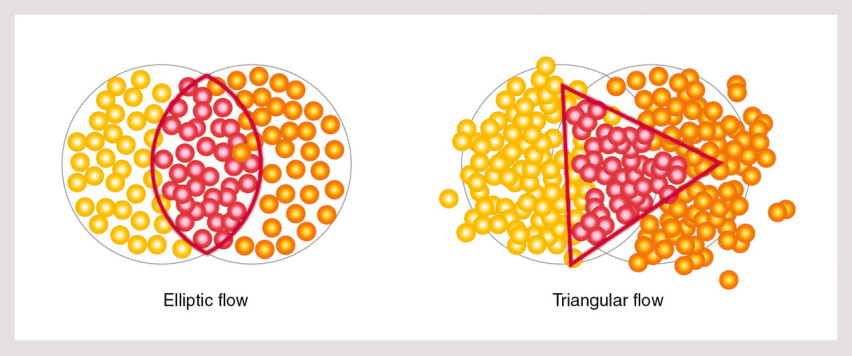

Figure 2.15: Two identical semi-central A+A collisions with different initial geometries due to nucleon-level fluctuations. Image reproduced from [122].

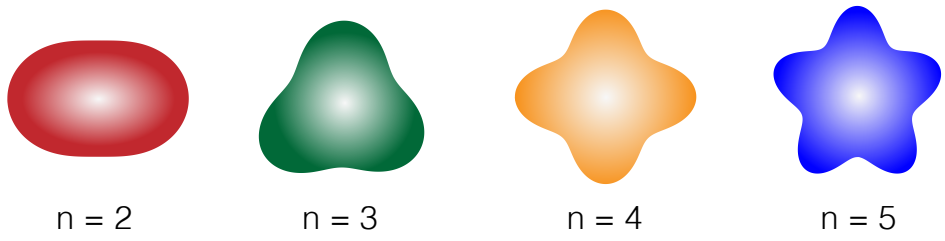

Figure 2.16: These shapes depict azimuthally-dependent radial modulations of the n^{th} order, as $r(\phi) \propto \cos(n\phi)$, illustrating the various orders of azimuthal anisotropy in particle emission.

Elliptic flow was among the first measurements carried out at RHIC in Au+Au collisions [31]. The fact that its value was found to be quite substantial was taken as evidence that the medium produced in the collisions was liquid-like, since weakly coupled gases would not respond anisotropically in the same way to pressure gradients. The formalism of ideal hydrodynamics was quickly applied to the experimental findings with great success [128]. Further evidence supporting the hydrodynamic picture came from the particle mass dependence of the measured v_2, among many other observations, as described in Ref. [119].

However, despite the success of ideal hydrodynamics, there is no such thing as a truly perfect (i.e., inviscid) liquid in nature. From kinetic theory, the shear viscosity of a gas can be shown to be

$$\eta \sim n\langle\vec{k}\rangle\lambda, \tag{2.51}$$

where n is the density, $\vec{k}$ is the momentum, and λ is the mean free path. But since $\lambda = 1/(n\sigma)$ with σ being the particle interaction cross section, then

$$\eta \sim \frac{\langle\vec{k}\rangle}{\sigma}. \tag{2.52}$$

Thus, a truly inviscid liquid for which $\eta \to 0$ would require $\sigma \to \infty$, showing that the perfect (or near-perfect) fluidity of the QGP stems from a very tight coupling between its constituent particles. Thinking conceptually about perfect fluids is not straightforward. We can gain some intuition by considering a toy problem of a volume of liquid flowing, say, along the $x-$axis with a transverse

velocity profile $v_x(y)$. The shear force between adjacent fluid layers is proportional to the velocity gradient, $F \propto \eta \nabla_y v_x(y)$. Thus, if the shear viscosity $\eta \to 0$, so too will the shear force. In other words, in a perfect liquid, perturbations in the flow do not propagate in the transverse direction. Often, for conceptual understanding, people will think of very *imperfect* everyday liquids such as honey as a stepping stone towards understanding perfect fluidity. This is a pitfall that must be avoided; honey, molasses, and pitch are viscous because of their chemistry (i.e., the electrostatic interaction of long, complex molecules), and not because of any feature of ballistic interactions between particles.

Thus, even if the QGP cannot be truly perfect, its viscosity may still be very small. However, it is notable that the near-perfect fluidity does not apply to the shear viscosity η alone, but rather to the (specific) shear viscosity η/s, which has been normalized by the entropy density. Calculations using the AdS/CFT correspondence [130] have determined that for quantum field theories at finite temperature and zero chemical potential, there is an absolute lower bound on this quantity of

$$\frac{\eta}{s} \geq \frac{1}{4\pi} \tag{2.53}$$

in natural units. It is interesting to note that the same value can be also be obtained by an uncertainty principle argument [82]. The value of η/s can be constrained by solving viscous hydrodynamics numerically and comparing the result with data [172]. More recent approaches have been based on global Bayesian fit analysis involving multiple experimental observables [59]. Fig. 2.17 shows $4\pi \times (\eta/s)$ as a function of temperature for a variety of the "best" liquids we know, including cold atom gases and superfluid helium. We can see that, despite large uncertainties, the QGP has the lowest viscosity of them all.

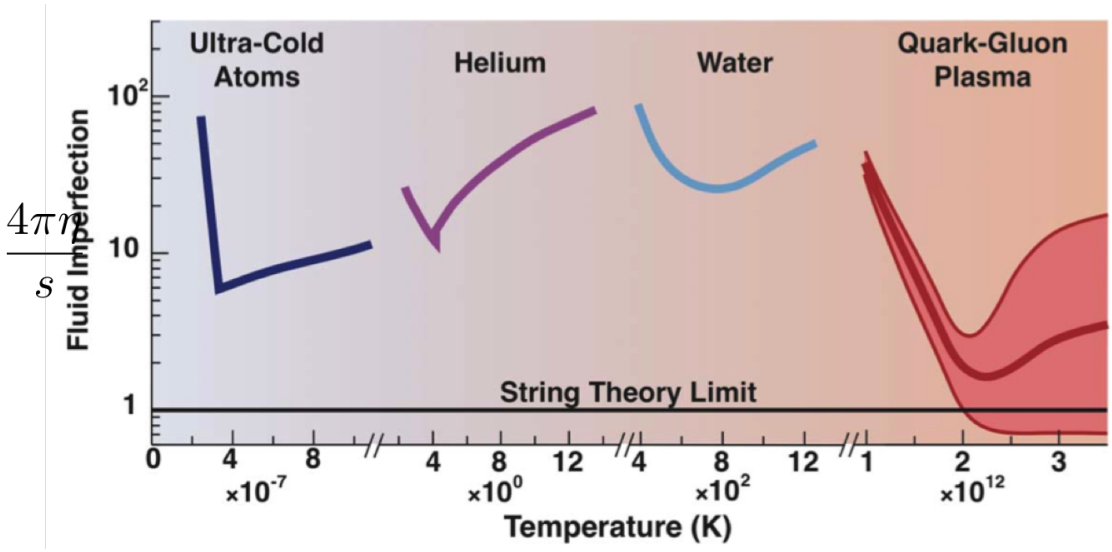

Figure 2.17: Shear viscosity to entropy ratio (scaled by 4π) as a function of temperature for a variety of liquids. Figure reproduced from [181].

Hydrodynamics with viscous corrections stands currently as the best model capable of describing a large wealth of accumulated data on collective behavior in heavy-ion collisions. For instance, Fig. 2.18 shows flow coefficients v_1 through v_5, measured in semicentral A+A collisions as a function of p_T, both RHIC and LHC energies. Also shown for comparison are the results of hydrodynamic calculations using the MUSIC model [176], with fluctuating IP-Glasma initial conditions [176], exhibiting excellent agreement with the data.

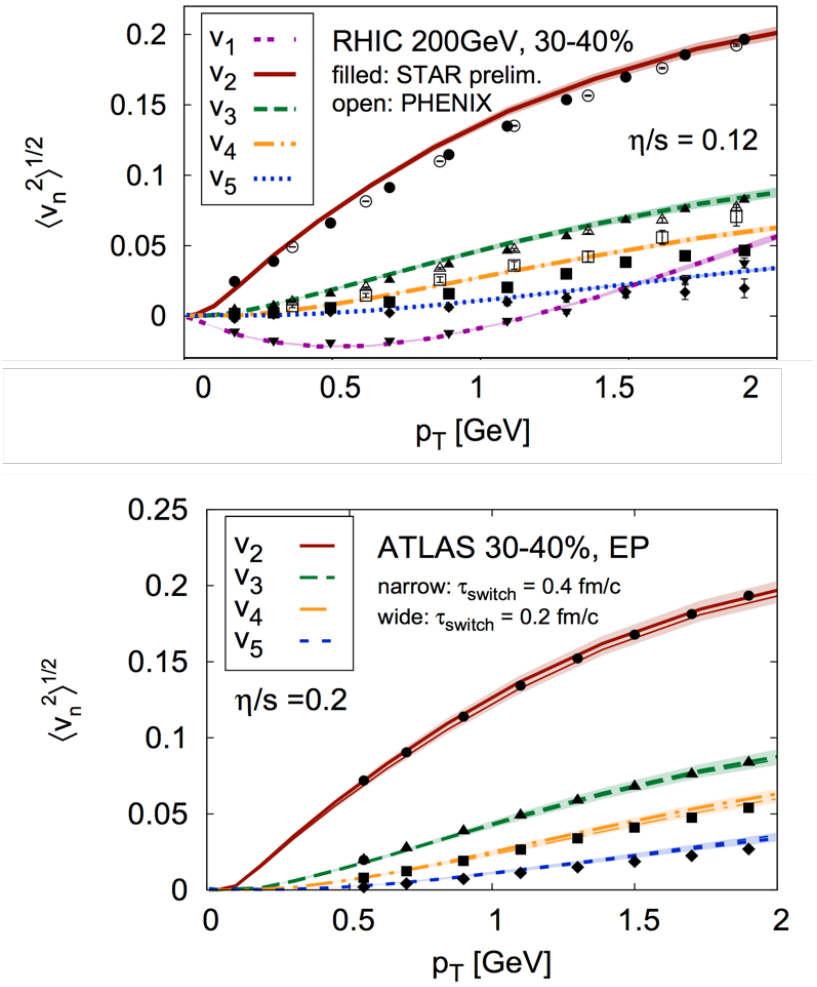

Figure 2.18: Azimuthal flow coefficients v_1 through v_5 measured at RHIC and LHC energies, along with hydrodynamic calculations in semi-central A+A collisions using IP-Glasma initial conditions and the MUSIC hydrodynamic framework. Figure reproduced from [104].

Chapter 3

Introduction to Collectivity in Small Collision Systems

3.1 Motivation

In heavy ion physics, the term 'small collision system' designates two distinct classes of collisions: nucleon-nucleon ($p + p$), and highly asymmetric x+A collisions where the target is typically Au or Pb, and the projectile x is a proton or a nucleus of very low atomic mass. To date, this last category comprises p+Au, p+Al, d+Au and ^{3}He+Au at RHIC, and p+Pb at the LHC. Of these systems, d+Au and p+Pb were originally of interest in the RHIC and LHC programs for the study of so-called *cold nuclear matter* (CNM) effects.

Collisions between nuclei cannot be treated theoretically as the mere superposition of individual nucleon-nucleon collisions, since the partonic structure of nucleons changes when embedded in the larger bound state that is the nucleus. That is, features of individual hard scattering processes between nucleons—otherwise calculable with standard perturbative techniques in QCD—become modified by the presence of the nuclear medium. Along these lines, the umbrella term 'CNM effects' refers to all such modifications. A non-exhaustive list of CNM effects includes gluon saturation, modifications of parton distribution functions in nuclei and the Cronin effect. The study of CNM effects is not only of importance to understand QCD in nuclear bound states, but it also allows for the correct interpretation of observations in A+A collisions, where both cold and hot nuclear matter effects are present. A rich experimental program has developed around CNM, which is beyond the scope of this dissertation.

From the start of the RHIC program in the early 2000s, small collision systems were con-

sidered excellent testing grounds for the study of CNM effects, since their small size was thought to preclude the formation of QGP. In the absence of any strongly interacting *hot* nuclear matter, any modification observed in, say, d+Au collisions[1] relative to the baseline $p + p$ could then be ascribed to physics originating from CNM effects.

Nevertheless, the assumption that no QGP could be formed in small system collisions came under scrutiny when measurements in $p+p$ and p+Pb at the LHC, and d+Au at RHIC, revealed an enhancement at small relative azimuth in two-particle long-range azimuthal correlations [124, 26, 4, 9, 74]. This feature is considered a hallmark signature of the formation of strongly interacting QGP in large collision systems, understood in the context of the standard model of heavy ion collisions presented in the previous chapter. The question then became whether the hydrodynamic paradigm is applicable to small collision systems, or if entirely different physics is responsible for these observations.

These initial observations prompted substantial theoretical and experimental efforts, bringing the question of QGP formation and collectivity in small systems to the forefront of heavy ion research. The approach taken has been one of systematically taking observables in A+A collisions which are well understood in the strongly-coupled fluid paradigm, and examining the extent to which they are also present in small systems. Numerous observables have been studied in this manner, both in the soft and hard sectors. In the soft sector, evidence for multi-particle collective behavior correlated with initial geometry is abundant. The hard sector, which deals with probes associated with hard parton scattering phenomena, such as jets and hadrons with heavy quark content, is also of interest as the modifications of hard probes in the QGP medium are indicative of energy loss at the partonic level. In particular, the energy loss of jets (i.e., correlated sprays of particles originating from parton fragmentation), known as *jet quenching* is a signature of QGP formation in A+A collisions. However, jet quenching has not been observed to date in small system

[1] It is interesting to note that d+Au—as opposed to p+Au—was the only small collision system available at RHIC from 2002 to 2013. While this choice may seem arbitrary, it follows from technical limitations of the collider itself when delivering such asymmetric system at the same center-of-mass energy per nucleon. In particular, the rigidity of the d beam is closer to that of the Au beam, compared to the p beam. Adjustments to the machine allowed ^{3}He+Au and p+Au collisions to be delivered in 2014 and 2015, respectively, following a strong physics motivation for comparing small systems with different intrinsic projectile geometries, as will be discussed later.

collisions. This is particularly striking if signals of collectivity are to be interpreted as arising from a strongly coupled fluid, since strong coupling necessarily implies parton energy loss. Nevertheless, it has been posited that if QGP is indeed formed in small system collisions, its spatial and time extent might be small enough that jet quenching signatures cannot develop.

The present chapter focuses on observables of multi-particle collectivity in the soft sector, for which two competing classes of theoretical models have been put forth: models based on gluon saturation physics, where collectivity arises from intrinsic momentum correlations of partons in the initial state; and models where spatial anisotropy in the initial geometry, and its event-by-event fluctuations, are translated to momentum space through final-state interactions. The latter class of models includes viscous hydrodynamics, which has been described in the previous chapter, as well as kinetic transport models. In the context of kinetic transport, the QGP is modeled not as a continous medium whose evolution is dictated by various conservation laws, but rather as a collection of well-defined quasiparticles whose scattering interactions accomplish the translation of initial geometry to final-state momentum anisotropy.

3.2 Collectivity in Small Collision Systems

In order to provide a survey of current experimental and theoretical results on small system collectivity, we focus exclusively on a set of observables related to bulk collectivity in the soft sector, which have been considered hallmark indicators of the formation of a strongly interacting QGP in A+A collisions, namely:

- Long-range two-particle angular correlation enhancement at small relative azimuth
- Azimuthal anisotropy v_n relative to the collision event plane
- Azimuthal anisotropy from higher order correlations using multi-particle cumulants
- Differential v_2 for hadrons of different mass

For a comprehensive review of other observables, including HBT radii and particle spectra, see [140].

3.2.1 Long-Range Two-Particle Azimuthal Correlations

As explained in Chapter 2, the collective expansion of the QGP under anisotropic pressure gradients leads to a characteristic azimuthal modulation in the final-state particle yield. Such modulation can be explicitly visualized by constructing two-particle correlation functions in relative η and ϕ using final-state hadrons. The leftmost panel of Fig. 3.2 illustrates such a correlation in Pb+Pb collisions at $\sqrt{s_{NN}} = 5.02$ TeV, after removing the underlying background originating from uncorrelated particles pairs. The enhancement around $\Delta\phi = \pi$ (i.e., the 'away side'), extending over many units in relative pseudorapidity arises from momentum conservation: jets from hard parton scattering emerge azimuthally back-to-back, while variations in the momentum fraction x of the partons give rise to correlations in $\Delta\eta$. The sharp peak around $(\Delta\eta, \Delta\phi) \approx (0, 0)$ comes from particles within the same jet cone. However, the near-side (i.e., around $\Delta\phi = 0$) enhancement of the correlation function at large $\Delta\eta$ reflects a global correlation attributed to the collective expansion of the QGP medium. This near-side enhancement at large relative pseudorapidity is commonly known as the *ridge*. When considering the correlation at large $|\Delta\eta|$, it is possible to see a prominent $dN/d\Delta\phi \propto \cos(2\Delta\phi)$ modulation extending over eight units in relative pseudorapidity, which can be quantified as a substantial elliptic flow coefficient v_2, directly related to the intrinsically elliptical shape of the overlap region.

This very same near-side ridge over a large $\Delta\eta$ range was observed in p+Pb collisions at $\sqrt{s_{NN}} = 5.02$ TeV, as shown in the central panel of Fig. 3.2. The existence of the ridge alone is a striking aspect of the correlation function, prompting the question of whether the same feature in two very different collision systems can be attributed to the same origin. However, although qualitatively similar to Pb+Pb, the azimuthal modulation in p+Pb is not predominantly proportional to $\cos(2\Delta\phi)$. The change in the correlation's shape arises from changes in the relative strength of the correlated flow signal and the signal from momentum conservation, and other non-flow processes.

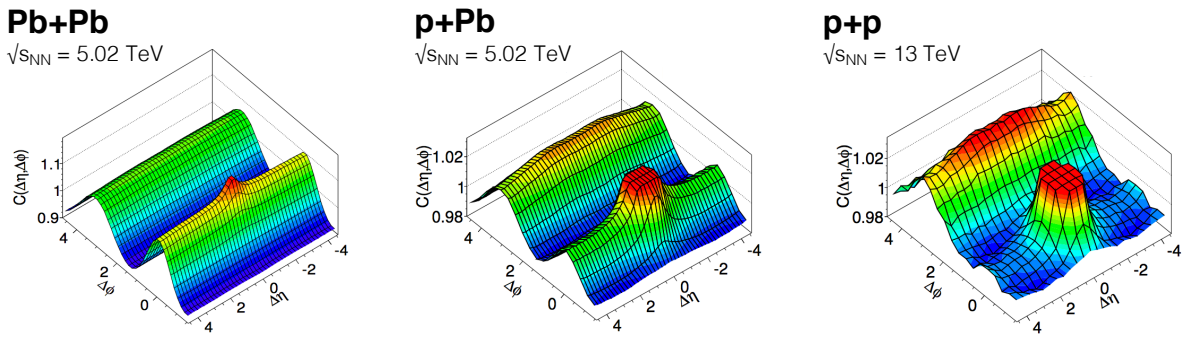

Figure 3.1: Two-particle correlations in $\Delta\eta - \Delta\phi$, measured among final-state particles in Pb+Pb, p+Pb, and $p + p$ collisions at the LHC.

Finally, the right panel of Fig. 3.2 shows the two-particle correlation for the case of $p + p$ collisions at $\sqrt{s_{NN}} = 13$ TeV. Though less pronounced than in the previous case, a long-range near-side ridge is clearly also present. Notice, additionally, that the peak in the correlation at $(\Delta\eta, \Delta\phi) \approx (0, 0)$ becomes much more prominent with decreasing system size; in fact, it has to be truncated in order to properly visualize the ridge in $p + p$ and p+Pb. This serves to illustrate the substantial presence of *non-flow effects* in small collision systems. We define as a non-flow effect any physical process—other than the collectivity of the bulk—that leads to angular correlations between particles. These include jet fragmentation, resonance decays, Coulomb correlations, and momentum conservation. While some can be trivially removed by requiring a large separation in pseudorapidity between particle pairs, others persist even with the pseudorapidity gap. The question of non-flow thus becomes central to the study of collectivity in small systems and will be addressed in greater detail in upcoming subsections.

3.2.2 Geometry Engineering

Back when they were first observed, long-range azimuthal anisotropy signals in p+Pb collisions at the LHC and in d+Au collisions at RHIC were compelling enough to warrant a close

examination of long-held assumptions about what 'collectivity' meant, the minimal conditions for it to come about, and its relation to the production of strongly interacting QGP matter. While the operational definition of collectivity, as it relates to a specific experimental observable v_n, was never in question, the physics of what was being measured certainly was. Along these lines, we distinguish two schools of thought:

- **Final-State Interaction Picture**

  The final state interaction picture is based on the idea that azimuthal anisotropy in the final-state (excluding non-flow contributions) can be directly traced back to the initial collision geometry. The translation from geometry to the final momentum space is accomplished by means of *final-state* interactions. That is, the interactions of physical entities produced after the collision has taken place, such as fluid elements hydrodynamic theory, or scattering partons in transport theory (discussed in Chapter 4).

  In the context of hydrodynamics, the final-state interaction picture claims that the standard model of heavy ion collisions essentially applies unmodified to small collision systems. That is, droplets of QGP are indeed formed during the collision, and their hydrodynamic expansion is driven by pressure gradients related to the initial geometry. This line of reasoning implicitly assumes that the small amount of QGP formed lives long enough to achieve the translation of initial spatial anisotropy into the final state; otherwise, no azimuthal anisotropy would be measured.

- **Initial-State Correlation Picture**

  Unlike the previous interpretation, the initial-state correlation picture explains the observed collectivity as arising from space-momentum correlations in the gluon fields in the *initial* state [178]. When nuclei are accelerated close the speed of light, otherwise short-lived virtual gluon fluctuations within the nucleons become Lorentz-dilated [107]. As a result, probing the nucleus on a time scale shorter than the characteristic lifetime of the fluctuations will reveal a partonic structure consisting of an abundance of gluons over quarks,

which becomes more pronounced with increasing energy. This has been well established in deep inelastic scattering (DIS) experiments, which reveal the dominance of gluons at low momentum fraction x in the structure function of the proton. As gluon occupancy grows with increasing(decreasing) energy(x), multi-parton processes involving gluon recombination become important, making the evolution of the parton distrubution function—as given by the DGLAP or BFKL equations—non-linear. Even though QCD in this small coupling régime should be normally tractable with pertubative techniques, the high gluon occupation and multi-parton interactions make such an approach unfeasible. In fact, when the gluon occupation reaches approximately $1/\alpha_s$, the use of perturbative techniques becomes impossible as an infinite number of Feynman diagrams would need to be resummed. The momentum scale below which these non-linear QCD effects become important is known as the saturation scale Q_s. Surprisingly, weak coupling methods can be applied to describe this region of *gluon saturation*. The color glass condensate (CGC) theory [193, 108] is a weakly coupled effective classical field theory, which treats 'fast' partons as static color charges since their dynamics are slowed down by relativistic time dilation, allowing us to track the evolution with energy of multi-gluon configurations.

As described above, CGC theory is a very general framework, of interest to many subfields of nuclear and particle physics insofar as changes to the partonic structure of a fast nucleon have a direct impact on particle production, which is interesting for a variety of reasons. In the case of heavy-ion collisions, gluon saturation physics has been proposed as influencing a variety of observables in small systems at RHIC and the LHC, including total particle production, forward particle suppression, and dihadron correlations including—for the purposes of this dissertation—ridge-like long-range two-particle angular correlations.

In this CGC framework, many approximations have been made to solve the Yang-Mills equations [177] to explain small system collectivity. One such approach accounts for the observed ridge in terms of the formation of color domains in the initial state of the collision.

That is, color fields within the nucleon fluctuate on an event-by-event basis, forming distinct regions where the field points in the same direction—conceptually analogous to magnetic domains in ferromagnetic materials—whose characteristic spatial extent is $1/Q_s$. When partons from the projectile nucleus impinge on the target, they will scatter off a given domain, receiving a 'kick' in the direction of the field provided their charge matches that of the domain. Therefore, the emission pattern of partons off the target will reflect the anisotropy present in the color fields, independently of the geometric configuration of the colliding nuclei. In principle, these domains exist both in large and small collision systems. However, the large number of domains in A+A dilute the strength of the correlations, since any preferred direction vanishes when averaging over all domains such that these initial-state correlation effects are negligible.

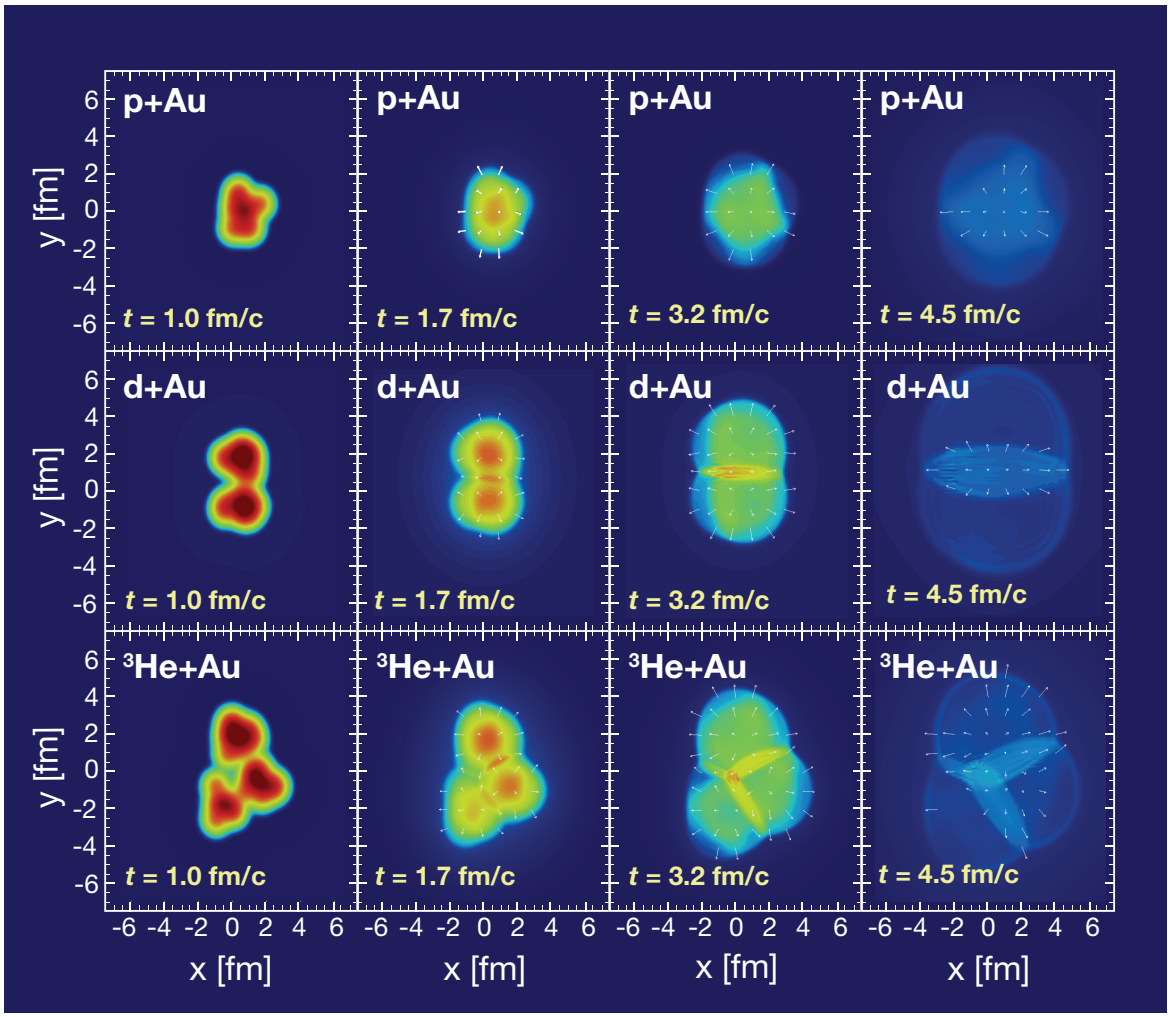

Figure 3.2: The leftmost column shows the spatial distribution of deposited energy in hydrodynamic simulations of a individual p+Au, d+Au, and ^{3}He+Au events, showing their intrinsic initial spherical, elliptical, and triangular geometry, respectively. As a function of time, the hydrodynamic evolution of each system is shown, where arrows indicate the momentum of individual fluid elements. The last column shows how the intrinsic initial geometry persists as a flow pattern in the final state.

The problem is then to devise a way of experimentally discriminating between the two possibilities described above. The key insight [151] was the realization that, just as it is possible to control the initial ellipticity ε_2 of A+A collisions by selecting on various centrality classes, it is also possible to control the initial geometry of asymmetric x+A small collisions by selecting projectile

nuclei x with different intrinsic geometric shapes, based on their number of nucleons. Along these lines, ^{3}He is triangular, deuteron is elliptical, and a single proton is point-like[2] , imparting their shape to the initial energy density distribution of the collision. If QGP is indeed formed in these small collisions, and if it is sufficiently long-lived, then the measured v_2 and v_3 should directly correlate with the known intrinsic collision geometry; that is, one would expect ^{3}He+A collisions to have the highest v_3 of all systems, and d+A to have the highest v_2. This is analogous to peripheral A+A collisions having a higher v_2 than central collisions, owing to their larger ε_2. This approach has come to be known as geometry engineering, and is illustrated in Fig. 3.2 using hydrodynamic simulations. The leftmost panels of the figure depict the initial energy density distribution for each system, showing a number of distinct hot spots corresponding to the number of nucleons in the projectile. Succesive panels towards the right show snapshots of the resulting hydrodynamic flow field at selected times in the system's evolution; it is clear from the figure that, at late times and in this particular event, the intrinsic geometry of the first panel is still present in the flow field.

The suite of three collision systems, p+Au, d+Au, and ^{3}He+Au at $\sqrt{s_{NN}}$ were delivered by the RHIC machine during the years 2015, 2008, and 2014, respectively. The PHENIX collaboration has measured v_2 and v_3 as a function of transverse momentum for 0-5% central events in these systems [41, 26, 24, 27, 38], as shown in Fig. 3.3. For comparison, Fig. 3.4 shows the measurements compared to results of hydrodynamic calculations. The SONIC calculations use Monte Carlo Glauber initial conditions, in which the eccentricity for the centrality class at hand is, in p+Au, d+Au, and ^{3}He+Au respectively, $\varepsilon_2 = 0.231, 0.540$, and 0.504. We observe a good agreement between data and calculations, and also that the relation between the measured elliptic flow coefficients $v_2^{d+\mathrm{Au}} \sim v_2^{^3\mathrm{He}+\mathrm{Au}} > v_2^{p+\mathrm{Au}}$ mirrors that among the initial ellipticity of these systems $\varepsilon_2^{d+\mathrm{Au}} \sim \varepsilon_2^{^3\mathrm{He}+\mathrm{Au}} > \varepsilon_2^{p+\mathrm{Au}}$. Similarly, the initial triangularity for d+Au and ^{3}He+Au is $\varepsilon_3 = 0.190$ and 0.283, respectively, and we correspondingly observe $v_3^{d+\mathrm{Au}} < v_3^{^3\mathrm{He}+\mathrm{Au}}$. These observations, together with the excellent agreement of hydrodynamic simulations with data constitute very strong positive

[2] While a single projectile proton may be point like, there will be large fluctuations upon collision with the large target nucleus. However, part of the intrinsic geometry of the projectile is preserved.

evidence in support of the final-state interaction picture of small system collectivity. It is important to mention, however, that while the measurements of v_2 are carried out in the same *centrality* class for every system, the multiplicity changes, necessarily impacting v_2. Along these lines, ^{3}He+Au has the highest event multiplicity, followed by d+Au and p+Au in that order. However, hydrodynamic calculations account for the effect of multiplicity on v_2, as well as the effect of event-by-event fluctuations in the initial geometry.

Additionally, the observations disfavor the initial-state correlation hypothesis, since color domains are correlated within individual nucleons, but not within the larger nucleus. Thus, the overall collectivity signal should decrease with an increasing number of nucleons in the projectile, contrary to observations.

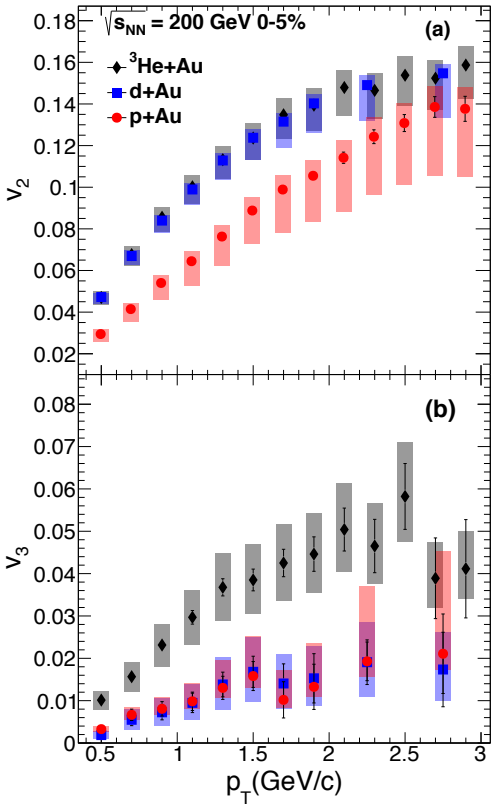

Figure 3.3: (top) Elliptic and (bottom) triangular flow $v_{2,3}(p_T)$ for 0-5% central p+Au, d+Au, and ^{3}He+Au collisions, as measured by the PHENIX experiment. Figure reproduced from [41].

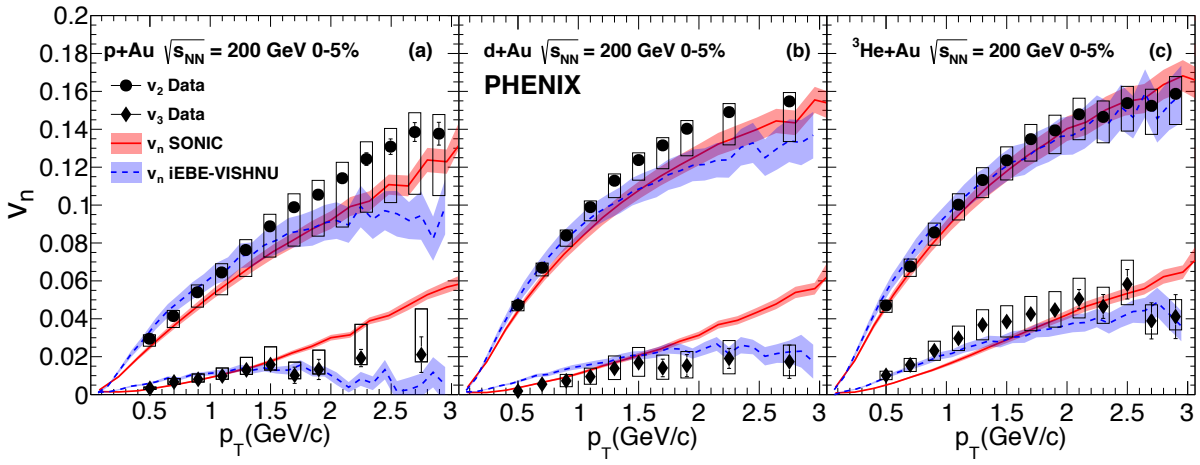

Figure 3.4: Elliptic and triangular flow, $v_2(p_T)$ and $v_3(p_T)$, for 0-5% central p+Au, d+Au, and ^{3}He+Au collisions at $\sqrt{s_{NN}} = 200$ GeV, as measured by the PHENIX experiment. The colored bands correspond to the same quantity calculated using the SONIC and iEBE-VISHNU hydrodynamic models. Figure reproduced from [41].

Following the above discussion, it is of interest to further scrutinize the relation between geometry and flow. The left panel of Fig. 3.5 shows the ratio v_2/ε_2 for all three systems. The lack of a common linear scaling $v_n \propto \varepsilon_n$ for all systems, as would otherwise be expected from ideal hydrodynamics up to viscous corrections in A+A collisions, far from indicating the absence of QGP, attests to the peculiarities of small systems as shown in the right panel of Fig. 3.5. There, the v_2/ε_2 ratio is shown for individual events from hydrodynamic simulations as a function of the initial ε. It can be seen that the desired scaling does exist, yet breaks for events with high ellipticity. The physical interpretation of this observation may be of short-lived QGP droplets that—when the initial hotspots are far enough apart—cannot achieve the full translation of the elliptical or triangular geometry into the final state.

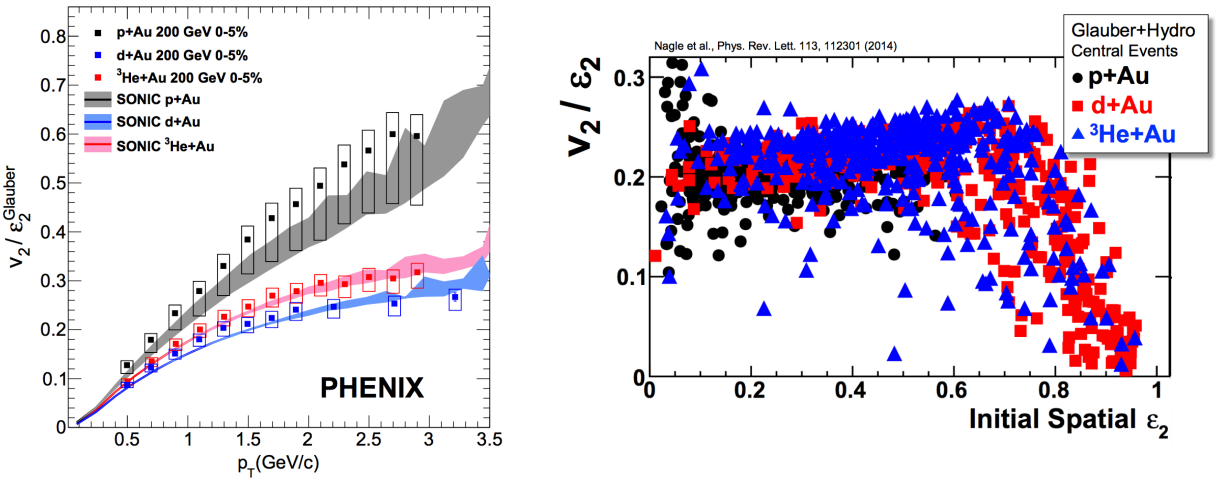

Figure 3.5: Ratio of elliptic flow $v_2(p_T)$ to initial eccentricity ε_2, for 0-5% central d+Au, and ^{3}He+Au collisions at $\sqrt{s_{NN}}$ = 200 GeV, as measured by the PHENIX experiment. The colored bands correspond to the same quantity calculated using the SONIC hydrodynamic model. Figures reproduced from [151, 38]

3.2.3 Multi-particle Correlations

Early measurements demonstrating collective behavior in small collision systems consisted of correlations involving only pairs of particles. However, if it is truly collective behavior related to the initial geometry that is being measured, then it should manifest itself as a global correlation among many particles in every event. These multi-particle correlations are measured using mathematical objects called cumulants [62], related to the moments of a probability distribution. The k^{th} order cumulant corresponding to the n^{th} flow harmonic is denoted $c_n\{k\}$, where k indicates the number of particles over which the correlation is being measured. The expressions for two-, four-, and six-particle cumulants are given below in terms of $\langle\langle k \rangle\rangle$—the so-called k-particle correlator—where

the double brackets denote the averaging over particles in a single event, and then over all events.

$$c_n\{2\} = \langle\langle 2\rangle\rangle = \langle\langle \cos[n(\phi_1 - \phi_2)]\rangle\rangle, \tag{3.1}$$

$$c_n\{4\} = \langle\langle 4\rangle\rangle - 2\langle\langle 2\rangle\rangle^2 = \langle\langle \cos[n(\phi_1 + \phi_2 - \phi_3 - \phi_4)]\rangle\rangle - 2\langle\langle 2\rangle\rangle^2, \tag{3.2}$$

$$c_n\{6\} = \langle\langle 6\rangle\rangle - 9\langle\langle 4\rangle\rangle\langle\langle 2\rangle\rangle + 12\langle\langle 2\rangle\rangle^3 = \langle\langle \cos[n(\phi_1+\phi_2+\phi_3-\phi_4-\phi_5-\phi_6)]\rangle\rangle - 9\langle\langle 4\rangle\rangle\langle\langle 2\rangle\rangle + 12\langle\langle 2\rangle\rangle^3. \tag{3.3}$$

The equations above explicitly contain averages taken over all combination of k particles, $\phi_1 \ldots \phi_k$ in a given event. In practice, finding all such combinations is computationally unfeasible even in events with modest multiplicity, so closed-form expressions for $\langle\langle k\rangle\rangle$ are used instead, as described in [62]. Flow anisotropies $v_n\{k\}$ can then be calculated from the cumulants as follows:

$$\begin{aligned} v_n\{2\} &= (c_n\{2\})^{1/2} \\ v_n\{4\} &= (-c_n\{4\})^{1/4} \\ v_n\{6\} &= (c_n\{6\}/4)^{1/6}. \end{aligned} \tag{3.4}$$

An advantage of the multi-particle cumulant formalism over other forms of calculating v_n is that many sources of angular correlations, collectively called non-flow, are not global, involving only a small number of particles. Along these lines, the $v_n\{k\}$ calculated using multi-particle cumulants becomes less sensitive to non-flow effects for higher values of k. Additionally, it has been shown that cumulants can provide information on event-by-event fluctuations in v_n [159], which are particularly relevant in small systems where the initial energy density is highly sensitive to fluctuations in nucleon coordinates upon impact.

Fig. 3.6 shows PHENIX measurements [40] of $v_2\{2\}$, $v_2\{2, |\Delta\eta| > 2\}$, and $v_2\{4\}$ for d+Au collisions at a variety of center-of-mass collision energies, ranging from $\sqrt{s_{NN}} = 19.6$ GeV, to $\sqrt{s_{NN}} = 200$ GeV. In this last case, the figure also shows $v_2\{6\}$. The salient feature of the plot

is that a real-valued $v_2\{4\}$ is measured at all collision energies, which constitutes evidence for collectivity. This point is reinforced at the highest collision energy where $v_2\{2\} < v_2\{4\} \approx v_2\{6\}$, indicating that the observed correlations are truly global in character and that non-flow involves only a limited number of particles. Multi-particle correlation techniques were also applied to p+Au collisions at $\sqrt{s_{NN}} = 200$ GeV, in which case a negative $c_2\{4\}$ was found, leading to complex-valued $v_2\{4\}$. A limitation of cumulant-based analyses in small systems at RHIC is the low multiplicity of this type of collisions making the results more sensitive to effects such as fluctuations, particularly at the lower collision energies. A full discussion of these limitations is beyond the scope of this thesis, and the reader is referred to Ref. [40].

On the other hand, small system collisions at LHC energies exhibit much higher event multiplicities than at RHIC. Fig. 3.7 shows $v_2\{k\}$ in $p+p$, p+Pb, and Pb+Pb at the LHC. Unlike at RHIC, it is possible to measure even $v_2\{8\}$ in p+Pb collisions. It can be seen that, just as in the large Pb+Pb system, small systems also exhibit a substantial elliptic flow, with $v_2\{2\} > v_2\{4\} \approx v_2\{6\} \approx v_2\{8\}$.

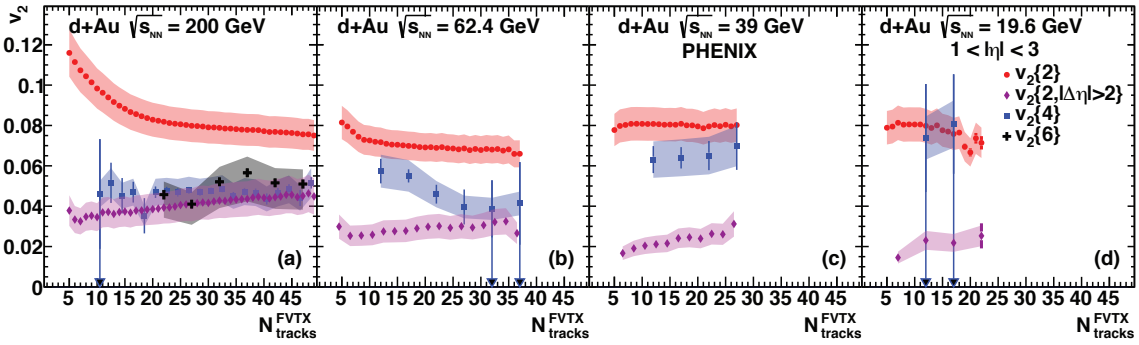

Figure 3.6: Multiplicity dependence of elliptic flow v_2, measured in d+Au collisions at RHIC, at a variety of collision energies, using multiparticle cumulants. Figure reproduced from [40].

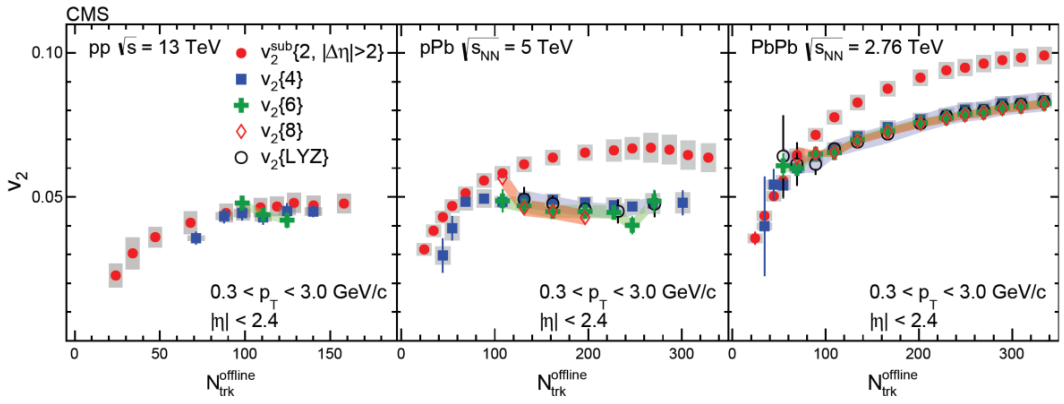

Figure 3.7: Multiplicity dependence of elliptic flow v_2, measured in $p+p$, p+Pb, and Pb+Pb collisions at the LHC using multiparticle cumulants and Lee-Yang zeroes. Figure reproduced from [127].

3.2.4 Mass Dependence of Azimuthal Anisotropy

The final signature consequence of collectivity in large systems, as considered in this dissertation, is the dependence of v_n on the mass of identified final-state particles. If we picture the the QGP as experiencing a strong radial expansion during the hydrodynamic phase, then upon hadronization of individual fluid elements each produced hadron will be subjected to a common velocity boost. As a consequence, hadrons of higher mass will exhibit an azimuthal anisotropy pattern that is shifted to higher p_T, resulting in a mass ordering of the measured v_n. This hallmark signature of hydrodynamic expansion is shown in Fig. 3.8 for $p+p$, d+Au, and p+Pb. There, it can be seen how heavy baryons appear to exhibit a 'lower' v_2 than the lighter mesons, as the curve is shifted to higher p_T.

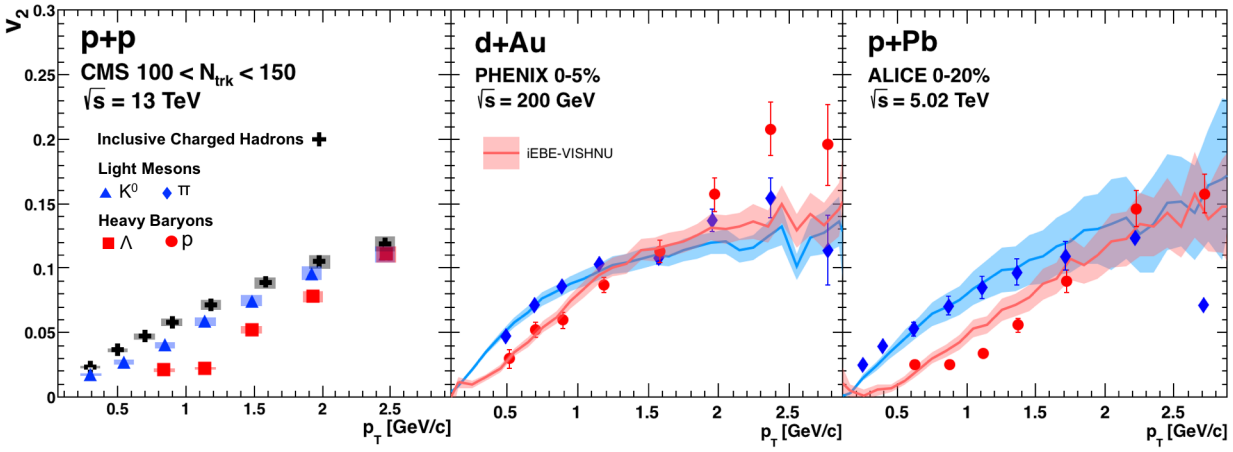

Figure 3.8: Transverse momentum dependence of v_2 as measured for identified protons and charged pions in p+Au, d+Au, and ^{3}He+Au collisions at $\sqrt{s_{NN}} = 200$ GeV at RHIC. The data are compared to hydrodynamic calculations from the iEBE-VISHNU model, with and without a hadronic rescattering stage. Figure reproduced from [154].

Chapter 4

A Kinetic Transport Approach to Collectivity in Small Collision Systems

The previous chapter presented a comprehensive survey of collective behavior in small collision systems. A wealth of experimental observations prove that in most respects, with jet quenching being a most notable exception, collectivity in both large and small systems is remarkably similar and directly related to the spatial anisotropy of the initial state. However, since the identification of collectivity signals with QGP formation is not yet univocal, it is of interest to examine other models besides viscous hydrodynamics also capable of accomplishing the translation of intial geometry into the final state.

Along these lines, this chapter will examine small system collectivity in the context of kinetic transport theory. Kinetic transport models are not new; in fact, they were being applied to heavy-ion collisions long before the advent of modern relativistic hydrodynamic models, in order to understand hot nuclear matter in terms of quasiparticle scattering. We begin by reviewing the history of transport models, focusing on a particular model called AMPT. We then systematically examine the origin of collective behavior in this model, and the extent to which it can account for experimental observations in a variety of small systems. Lastly, we examine the minimal conditions and assumptions required to sucessfully account for the observed experimental results.

The results of this chapter have been published in the following journal articles:

- J. Orjuela Koop, A. Adare, D. McGlinchey, J.L. Nagle. *Azimuthal anisotropy relative to the participant plane from a multiphase transport model in central p + Au , d + Au , and ^{3}He + Au collisions at $\sqrt{s_{NN}} = 200$ GeV.* Physical Review C 92 054903 (2015)

- J. Orjuela Koop, R. Belmont, P. Yin, and J.L. Nagle. *Exploring the Beam Energy Dependence of Flow-Like Signatures in Small System d+Au Collisions.* Physical Review C 93 044910 (2016)

- J.L. Nagle, R. Belmont, K. Hill, J. Orjuela Koop, D.V. Perepelitsa, P. Yin, Z-W. Lin, D. McGlinchey. *Minimal conditions for collectivity in e^+e^- and $p+p$ collisions.* Physical Review C 97 024909 (2018)

- J.L. Nagle, J. Orjuela-Koop. *A Quasiparticle Transport Explanation for Collectivity in the Smallest of Collision Systems ($p+p$ and e^+e^-).* Proceedings of the 27th International Conference on Ultrarelativistic Nucleus-Nucleus Collisions (Quark Matter 2018) Venice, Italy, May 14-19, 2018. `arXiv:1807.04619`

4.1 Introduction to Transport Models in Heavy Ion Collisions

4.1.1 Why Transport Models?

The standard model of heavy-ion collisions relies on two different types of theoretical calculations. On one hand, lattice QCD provides information on the bulk thermodynamics of the QGP from first principles—most notably, the equation of state. On the other hand, the dynamic evolution—impossible to derive from first principles—is described by relativistic viscous hydrodynamics. Hydrodynamic models as applied to heavy-ion collisions have a long history, which can be traced back to Landau [133] and his study of strong interaction phenomenology and statistical particle production in $p+p$ collisions. However, it was not until half a century later that the theory of ultrarelativistic viscous hydrodynamics and its numerical implementation was developed to the point of allowing key parameters of the QGP, such as the shear viscosity, to be constrained from experimental data [171]. Prior to the hydrodynamic paradigm of the standard model of nuclear collisions, a variety of models existed, each one addressing limited aspects of nuclear collisions.

Among these, transport models were developed starting in the late 1980s to provide a fully microscopic description of high energy heavy-ion collisions, starting from as fundamental physi-

cal principles as possible. Transport models make use of kinetic theory, a general mathematical formalism suited to describe the dynamics of many-body systems of particles in terms of a distribution function in phase space, $f(\vec{r},\vec{p})$ [75]. Physically, the distribution function provides the average number of particles $f(x,p)d^3xd^3p$ with momenta between $\vec{p}$ and $\vec{p}+d\vec{p}$, within a volume d^3x. Several important quantities can be defined in terms of the distribution function, such as the energy momentum tensor

$$T^{\mu\nu} = \int \frac{d^3p}{p^0} p^\mu p^\nu f(x,p), \tag{4.1}$$

and the particle four-flow

$$N^\mu(x) = \int \frac{d^3p}{p^0} p^\mu f(x,p). \tag{4.2}$$

In turn, the above quantities can be used to calculate macroscopic system variables such as the particle density $n = N^\mu u_\mu$, and energy density $\varepsilon = u_\mu T^{\mu\nu} u_\nu$, with u^μ being the hydrodynamic four-velocity.

When the system experiences an external perturbation that causes it to depart from equilibrium, the distribution function starts to evolve in space and time, governed by an integro-differential equation known as the kinetic equation which describes changes in the occupancy of boost-invariant elements of phase space. The earliest such equation is the Boltzmann equation. In a collisionless system, the net flux of particles through the surface Δ^3x of a 4-volume Δ^4x vanishes,

$$\int_{\Delta^4x}\int_{\Delta^3x} d^4x \frac{d^3p}{p^0} p^\mu \partial_\mu f(x,p) = 0, \tag{4.3}$$

leading to the Boltzmann equation, as follows

$$\left(\partial_t + \frac{\vec{p}}{p^0}\cdot\nabla\right) f(x,p) = 0. \tag{4.4}$$

If particle collisions are now included, the net flux of particles, as described by Eq. 4.3, will no longer vanish. Instead, it will take the form

$$\int_{\Delta^4x}\int_{\Delta^3x} d^4x \frac{d^3p}{p^0} p^\mu \partial_\mu f(x,p) = \Delta^4x \frac{\Delta^3p}{p^0} C(x,p), \tag{4.5}$$

where certain assumptions are needed to calculate the function $C(x,p)$. Namely, Boltzmann transport assumes (i) that the system is dilute enough so that only $2 \to 2$ scattering is important; (ii)

that the momenta of interacting pairs of particles are uncorrelated; (*iii*) that $f(x,p)$ is a slowly varying function; and (*iv*) that scattering events are instantaneous. In that case, the Boltzmann equation becomes

$$p^\mu \partial_\mu f = \frac{1}{2}\int \frac{d^3p_2}{p_2^0}\frac{d^3p_3}{p_3^0}\frac{d^3p_4}{p_4^0} W(p_3p_4 \mid p_1p_2) \times[f(x,p_3)f(x,p_4) - f(x,p_1)f(x,p_2)], \tag{4.6}$$

where the $W(p_3p_4 \mid p_1p_2)$ factor corresponds to the transition rate for the $\vec{p}_1 + \vec{p}_2 \rightarrow \vec{p}_3 + \vec{p}_4$ scattering process [75].

As written above, the transport equation describes classical systems, such as the gases Boltzmann originally studied in the 19$^{\text{th}}$ century. However, various refinements are possible. The first such refinement considered here is the inclusion of quantum effects arising from the bosonic or fermionic nature of the particles. When dealing with fermions, certain scattering events can be Pauli-blocked, whereas the probability of certain scattering processes will be enhanced for bosons. It can be shown that the Boltzmann equation will then take the following form

$$p^\mu \partial_\mu f = \frac{1}{2}\int \frac{d^3p_2}{p_2^0}\frac{d^3p_3}{p_3^0}\frac{d^3p_4}{p_4^0} W(p_3p_4 \mid p_1p_2)[f(x,p_3)f(x,p_4)\bar{f}(x,p_1)\bar{f}(x,p_2) - f(x,p_1)f(x,p_2)f\bar{f}(x,p_3)\bar{f}(x,p_4)], \tag{4.7}$$

where $\bar{f} = 1 + \epsilon h^3 f$, with $\epsilon = 1$ for bosons and $\epsilon = -1$ for fermions. This equation is known as the Boltzmann-Uehling-Uhlenbeck (BUU) equation [75].

The above semi-classical transport equation can be solved numerically with a Monte Carlo approach, treating the partons as point-like particles following classical trajectories and undergoing binary scattering. A collision between two partons is said to occur if they come within a distance $\sqrt{\sigma_{\text{part}}/\pi}$ of each other. Ref. [106] provides a detailed description of how the Monte Carlo sampling of particle pairs is carried out in accordance with the transport equation. This approach, while admittedly Glauber-like, is referred to in the literature as a partonic cascade. It is particularly useful for the study of hot nuclear matter since it makes no assumption about the phase space distribution of partons, thus allowing for the study of systems far from equilibrium.

4.1.2 A Multi-Phase Transport Model—AMPT

The AMPT model was developed in the early 2000s to provide a unified description of the full space-time evolution of heavy-ion collisions [138]. Organized as a workflow of various algorithms, each modeling a specific stage of the system's evolution as discussed in Chapter 3, it uses standard kinetic theory to model the QGP stage as a collection of interacting quasiparticles, thus accounting for its the non-equilibrium dynamics of the many-body system. Historically, this avenue of investigation was motivated by the belief that the QGP could never fully reach thermal equilibrium. Even though such viewpoint eventually lost ground to the hydrodynamic paradigm of heavy-ion collisions, AMPT remained a useful model for the exploration of new ideas[1] , particularly in regimes where hydrodynamics is expected to break down, such as small collision systems.

There are two variants of the AMPT model: the *default* and the *string melting* version, the latter being applicable when the energy density is well above the critical density of the phase transition in QCD, as is typically the case at RHIC collision energies. Both versions consist of the same sequence of stages—(*i*) initial conditions, (*ii*) partonic scattering, (*iii*) hadronization, and (*iv*) hadronic scattering—albeit with variations in their implementation. The present dissertation analysis makes use of the string melting version with a series of custom modifications. We now describe each stage of the model, with emphasis on the string melting implementation. Fig. 4.1 compares the stages involved in each implementation of the model, as described in the following subsections.

[1] A notable example of such use of AMPT was the introduction of triangular flow v_3 from event-by-event fluctuations in the initial geometry of A+A collisions [46]. This study demonstrated that long-range azimuthal two-particle correlations measured experimentally contain a third-order harmonic contribution whose magnitude is proportional to the triangularity ε_3 of the participant nucleons, as induced by nucleon coordinate fluctuations in an otherwise intrinsically elliptic geometry. This finding definitively dispelled the notion that such higher harmonics originated from *Mach cones* in the GQP [192].

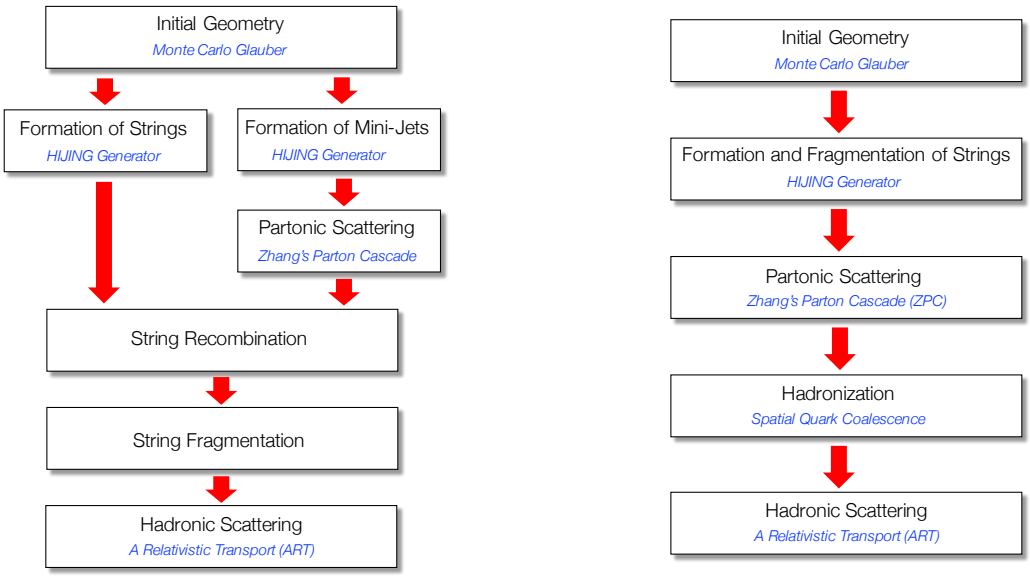

Figure 4.1: Structure and workflow of the AMPT model in its (left) default and (right) string melting implementations.

4.1.2.1 Initial Conditions

This stage consists of two distinct parts: the determination of initial geometry, and the production of partons from nucleon-nucleon collisions. For both of these, AMPT uses the HIJING event generator [197].[2] The initial coordinates of the nucleons in the projectile and target nuclei are sampled randomly from the appropriate density distribution for the nuclear species at hand. By default, the coordinates for any nucleus are sampled from the Woods-Saxon distribution

$$\rho(r) = \frac{\rho_0}{1 + \exp((r - R)/a)} \tag{4.8}$$

[2] The HIJING model is a Monte Carlo event generator for the study of $p + p$, p+A, and A+A collisions developed in the early 1990s for the study of various phenomenological aspects of heavy ion collisions. It is noteworthy in that it incorporates both soft (i.e., production of Lund color strings) and hard physics for particle production (i.e., perturbative QCD processes as implemented in PYTHIA), while also accounting for shadowing (as a cold nuclear matter effect in the initial state) and energy loss (as a final-state effect in hot nuclear matter). This made the model particularly useful for studying the initial conditions of heavy ion collisions, at a time of transition between the lower SPS and AGS energies, and the higher RHIC energies where pQCD was expected to play a more significant role in particle production than before. A full description of the HIJING generator can be found in [197], with details provided here only as necessary to describe the initialization of AMPT.

with $R \sim A^{1/3}$ and a being the diffuseness parameter. However, in the case of deuteron, the nucleon coordinates are sampled from the Hulthén wavefunction [33]

$$\psi_d(r) = \sqrt{\frac{\alpha\beta(\alpha+\beta)}{2\pi(\alpha-\beta)^2}}\frac{\exp(-\alpha r) - \exp(-\beta r)}{r} \tag{4.9}$$

whose norm $|\psi_d|^2$ corresponds to the probability of the proton and neutron being separated by a distance r, with $\alpha = 0.228$ fm $^{-1}$ and $\beta = 1.18$ fm $^{-1}$. Finally, in the case of ^{3}He, we modified the code to use the nucleon coordinates as determined from a Green's function Monte Carlo calculation using the AV18+UIX model of three-body interactions [73].

Having defined the coordinates of nucleons in the projectile and target, wounded nucleons are determined based on a diffuse nucleon cross section, which we modified to be a sharp cross section, or black disk, to better match the Monte Carlo Glauber approach in Ref. [139]. Multi-nucleon interactions are treated in the eikonal approximation, in which projectile nucleons remain undeflected as they bore a hole through the target. Particle production then proceeds depending on the scale of momentum transfer. Above some cutoff momentum, pertubative QCD is used to evaluate hard processes leading to the production of so-called minijets.[3] Below the cutoff, soft particle production is treated through the formation of Lund color strings [49]. In the default version of AMPT, only the minijet partons enter the subsequent parton scattering stage. On the other hand, in the string melting version, the strings fragment into hadrons which disassociate into their respective quark content, entering the partonic scattering stage along with the minijet partons.

However, partons do not start interacting immediately after their production. A *formation time* is imposed, defined as an interval during which the partons free-stream before being allowed to interact. Such a construct is introduced to account for the early time multi-body dynamics during which partons cannot be treated as independent particles. In reality, there is no reason

[3] Technically, there is a distinction between *jets* and *minijets*. Jets are usually defined as correlated sprays of particles associated with a hard parton scattering process, whose energy and shape can be determined experimentally. Nevertheless, hard processes will lead to the same type of particle correlations even if their energy is too low to be reconstructed over the underlying event background. In that case, they receive the name 'minijets'. In the context at hand, we are not interested in this distinction and the term is used simply to refer to particles originating from hard processes, calculable with perturbative QCD.

to believe that partons do not interact during this time, but the impossibility of modeling that early-time physics leads to this simplifying assumption. In the string melting version of the model, the formation time of a given parton is defined as

$$t_f = \frac{E}{m_T^2}, \tag{4.10}$$

where E and m_T are the energy and mass of the *hadron* from which it emerged. The form of this particular expression can be shown to follow from uncertainty principle arguments, and is important for the interpretation of AMPT results. This will be the subject of subsection 4.2.6. However, the dependence of the formation time on the hadron—rather than the parton—kinematics is an ad hoc choice, intended as a bookkeeping device for the subsequent coalescence of partons back into hadrons. For this very reason, all partons in the AMPT model are exclusively (anti)quarks, with gluons not being incorporated.

4.1.2.2 Partonic Scattering

The implementation of partonic scattering using Zhang's Parton Cascade (ZPC) [205] is common to both versions of the AMPT model. This is the core of the model, where the hot nuclear matter medium is represented as a collection of scattering quasiparticles, with the particular feature that all partons are (anti)quarks, with no gluons. In this stage, the partons produced in the collision (both string and minijet partons in the string melting version, and only minijet partons in the default version) are allowed to interact according to the following set of Boltzmann transport equations for the time evolution of the phase space density distribution $f(\vec{x}, \vec{p}, t)$:

$$\begin{aligned} p^\mu \partial_m f_a(\vec{x}, \vec{p}, t) = &\sum_m \sum_{b_1, b_2, \cdots, b_m} \int \prod_{i=1}^{m} \frac{d^3 p_{b_i}}{(2\pi)^3 2E_{b_i}} f_{b_i}(\vec{x}, \vec{p}_b, t) \\ &\times \sum_n \sum_{c_1, c_2, \cdots, c_n} \int \prod_{j=1}^{n} \frac{d^3 p_{c_j}}{(2\pi)^3 2E_{c_j}} |M_{m\to n}|^2 \\ &\times (2\pi)^4 \delta^4 \left(\sum_{k=1}^{m} p_{b_k} - \sum_{l=1}^{n} p_{c_l} \right) \\ &\times \left[-\sum_{q=1}^{m} \delta_{ab_q} \delta^3(\vec{p} - \vec{p}_{b_q}) + \sum_{r=1}^{n} \delta_{ac_r} \delta^3(\vec{p} - \vec{p}_{c_r}) \right]. \end{aligned} \tag{4.11}$$

The formulation of the above equations is very general, describing multiparton interactions with matrix elements $|M_{m\to n}|$. The equations are simplified considerably by restricting the model to the case of two-body quark-quark interactions, which are then numerically solved in time steps by the ZPC code. Two partons are said to interact when at a given time step they come within a distance $b = \sqrt{\sigma/\pi}$ of each other. The scattering cross section σ is calculated in QCD to leading order [205, 138], for scattering angles within $0 < \phi < \pi$, yielding

$$\frac{d\sigma}{dt} \approx \frac{9\pi\alpha_s^2}{2t^2}, \tag{4.12}$$

where t is the standard Mandelstam variable and α_s is the strong coupling constant. The expression is undefined at $t = 0$, so a parameter μ is introduced to regularize the divergence as follows:

$$\frac{d\sigma}{dt} = \frac{9\pi\alpha_s^2}{2(t-\mu)^2}. \tag{4.13}$$

This regularization parameter is physically interpreted as the Debye screening mass, or equivalently, the inverse screening length for a parton in the medium. The expression for the differential cross section can be integrated to arrive at the total partonic cross section used in the AMPT model:

$$\sigma \approx \frac{9\pi\alpha_s^2}{2\mu^2}. \tag{4.14}$$

In the model, a fixed scale $\alpha_s = 0.47$ is selected, and it is the parton screening mass that is specified, uniquely related to the cross section as follows,

$$\mu[\mathrm{fm}^{-1}] = \sqrt{31.2287/\sigma[\mathrm{mb}]}. \tag{4.15}$$

Another important feature of parton scattering, as calculated in QCD, is the anisotropic distribution of parton-parton scattering angles. The left panel of Fig. 4.2 shows the probability distribution of the scattering angle θ in $2 \to 2$ parton interactions. The solid black curve, for all partons, demonstrates that partons are much more likely to scatter at forward angles. However, if we discriminate by the center-of-mass energy of the scattering event, it is possible to see that the distribution becomes more isotropic with decreasing energy. This preferential scattering direction will be seen, in the following sections, to play a large role in the development of collectivity in

very small collision systems without a clear initial geometry. For comparison, the right panel of Fig. 4.2 shows the unnormalized distribution of scattering angles in another partonic transport model, called BAMPS [202, 203]. In the particular case of $2 \rightarrow 2$ scattering, the distribution is also anisotropic and qualitatively similar to AMPT.

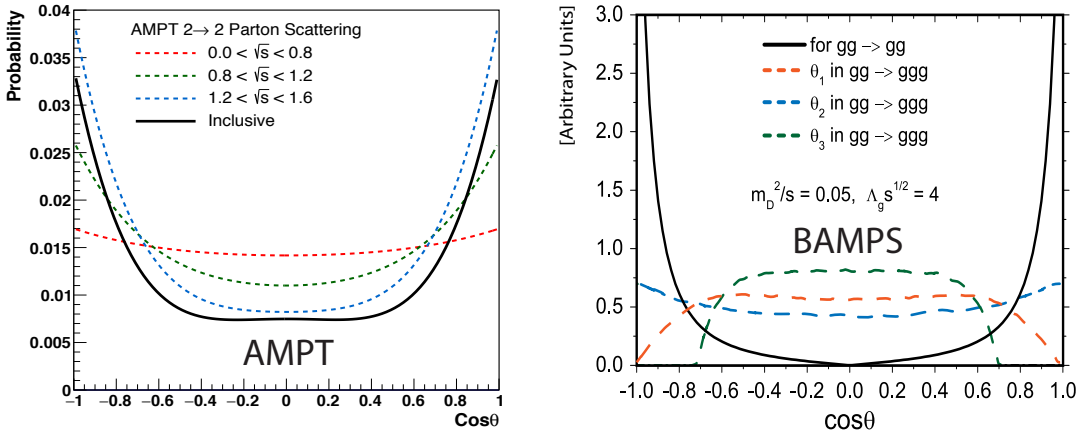

Figure 4.2: (left) Distribution of scattering angles in AMPT for various center-of-mass energies of the parton-parton interaction. (right) Distribution of scattering angles in the BAMPS model.

4.1.2.3 Hadronization

The two versions of the AMPT model have very different approaches to hadronization. The string melting version uses a straightforward coalescence approach based on spatial proximity, grouping nearby partons into quark-antiquark pairs to form mesons, and into groups of three (anti)quarks to form baryons. Unlike other coalescence prescriptions [102], the model does not consider the relative momentum of the partons as a criterion for recombination. That is, a pair of partons with momenta in opposite directions have the same chance of recombining as they would if their momenta were colinear, provided they are spatially close together. This process can take place all throughout the partonic cascade stage, following the kinetic freezeout of individual partons, resulting in a mixed parton-hadron phase. The species of the resulting hadron is determined by the flavor of the recombined quarks, treated as valence particles. In the case of hadrons with the

same valence quark content, the choice is disambiguated by selecting the hadronic state whose mass is closest to the invariant mass of the quarks. In this coalescence procedure, the formation of the η', Σ^*, Ξ^*, K_S^0, and K_L^0 states is explicitly precluded, as they are not implemented in the hadronic cascade stage of the model. As described, this simple coalescence procedure violates the conservation of four-momentum (though three-momentum *is* conserved), as well as the second law of thermodynamics, which is a common feature of all coalescence models.

On the other hand, the default AMPT model makes use of a more sophisticated approach to hadronization, in which the minijet partons taking part in ZPC recombine with the soft strings at the end of the cascade. This leads to the formation of excited strings, which fragment into hadrons according to the Lund string model [49].

4.1.2.4 Hadronic Scattering

Once hadronization has taken place, the hadrons enter a final scattering stage, including both elastic and inelastic hadronic interactions, consisting of a modified version of the model known as A Relativistic Transport (ART) [136], common to both the default and string melting versions of AMPT. The ART model was originally developed in the mid-1990s to study nuclear collisions at AGS energies. It implements a numerical solution of the previously described Boltzmann-Uehling-Uhlenbeck (BUU) kinetic equation, explicitly including (in)elastic processes for baryon-baryon, meson-baryon, and meson-meson interactions with isospin degrees of freedom. The fundamental reactions are as follows, with details on the cross sections found in [136].

- $NN \longleftrightarrow N\Delta$, $NN^*(1440)$, $NN^*(1535)$
- $NN \longleftrightarrow \Delta\Delta$, $\Delta N^*(1440)$
- $NN \longleftrightarrow NN\rho$, $NN\omega$, $\Delta\Delta\pi$
- $NN \longleftrightarrow \Delta\Delta\rho$
- $N\Delta \longleftrightarrow NN^*(1440)$, $NN^*(1535)$

- $\Delta\Delta \longleftrightarrow NN^*(1440),\ NN^*(1535)$
- $\Delta N^*(1440) \longleftrightarrow NN^*(1535)$
- $\pi N \longleftrightarrow \Delta,\ N^*(1440),\ N^*(1535)$
- $\eta N \longleftrightarrow N^*(1535)$
- $\pi + N(\Delta, N^*) \rightarrow \pi + N(\Delta, N*)$
- $\rho + N(\Delta, N*) \rightarrow \rho + N(\Delta, N*)$
- $K + N(\Delta, N*) \rightarrow K + N(\Delta, N*)$
- $\pi + \pi \rightarrow \rho$
- $\pi + \pi \rightarrow \pi + \pi$

4.1.3 Origin of Azimuthal Anisotropy in AMPT

Having described the structure and physics behind the AMPT model, but before delving into the analysis of various aspects of collectivity in the Section 4.2, it is necessary to first establish the basic underlying mechanism by which azimuthal anisotropy in momentum space develops in AMPT. Even though ideal hydrodynamics follows from kinetic theory in the zero-mean free path limit[4] [169], the majority of the final-state azimuthal anisotropy in AMPT does not build up through repeated collisions of partons following some collective velocity field (i.e., a hydrodynamic-like mechanism). Instead, He et al. have shown [117] that in AMPT the dominant mechanism responsible for final-state azimuthal anisotropy is the spatially anisotropic probability of partons to 'escape' the partonic scattering stage—that is, to hadronize. This holds true both in large and small collision systems.

To see how this comes about, consider Fig. 4.3(a), which shows the probability of a given parton to freeze out after having undergone N_{coll} collisions, or scatterings, during the partonic

[4] Viscous hydrodynamics can be recovered from higher order corrections to this limit.

scattering stage, in central d+Au and semi-central Au+Au collisions. In both cases, the most likely outcome for a given parton is to not scatter at all (i.e., $N_{\rm scatt} = 0$). The probability of not scattering is much higher in d+Au because fewer partons are produced, even in central collisions, compared to semi-central Au+Au events. Figure 4.3(b) shows the transverse radial distribution of partons for various values of $N_{\rm scatt}$. We see that the partons that freezeout without ever scattering tend to reside far away from the center of the interaction region (solid red line), whereas those that freeze out after $N_{\rm scatt} = 5$ are found closer to the center (solid blue line). The dashed lines correspond to partons that continue to scatter after a given number of collisions have taken place (so-called *active* partons), again showing that those that scatter more are found near the center. These plots suggest a picture of an inwardly moving freeze-out surface. The fact that most partons do not scatter in d+Au lends credence to the idea that the hydro-like mechanism is subdominant in this transport model. Instead, the geometry of the interaction region and the dynamics of freeze-out become relevant to understanding how momentum azimuthal anisotropy develops.

Fig. 4.4(a) shows, for semicentral Au+Au collisions, the evolution of v_2 for partons, as a function of the number of scatters they experience, $N_{\rm scatt}$. For a given value of $N_{\rm scatt}$, partons can be classified into two groups: those that scatter exactly $N_{\rm scatt}$ times before freezing out, and those that will continue to scatter at least $N_{\rm scatt} + 1$ times. The solid blue curve, corresponds to both these groups combined. At $N_{\rm scatt} = 0$, the v_2 vanishes because, at the moment of creation, all partons are emitted radially from a color string, regardless of whether they will subsequently scatter. Then, a modest positive v_2 develops with increasing number of parton scatters.

If we now examine the partons that scatter exactly $N_{\rm scatt}$ times before freezeout (red solid curve), it is seen that partons with $N_{\rm scatt} = 0$ have a very large v_2. This can be understood if, due to purely geometric effects, partons have a greater probability of freezing out along the minor axis of the elliptic overlap region, than along the major axis. This is referred to as the anisotropic probability of escaping the parton cascade. However, as partons continue to scatter, the initial ellipticity of the interaction region becomes more circular, with the freezeout probability becoming more spatially isotropic, leading to the observed decrease in v_2.

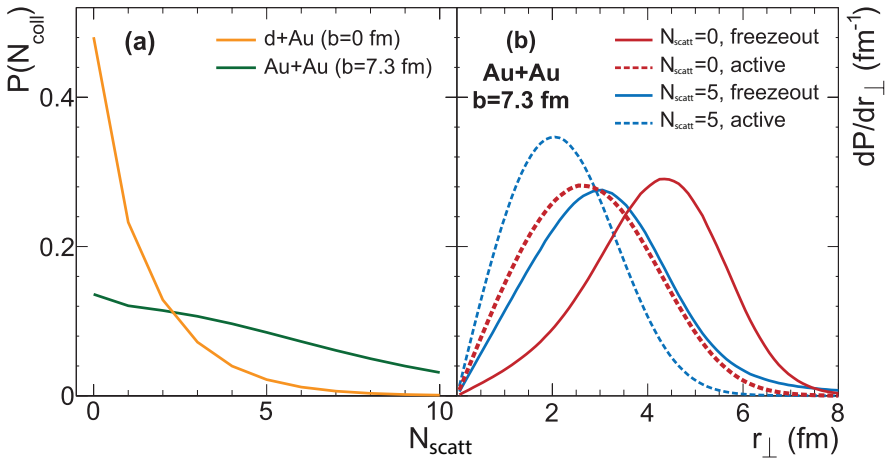

Figure 4.3: (a) Probability of partons to freeze out of the scattering stage following $N_{\rm scatt}$ scatterings, in central d+Au and semi-central Au+Au collisions in AMPT with $\sigma_{\rm part} = 3.0$ mb. (b) Transverse radial distribution of partons that freeze out after exactly $N_{\rm scatt}$ scatterings (solid line), and those that continue to interact (dashed line). Plot adapted from [117].

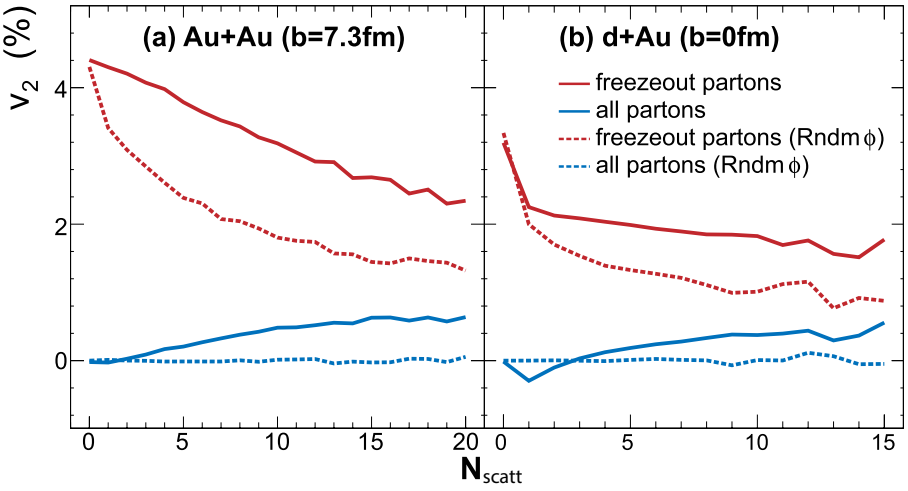

Figure 4.4: Parton elliptic flow v_2 as a function of the number of collisions $N_{\rm scatt}$ experienced by freezeout and inclusive partons in AMPT, in (a) semicentral Au+Au, and (b) central d+Au events. Dashed lines correspond to the case where the azimuthal orientation of a parton is randomized following each collision. Plot adapted from [117].

It is now of interest to disentangle the anisotropic escape probability from the hydrodynamic-like source of final-state azimuthal anisotropy. Since the hydro-like mechanism proceeds through repeated parton scattering, it can be "turned off" by randomizing the angle of every scattered parton *in the lab frame*. Clearly, this artificial procedure violates the conservation of momentum, yet in doing so also gets rid of the hydrodynamic flow field, which depends on energy-momentum conservation, $\partial_\mu T^{\mu\nu}=0$. The dotted lines in Fig. 4.4(a) correspond to the randomization of scattering angles. In such case, the v_2 of inclusive partons collapses to zero, while that of partons freezing after exactly $N_{\rm scatt}$ is still substantial, yet lower than when the angle is not randomized. Panel 4.4(b) shows that this same argument holds in d+Au collisions

The anisotropic escape mechanism described above accounts for azimuthal anisotropy arising from the partonic scattering phase *alone*. The other stages following partonic scattering, namely hadronization and the hadronic cascade, also contribute to the the azimuthal anisotropy measured among final-state hadrons, as will be discussed in Section 4.2.

4.2 Results of the Study of Small System Collectivity in AMPT

Having described the AMPT model, we now turn to the study of small system collectivity observations in the context of transport models, where the QGP is thought of as a collection of scattering quasiparticles. In the context at hand, the term *quasiparticle* refers to the partons having a well defined mass and momentum. We present the contribution of this dissertation to the understanding of small system collectivity, regarding geometry engineering and the translation of initial geometry into final-state anisotropy in transport models, proceeding then to examine the lowest threshold, both in system size and collision energy, for the observation of collective behavior.

4.2.1 Geometry Engineering in Asymmetric Systems

Section 3.2 presented an argument for the formation of QGP droplets in the collisions of small asymmetric systems, as a means of explaining observed momentum-space azimuthal anisotropy among final state particles. The crux of the argument consists in varying the initial intrinsic geom-

etry of the projectile nucleus in a controlled manner, and correlating the topology of the collision with the angular emission pattern of the final-state particles, as quantified through anistropy moments v_n. Independently of any comparison with theoretical models, the *geometry engineering* experiments provide strong evidence that initial geometry is translated into the final-state momentum space; any support for a given theory of small system collectivity then arises from agreement between its calculations and experimental evidence. Nevertheless, objections regarding the validity of the near-inviscid hydrodynamic calculations in small systems have been put forth in regards to the expansion around steep energy density gradients in these systems, as well as their limited size and lifetime [168, 167, 155].

It is therefore interesting to examine an altogether different kind of model—namely AMPT, as an instance of the broader class of transport models—which can also translate initial geometry into the final state. Since the mechanism by which this translation comes about is very different from hydrodynamics, the possibility of incoherent parton scattering also describing experimental data related to small system collectivity is quite interesting. It has been shown [67, 141] that AMPT can reproduce long-range azimuthal correlations and elliptic flow in high-multiplicity $p+p$ and p+Pb at LHC energies. Therefore, it is of interest to determine whether AMPT can provide a unified framework to describe the results of geometry engineering experiments, involving p+Au, d+Au, and ^{3}He+Au at RHIC energies.

We use AMPT in its string melting implementation, with the custom modifications described in Section 4.1.2.1 relating to the initialization of event geometry. We ran approximately 10 million central p+Au, d+Au and ^{3}He+Au events at $\sqrt{s_{NN}} = 200$ GeV, with an impact parameter $b < 2$ fm, using a parton-parton cross section $\sigma_{part} = 1.5$ mb, and a nucleon-nucleon cross section $\sigma_{NN} = 42$ mb. There is admittedly a lot of freedom in selecting the partonic cross section, since partonic interactions in the energy scale at hand are highly non-perturbative and, therefore, not calculable from first principles. Thus, we selected the smallest of the values usually used in the literature to describe A+A collisions, which range from $\sigma_{part} = 1.5$ mb to $\sigma_{part} = 10$ mb [12, 144, 137], to explore how a minimal partonic scattering strength leads to the development of collectivity in

this model. The characterization of each class of collisions, both in initial geometry and particle production, is shown in Table 4.1, where the initial eccentricity is calculated as

$$\varepsilon_n = \frac{\sqrt{\langle r^2 \cos(n\phi)\rangle^2 + \langle r^2 \sin(n\phi)\rangle^2}}{\langle r^2 \rangle}, \tag{4.16}$$

averaging over the individual nucleon coordinates $\vec{x}_i = (r_i, \phi_i)$ in every event, smeared by a Gaussian of width $\sigma = 0.4$ fm.

Table 4.1: Particle production and geometric characterization of central small-system collisions in AMPT. For each collision system, we show the mean number of participant nucleons per event, the mean number of partons at freeze out, the mean number of hadrons after the hadron cascade, and the mean initial ε_2 and ε_3.

System	$\langle N_{part} \rangle$	$\langle N_{partons} \rangle$	$\langle N_{hadrons} \rangle$	$\langle \varepsilon_2 \rangle$	$\langle \varepsilon_3 \rangle$
p+Au	10.45	246	98	0.24	0.16
d+Au	18.3	436	168	0.57	0.17
^{3}He+Au	22.3	586	245	0.48	0.23

We construct long-range two-particle correlations functions

$$C(\Delta\phi, p_T) = \frac{1}{N_{trig}} \frac{dN(p_T)}{d\Delta\phi} \tag{4.17}$$

by taking the angular difference $\Delta\phi$ of charged hadrons pairs separated in pseudorapidity by $2.0 < |\Delta\eta| < 3.0$, with the trigger and associated hadrons belonging to the same p_T bin. The correlations $C(\Delta\phi, p_T)$ for ^{3}He+Au and $p+p$ collisions are shown in Fig. 4.5(a) for $p_T^{assoc}, p_T^{trigger} \in [0.9, 1.04]$ GeV/c, and are observed to be qualitatively very different. The $p+p$ correlation function has a flat near-side (i.e., at small relative azimuth $\Delta\phi \approx 0$) since particle pairs from a given jet fragmentation in the same jet cone cannot be separated by more than two units in pseudorapidity. The away-side, on the other hand, exhibits a prominent enhancement from jets, back-to-back in azimuth but not in pseudorapidity, reflecting the fact that the two partons involved in the fragmentation carry different fractions x of their nucleon's momentum. On the other hand, the correlation function for ^{3}He+Au has a prominent near-side enhancement which can be attributed to collective behavior, as well as a more prominent away-side peak relative to $p+p$. If we assume that the jet contribution to the away-side in $p+p$ remains unchanged in ^{3}He+Au, we can subtract the former from the latter, obtaining the correlation function shown in Fig. 4.5(b).

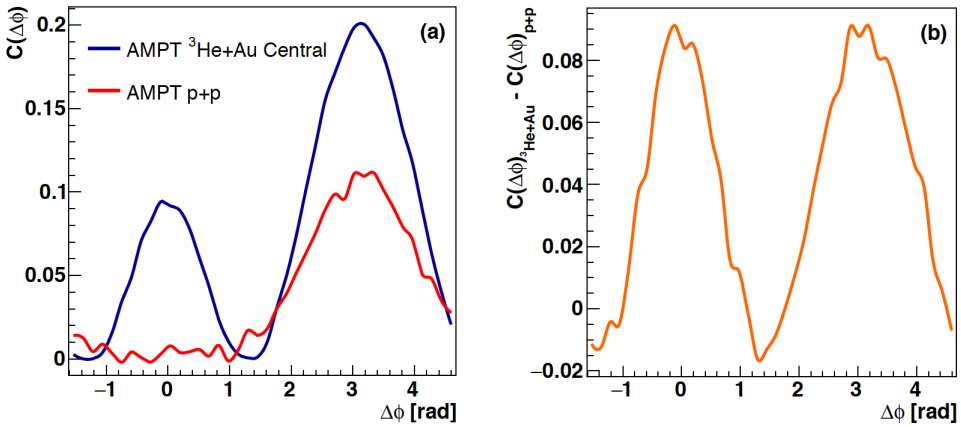

Figure 4.5: (a) Two-particle correlation for charged hadrons within $0.90 < p_T < 1.04$ GeV/c in $p+p$ and ^{3}He+Au AMPT events at $\sqrt{s_{NN}} = 200$ GeV. (b) Contributions to the correlation function from jet fragmentation are removed by subtracting away the per-trigger yield from p+p events. Figure reproduced from Ref. [161].

Although qualitative in nature, this exercise of constructing long-range azimuthal correlations demonstrates the existence of collectivity signals in AMPT, in the collision systems and energies of interest. Additionally, it shows that part of the collectivity signals in AMPT can be attributed to non-flow effects, and that they must be accounted for in quantitative calculations. However, let us define from the outset *flow* to be signals of collectivity related directly to the initial geometry of the collision, and *non-flow* to be signals of collectivity unrelated to that geometry. This distinction is artificial, in the sense that it cannot be made in experimental data. However, in AMPT, where we have access to the information of the entire collision evolution—including the initial state— it becomes a useful tool for understanding small system collectivity.

In order to measure the *true* v_2, that is, as it relates to the initial geometry, we calculate the participant plane angle Ψ_n for every event from the coordinates of each participant nucleon

$$\Psi_n = \frac{\text{atan}(\langle r^2 \sin(n\phi)\rangle, \langle r^2 \cos(n\phi)\rangle)}{n} + \frac{\pi}{n}. \tag{4.18}$$

This approximates the orientation of the impact parameter vector of the colliding nuclei in space, from the coordinates of the participant nucleons. Since we are interested in the angular emission

pattern of particles relative to this plane, we compute the true azimuthal anisotropy of unidentified charged hadrons within $|\eta| < 2$ as follows, where the average is taken over many events:

$$v_n = \langle \cos[n(\phi - \Psi_n)] \rangle. \tag{4.19}$$

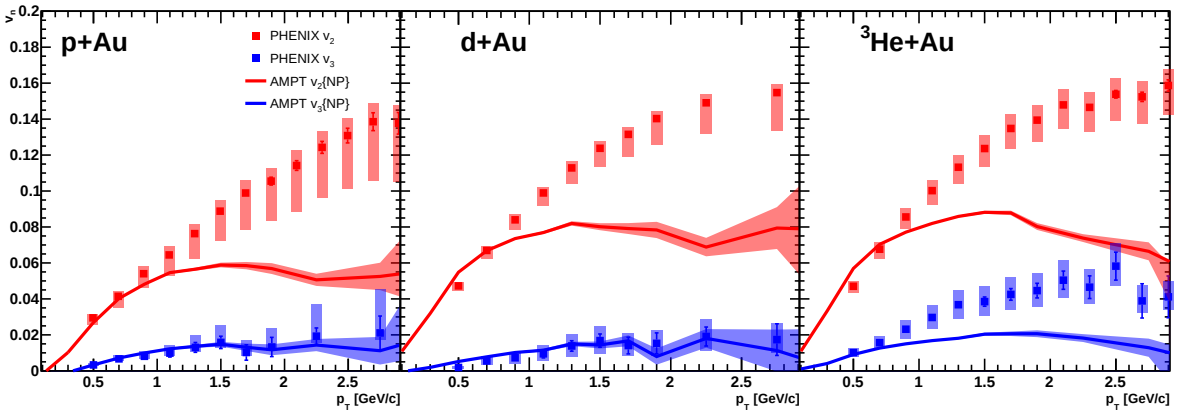

Figure 4.6: Transverse momentum dependence of v_2 (red) and v_3 (blue) in small systems as calculated relative to the participant nucleon plane (NP) in AMPT, compared to the corresponding PHENIX measurements [38, 41].

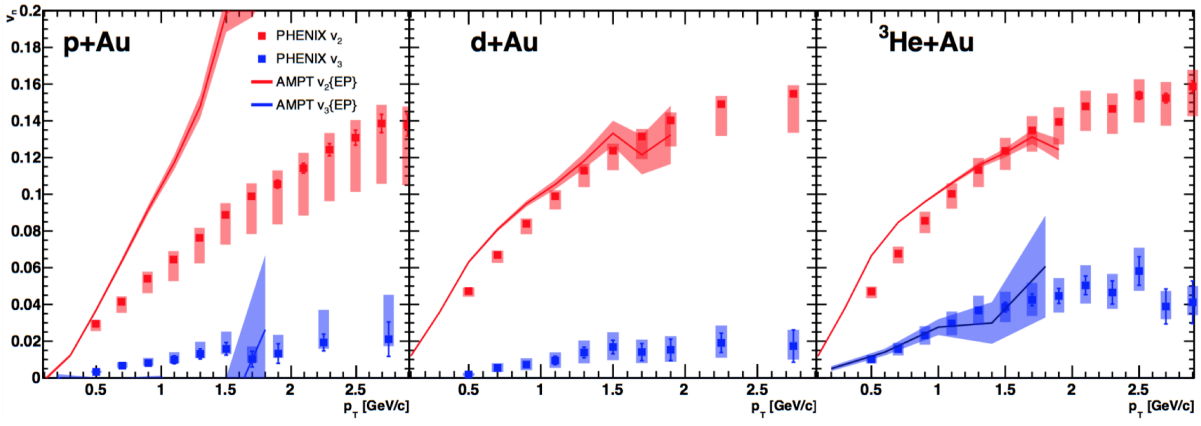

Figure 4.7: Transverse momentum dependence of v_2 (red) and v_3 (blue) in small systems relative to the event plane (EP), as calculated using final-state hadrons in AMPT, compared to the corresponding PHENIX measurements [38, 41].

The resulting $v_n(p_T)$ for all three systems under consideration are shown in Fig. 4.6, compared to measurements by the PHENIX Experiment [38, 41]. It is noteworthy that these AMPT results were originally published [161] as predictions for ^{3}He+Au and p+Au prior to the availability of experimental data. We observe a reasonable agreement between the AMPT calculation and the published data below $p_T \approx 1.5$ GeV/c, demonstrating that the ordering of $v_n(p_T)$ is consistent with the ordering of ε_2, as in hydrodynamic calculations. However, the comparison shown in Fig. 4.6 is not strictly like-for-like; the AMPT curves correspond to true flow, whereas experimental measurements include non-flow effects.

In order to compare the model and measurements on equal footing, we analyzed the output of AMPT with the same method used on PHENIX data, where the event plane is calculated from final-state particles, as described in Ref. [196]. To briefly summarize, let A, B, C denote the set of final-state particles in three different acceptance regions, referred to as 'subevents'; and let the flow vector for the j^{th} subevent be

$$\vec{Q}^{(j)} = \left\{ \sum_i \cos(n\phi_i), \sum_i \sin(n\phi_i) \right\}, \tag{4.20}$$

where the sum runs over all particles in the subevent. The event plane Ψ_n is given by

$$\Psi_n^{(j)} = \frac{\arctan(Q_y/Q_x)/n}{\text{Res}(\Psi_n^{(j)})}, \tag{4.21}$$

where $\text{Res}(\Psi_n^{(j)})$ is the event plane resolution,

$$\text{Res}(\Psi_n^{(j)}) = \sqrt{\frac{\langle \cos[n(\Psi_n^A - \Psi_n^B)] \rangle \langle \cos[n(\Psi_n^A - \Psi_n^C)] \rangle}{\langle \cos[n(\Psi_n^B - \Psi_n^C)] \rangle}}. \tag{4.22}$$

The v_n coefficients are then calculated as before, relative to Ψ_n. However, in this method, the measurement will be sensitive to both flow and non-flow. Fig. 4.7 shows the measured v_n compared to $v_n\{\text{EP}\}$ from AMPT. The third panel is particularly striking, since a good description of the data is achieved for ^{3}He+Au collisions; in the case of d+Au, v_2 is well described by AMPT, yet there is no corresponding v_3 calculation due to the third-order event plane resolution being an imaginary number. Lastly, the first panel shows that AMPT does not provide a good description of the p+Au

data; the v_2 overestimates the data due to an increased sensitivity to non-flow, whereas the v_3 is found to be negative.

Having determined the extent to which AMPT can explain experimental measurements, it is of interest to examine whether a quantitative scaling relation between the true $v_n\{NP\}$ and ε_n holds in the model (e.g., in ideal hydrodynamics the scaling relation $v_n \propto \varepsilon_n$ holds true [156]), and whether the lifetime of the system is long enough to maximally translate the initial geometry into the final state. To that end, Fig. 4.8 shows the ratio of $v_n/v_n^{d+\mathrm{Au}}$ (solid circles) and $\varepsilon_n/\varepsilon_n^{d+\mathrm{Au}}$ (dashed lines) for p+Au and ^{3}He+Au. The v_n ratios are approximately p_T-independent above $p_T \approx 0.6$ GeV/c, with strong deviations below that. The ε_n ratios are observed to be lower than the v_n ratios by approximately $15-30\%$. Thus, we are able to identify a scaling relation—albeit an imperfect one—between geometry and momentum-space azimuthal anisotropy in AMPT.

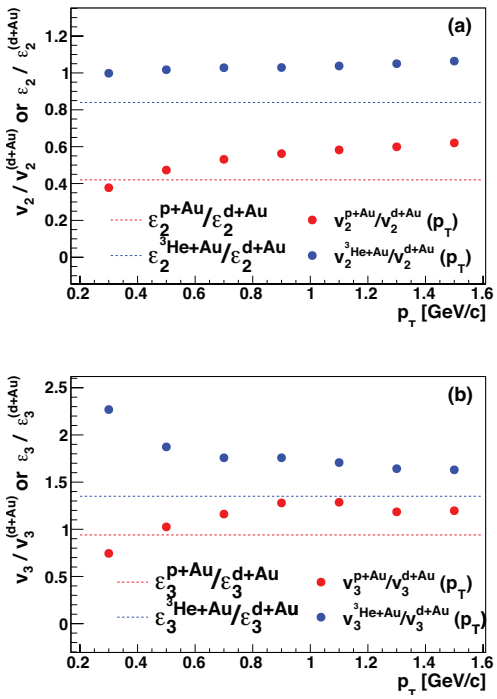

Figure 4.8: (a) Ratio of elliptic and (b) triangular anisotropy as a functio of transverse momentum in p+Au and ^{3}He+Au compared to d+Au. The dashed lines indicate the ratio of elliptic and triangular eccentricity from initial geometry. Figure reproduced from [161].

In particular, while partonic scattering remains the core of the model, encapsulating the description of strongly interacting matter as a collection of quasiparticles scattering incoherently, our understanding would be amiss if we failed to recognize that subsequent stages of the model—namely, hadronization and hadronic cascade—also have an impact on the final-state v_n. Therefore, we can calculate v_2 and v_3 but disabling partonic and hadronic scattering in steps[5] , as shown in Fig. 4.9 for p+Au and ^{3}He+Au. Panels (a) and (b) corresponds to v_2 and v_3 in ^{3}He+Au collisions, respectively. The violet curves correspond to the azimuthal anisotropy when including both hadronic and partonic scattering. If the hadronic scattering stage is disabled, v_n drops substantially, as indicated by the blue curves; the late-stage hadronic scattering stage is thus seen to increase v_2 by about 20% at $p_T > 1$ GeV/c, and by over 100% at $p_T < 0.5$ GeV/c, with the effect being more pronounced in v_3. Now, if partonic scattering is disabled, leaving only the hadronic scattering stage, the green curves show that a sizable v_n still develops from final-state hadronic interactions alone. Now, if both hadronic and partonic scattering are disabled, the v_n becomes zero, as expected and demonstrated by the orange curves. If we now examine p+Au collisions, in panels (c) and (d), we observed that including the hadronic scattering stage has a much smaller effect on v_n, and that the v_n originating from hadron scattering alone is much less substantial than in ^{3}He+Au, demonstrating that the bulk of the anisotropy develops in the partonic scattering stage in this particular collision system.

Lastly, we turn to the role of hadronization on v_n, as shown in Fig. 4.10, where v_2 and v_3 are calculated for p+Au and ^{3}He+Au using partons at freeze-out, and hadrons immediately after their formation, therefore allowing us to discern whether coalescence alone has any impact on v_n. We observe that, at high p_T, hadronization increases both v_2 and v_3, yet decreases them below $p_T \approx 0.5$ GeV/c. The exact mechanism responsible for this requires further elucidation, especially when considering that coalescence in AMPT proceeds by grouping together partons in close spatial proximity. Nevertheless, it has been established that hadronization and the subsequent hadronic cascade have a significant impact, enhancing the measured azimuthal anisotropy which begins to

[5] While the hadronic cascade can be explicitly excluded from the AMPT workflow, the partonic scattering stage cannot. Hence, we effectively disable it by setting the parton scattering cross section to a very small number $\sigma \sim 10^{-3}$ mb.

build up during the partonic scattering stage. The modifications to v_n appear to be both p_T- and collision system-dependent, thus accounting for the deviations from geometric scaling shown in Fig. 4.8.

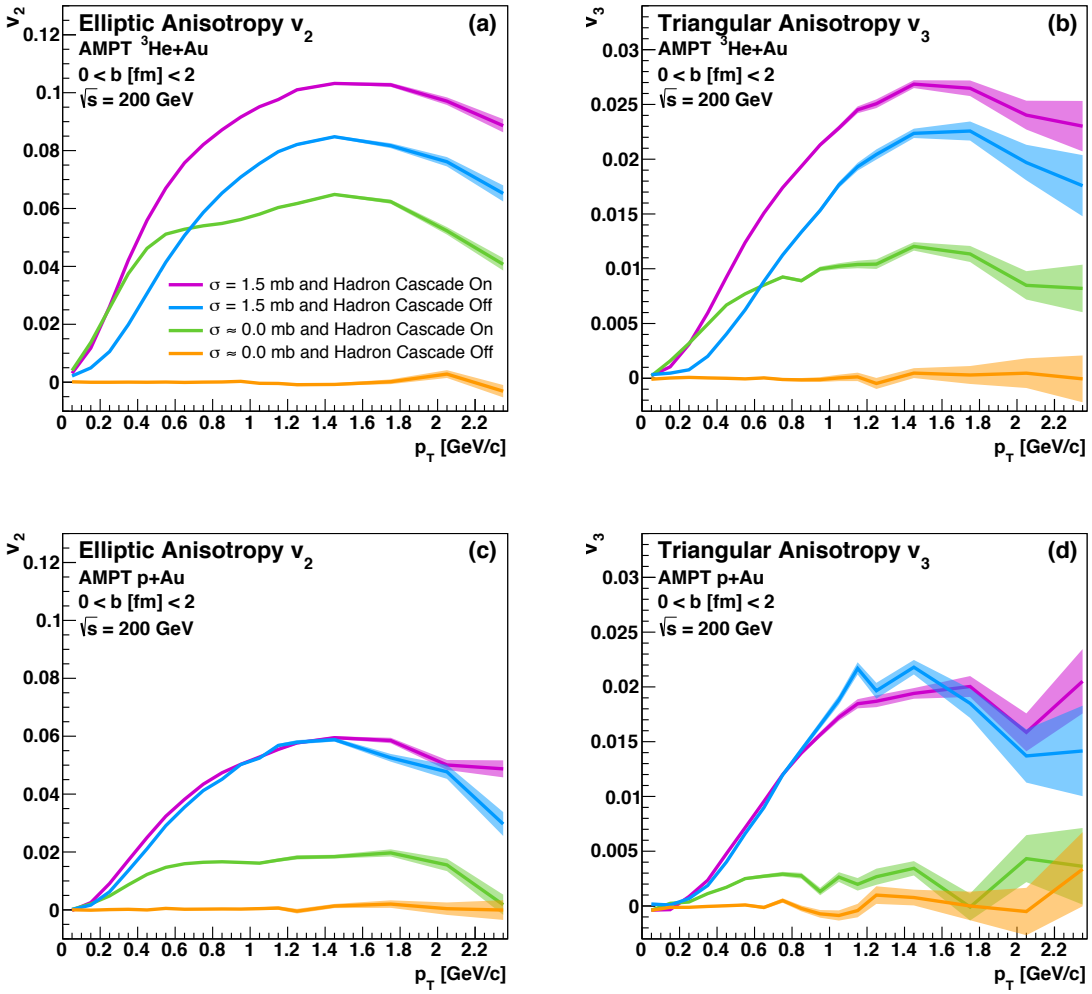

Figure 4.9: Impact on v_n of the parton scattering phase and the hadronic cascade in AMPT for ^{3}He+Au—panels (a) and (b), and p+Au—panels (c) and (d). Figure reproduced from Ref. [161].

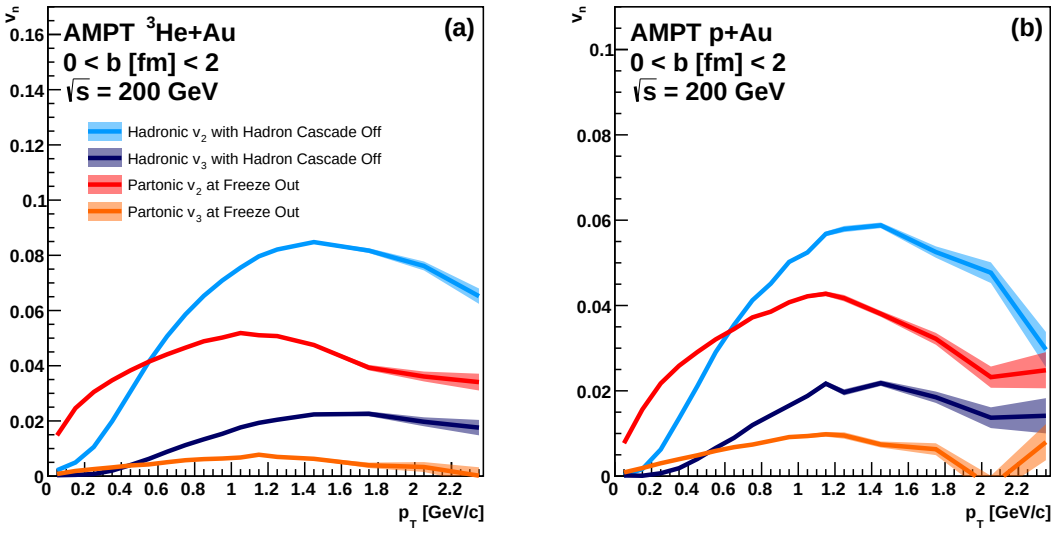

Figure 4.10: Impact on v_n of hadronization by coalescence in (left) ^{3}He+Au and (right) p+Au collisions in AMPT.

4.2.2 Center-of-Mass Energy Dependence of Collectivity in d+Au Collisions

Geometry engineering has yielded valuable insight into small system collectivity, demonstrating that final-state collectivity signals can be traced back directly to the initial geometry of the collision. However, if the hydrodynamic paradigm is to be applied to small systems, we must recognize that the relative importance of its various stages may be different than in larger A+A collisions. That is, pre-equilibrum dynamics and late-stage hadronic interactions are expected to play a larger role in small systems, owing to a shorter stage of hydrodynamic expansion of the QGP. Experimentally, these questions can be addressed by examining the behavior of collectivity signals as a function of the center-of-mass energy in small collision systems, as delivered by RHIC in its 2016 running period when d+Au was collided at $\sqrt{s_{NN}} = 200, 62.4, 39.6$, and 19 GeV.

As before, physical insight is obtained by comparing experimental data [39, 40] with theoretical calculations. Therefore, we begin by examining whether hydrodynamics predicts a threshold below which no amount of QGP is produced. Fig. 4.11 shows the integrated hyper-volume in space and time of all fluid elements in hydrodynamic simulations of d+Au collisions hotter than the

transition temperature, as a function of the collision energy. That is, it effectively shows how much QGP is produced overall at each collision energy. We observe a five-fold increase in the volume of QGP between the lowest energy of $\sqrt{s_{NN}} = 7.7$ GeV and the highest energy of $\sqrt{s_{NN}} = 5.02$ TeV. Yet, even at the lowest energy, a volume of approximately 8 fm$^2\Delta y$ fm/c is not insignificant. In fact, it can be thought of as a 2 fm $\times$ 2 fm transverse area of QGP (a transverse area is quoted since the SONIC model used in this calculation implements 2+1 dimensional hydrodynamics.), living for a 2 fm/c time interval within rapidity Δy. For comparison, the volume at the highest energy can be thought of as a 3 fm $\times$ 4 fm area living for 3 fm/c. Thus, within the context of viscous hydrodynamics, there seems to be no sharp turnoff in the translation of geometry into the final momentum space, as would follow from a negligible volume of hot nuclear matter.

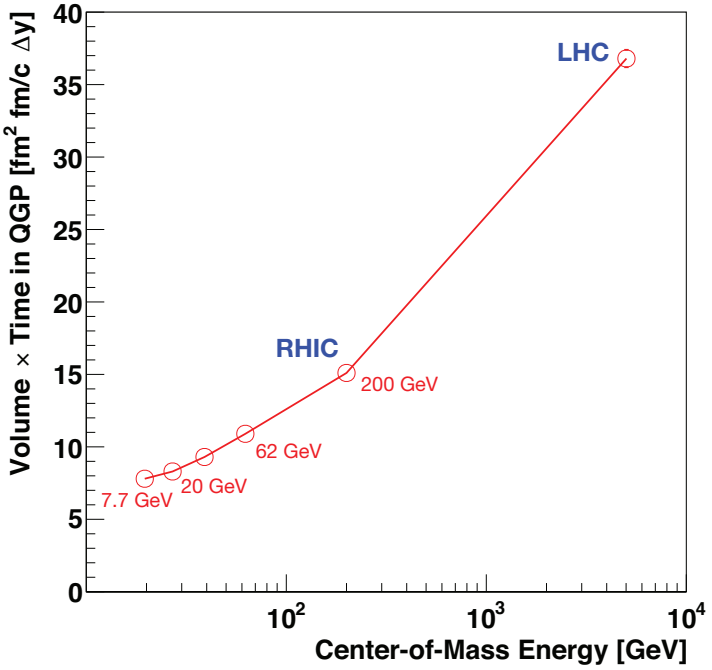

Figure 4.11: Collision energy dependence of the summed space-time hyper-volume of QGP in viscous hydrodynamics calculations. Figure reproduced from Ref. [162].

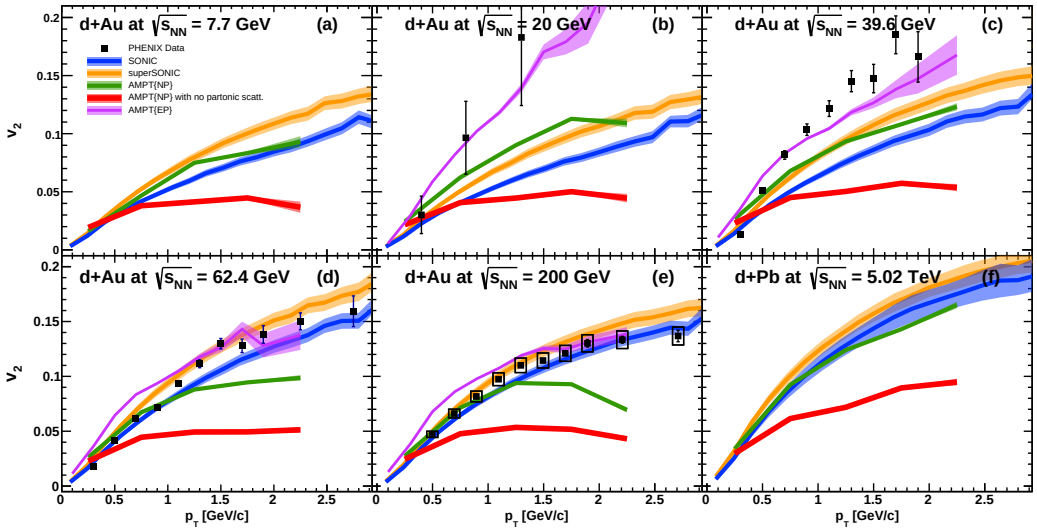

Figure 4.12: Beam energy dependence of $v_2(p_T)$ in central d+Au collisions, from $\sqrt{s_{NN}} = 7.7$ GeV, to $\sqrt{s_{NN}} = 200$ GeV; and for d+Pb collisions at $\sqrt{s_{NN}} = 5.02$ TeV, from hydrodynamics and AMPT. Experimental results are shown where available for comparison. Figure adapted from Refs. [162, 39].

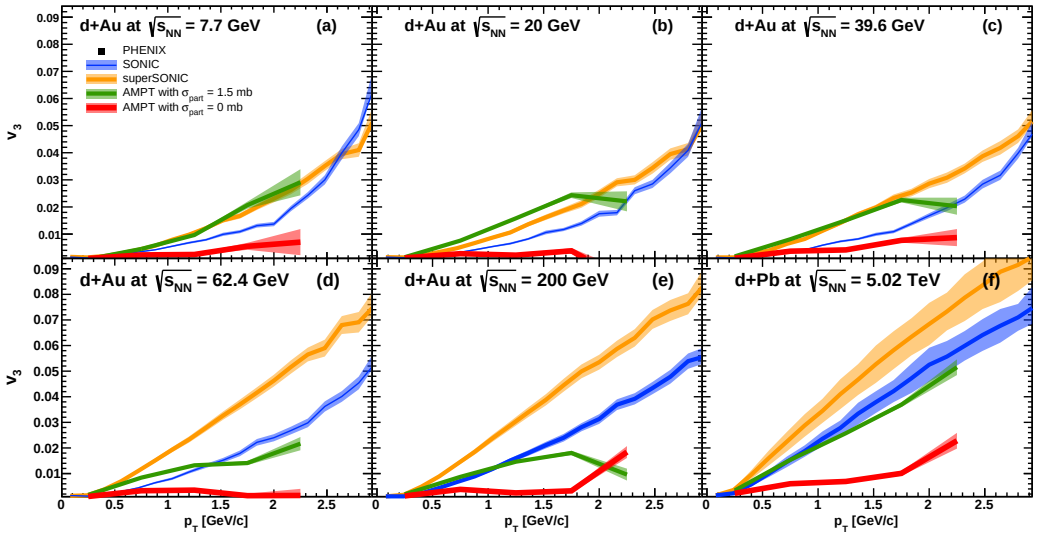

Figure 4.13: Beam energy dependence of $v_3(p_T)$ in central d+Au collisions, from $\sqrt{s_{NN}} = 7.7$ GeV, to $\sqrt{s_{NN}} = 200$ GeV; and for d+Pb collisions at $\sqrt{s_{NN}} = 5.02$ TeV, from hydrodynamics and AMPT. Figure reproduced from Ref. [162]

Table 4.2: Nucleon-nucleon cross section as a function of collision energy.

$\sqrt{s_{NN}}$ [GeV]	σ_{NN} [mb]
7.7	31.2
20.0	32.5
39.0	34.3
62.4	36.0
200.0	42.3
5020.0	60.3

Fig. 4.12 shows PHENIX measurements of $v_2(p_T)$ in d+Au at $\sqrt{s_{NN}} = 19.6, 39.6, 62.4$, and 200 GeV, along with a series of predictions from hydrodynamics and AMPT for the previously mentioned collision energies as well as $\sqrt{s_{NN}} = 7.7$ GeV and d+Pb at $\sqrt{s_{NN}} = 5.02$ TeV where no experimental measurements have been made. Notice that theory calculations were not carried out at $\sqrt{s_{NN}} = 19.6$ GeV, but rather $\sqrt{s_{NN}} = 20$ GeV, which constitutes a negligible difference. Let us consider the hydrodynamic calculations first, from the SONIC (blue curves) and SUPERSONIC (yellow curves) models [168]. The latter is an extension of the former, where the AdS/CFT correspondence has been used to arrive at a relation between the gradient of the initial energy density distribution and the radial dependence of fluid cell velocities in order to account for pre-equilibrium dynamics. A substantial v_2 is observed at all energies, with the data being higher than hydrodynamic calculations at the lowest collision energies, likely due to the substantial non-flow contribution there. At the highest collision energies, a good agreement with the data is seen. At the time the predictions were made, it was hoped that the experimental data would provide discriminating power between the two models, effectively quantifying the extent to which, in small systems, the collectivity signal from hydrodynamic expansion does not reach saturation, and does not come to dominate over flow contributions from the pre-equilibrium stage. Unfortunately, the uncertainties on the data and the

hydrodynamic calculations, as well as the dominance of non-flow at the lower energies, prevent any such conclusion from being drawn.

From a kinetic transport perspective, Fig. 4.12 shows three different AMPT calculations of $v_2(p_T)$. The green curves correspond to the true flow computed relative to the nucleon participant plane, following the procedure described in Section 4.2.1 using an energy-dependent nucleon-nucleon cross section values for the Monte Carlo initialization of the initial geometry, as shown in Table 4.2. Across collision energies, the result is consistent with hydrodynamic calculations at low p_T, yet with the characteristic drop for $p_T \gtrapprox 1.5$ GeV, previously discussed. On the other hand, the violet curves correspond to a calculation of flow relative to the event plane that mirrors that which was used to obtain the experimental measurements, also discussed in Section 4.2.1. In that case, very good agreement with the data is seen, confirming the dominance—within AMPT—of non-flow at the lowest energies, as quantified by the difference between the green and violet curves. Finally, the red curves correspond to a calculation of flow relative to the nucleon participant plane, yet with no partonic scattering. This calculation was motivated by the hypothesis that, at a low enough collision energy, no GQP would be formed such that the system might come to be described as purely hadronic. In hindsight, given the large contribution of non-flow to the v_n signal, this possibility is not necessarily ruled out.

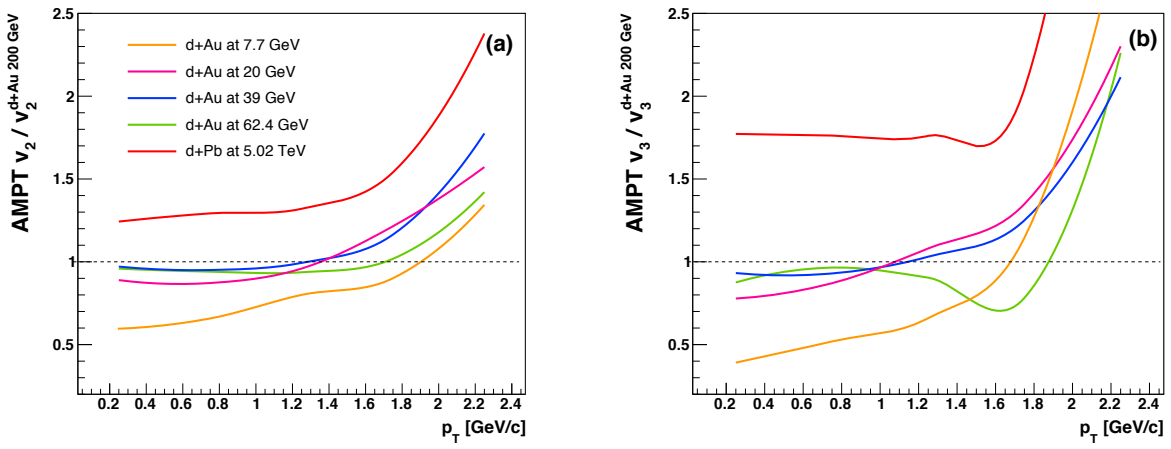

Figure 4.14: Ratio of (a) v_2 and (b) v_3 in d+Au at different energies to $\sqrt{s_{NN}} = 200$ GeV from AMPT relative to the nucleon participant plane. Figure reproduced from Ref. [162].

Fig. 4.13 shows predictions for triangular flow $v_3(p_T)$ from SONIC, SUPERSONIC, and AMPT (the true flow relative to the nucleon participant plane, both with and without partonic scattering). In this case, there are no experimental measurements to compare to except at $\sqrt{s_{NN}} = 200$ GeV. Fig. 4.14 quantifies the change of v_n with collision energy, showing the ratio of $v_n(p_T)$ relative to the nucleon participant plane at each energy relative to that at $\sqrt{s_{NN}} = 200$ GeV from AMPT. It is possible to see that v_2 decreases by about $25-30\%$ from 5.02 TeV to 200 GeV, and then about $25-40\%$ from 200 GeV to 20 GeV. On the other hand, v_3 decreases dramatically by approximately 300% between 200 GeV and 7.7 GeV. Thus, triangular flow is a more sensitive observable to the duration of the QGP phase. This is also the reason why the inclusion of pre-equilibrium has a much larger effect on v_3 than v_2 in the hydrodynamic calculations.

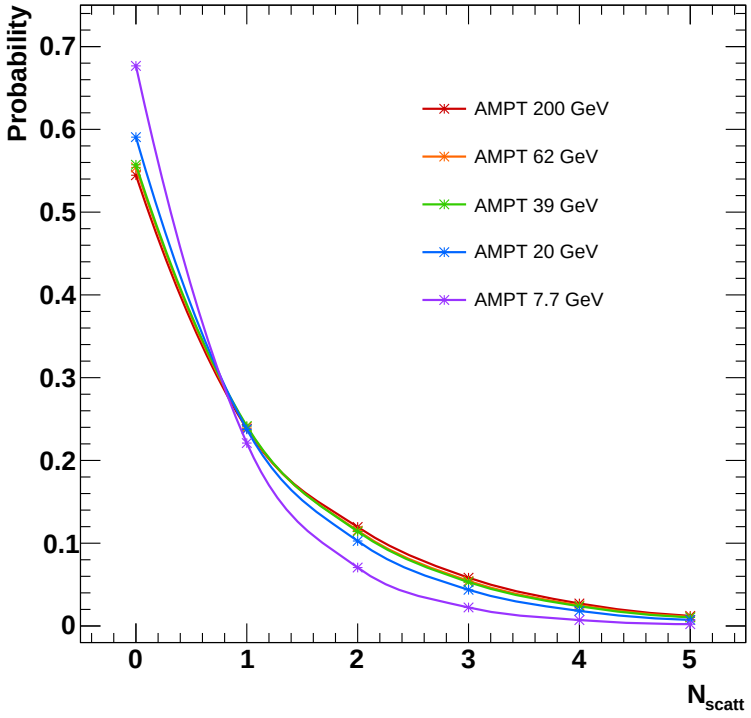

Figure 4.15: Probability of a parton in AMPT to undergo N_{scatt} scatterings in the parton cascade stage, for d+Au collisions at a variety of center-of-mass energies. Figure reproduced from Ref. [162].

Having examined the collision energy dependence of v_n in the AMPT model, it is instructive to examine the sensitivity of the underlying mechanism—namely, partonic scattering—to varying the collision energy. Fig. 4.15 shows the probability of a given parton in d+Au events to undergo N_{scatt} scattering events prior to freeze-out, for every collision energy. It is noteworthy that, even at the highest energy in d+Pb, 65% of partons do not scatter at all, with the remainder scattering only a limited number of times—mostly once. In the case of d+Au at RHIC energies, we observe a monotonic increase with collision energy in the probability of not scattering. However, despite the wide range of collision energies under consideration, the variation in the scattering probability is of order 10%.

4.2.3 Collectivity in $p+p$ Collisions with Constituent Quark Geometry

Section 4.2.1 dealt with the technique of geometry engineering, which relies on a detailed characterization of the intrinsic collision geometry. Of the three asymmetric systems considered, p+Au is the most unconstrained in this regard. Unlike d+Au and ^{3}He+Au, the initial geometry in this case is not driven by the number of 'hotspots' where individual projectile nucleons collide with the target, but rather by parton-level fluctuations within the hotspot. This state of affairs implies that if the geometry translation paradigm is to be tested in the problem of collectivity in $p+p$ collisions, one must define the initial geometry at the sub-nucleonic level.

The first hydrodynamic studies of $p+p$ collisions with the SONIC model incorporated a Monte Carlo Glauber geometry picture of a round proton with event-by-event shape fluctuations and a varying relaxation time [113], demonstrating the applicability of hydrodynamics to this class of collisions. However, the model predicted a vanishing v_2 for very high multiplicity events on account of the very round geometry, in conflict with experimental data. The calculation was later refined by modeling the constituent quark structure of the proton [198], successfully describing v_n for a wide range of systems, namely $p+p$, p+Pb, and Pb+Pb, as shown in Fig. 4.16. While describing collectivity in $p+p$ may be considered an exacting standard for hydrodynamics to have met, it does not unequivocally establish the formation of QGP in this regime; it is now accepted that a hydrodynamic description may be applicable even before the onset of equilibration [170]. Considering the success of hydrodynamics, it is of interest to determine whether kinetic transport can also correctly describe collectivity in $p+p$ collisions, and to examine the specific assumptions that have to be made for the quasiparticle picture to hold in this smallest of systems. In particular, we focus on $p+p$ collisions at LHC energies of $\sqrt{s_{NN}} = 13$ TeV, where measurements have been made by several experiments [5, 126, 1].

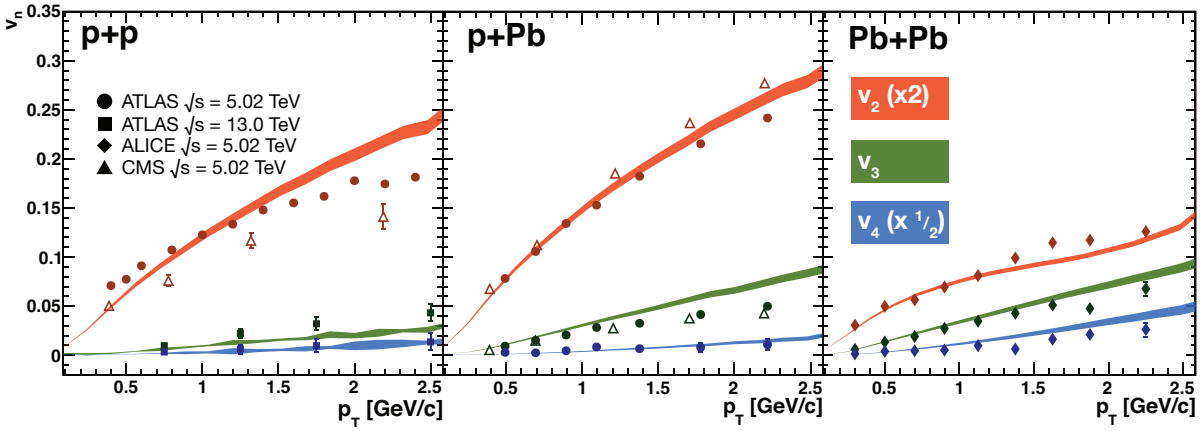

Figure 4.16: Azimuthal anisotropy coefficients v_2, v_3, and v_4, calculated using the SONIC hydrodynamic model, for p+p, p+Pb, and Pb+Pb collisions at LHC energies. Figure reproduced from [154].

The AMPT model, by default, treats individual nucleons as disk-like with a diffuse interaction radius. When pairs of nucleons interact, two color strings are extended between them, separated by the impact parameter of the nucleon-nucleon collision. We have modified this default treatment, giving the nucleon a three-constituent quark structure, following calculations detailed in [147] to determine their spatial coordinates in every event. Each individual quark is modeled as disk-like, with a sharp interaction radius corresponding to a quark-quark cross section of $\sigma_{qq} = 19.7$ mb. The effective proton-proton interaction cross section is then $\sigma_{pp} = 68$ mb, which compares favorably to the reference value of $\sigma_{pp}^{\mathrm{ref}} = 72$ mb at $\sqrt{s_{NN}} = 13$ TeV. Two color strings are then extended between every pair of interacting quarks, separated by the impact parameter of the quark-quark collision. Notice that, in this simplified constituent quark picture, we do not model the parton distribution function and thus all quarks carry exactly one third of the total nucleon's momentum.

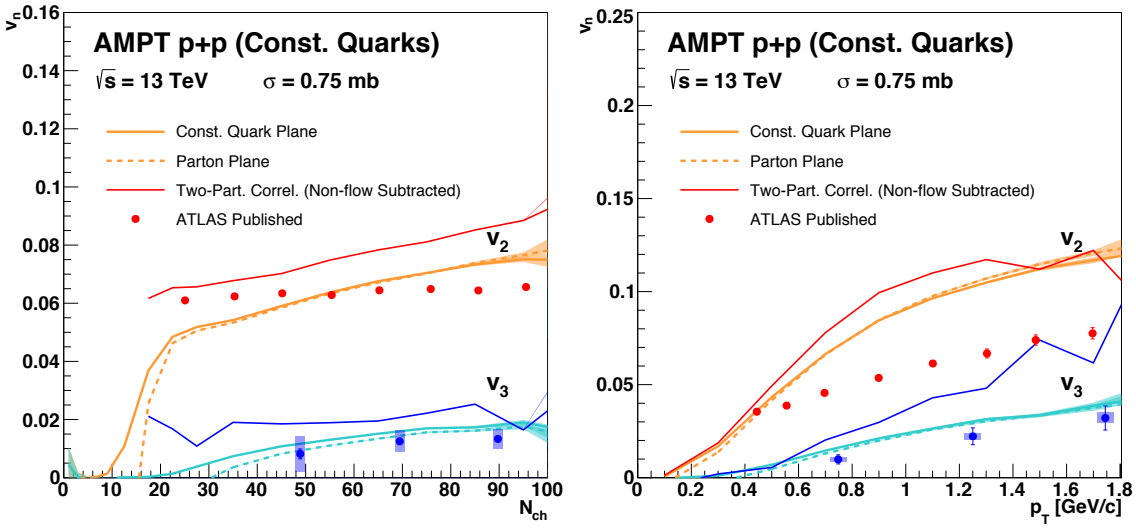

Figure 4.17: (left) Multiplicity and (right) transverse momentum dependence of v_2 and v_3 in $p+p$ collisions at $\sqrt{s_{NN}} = 13$ TeV, modeled with constituent quarks in AMPT. Figure reproduced from Ref. [153].

We begin by measuring the true flow, $v_n = \langle \cos[n(\phi - \Psi_n)] \rangle$, relative to the event plane calculated from the initial coordinates of the participant quarks smeared by a Gaussian of width $\sigma = 0.2$ fm, as well as from the string melting partons at early times. The result, as a function of event multiplicity N_{ch} (defined as the number of charged hadrons within $|\eta| < 2.5$), and p_T is shown in Fig. 4.17. The calculation is seen to reproduce the qualitative trends of the data, demonstrating that—even without a careful tuning of model parameters—this simple physical picture captures the gross features of the anisotropy. A small difference is observed when calculating flow relative to the event plane defined by constituent quarks and string melting partons, particularly at low N_{ch}, owing to the fact that fluctuations in parton coordinates become more significant in low-multiplicity events, making the difference between the two event planes more pronounced, as depicted in Fig. 4.18.

However, the above calculation of the 'true' flow is not directly comparable to experimental measurements of v_n since non-flow effects can be substantial in $p+p$ collisions, following the trend we have previously discussed of increasing relative importance with decreasing system size and

multiplicity. While it would be desirable to be able to discriminate between flow and non-flow effects in a data-driven manner, there is currently no experimental technique to unambiguously resolve the issue.[6] Various experimental collaborations have attempted to account for non-flow in different ways, yet relying on assumptions, model dependencies, and comparisons with a baseline event category where non-flow is assumed to be well understood in the absence of flow.

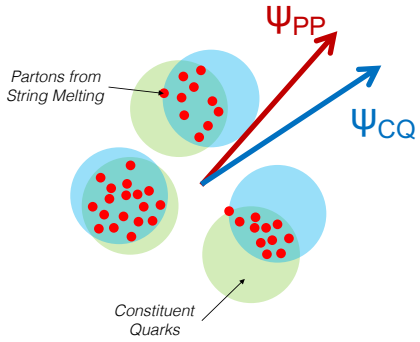

Figure 4.18: Cartoon depiction of a $p+p$ collision with constituent quarks, shown as green and blue disks, and their associated event plane Ψ_{CQ}. Also shown in red are the partons emerging from string melting at the site of every quark-quark collision, and their associated event plane Ψ_{PP}.

For instance, the PHENIX experiment [27] uses $p+p$ collisions as a baseline, taking the ratio of multiplicity at forward rapidity in the system of interest to that in the baseline, to estimate the magnitude of non-flow which is usually reported as an uncertainty on the measurement. However, other collaborations attempt to *correct* the measurement, effectively claiming to remove the non-flow contribution from the flow signal. Along these lines, the ATLAS result shown in Fig. 4.17 were extracted via two-particle correlations using a template fitting method [5] where the shape of measured correlation $C(\Delta\phi)$ is assumed to have a non-flow contribution, modeled using a reference low multiplicity ("peripheral") event category, plus a contribution from true flow. Mathematically, the

[6] In a strict sense non-flow can be suppressed through the use of multi-particle cumulants, since such correlations typically involve only a small number of particles, and cumulants are used to quantify correlations among arbitrarily large number of particles. However, the applicability of such methods is limited in small systems due to their low multiplicity [40].

shape of the peripheral correlation function is extracted with fit, obtaining a template $C^{\text{periph}}(\Delta\phi)$. The measured correlation is then fit with the following function:

$$C^{\text{measured}}(\Delta\phi) = C^{\text{ridge}}(\Delta\phi) + F \times C^{\text{periph}}(\Delta\phi), \tag{4.23}$$

with

$$C^{\text{ridge}}(\Delta\phi) = G\left(1 + \sum_{n=1}^{\infty} 2v_n \cos(n\Delta\phi)\right), \tag{4.24}$$

where the true flow measurement is extracted from $C^{\text{ridge}}(\Delta\phi)$. The identical procedure was carried out in AMPT, in order to provide a direct comparison with published data, as shown by the red and blue lines in Fig. 4.18.

In this particular case, the agreement with ATLAS published data is merely qualitative, both as a function of multiplicity and transverse momentum. However, the results presented demonstrate that, within the framework of AMPT, it is possible to interpret collectivity even in $p+p$ collisions as being geometric in origin. The lack of quantitative agreement can be attributed to a number of factors, including the simplicity of the constituent quark implementation, the particular tune of AMPT used, or the fact that the assumptions of the template fitting method do not hold in the model.

4.2.4 Minimal Conditions Required for Collectivity in AMPT

Once considered an elusive hallmark indicating the formation of QGP, the observation of collectivity in a variety of ever *smaller* collision systems, both in size and initial temperature, has given rise to intense scientific interest in the minimum size, lifetime, and number of initial partons required for QGP formation. While making the systems smaller may shorten the duration of the QGP phase, the nearly-inviscid expansion of the liquid achieves the translation of initial geometry into the final state. However, it is of interest to explore if such a threshold exists in the transport picture of small system collectivity, as has been presented and discussed in this chapter. To that end, we explore the smallest of systems in AMPT: $e^+ + e^-$ collisions. Given that a modest number of scatterings among quasiparticles can give rise to collectivity signals even in $p+p$ collisions, can

these leptonic collisions have a high enough partonic density for collectivity to be observed? First attempts aimed at reexamining e^+e^- archived data from the LEP accelerator [135] have not yielded any evidence of collective behavior among final-state particles in this collision system, yet this does not invalidate the question at hand.

In order to model e^+e^- collisions, we exclusively consider e^+e^- annihilation as mediated by a virtual Z boson which decays into a $q\bar{q}$ pair, as depicted in Fig. 4.19. We carry out this study with a custom version of the AMPT generator, running at a center of mass energy corresponding to the rest mass of the Z boson, $m_Z = 91.18$ GeV/c^2. A single color string is created between the receding $q\bar{q}$ pair, which then undergoes string melting. The parameters of the symmetric Lund splitting function

$$f(z) \propto z^{-1}(1-z)^a \exp(-bm_T^2/z) \tag{4.25}$$

were tuned to $a = 0.15$ and $b = 2.5$ to match the experimentally observed average charged particle multiplicity at $\sqrt{s} = 91$ GeV [48, 6].

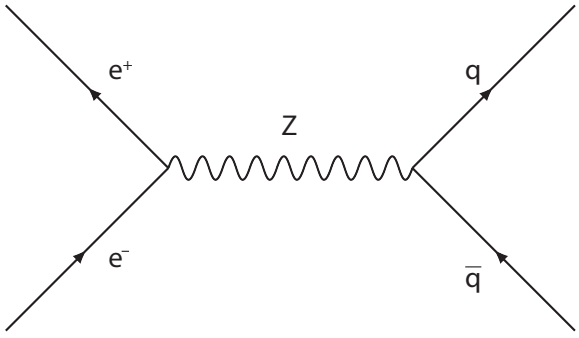

Figure 4.19: Electron-positron annihilation mediated by a virtual Z boson.

Since we model the collision with a single color string, in a strict sense there is no intrinsic initial collision geometry. Partons are emitted radially at an average distance of $0.1 - 0.2$ fm away from the string in the transverse plane—as a consequence of the formation time prescription—with

a strong space-momentum correlation, as shown in the left panel of Fig. 4.20. We construct two-particle long-range azimuthal correlations for pairs of final-state charged hadrons satisfying $p_T > 0.5$ GeV/c and $|\Delta\eta| > 2$, as shown in Fig. 4.21(a) for the two distinct cases of enabled and disabled final-state interactions.[7] As has been previously discussed, disabling interactions among partons and hadrons prevents the transcription of the event geometry leading to no collectivity in the final-state. Both correlation functions are observed to have very similar shapes, with no discernible near-side enhancement, indicating that—in this regime—particle interactions play an almost negligible role in the development of collectivity signals, quite unlike in the asymmetric systems we have studied. The absence of a near-side peak should not be interpreted a the absence of *any* collectivity. In fact, Fig. 4.21(a) quotes the magnitude of the second Fourier harmonic of the correlations, which is small yet non-zero. We can gain further insight by examining Fig. 4.21(b), which shows $v_2(p_T) = \langle\cos[2(\phi - \Psi_2)]\rangle$, quantifying collectivity relative to the initial event orientation Ψ_2, as defined by early stage partons. As there is no true intrinsic initial geometry, the negative anisotropy should be interpreted as arising from fluctutions by which partons expand perpendicularly to Ψ_2, yielding negative v_2 values by construction, since $v_2 = \langle\cos[2(\phi - \Psi_2)]\rangle$. Regardless of this feature, we again see that final-state interactions play a minimal role in the development of v_2, which can be interpreted as consistent with no collectivity in our model of e^+e^- collisions.

It is now of interest to devise a different initialization of the geometry, to see how the final results change. Motivated by the standard treatment of individual nucleon-nucleon collisions in the standard version of AMPT, we define *two strings* of energy equal to half the Z boson mass and separated by a transverse distance of 0.5 fm. The introduction of the second string makes for important differences relative to the one-string configuration. Most notably, the fraction of partons that do not undergo scattering is reduced to approximately 60%, from 90% in the case of one string. Additionally, the separation of strings in the transverse plane endows the collision with a well-defined initial geometry in which the event plane is oriented normally to the axis connecting the strings. The long-range azimuthal correlations—with and without interactions—for the two-string

[7] The disabling of interactions refers to both partonic and hadronic scattering.

case are shown in Fig. 4.22(a). When interactions are disabled, we observe no discernible near-side structure and obtain a c_2 value consistent with that of the one-string case. However, we see that enabling final-state interactions now plays a substantial role in the development of collectivity, with a prominent near-side peak, and large positive $v_2(p_T)$ relative to Ψ_2, as shown in Fig. 4.22(b).

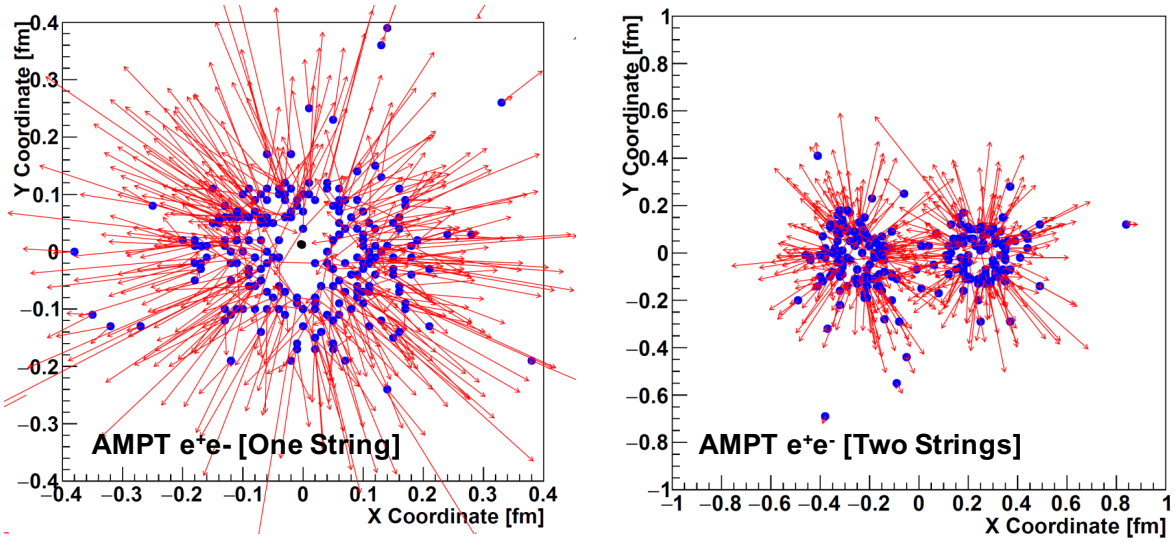

Figure 4.20: Spatial distribution and momentum orientation of partons in an AMPT e^+e^- event with one string (left) and two strings (right). Notice the difference in scale between the two panels. Image credit: Jamie Nagle.

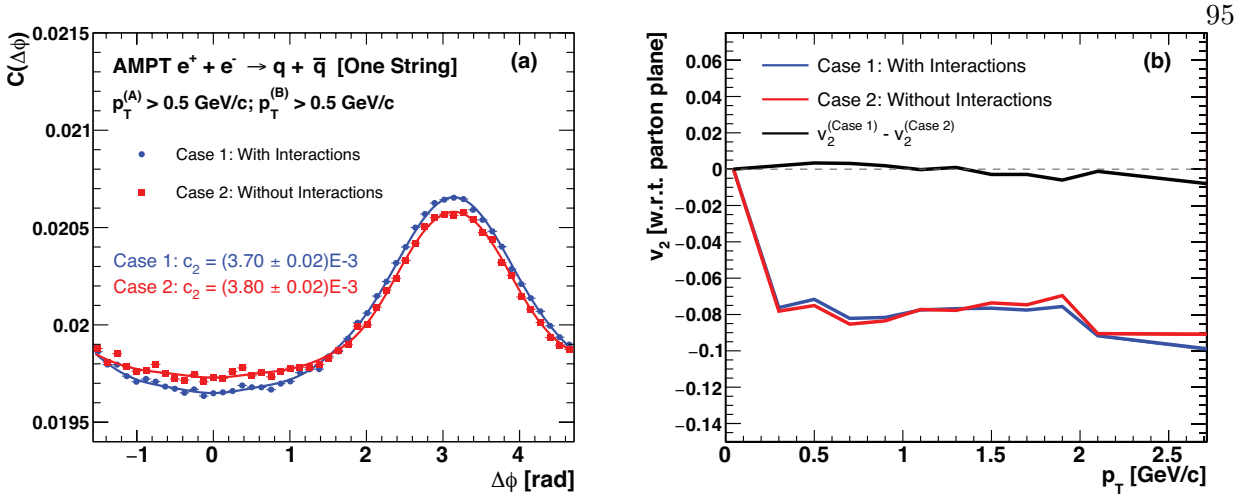

Figure 4.21: AMPT events with a single color string, modeling $e^+e^- \to Z \to q\bar{q}$. (a) Long-range azimuthal two-particle correlations with $|\Delta\eta| > 2$ among hadrons with and without final-state interactions. (b) Elliptic flow v_2 calculated relative to the initial parton plane, with and without final-state interactions, as well as the difference between the two. Figure reproduced from Ref. [152].

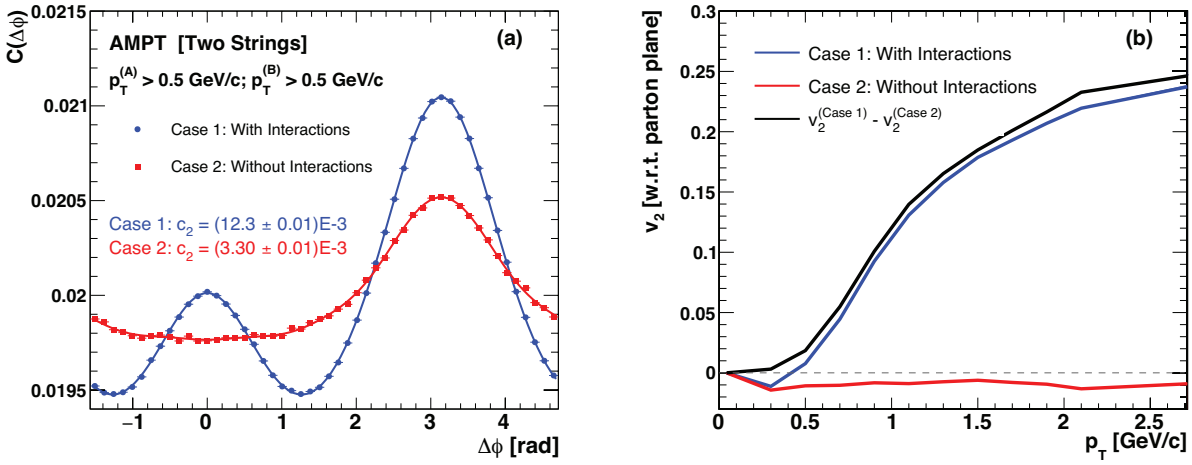

Figure 4.22: AMPT events with two color strings. (a) Long-range azimuthal two-particle correlations with $|\Delta\eta| > 2$ among hadrons with and without final-state interactions. (b) Elliptic flow v_2 calculated relative to the initial parton plane, with and without final-state interactions, as well as the difference between the two. Figure reproduced from Ref. [152].

Having found a configuration leading to collectivity in the final state, it is of interest to

examine its dependence on collision energy. We carried out a scan in collision energy, from 4.5 GeV to 184 GeV, as shown in Table 4.3, for the two-string configuration. Table 4.3 shows that particle production, as measured by the mean number of partons and the mean number of charged hadrons within $|\eta| < 2$, drops dramatically with energy, while the fraction of partons that do not undergo scattering exhibits a much weaker dependence. Fig. 4.23 shows long-range two-particle correlations for $\sqrt{s} = 54, 30$, and 10 GeV. At the highest of these energies, there is still a visible near-side peak when interactions are enabled. The ridge structure disappears for $\sqrt{s} = 30$ GeV, yet the flattening of the near side still indicates the presence of collectivity. At the lowest energy, the ridge disappears completely as the away-side enhancement from momentum conservation becomes more prominent.

As has been discussed before, such non-flow effects become quite dominant with decreasing energy and multiplicity. Thus, we examine the energy dependence of collectivity relative to the event geometry as shown in Fig. 4.24. However, in order to avoid the effect of fluctuations, particularly at the lowest energies, we compute v_2 relative to $\Psi_2 = \pi/2$ (i.e., perpendicular to the line connecting the strings in the transverse plane). Unlike with the two-particle correlations, we observe a weak dependence of v_2 on collision energy, except for the lowest values below $\sqrt{s} = 10$ GeV. The figure also shows the fraction of partons that undergo scattering as a function of collision energy, which follow the same trend as v_2, demonstrating an approximate scaling relation between the two quantities.

Table 4.3: Particle production and fraction of partons that do not undergo scattering as a function of collision energy in e^+e^- collisions modeled with two color strings in AMPT.

Energy [Gev]	$\langle N_{\text{partons}} \rangle$	$\langle N_{ch} \rangle$ in $\lvert\eta\rvert < 2$	Partons w/ $N_{\text{scatt}} = 0$
184	95	11.6	59.6%
91	75	11.2	59.7%
60	63	10.5	60.8%
45	55	9.7	61.3%
30	44	8.3	62.4%
10	19	6.5	75.4%
4.5	9	3.7	88.7%

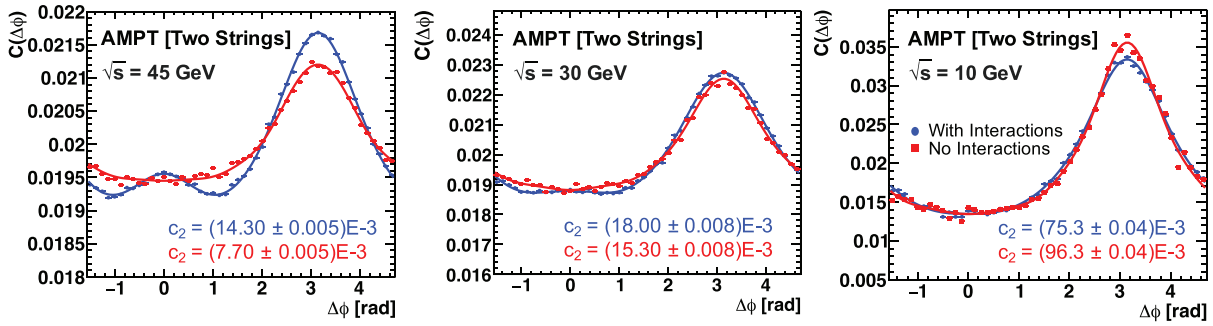

Figure 4.23: Long-range two particle correlations from AMPT events with two color strings, for various values of the collision energy, with and without final-state interactions. Figure reproduced from Ref. [152].

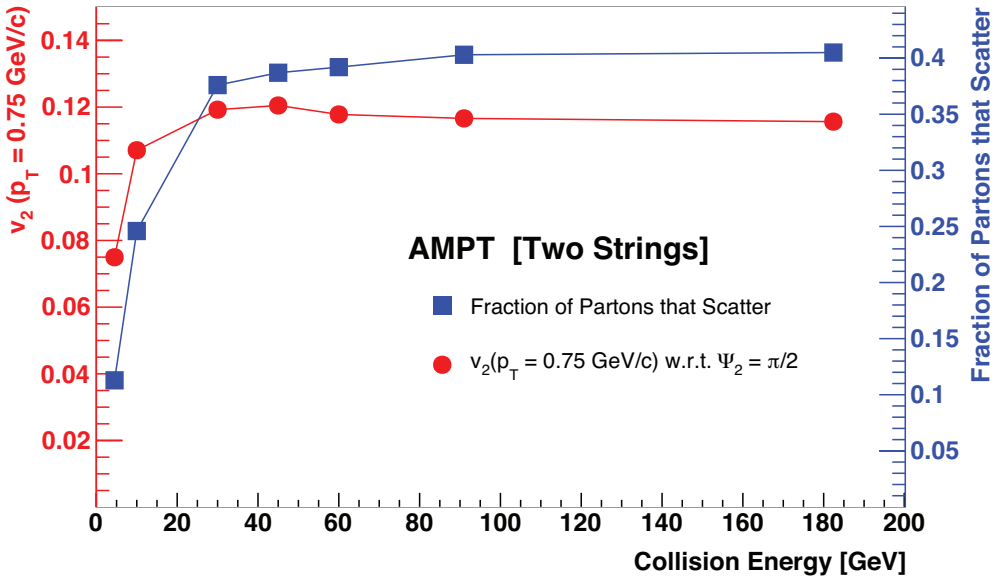

Figure 4.24: Elliptic flow v_2 at $p_T = 0.75$ GeV/c, calculated in AMPT relative to the true geometry, as a function of the total energy, in two-string configuration. Also shown is the fraction of partons that suffer at least one scattering. Figure reproduced from Ref. [152].

4.2.5 Parton Formation Time and the Limits of the Transport Picture

In a semiclassical picture, such as that of partonic scattering in the AMPT model, the characteristic range of parton interactions is simply the de Broglie wavelength $\lambda_B = h/p$. Now, par-

tons in AMPT are endowed with a property known as *formation time*. As a feature of parton cascades [105, 182], the introduction of the formation time attempts to account for complex early-time, multi-body quantum interference phenomena during the time it takes for wave packets to separate [132] and form well-defined quasiparticles. However, in practice it corresponds to the time elapsed between parton formation and the moment when they are allowed to interact. For $t < t_{\text{form}}$, partons simply free-stream, since it is not known how to model these early dynamics. Therefore, it is reasonable to identify the formation time with the time it takes the partons to travel one de Broglie wavelength, or in natural units, $t_{\text{form}} = \lambda_B$, with other possibilities being discussed below.

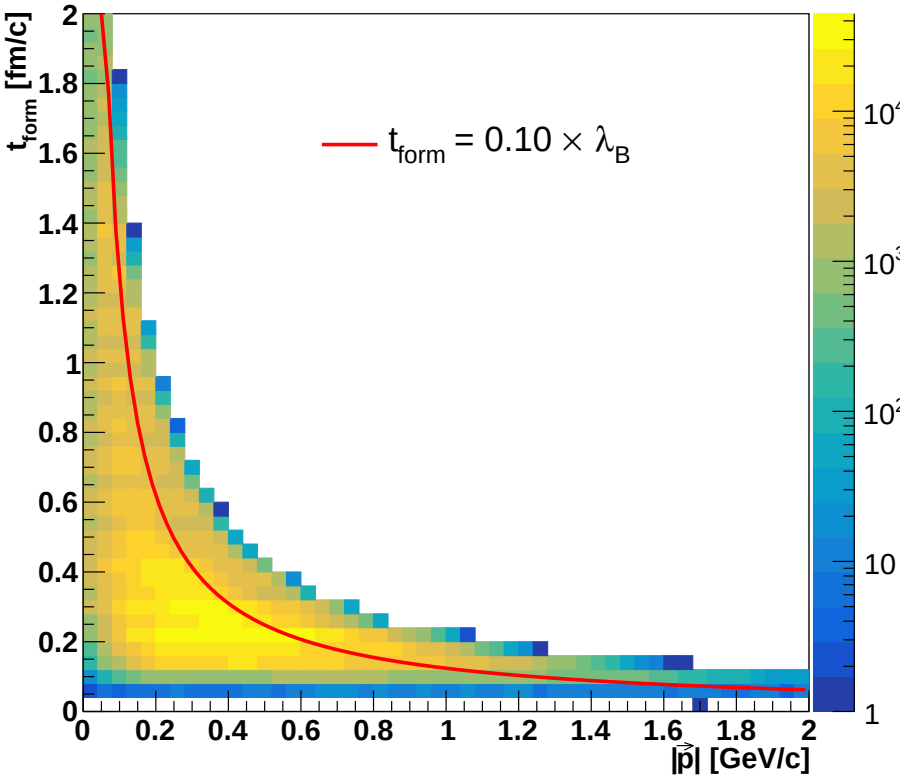

Figure 4.25: Distribution of formation times as a function of total parton momentum in AMPT with string melting. For reference, the line $t_{\text{form}} = 0.1 \times \lambda_B$ is shown, indicating that, on average, partons start to interact after traveling one-tenth of the de Broglie wavelength.

In the default version of AMPT, parton formation times are distributed following a Lorentzian of half-width $\hbar E/m_T^2$. In the string melting version of the model, parton formation times are calculated as $t_{\rm form} = \hbar E/m_T^2$, where E and m_T are the energy and transverse mass of the parton's *parent hadron*, as a consequence of how string melting is implemented. This prescription gives rise to a smearing, such that a parton of a given momentum can take on a range of possible formation time values as shown in Fig. 4.25. The form of the $\hbar E/m_T^2$ factor is motivated by Heisenberg's uncertainty principle [205]. To see how this comes about, consider high-momentum particles at midrapidity for which $p_T \approx p$. In that case,

$$\begin{aligned} t_{\rm form} &= \frac{\hbar E}{m_T^2} \\ &= \frac{\hbar\sqrt{p^2+m^2}}{p_T^2+m^2} \\ &\approx \frac{\hbar}{\sqrt{p^2+m^2}} \\ &\approx \frac{\hbar}{p}. \end{aligned} \tag{4.26}$$

Using the uncertainty principle, one can estimate the characteristic distance traveled during the early time as $\Delta x \approx \hbar/\Delta p$; asumming a 100% uncertainty on the value of the momentum yields $t_{\rm form} = \hbar/p$, just like Eq. 4.26.

Thus, there are two similar "finger physics" arguments to estimate the length of the formation time. In one case, one obtains $t_{\rm form} = h/p = \lambda_B$ (well motivated in the semi-classical kinetic theory approximation), while using the uncertainty principle (with the admittedly odd assumption of $p \sim \Delta p$ for on-shell particles, and using a given parton's parent hadron kinematics) leads to $t_{\rm form} = \hbar/p = \lambda_B/(2\pi)$.[8] The discrepancy of 2π between them, corresponding to almost an order of magnitude, is no small matter. In general, longer formation times make partons travel for a longer distance without interacting, hinder the build-up of collectivity, particularly at low-momentum. It is even possible, if following the de Broglie prescription, for the distance traveled to be larger than

[8] Factors of 2π matter. Another example where the uncertainty principle has been used, along with $\Delta p \sim p$, to derive important properties of the QGP is in Ref. [82], which presents an early calculation of the famous KSS bound on kinematic viscosity $\eta/s > \frac{1}{4\pi}$, long before its rigourous derivation from string theory. Had the thermal de Broglie wavelength been used in the calculation, a values of $\eta/s > \frac{1}{2}$ would have been found.

the system size, particularly for low-momentum partons, as shown in the $p+p$ event display in Fig. 4.26. There, a blue circle of radius equal to λ_B is drawn centered on a particular parton with $p = 0.81$ GeV, while a much smaller red circle is drawn for the same parton, of radius $\lambda_B/(2\pi)$.

We can quantify the effect on v_2 of extending the formation time, for the particular case of $p+p$ collisions with constituent quarks, as described in the previous section. Fig. 4.27 shows v_2 as a function of parton formation time, where the calculation of $t_{\rm form}$ has been modified to not depend on the parent hadron of a given parton, but to be simply a multiple of its own de Broglie wavelength. The red curve, corresponding to the partonic cross section $\sigma_{\rm part} = 0.75$ mb used in the calculations of the previous section, shows a dramatic drop in v_2 relative to the default formation time prescription in AMPT. The yellow and green curves demonstrate that even increasing the cross section by a factor of nearly 7, which naturally tends to enhance v_2, does not compensate for the reduction stemming from a longer formation time. Thus, despite the various ways in which the AMPT model can be tuned, the formation time appears as a quantity of central importance to constructing a theory of small system collectivity from the perspective of kinetic transport.

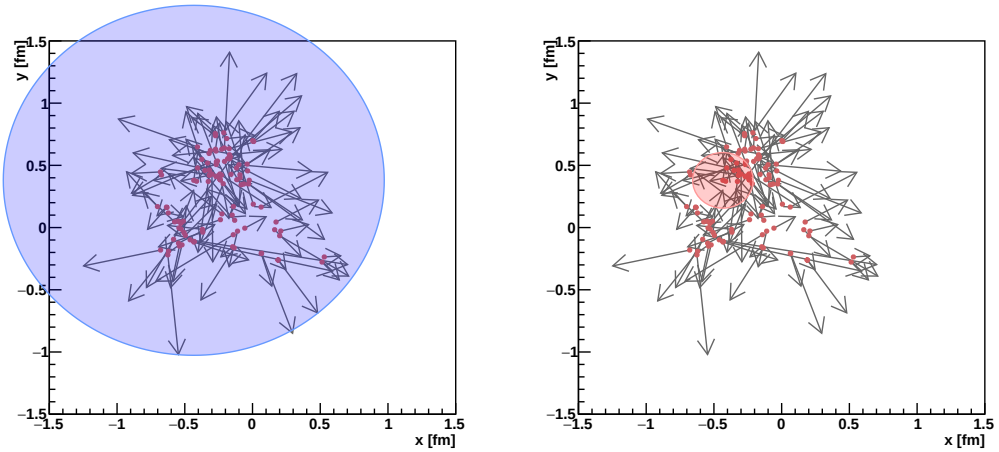

Figure 4.26: Event display showing partons from string melting in a simulated AMPT p+p event with constituent quark geometry. A circle of radius (left) $r = h/p$ and (right) $r = \hbar/p$ is drawn centered on a particular parton of momentum $p = 0.81$ GeV, to illustrate the spatial extent corresponding to its formation time. See text for discussion of the implications.

The present chapter has shown that kinetic transport can provide a good account of experimental observations of small system collectivity. This is noteworthy because the mechanism by which collectivity develops is fully independent of hydrodynamics. That is, in the context at hand, it is not true that the validity of hydrodynamics necessarily requires kinetic transport to also be valid. Thus, given that recent theoretical developments demonstrate that hydrodynamics is no longer synonymous with the existence of a thermalized strongly coupled medium, the results presented motivate the need for further examination of transport models and the implications for the physical interpretation of hot nuclear matter in small systems.

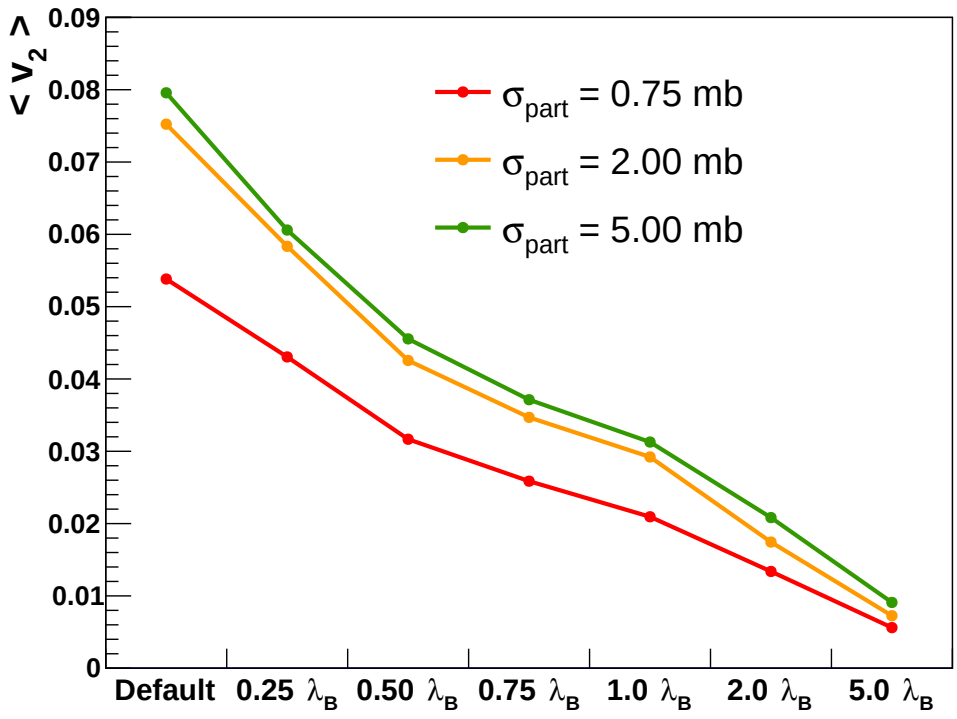

Figure 4.27: Elliptic flow v_2 for $p+p$ collisions with constituent quarks as a function of parton formation time in units of the de Broglie wavelength. The result is shown for different values of the partonic cross section σ_{part}, showing that raising the cross section cannot compensate for the reduction in v_2 from a longer formation time.

Chapter 5

Introduction to Heavy Flavor in Nuclear Collisions

This chapter marks the beginning of the second part of this dissertation, dealing with an experimental measurement of open heavy flavor production in $p+p$ collisions at $\sqrt{s_{NN}} = 200$ GeV. The chapter at hand provides an introduction to heavy flavor production in hadron collisions, as well as the role of open heavy flavor as a probe of hot nuclear matter, surveying recent experimental results. Subsequent chapters will discuss the RHIC accelerator complex, the PHENIX detector, and the actual displaced-vertex measurement of separated charm and bottom production using the PHENIX silicon tracker.

5.1 Production of Heavy Flavor in Nucleon-Nucleon Collisions

In the context of ultrarelativistic nucleus collisions, the term *heavy flavor* designates charm and bottom quarks, and it is sometimes also used as shorthand for the hadrons which contain them. Along these lines, a distinction is drawn between *open* heavy flavor hadrons, consisting of a heavy quark accompanied by a light quark, and *hidden* heavy flavor—or quarkonia—consisting of a heavy quark-antiquark pair. We ignore the top quark in this discussion, as its production is precluded at RHIC energies due to its large mass.

The study of heavy flavor production in elementary $p + p$ collisions is of interest from a variety of vantage points [53, 50]. For instance, such measurements provide a baseline against which corresponding results in larger p+A and A+A collisions can be compared to, in the study of cold and hot nuclear matter effects, respectively. Additionally, heavy flavor measurements in

$p+p$ provide a valuable testing ground for perturbative QCD (pQCD) calculations. Unlike with light quarks, the large masses of charm and bottom ($m_c \approx 1.3$ GeV and $m_b \approx 4.2$ GeV) allow for the perturbative calculation of quark production even at low p_T. This can be understood by considering that, in hadron collisions, the production of heavy quarks is dominated at leading order (LO) $\mathcal{O}(\alpha_s^2)$ by gluon fusion and quark-antiquark annihilation, as shown in Fig. 5.1 (a) and (b). Other processes, such as flavor excitation and gluon splitting, contribute at next-to-leading order (NLO) $\mathcal{O}(\alpha_s^3)$, as shown in panels (c)-(f). In NLO calculations, the mass of the heavy flavor quarks acts as an infrared cutoff on collinear singularities. However, this does not hold when the quark's p_T is much greater than its mass. In that case, large terms of the following form appear at all orders:

$$\alpha_s^2 \left[\alpha_s \ln \frac{p_T}{m}\right]^k, \tag{5.1}$$

$$\alpha_s^3 \left[\alpha_s \ln \frac{p_T}{m}\right]^k. \tag{5.2}$$

The logarithmic α_s^2 and α_s^3 terms are referred to as leading-log (LL) and next-to-leading-log (NLL) terms, respectively. Currently, the most advanced available pQCD calculations of heavy flavor hadroproduction incorporate schemes to resum these logarithmic terms. The fixed-order-plus-next-to-leading-log (FONLL) approach [70] matches the massive NLO cross section calculated at low p_T using fixed order perturbation theory[1] , with the massless NLO calculation at high p_T where the logarithmic terms have been resummed. The FONLL cross section is thus written as follows

$$d\sigma_{\mathrm{FONLL}} = d\sigma_{\mathrm{FO}} + G(m_Q, p_T) \times (d\sigma_{\mathrm{RS}} - d\sigma_{\mathrm{FOM0}}), \tag{5.3}$$

where $d\sigma_{\mathrm{FOM0}}$ is the fixed order cross section $d\sigma_{\mathrm{FO}}$ in the limit where p_T is much greater than the quark mass, and $d\sigma_{RS}$ is the resummed cross section. The interpolating function, dependent on the heavy flavor quark mass m_Q and some constant a, is given by

$$G(m_Q, p_T) = \frac{p_T^2}{p_T^2 + a^2 m_Q^2} \tag{5.4}$$

[1] The calculation is carried out in the fixed-flavor number scheme (FFNS), where the massive heavy flavor quark is not an active parton in the proton, appearing only in the final state. In this calculation, the number of light flavors is fixed to $n = 3$ for charm, and $n = 4$ for bottom.

such that the desired limits are recovered $G(m_Q, p_T \to 0) \to 0$ and $G(m_Q, p_T \to \infty) \to 1$.

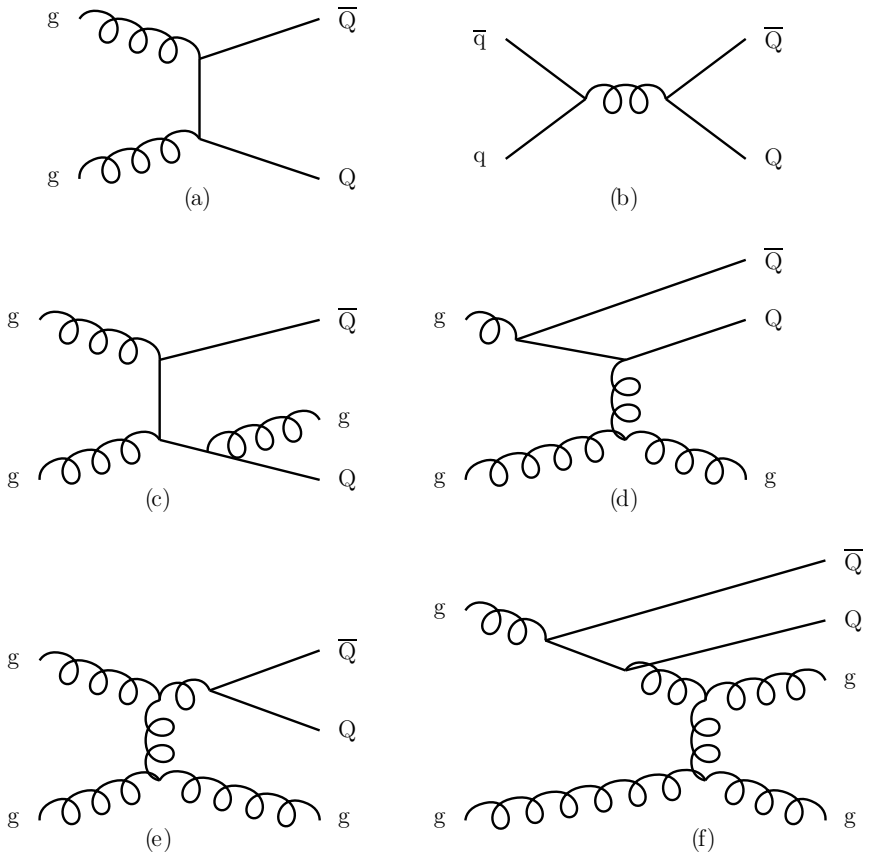

Figure 5.1: Feynman diagrams depicting heavy flavor production at various orders. Panels (a) and (b) depict leading order processes, while (d)-(f) represent next-to-leading order contributions. Image reproduced from Ref. [70].

Other analytic pQCD approaches to heavy flavor hadroproduction, which will not be discussed here, include the Zero-Mass and General-Mass Variable Flavor Number Schemes (ZM-VFNS and GM-VFFN) [190]. Additionally, a number of common Monte Carlo generators, such as PYTHIA [183] and HERWIG [57], have the advantage of modeling the hadronic final state in full, yet calculate the partonic cross section only at the LO+LL level of accuracy. Other generators, such as POWHEG [157] and MC@NLO [103] incorporate next-to-leading order calculations.

The pQCD calculations above provide the heavy flavor cross section, but the hadronization of the $q\bar{q}$ pair is described by fragmentation functions [69] which are considered to be universal, and can be measured in e^+e^- collisions. Hadronization can proceed in two different ways. Namely, the quark pair can remain together in a quarkonium state, or the quarks can fragment independently, giving rise to two different open heavy flavor hadrons. The latter possibility is the most common, occurring over 98% of the time [53].

Experimentally, the production of heavy flavor in hadron collisions can be determined by studying heavy flavor decay products. Three main methods can be identified: (*i*) by measuring the products of *hadronic* decays, either by reconstructing the full decays (e.g., $B^0 \rightarrow J/\psi + K^0_s$, $D^0 \rightarrow \pi^+K^-$), or by focusing on a given type of decay particle (e.g., J/ψ) and selecting those pointing back to a displaced vertex; (*ii*) by measuring leptons from heavy flavor decays, either by identifying those pointing back to a displaced vertex, or using a cocktail to statistically remove background; and (*iii*) by tagging charm and bottom jets. Fig. 5.2 shows a world data compilation of the total charm and bottom production cross section in $p + p$, $p + \bar{p}$, and $p + A$ collisions as a function of collision energy, along with NLO and FONLL pQCD calculations, which emcompass the data within uncertainties.

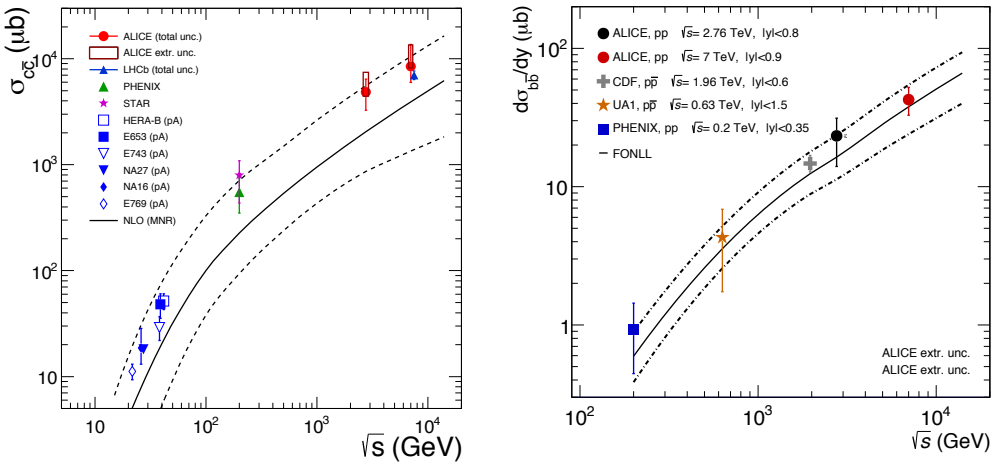

Figure 5.2: World data of total $c\bar{c}$ left and $b\bar{b}$ (right) cross section as a function of collision energy. Points corresponding to small collision system data have been scaled down by the number of binary collisions. Shown for comparison are NLO and FONLL calculations. Figure reproduced from Ref. [50].

5.1.1 Heavy Flavor Measurements at RHIC

Of the three methods of measuring heavy flavor production mentioned in the previous subsection, the PHENIX experiment has focused primarily on measuring semileptonic decay products, while STAR has additionally carried out direct decay reconstruction. In this subsection, emphasis will be placed on existing heavy flavor measurements made by PHENIX prior to the installation of the silicon vertex detector upgrade in 2011. This subsection will follow the reviews presented in Refs. [53, 50].

As will be discussed in detail in the next chapter, the PHENIX detector has two spectrometer arms, spanning $|\eta| < 0.35$ with tracking and particle identification capabilities, in which charged hadrons, photons, and electrons can be measured. This allows for a clean sample of inclusive electron candidates to be isolated, containing contributions from the decay of the desired heavy flavor hadrons as well as abundant background particles. The heavy flavor contribution is isolated by constructing a simulated background electron cocktail and subtracting it from the electron

candidate sample. The dominant components of the cocktail correspond to electrons from the Dalitz decay of π^0 and from the conversion of photons in the detector material. When the inclusive heavy flavor measurements were made in 2004, the material budget of the detector at midrapidity amounted to less than 1% of a radiation length, such that the ratio of conversion to Dalitz electrons was very low. In addition to neutral pions, the cocktail comprised other light mesons, most notably the η, as well as the ρ, ω, and ϕ. The three-body decay electrons of $K^{\pm}$ and K^0_s are also included, as well as those from J/ψ and Υ decays, and the Drell-Yan process, which account for a substantial fraction of the background above $p_T \approx 5$ GeV/c. In order to construct such a cocktail it is necessary to have previously measured the production cross section of all the necessary primary particles in order to simulate them.

At low $p_T < 2$ GeV/c, the applicability of the cocktail method is limited by the increase in signal-to-background ratio. To isolate the heavy flavor electrons in this kinematic region, the PHENIX collaboration introduced a copper cylinder symmetrically around the beam pipe to act as a converter for photons. Since photonic background has a fixed ratio of conversion to non-conversion electrons, increasing conversions by a known factor allows for the subtraction of the entire photonic background. Both the converter and cocktail methods are consistent in their overlap region. Full details of this analysis can be found in Refs. [20, 15], with the inclusive invariant cross section of heavy flavor electrons shown in Fig. 5.3. Also shown in the figure are FONLL calculations for all heavy flavor electrons, as well as those from charm and bottom decays individually. The data are in good agreement with FONLL within its large uncertainties, as evidenced by the ratio plot in the bottom panel.

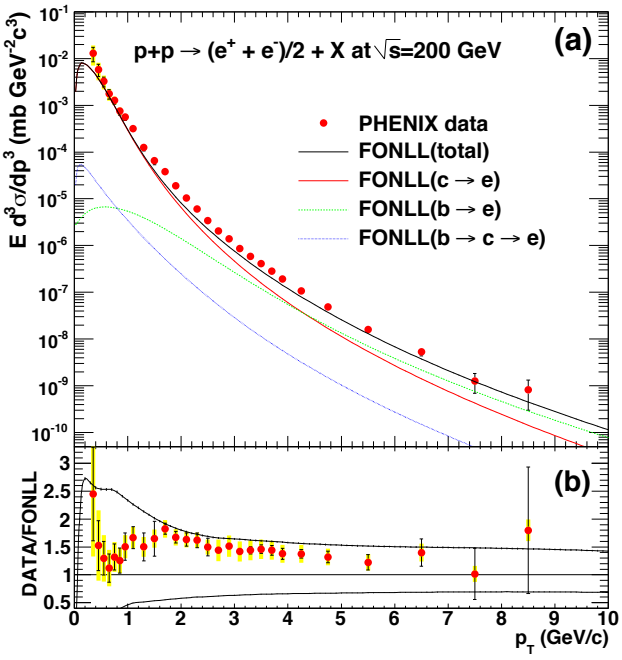

Figure 5.3: Invariant cross section of inclusive heavy flavor electrons measured by the PHENIX experiment. Shown for comparison are FONLL pQCD calculations of the total heavy flavor electron $c + b \rightarrow e$ production, as well as the individual $c \rightarrow e$ and $b \rightarrow e$ contributions. The bottom panel shows the ratio of the data to the FONLL calculation. Figure reproduced from Ref. [20].

The STAR experiment has also measured inclusive heavy flavor electron production, as described in Ref. [36]. These results are consistent with those from PHENIX, as shown in Fig. 5.4. However, it should be mentioned that STAR does not use the cocktail method for background subtraction. Instead, photonic background is identified by exploiting the fact that photonic electron pairs have a very low invariant mass, in a procedure that does not require a detailed knowledge of the detector's material budget; although the limited acceptance of the detector does not allow for all electron pairs of interest to be measured, the efficiency of the procedure can be determined using simulations.

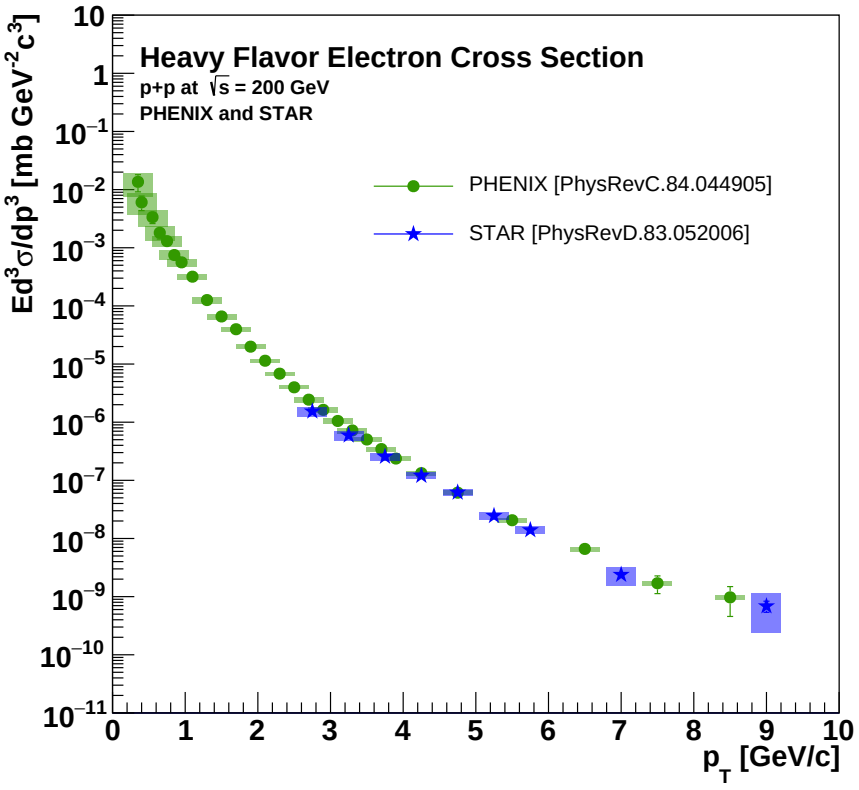

Figure 5.4: Invariant cross section of heavy flavor electrons in $p+p$ collisions at $\sqrt{s_{NN}} = 200$ GeV, as measured by the PHENIX [20] and STAR [36] collaborations.

The comparison of the inclusive heavy flavor electron cross section to FONLL calculations, as shown in Fig. 5.3, suggests that charm decays dominate heavy flavor production at low p_T, with bottom coming to dominate above $p_T \approx 4$ GeV/c. It is, therefore, of interest to confirm this experimentally by measuring the electron yield from each heavy quark flavor separately. To that end, both PHENIX and STAR have measured electron-hadron correlations, relying on the fact that electrons from charm and bottom decays are correlated differently with the hadronic decay products.

The approach followed by PHENIX [17] is based on partially reconstructing the $D^{\pm} \rightarrow e^{\pm}K^{\mp}X$ decay and measuring the invariant mass distribution of unlike-charge electron-hadron pairs. The distribution will exhibit a correlation from the heavy flavor decay kinematics, as shown

in the left panel of Fig. 5.5 for two different hadron p_T bins, normalized to the inclusive heavy flavor electron yield. Then, the EVTGEN [134] (a Monte Carlo event generator specialized in B physics) and PYTHIA generators are used to generate templates for the invariant mass distribution using only charm and bottom decay electrons, as indicated by the dashed lines. The data are fit with the sum of the two templates, with the only free parameter corresponding to the relative normalization of charm and bottom. The resulting fraction of bottom-to-inclusive heavy flavor electrons is shown in the right panel of Fig. 5.5. Despite large uncertainties on the measurement, the expected rise of the bottom contribution with p_T is seen, and agreement with FONLL is observed.

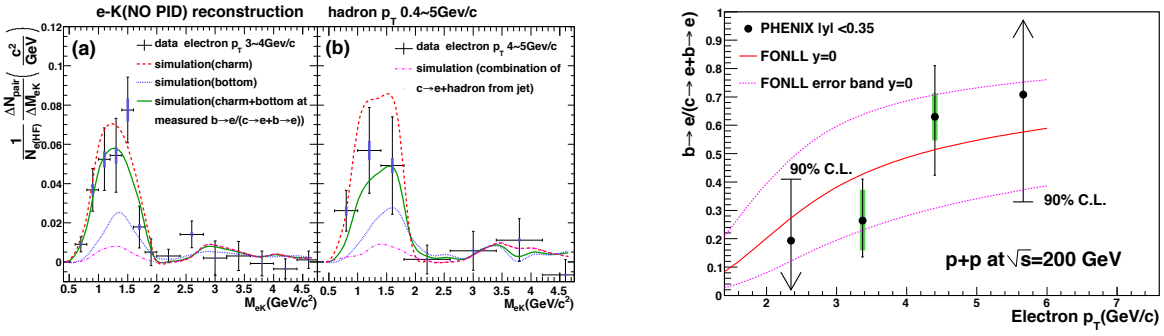

Figure 5.5: (left) Invariant mass distribution of inclusive electron-hadron pairs measured by PHENIX, compared with PYTHIA templates for charm and bottom decay electrons. (right) Fraction of electrons from bottom decays to inclusive heavy flavor electrons, as determined from the correlations shown on the right. A comparison with a FONLL calculation is also shown. Figure reproduced from Ref. [17].

Unlike PHENIX, the STAR experiment [37] measures *azimuthal* correlations between heavy flavor electrons and charged hadrons, as shown for two p_T bins in the left panel of Fig. 5.6. Due to differences in decay kinematics, bottom correlations will exhibit a broader near-side peak than those from charm. PYTHIA is used to generate templates for charm and bottom correlations, which are used to fit the data with a single free parameter, from which the corresponding bottom electron fraction, shown in the right panel of the figure, can be extracted. Notice that, compared

to the corresponding PHENIX measurement, the STAR result has more data points and smaller uncertainties as a consequence of the larger detector acceptance. Notice that this approach to heavy flavor separation using correlations can only be applied in $p+p$ collisions, as it is limited by the very large combinatorial background in A+A collisions.

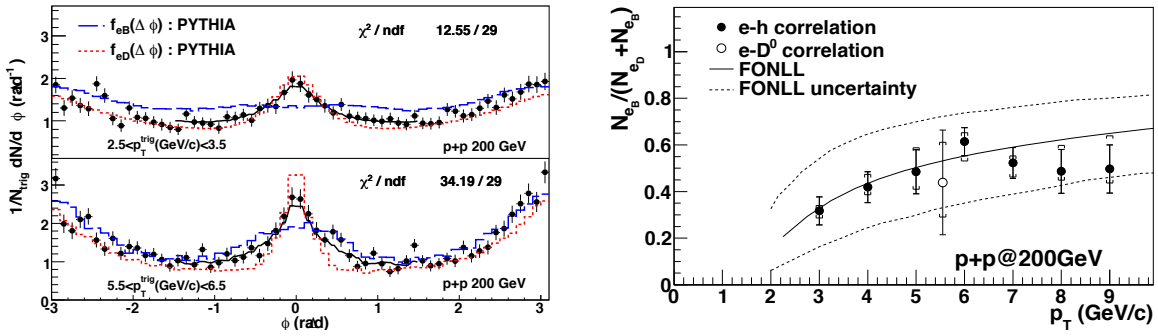

Figure 5.6: (left) Azimuthal angular correlations between heavy flavor decay electrons and charged hadrons, as measured by STAR in two different p_T bins, compared to templates for charm and bottom electrons as calculated with PYTHIA. (right) Fraction of electrons from bottom decays to inclusive heavy flavor electrons, as determined from the correlations shown on the right. A comparison with a FONLL calculation is also shown. Figure reproduced from Ref. [37].

Besides heavy flavor electrons, the STAR experiment has also successfuly measured heavy flavor by reconstructing exclusive decays in full, namely $D^0 \rightarrow K^-\pi^+$ and $D^{*+} \rightarrow D^0\pi^+$, as discussed in Ref. [13]. This allows for the measurement of the $c\bar{c}$ cross section, as shown in Fig. 5.7. Notice that the data compares favorably with the FONLL calculation, yet lies very close to the upper edge of its uncertainty band.

To finalize this subsection, in addition to measurements of electrons at midrapidity, the PHENIX muon spectrometers allow for heavy flavor measurements at forward rapidity through semimuonic decay channels. These results will not be reviewed here, and the interested reader is referred to Ref. [35].

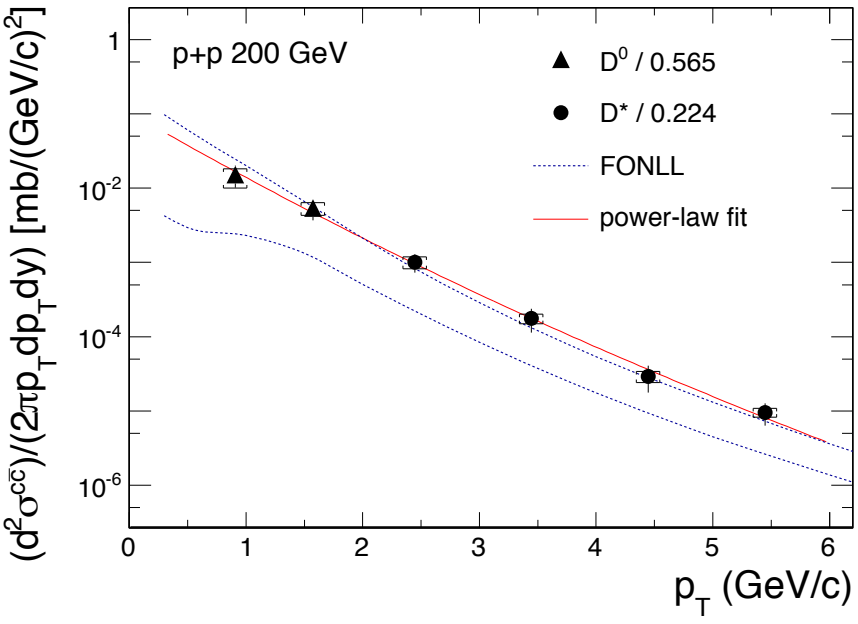

Figure 5.7: Charm production cross section as a function of p_T as determined from D^0 and D^* production measurements by STAR. The dashed lines form a band representing the edge of the FONLL calculation uncertainties; the central FONLL curve is not depicted. Figure reproduced from Ref. [13].

5.1.2 Heavy Flavor Measurements at the LHC

Even though the focus of this dissertation is the measurement of heavy flavor production in $p+p$ to serve as a baseline for corresponding measurements in larger collision systems at RHIC, it is of interest, for the sake of completeness, to discuss some heavy flavor production results from LHC experiments. Here, a brief catalog of results is presented, which is not intended to be comprehensive. For a full discussion, see Ref. [50].

LHC detectors explore heavy flavor through all three possible observables—leptons, full hadron decay reconstruction, and jet tagging. Both the ALICE and ATLAS experiments have measured electrons and muons from heavy flavor decays over wide rapidity ranges [8, 7, 2, 10], as shown in Fig. 5.8 and Fig. 5.9. Like the results at RHIC energies, these measurements are well described by FONLL, in addition to other NLO calculations such as that used in the POWHEG [157]

Monte Carlo generator.

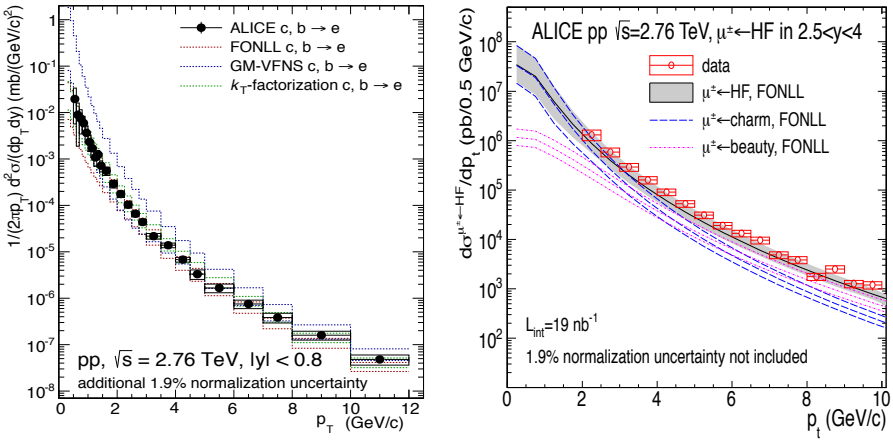

Figure 5.8: Invariant cross section of heavy flavor electrons and muons as measured by the ALICE collaboration. Figure (left) reproduced from Ref. [10]. Figure (right) reproduced from Ref. [7].

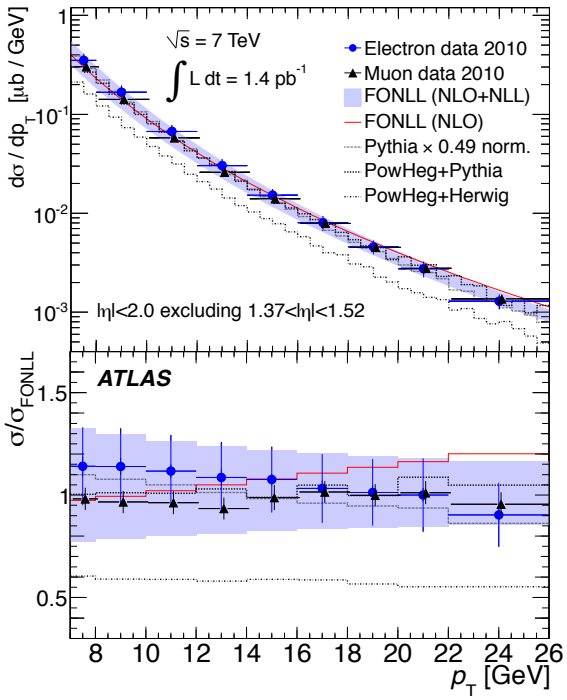

Figure 5.9: Cross section of heavy flavor electrons and muons as measured by the ATLAS collaboration, compared with a variety of theory calculations. Figure reproduced from Ref. [2].

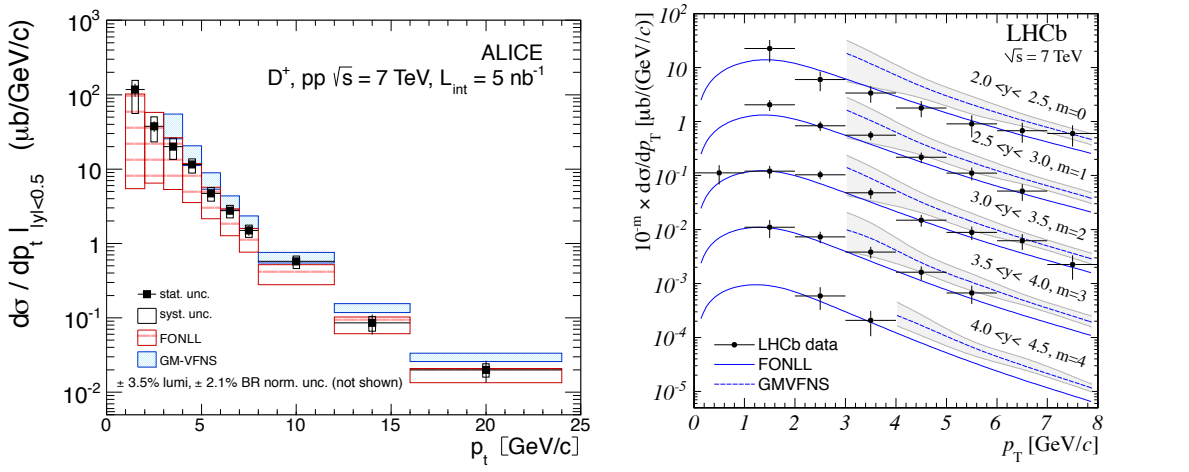

Figure 5.10: (left) Cross section measurement of D^+ at $\sqrt{s_{NN}} = 7$ TeV by the ALICE experiment and (right) D_s^+ at the same collision energy by LHCb.

Regarding open charm measurements, LHC experiments follow the same approach as STAR, of reconstructing exclusive D meson decays in full. Thus, pairs or triplets of appropriately charged tracks constitute D meson candidates, with substantial background being rejected by topological cuts on secondary vertices. Fig. 5.10 presents a few selected D meson measurements. The left panel shows the cross section of prompt D^+ in $p+p$ collisions at $\sqrt{s_{NN}} = 7$ TeV as measured by ALICE, whereas the right panel shows a rapidity-dependent measurement of the D_s^+ cross section by LHCb. Comparisons to pQCD calculations are shown; both FONLL and GMV-FNS agree with the data within uncertainties, with the former tending to under-predict and the latter to over-predict it.

Lastly, we briefly consider open bottom measurements. Like open charm production, B mesons are identified by reconstructing their hadronic decays, through displaced charmonium measurements, or jet b-tagging. Precision measurements of bottom production are important to constrain theoretical models which suffer from very large uncertainties arising from the quark mass, as well as the factorization and renomalization scales. Fig. 5.11 shows two measurements, by CMS [125] and ATLAS [3], of the B^+ cross section, where the hadron is identified by reconstructing its $B^+ \to J/\psi K^+ \to \mu^+\mu^- K^+$ decay. Theory comparisons are also shown; again, FONLL and NLO calculations yield reasonable agreement with the data within uncertainties, but PYTHIA,

shown in the leftmost panel, does not owing to its limited LO+LL accuracy.

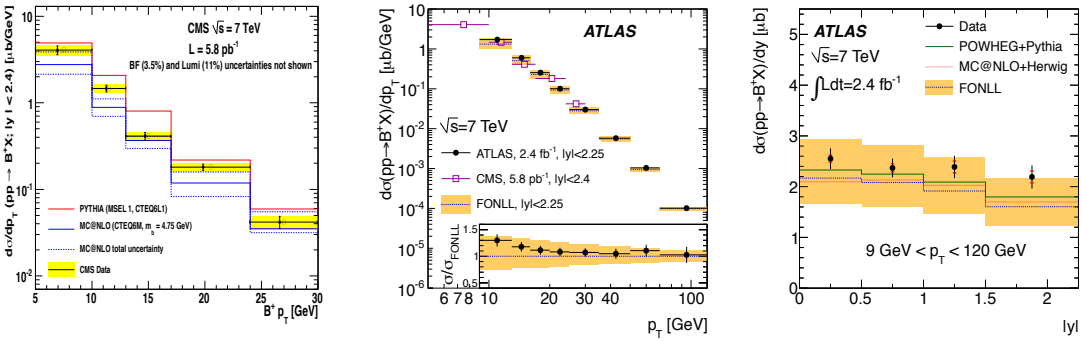

Figure 5.11: Production cross section of B^+ hadrons as a function of p_T in $p+p$ collisions at $\sqrt{s_{NN}} = 7$ TeV, as measured by CMS (left) and ATLAS (center), compared to various theory calculations. ATLAS has also measured the rapidity dependence of B^+ production (right). Figures reproduced from [125, 3].

5.2 Heavy Flavors as Probes of the Quark-Gluon Plasma

In the context of ultrarelativistic nucleus-nucleus collisions, heavy flavor quarks are of particular interest since their mass ($m_c \approx 1.3$ GeV and $m_b \approx 4.2$ GeV) is well above the temperature of the QGP. As a result, their thermal production is Boltzmann-suppressed in the QGP medium, even at LHC energies, with heavy flavor quarks originating instead in hard partonic processes in the early stages of nuclear collisions. As a result, heavy quarks transit through the full evolution of the QGP medium, from equilibration to hadronization, without experiencing modifications to their total yield in the process.

Heavy quark production measurements in $p+p$ collisions provide a baseline for the corresponding observables in heavy-ion collisions, where a variety of nuclear effects are expected to modify the heavy flavor spectra, inducing deviations from binary scaling. The nuclear modification factor, as defined below, serves to quantify such deviations:

$$R_{AA} = \frac{1}{\langle N_{\text{coll}} \rangle} \frac{dN^{A+A}/dp_T}{dN^{p+p}/dp_T}. \tag{5.5}$$

In the above equation, dN^{A+A}/dp_T and dN^{p+p}/dp_T correspond to the spectra measured in A+A and p+p collisions, respectively, and $\langle N_{\rm coll}\rangle$ is the number of binary collisions in the A+A centrality class under consideration. In the absence of nuclear effects, the expectation is for $R_{AA} = 1$. Equivalently, the nuclear modification factor can be written as

$$R_{AA} = \frac{1}{\langle T_{AA}\rangle}\frac{dN^{A+A}/dp_T}{d\sigma^{p+p}/dp_T}, \tag{5.6}$$

where $\langle T_{AA}\rangle$ is the nuclear thickness function defined in Chapter 4, relating $\langle N_{\rm coll}\rangle$ to the nucleon-nucleon cross section.

Two classes of nuclear modifications are possible. Initial-state effects, or so-called *cold nuclear matter* effects, are best studied in asymmetric $p(d)$+A collisions. These include a variety of phenomena, which will not be discussed here, such as isospin effects, modifications of parton distribution functions in nuclei, and initial-state energy loss. For a discussion of heavy flavor as probes of cold nuclear matter, see Ref. [194]. On the other hand, final-state effects refer to modifications to the phase-space distributions of heavy flavor quarks due to the presence of the QGP medium in A+A collisions, which soften the heavy flavor spectra relative to those measured in the $p + p$ baseline.

The study of how heavy flavors are modified by the QGP medium is useful to understand the dynamics of parton-medium interactions, particularly as they are responsible for the color-opacity of the QGP. It has been known for quite some time that high-energy color charges traversing the QGP lose energy in the process [112], manifested as a suppression of the nuclear modification factor for a variety of hadronic observables including individual particles and fully reconstructed jets. As an illustration, Fig. 5.12 shows a compilation of R_{AA} measurements carried out by PHENIX for a variety of species in Au+Au collisions at $\sqrt{s_{NN}} = 200$ GeV. Notice how photons, which do not interact strongly, exhibit an R_{AA} consistent with unity, whereas pions are substantially suppressed.

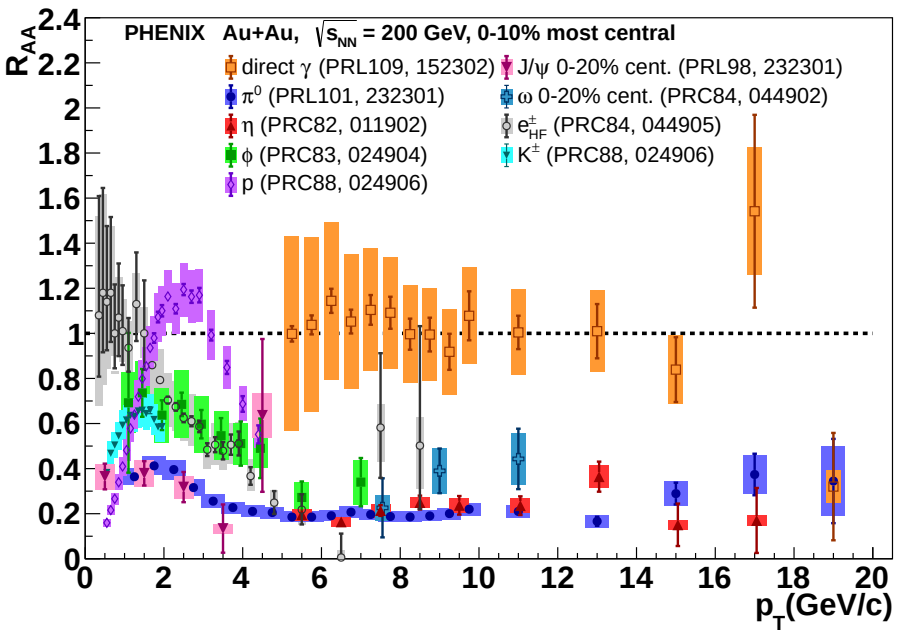

Figure 5.12: Nuclear modification factor R_{AA} for a variety of particle species, as measured by the PHENIX experiment at in Au+Au collisions at $\sqrt{s_{NN}} = 200$ GeV. Image credit: PHENIX collaboration.

For a long time it was assumed that gluon radiation, or gluon bremsstrahlung, by moving color charges constituted the dominant mechanism responsible for energy loss in the QGP medium. In fact, the energy loss of light quark flavors, as evidenced by the suppression of light hadrons shown in Fig. 5.12, can be well accounted for by models of radiative energy loss [174, 206, 81]. In these models, the multiple rescattering of a fast parton traversing the medium is responsible for the emission of gluons, with two regimes being distinguished. Let μ be the characteristic momentum transfer in a single scattering.[2] If the wavelength μ^{-1} associated with the typical momentum transfer is much smaller than the mean free path λ in the medium, then successive scatterings can be treated as independent and the energy loss cross section is given by the standard Bethe-Heitler formula for bremsstrahlung [61]. On the other hand, if the typical momentum transfer is such that the wavelength becomes much longer than λ, then scatterings are no longer independent and a suppression of the radiated energy spectrum is observed, by a factor of $\sqrt{\lambda\mu^2/\omega}$, where ω is the

[2] In the QGP, μ can be identified with the Debye screening mass.

energy of the gluon. This is the QCD analog of the Landau-Pomeranchuk-Migdal effect which, in standard QED, leads to a suppression of photon emission at low energies, while in QGP it is responsible for the suppression of gluons at high energies. In this regime, it can be shown that the total energy loss of a fast parton is proportional to the square of the distance L traveled in the medium, by integrating the following expression

$$-\frac{dE}{dz} = \frac{\alpha_s}{\pi} N_c \frac{\mu^2}{\lambda} L, \tag{5.7}$$

where N_c is the color charge of the parton. See Ref. [55, 86] for further details. From the above expression, it is possible to see that gluons—with a larger color coupling N_c—will experience a greater energy loss than quarks.

Furthermore, a distinction in the angular emission pattern of gluon radiation must be drawn between light and heavy flavors. Namely, radiation is supressed at small angles relative to the quark momentum, with the effect becoming more pronounced with increasing mass. This phenomenon is known as the dead cone effect [86], in which gluon radiation for $\theta < \theta_0$ is suppressed by a factor F given by [189]

$$F = \frac{k_\perp^2}{k_\perp^2 + \omega^2\theta_0^2} = \frac{\sin^2\theta}{\sin^2\theta + \theta_0^2}. \tag{5.8}$$

In the above equation, $\theta_0 = m/E$ where m and E are the mass and energy of the quark, and ω is the energy of the radiated gluon. From the expression, it becomes apparent that there is no difference in radiation patterns between light and heavy quarks at very high p_T. Nevertheless, in the kinematic region of interest for the measurement at hand, namely $5 < p_T[\mathrm{GeV}/c] < 10$, the expectation is for light hadrons to exhibit a greater suppression than those with heavy flavor content. However, the R_{AA} compilation in Fig. 5.12 demonstrates that heavy flavor decay electrons are suppressed just as much as light mesons within $5 < p_T[\mathrm{GeV}/c] < 10$. Since the yield of heavy flavor quarks is conserved—unlike that of light flavors—the observed suppression of heavy flavor electrons at high p_T is accompanied by corresponding enhancement at low p_T. This state of affairs invites further refinements to our understanding of energy loss in the QGP. In particular, the inclusion of elastic collisional energy loss becomes important for heavy quarks, as its contribution to total energy loss

has been estimated, at first order, to be equal to that of gluon radiation [149].

In addition to the nuclear modification factor R_{AA}, the elliptic flow v_2 of heavy flavor constitutes another important observable of parton-medium interactions. While charm and bottom were originally deemed too heavy to "flow" with the medium owing to their long relaxation (thermalization) times, it was realized [56] that the observation of a large heavy flavor v_2 could provide evidence for the existence of very strong interactions of partons with the QGP. Thus, models of energy loss must necessarily account for both these observables, which originate from the same parton-medium interactions. Fig. 5.13 shows R_{AA} and v_2 measured by PHENIX [15] for inclusive heavy flavor electrons in Au+Au collisions. Also shown are a series of calculations from a variety of theoretical models. Curves I corresponds to a pQCD calculation with radiative energy loss, using a very large transport coefficient. Notice how this model alone, with no collisional energy loss, can account resonably well for the R_{AA} but not the v_2. On the other hand, curves II incorporate elastic scattering mediated by resonance excitations, achiving a description of both observables. Finally, curves III represent another class of models, namely Langevin models with drag and diffusion. In this stochastic picture, the large-scale motion of a quark is dictated by the viscous drag force, but with a series of uncorrelated momentum "kicks" which give rise to fluctuations in the quark coordinates, following Brownian motion.

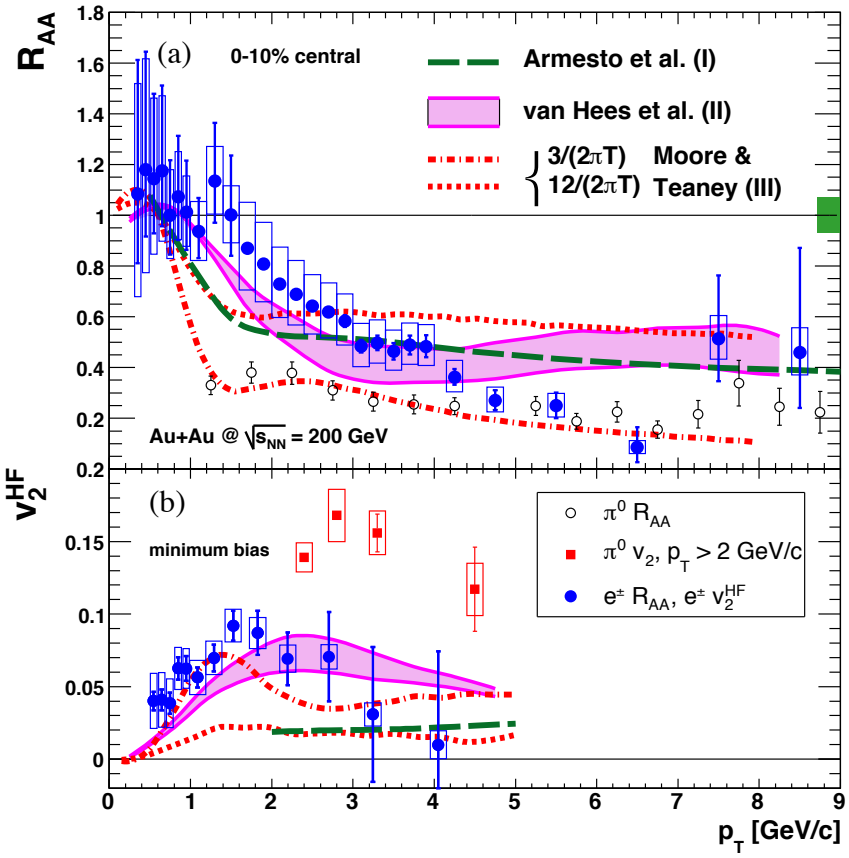

Figure 5.13: Fraction of bottom to inclusive heavy flavor electrons measured by PHENIX via a displaced vertex analysis in Au+Au collisions at $\sqrt{s_{NN}} = 200$ GeV. Image reproduced from [15].

Despite significant progress in understanding parton-medium interactions, including novel approaches using the AdS/CFT correspondence [120], further study is required to fully elucidate the physics underlying the strong suppression of heavy flavor electrons at RHIC. In recent years, as the field of heavy-ion physics has moved towards a new era of precision measurements, new instrumentation has become available. For instance, PHENIX and STAR have installed silicon vertex detectors allowing for precision event vertex determination. In particular, this allows for the differential measurement of charm and bottom production. Owing to the significant mass difference between charm and bottom quarks, these new measurements can provide important discriminating constraints for theories attempting to describe parton energy loss. For instance, the effect of varying

the quark mass in a drag-diffusion model should be immediatly apparent.

The PHENIX experiment, using the first Au+Au data collected with its silicon vertex detector in 2011, successfully carried out a separation of charm and bottom hadron production via displaced vertex measurements of their decay electrons [29]. The measurement exploits the fact that bottom hadrons have a longer lifetime than charm hadrons, traversing a longer distance before decaying. Thus, electrons from $b \to e$ originate from a displaced vertex farther away from the primary vertex than those from $c \to e$. Experimentally, the distance of closest approach (DCA) of inclusive heavy flavor electron tracks to the primary vertex was measured, and an unfolding procedure was used—along with a model of heavy flavor hadron decay—to infer the yields of the parent hadrons. Fig. 5.14 shows the ratio of bottom to inclusive heavy flavor decay electrons, where the band corresponds to the 1σ limits of the total point-to-point correlated errors. The bottom electron fraction is seen to agree with FONLL within the large uncertainties of both the measurement and the calculation, albeit with a steeper slope at low p_T and hints of a peak around $p_T \approx 3$ GeV/c.

As of the date of publication of this heavy flavor separation analysis in Au+Au collisions, there was no corresponding measurement carried out in $p + p$ at RHIC. In fact, the first $p + p$ dataset using the PHENIX silicon vertex detector was collected in 2015. Thus, results from the STAR heavy flavor separation analysis in $p+p$ collisions using electron-hadron correlations, as previously discussed and shown in Fig. 5.6, were used as a baseline to calculate the nuclear modification factor R_{AA} for charm and bottom decay electrons separately. The result is shown in Fig. 5.15. The top panel shows the individual R_{AA}, indicating the stronger suppression of charm over bottom at low p_T. At high p_T, which is the region of interest, bottom electrons appear to be more suppressed than those from charm, yet the very large uncertainties on the measurement prevent any strong conclusion from being drawn. The bottom panel of the figure shows the ratio between the two R_{AA} curves, consistent with unity within uncertainties at high p_T.

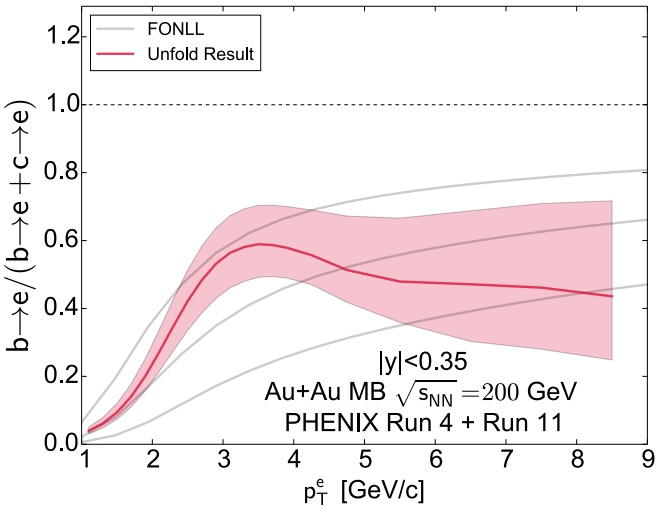

Figure 5.14: Fraction of bottom to inclusive heavy flavor electrons measured by PHENIX via a displaced vertex analysis in Au+Au collisions at $\sqrt{s_{NN}}$ = 200 GeV. Figure reproduced from Ref. [29].

Whereas the large uncertainties on the measured bottom electron fraction of Fig. 5.14 are driven primarily by the size of the statistical sample of reconstructed electron tracks in Au+Au, the uncertainties on the R_{AA} measurement are driven additionally by the large uncertainty from the baseline measurement used. Steps to improve the measurement in Au+Au have already been taken, using a much larger dataset recorded by PHENIX in 2014 [150], allowing even for heavy flavor separation in centrality categories. Thus, the next necessary step is to measure the charm and bottom spectrum in $p+p$ collisions using the identical technique as was used in Au+Au. That is the subject of the second part of this dissertation.

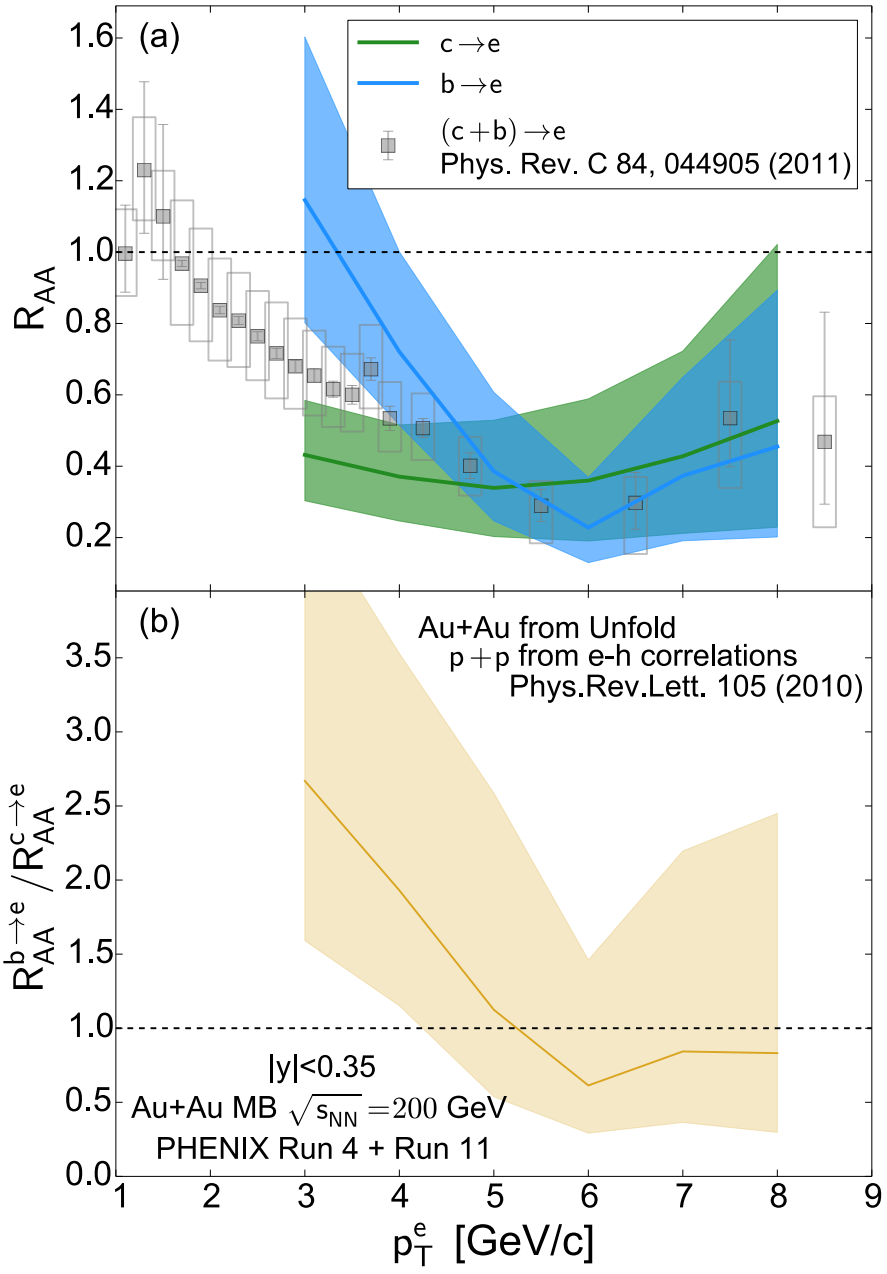

Figure 5.15: R_{AA} of charm and bottom decay electrons measured by PHENIX via a displaced vertex analysis in Au+Au collisions at $\sqrt{s_{NN}} = 200$ GeV. Figure reproduced from Ref. [29].

Chapter 6

Experimental Setup

6.1 The Relativistic Heavy Ion Collider—RHIC

The Relativistic Heavy Ion Collider (RHIC) [116] is currently the United States' sole superconducting hadron collider, operating at Brookhaven National Laboratory (BNL) in Upton, New York. As the world's first dedicated relativistic heavy-ion collider, starting operations in the year 2000, it opened the door to a new age in the study of the QCD structure of matter in the high-energy regime. In its now eighteen years of operation, RHIC has delivered collisions of a variety of nuclear species, including Au+Au, Cu+Cu, Cu+Au, U+U, p+Au, p+Al, d+Au, ^{3}He+Au, and $p+p$ at a variety of collision energies from $\sqrt{s_{NN}} = 7.7$ to 510 GeV, as summarized in Fig. 6.1. Moreover, its unique capability to collide spin-polarized protons has fostered a strong program in spin physics, which is described in detail in Ref. [51]. The layout of the RHIC complex, consisting of the main collider and a series of auxiliary accelerators for injection, is shown in the left panel of Fig. 6.2.

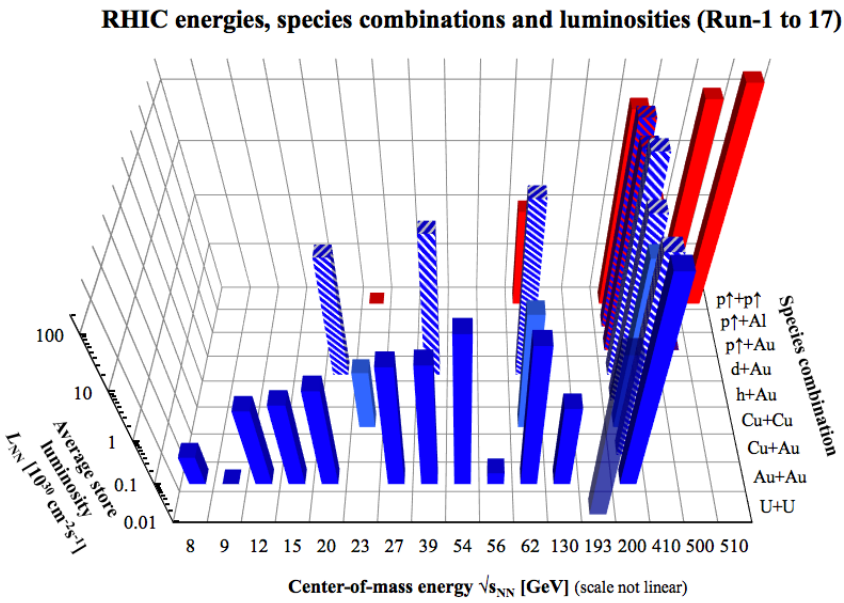

Figure 6.1: Operating modes of RHIC from years 2000-2017 and corresponding average store luminosity. Image credit: Collider Accelerator Department, Brookhaven National Laboratory.

The right panel of Fig. 6.2 shows a schematic diagram of the RHIC injection chain. The versatility to collide such a wide array of nuclei originates in the Electron Beam Ion Source (EBIS) [165], an electron beam ionization source installed in 2009 as part of the pre-injection system, capable of delivering ions from He_3^{2+} to U_{238}^{38+}, replacing the previously used sputter ion source and tandem van de Graaf accelerator. Let us follow the acceleration chain of Au ions, from EBIS to RHIC. Ions from EBIS, housed in the proton linear accelerator (LINAC) area, are accelerated by a pair of small LINACs and injected to the Booster synchrotron. The Booster accelerates them to an energy of 95 MeV, at which point they are transfered to the Alternating Gradient Synchrotron (AGS), with any remaining electrons—except for a pair in the innermost K-shell of the atom—being stripped away in the process. It takes four Booster cycles to fill the AGS, which accelerates the Au ions to 8.86 GeV. The ions are then transfered to the AGS-to-RHIC (AtR) beamline, at which point they are completely stripped of electrons, and inserted into the RHIC rings, one bunch at a time. The AGS cycle is repeated until 56 bunches are placed in the 360 RF buckets of the RHIC rings. In the case of proton collisions, the EBIS source is not used; instead, hydrogen is ionized and accelerated

in the 200 MeV proton LINAC, achieving an energy of 28.3 GeV after injection in the AGS. The top energy at RHIC is 100 GeV per Au beam, and 255 GeV in the case of proton beams.

The RHIC machine comprises two concentric hexagonal storage rings, 3.8 km in circumference, where particles are accelerated in opposite directions (called the *blue* and *yellow* rings, for clockwise and counterclockwise acceleration, respectively). The rings comprise a variety of superconducting magnets, namely 288 arc-sized dipoles, 108 insertion dipoles, 276 arc quadrupoles, and 216 insertion quadrupoles. Dipole magnets are used to *bend* the beam, while quadrupoles are used to *focus* it. The nominal magnetic rigidity for Au beams is $B\rho = 8401$ Tm, maintained by a magnetic field of approximately 3.5 T at top energy. The rings intersect at six points along their circumference, four of which house detector experiments with complementary physics programs, as cursorily listed below.

(1) PHENIX (Pioneering High-Energy Nuclear Interaction Experiment) [90] comprises a central axial field magnet, with a central spectrometer of limited acceptance consisting of various layers of tracking, electromagnetic calorimetry and particle identification. Two muon spectrometers, for muon identification, are located parallel to the beam direction and consist of muon magnets, muon filters, and tracking detectors. PHENIX was operational from 2000-2016. It has since been decommissioned to make way for the future sPHENIX detector [28] in the same experimental hall.

(2) STAR [91] (Solenoidal Tracker at RHIC) is built around a large solenoidal time-projection chamber (TPC), allowing for charged particle tracking within $|\eta| < 1$ and 2π azimuthal coverage, with particle identification (PID) capabilities. Electromagnetic calorimeters in the barrel and endcap allow measurements of electron and photon energy. STAR has been in operation since RHIC startup in 2000, and is expected to remain operational at least through 2019-2020, when the Au+Au Beam Energy Scan II program (BES-II) will take place, to search for the critical point of deconfinement.

(3) PHOBOS [88] (Not an acronym, but named after the largest moon of Mars), one of the two

smaller RHIC experiments, comprises a two-arm magnetic spectrometer and a large number of silicon detectors at various distances around the interaction region. The experiment operated from 2000-2006.

(4) BRAHMS [93] (Broad Range Hadron Magnetic Spectrometers Experiment), the other small RHIC experiment, comprises two magnetic spectrometers. One arm is oriented at forward rapidity, and the other at mid-rapidity, covering a limited acceptance. BRAHMS, like PHOBOS, operated from 2000-2006.

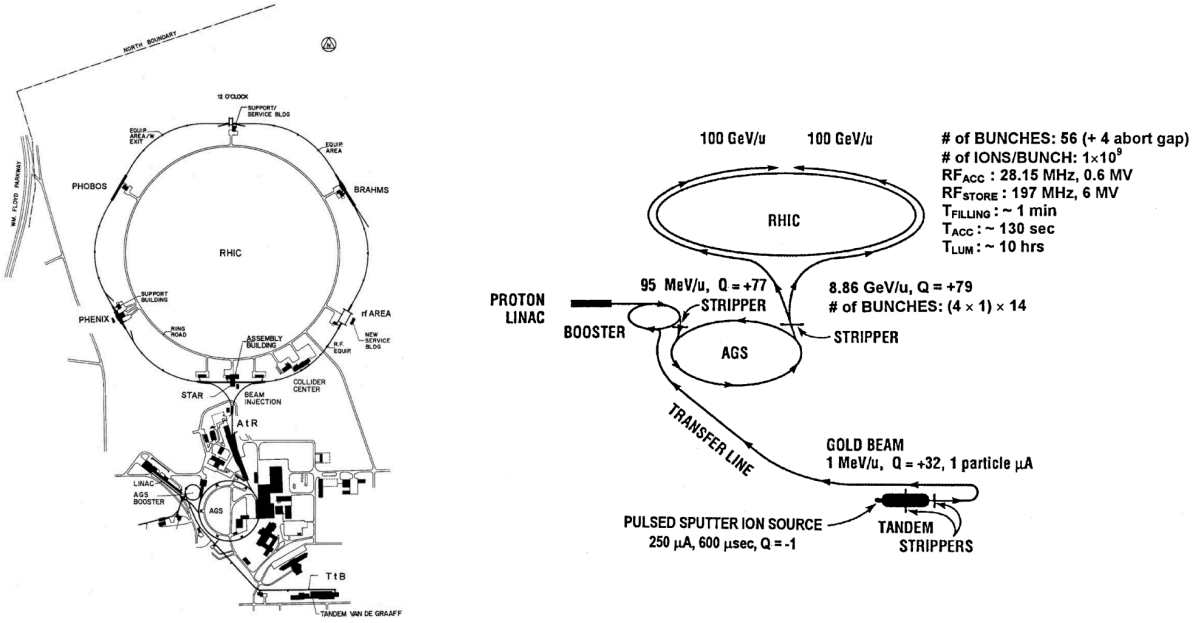

Figure 6.2: (left) Layout of the RHIC-AGS accelerator complex, to scale. (right) Schematic depiction of the RHIC injection chain. Figures reproduced from [115].

6.2 The Pioneering High-Energy Nuclear Interaction Experiment—PHENIX

6.2.1 Detector Overview

The PHENIX experiment [90], as one of two large detectors at RHIC, was designed to support a very broad physics program. With a high rate capability, PHENIX can measure leptons, identified hadrons, and photons over a wide p_T range with excellent momentum and energy resolution. The experiment comprises a number of subsystems organized into four spectrometer arms, and a series of global event characterization detectors, as shown in Fig. 6.3. Since its inception, upgrades and subsystems have been added to and removed from PHENIX over the years. The present discussion focuses on the subsystem configuration for the 2015 run period, when the data for this dissertation was recorded. Global detectors include (*i*) the Beam-Beam Counters (BBC), located symmetrically at forward rapidity around the interaction point, providing timing information which can be used, among other things, for vertex determination and triggering; (*ii*) Zero-Degree Calorimeters (ZDC), located at very backward and forward rapidity, used to detect spectator neutrons; (*iii*) the Silicon Vertex Detector (VTX), comprising various layers of silicon pixels and strips, used for precision tracking and vertexing close to the interaction point; and (*iv*) the Forward Silicon Vertex Tracker (FVTX), comprising two annular endcaps of silicon strips for tracking at forward rapidites.

Two central arm spectrometers, located at midrapidity, surround a central magnet that creates a field predominantly parallel to be beam axis. The spectrometers comprise a layer of electromagnetic calorimetry (lead-glass and lead-scintillator), tracking (with pad chambers, drift chambers, and a time expansion chamber), and particle identification (with time-of-flight detectors and a ring imaging Cherenkov detector). Finally, the muon spectrometer arms, providing full azimuthal coverage at forward and backward rapidity, comprise a muon tracker made up of layers of multi-plane drift chambers in a radial magnetic field, and a muon identifier consisting of alternating layers of steel absorbers and low-resolution tracking. In addition to the above, a series of specialized subsystems, known as the Muon Piston Calorimeter (MPC), and the Muon Piston Calorimeter Extension (MPC-EX) [72] were in place during the 2015 run period, to explore

previously inaccessible kinematic regions for the study of low-x physics.

Table 6.1 provides a summary of selected PHENIX subsystems. In the following subsections, we will provide a detailed description of the subsystems used in this dissertation, namely the BBC for global event characterization, the central arm spectrometers for tracking and electron identification, and the VTX for precision tracking.

Table 6.1: Summary of selected PHENIX subsytems for global event characterization and spectrometry. Table adapted from [90].

Subsystem	η Acceptance	ϕ Acceptance	Function
Global Detectors			
Beam-Beam Counter (BBC)	$3.1 < \|\eta\| < 3.9$	360	Event timing, vertexing
Zero-Degree Calo (ZCD)	$\pm$ 2 mrad	360	Triggering/centrality
Silicon Tracker (VTX)	$\|\eta\| < 1.2$	140×2	Precision tracking
Forward Silicon (FVTX)	$1.2 < \|\eta\| < 2.2$	360	Forward tracking
Central Arm Spectrometers			
Drift Chambers (DC)	$\|\eta\| < 0.35$	$90^\circ \times 2$	Tracking
Pad Chambers (PC)	$\|\eta\| < 0.35$	$90^\circ \times 2$	Tracking
Cherenkov Detector (RICH)	$\|\eta\| < 0.35$	$90^\circ \times 2$	Electron ID
PbGl EMCal	$\|\eta\| < 0.35$	45°	EM Calorimetry
PbSc EMCal	$\|\eta\| < 0.35$	$90^\circ + 45^\circ$	EM Calorimetry
Time of Flight (TOF)	$\|\eta\| < 0.35$	45°	Hadron ID
Muon Arm Spectrometers			
Muon Tracker South(North)	$1.15 < \|\eta\| < 2.25(2.44)$	360°	Muon tracking
Muon ID South(North)	$1.15 < \|\eta\| < 2.25(2.44)$	360°	Muon identification

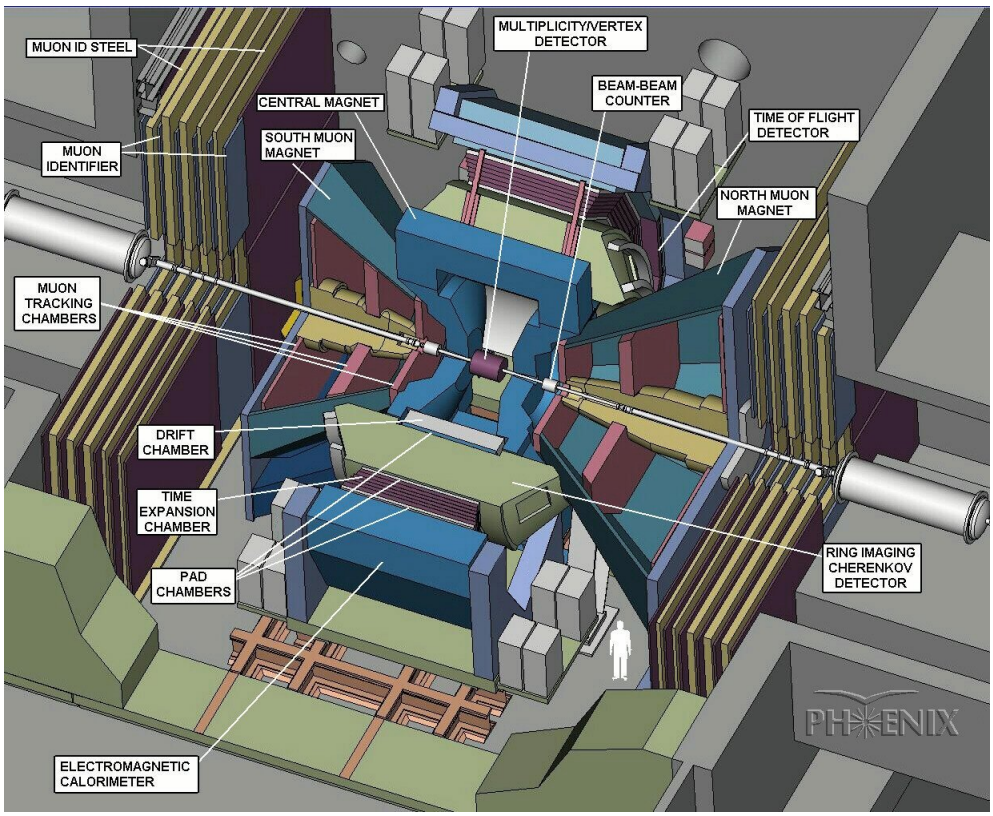

Figure 6.3: Rendering of the PHENIX experiment showing the layout of various detector subsystems, in their 2003 configuration. Recent detector upgrades, including the Silicon Vertex Detector (VTX) and Forward Vertex Detector (FVTX) are not shown. Image credit: PHENIX Collaboration.

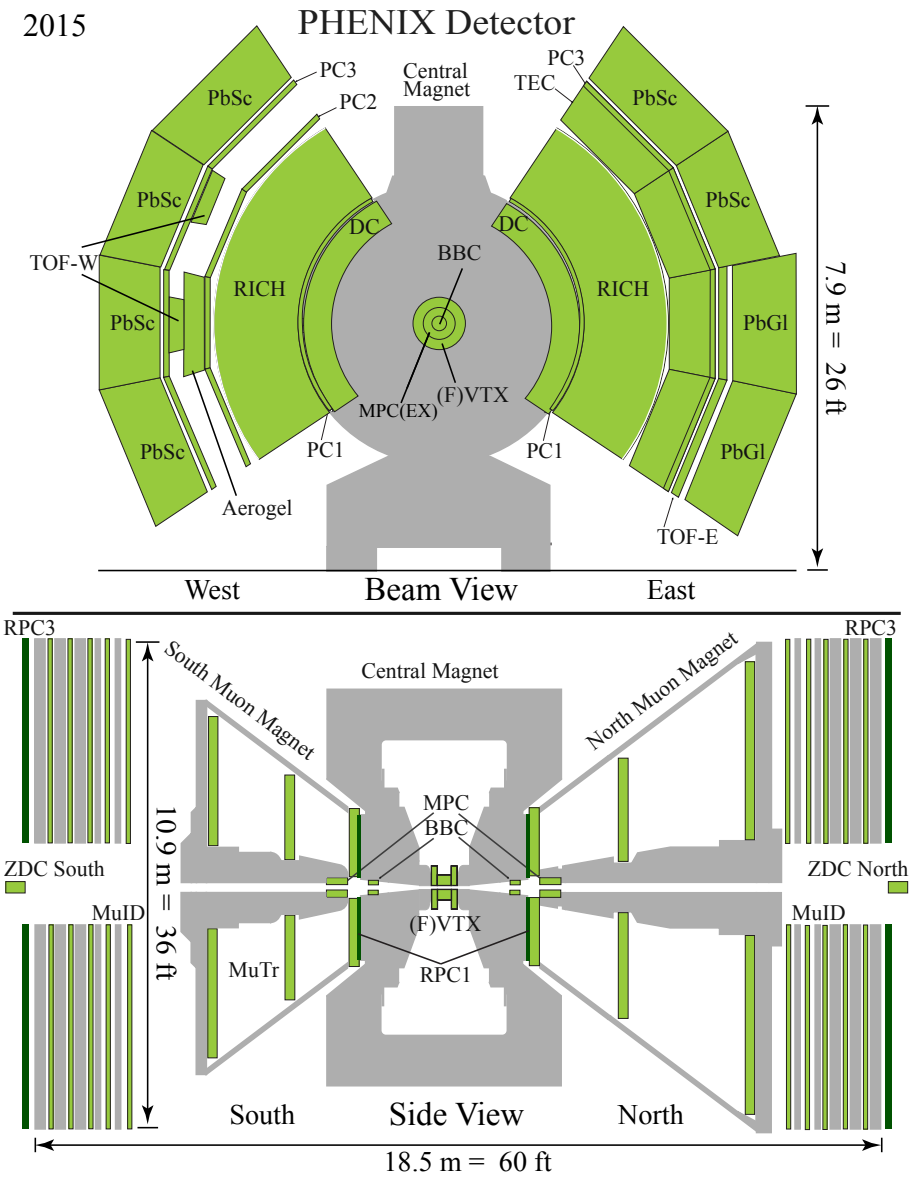

Figure 6.4: (top) Beam-line view of the PHENIX detector in its 2015 configuration, with central magnet and central arm spectrometers visible. (bottom) Side view of PHENIX, with muon spectrometers visible. Image credit: PHENIX Collaboration.

6.2.2 The Central Magnet

The PHENIX magnet system [96] makes use of three magnets: two for the muon arms, and one for the central arm spectrometers. Fig. 6.5 shows a rendering of the central magnet and the

muon magnets in the experimental hall. All three are warm iron yoke magnets with water-cooled copper coils. The muon magnets, which will not be discussed here, produce a radial magnetic field of strength 0.72 T. The central magnet was designed to produce an axial magnetic field at midrapidity, with no mass in the aperture of the central arm spectrometers, yet with substantial mass at forward and backward rapidity to act as a hadron aborber for the muon arms. The magnet is 9 m tall, and weighs 421 metric tons. The field is created by two pairs of circular coils in the pole faces, called the inner and outer coils, of radius 0.66 m and 1.73 m, respectively, as shown in Fig. 6.6. Electric current through the two coils can be made to circulate in the same, or in opposite directions, thus enhancing or reducing the strength of the magnetic field in the region close to the beam pipe. When current runs in the same direction (i.e., the ++ configuration), a maximum magnetic field of 0.9 T is achieved at a radial distance of $r = 0$, whereas when currents run in opposition (i.e., the +− configuration), the magnetic field effectively cancels in that region. Fig. 6.7 shows the total magnetic field strength as a function of r for the ++, +−, and + (i.e., outer coil alone) current configurations. In all cases, the strength of the field is the same at $r \gtrsim 1$ m. In particular, notice that the field strength is close to zero for $r > 2$ m, in order to minimize the smearing of low-momentum electron rings in the Ring Imaging Cherenkov (RICH) subsystem, described in Section 6.2.3.2.

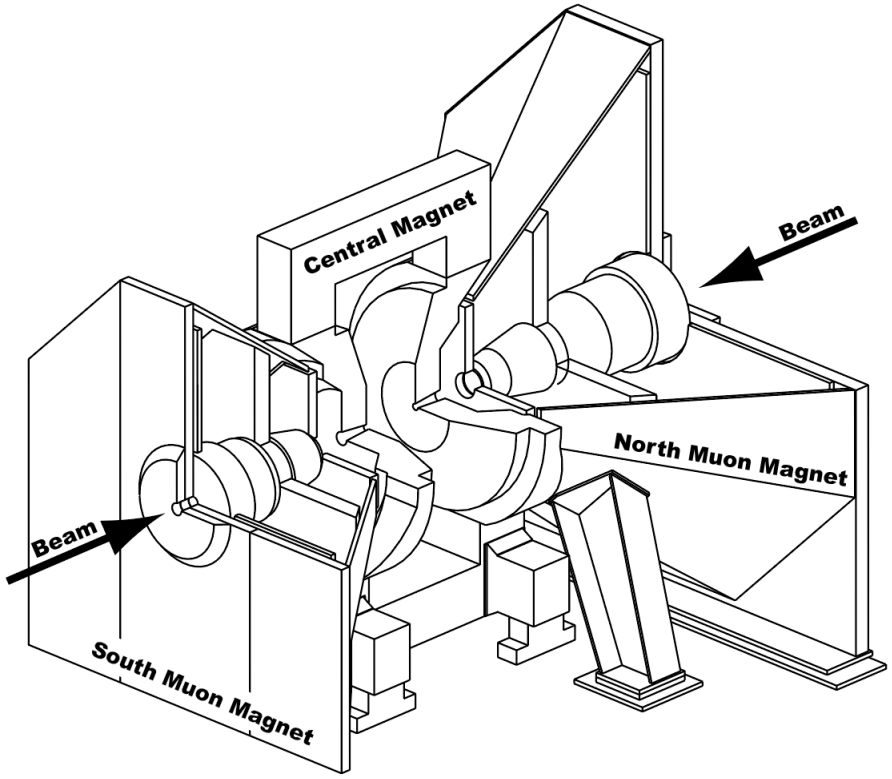

Figure 6.5: Illustration of the PHENIX central magnet and muon arm magnets. Figure reproduced from [96].

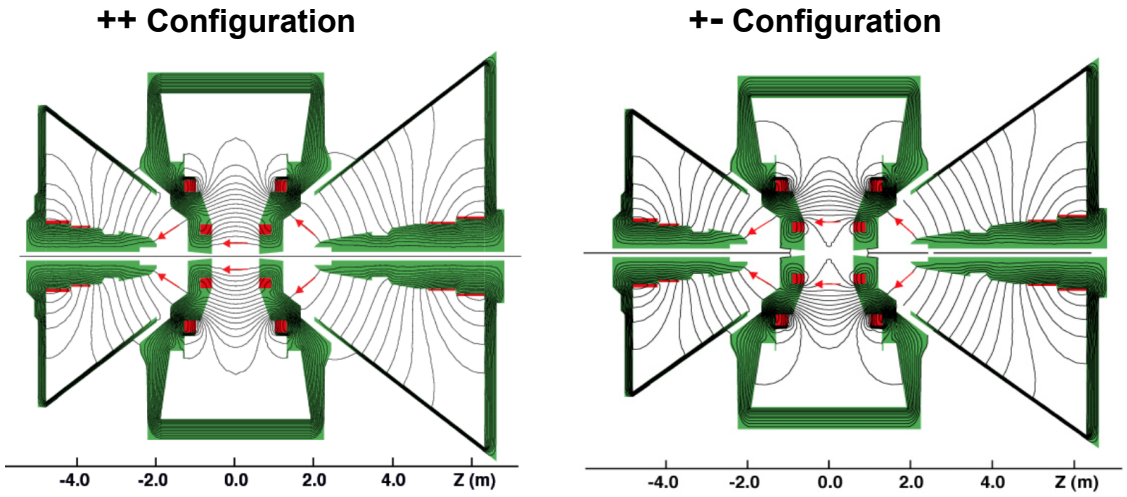

Figure 6.6: Illustration of the PHENIX magnetic field lines when the central magnet runs in the ++ and +− configurations. Figure reproduced from [121].

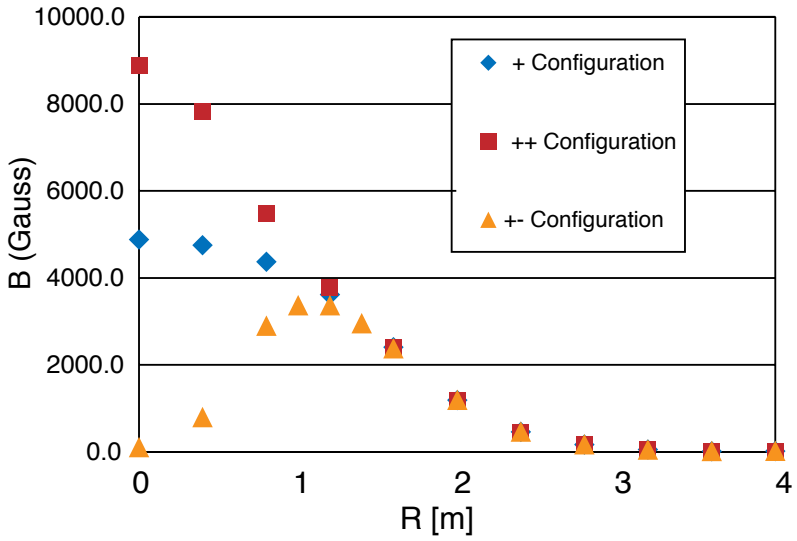

Figure 6.7: Total magnetic field strength as a function of radial distance from the beam pipe when current runs only the outer coil (+ configuration); in the same direction in both coils (+−) configuration; and in different directions (+−) configuration. Figure adapted from [96].

6.2.3 Tracking and Particle Identification: The Central Arm Spectrometers

6.2.3.1 The Drift Chamber

The drift chamber (DC) is the innermost subsystem of the central arm spectrometers [89, 173]. It consists of two independent partial cylindrical volumes, one in each arm, of length 2.5 m along the beam axis, inner radius of 2.02 m, outer radius of 2.46 m, and subtending an azimuthal angle of 90°, as shown in Fig. 6.8. Each volume is filled with a gas mixture of equal parts Ar and C_2H_6 at atmospheric pressure, such that a charged particle traversing the chamber will ionize the gas, leaving a trail of electron-ion pairs. Electrons then drift in an electric field towards a series of sensing wires, such that position information can be inferred from the measured drift times.

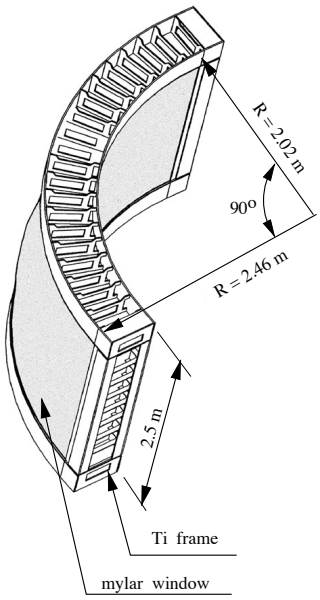

Figure 6.8: Geometry of a single DC arm frame. Figure reproduced from Ref. [89].

Each volume is divided into 20 independent sectors, each covering 4.5° in azimuth. Within each sector are six sets of wires, called X1, U1, V1, X2, U2, and V2. The X wires are arranged parallel to the beam axis, to allow measurements in the $r - \phi$ plane. The U and V wires provide information along the longitudinal z direction since they are arranged at stereo angles of about 6° (specifically, U1, V1, U2 and V2 are oriented at 5.376°, 5.512°, 5.900°, and 6.040°, respectively) relative to the X wires. Fig. 6.9 shows the detailed layout of wires in a given DC sector. In particular, the figure inset illustrates how anode (i.e., sensing) wires—shown as dashed open circles—within a given plane are separated by "potential" wires, and surrounded by "gate" and "back" wires. The potential wires create the electric field, while gate wires limit the drift length, and the back wires terminate drift lines thus limiting the region where charges can propagate. Anode wires are divided into two electrically isolated halves, each being read out independently. Thus, the approximately 6500 anode wires in the DC correspond to 13000 readout channels.

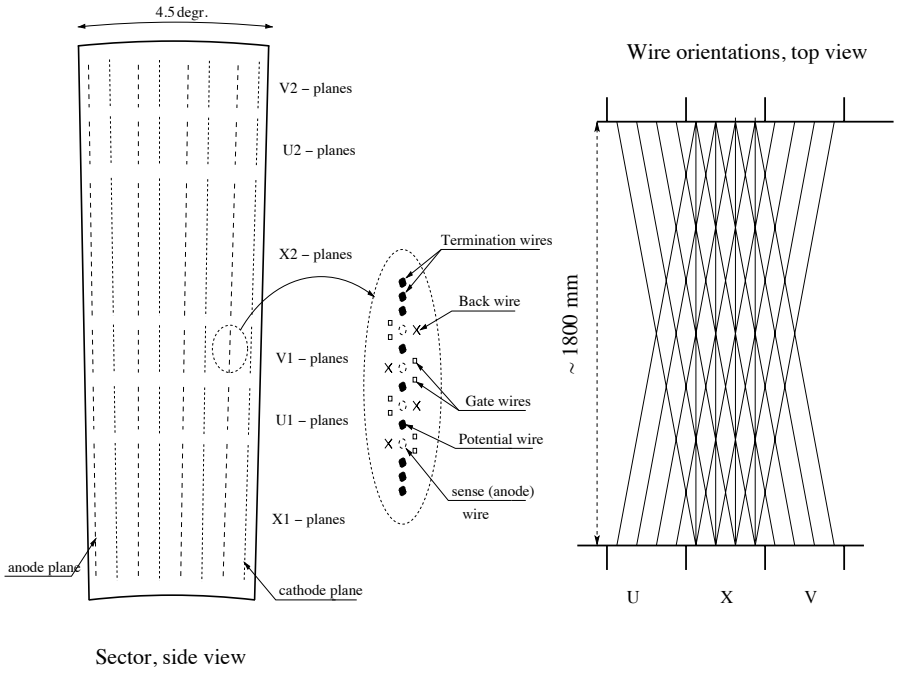

Figure 6.9: Wire configuration in a single DC sector. Figure reproduced from Ref. [89].

6.2.3.2 The Ring Imaging Cherenkov Detector

The Ring Imaging Cherenkov Detector (RICH) [94] is the main subsystem in PHENIX responsible for electron identification. The RICH comprises two CO_2-filled volumes, one in each central spectrometer arm, located radially within $1.5 < r < 4.1$ m, between the inner (i.e., the DC and PC1) and outer (i.e., PC2 and PC3) tracking subsystems. The physical mechanism underlying the detector's operation is straightforward. When a particle propagates in a dielectric medium of index of refraction n, with a velocity greater than c/n, it will emit Cherenkov radiation in a distinct conical shape of opening angle $\cos\theta = 1/(n\beta)$. Given the low mass of electrons, they radiate at a much lower momentum than, for example, pions. In fact, for a particle of rest mass m, the momentum threshold for producing Cherenkov radiation can be written as $p_{\rm min} = mc/\sqrt{n^2-1}$. Thus, $p^{(e)}_{\rm min} = 0.017$ GeV/c for electrons, and $p^{(\pi)}_{\rm min} = 4.65$ GeV/c for pions in CO_2. This large difference in the momentum threshold provides excellent discimination between electron tracks and hadron background up to $p \approx 5$ GeV/c. For higher momentum tracks, other subsystems can be used to

separate electrons from hadrons. Given the location of the RHIC, in between tracking detectors and in front of electromagnetic calorimeters, it is desirable to minimize its material budget. Overall, the gas-filled detector has a thickness equivalent to 2% of a radiation length.

Each RICH arm covers a volume of 40 m^3, whose internal structure is depicted in Fig. 6.10. Each arm is equipped with 48 mirror panels to reflect Cherenkov light, arranged in two intersecting spherical surfaces with an area of 20 m^2 overall. Reflected light is focused onto 1280 photomultiplier tubes (PMTs), organized into two arrays, one on either side of the detector's entrance window. The angular segmentation of this arrangement is 1×1 degrees in polar and azimuthal angles. Since Cherenkov light is emitted in a cone, its reflection will give rise to distinct annular arrays of triggered PMTs for each particle track. If the projection of a given track reconstructed by the central arm tracking subsystems lies within the center of the cluster of PMTs, the PMTs are said to be associated with that track. As will be described in a later chapter, the number of hit PMTs associated with a given track will provide an important criterion for electron/hadron discrimination.

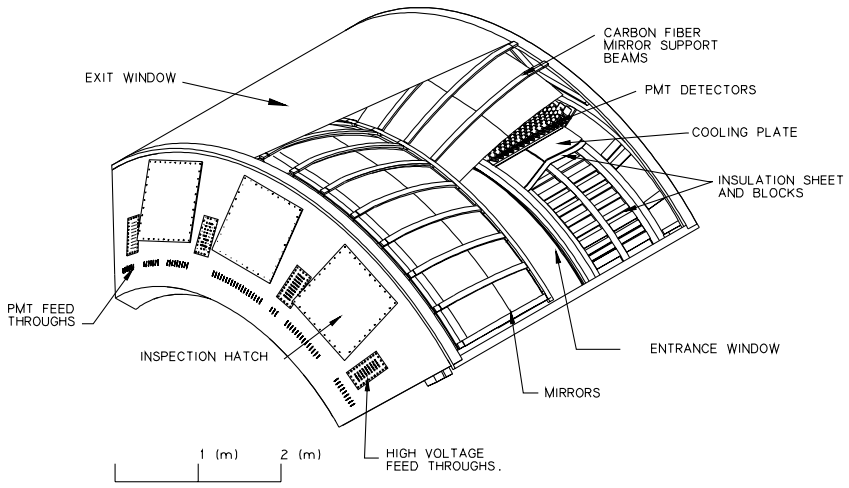

Figure 6.10: View of a single RICH arm. Figure reproduced from [94].

6.2.3.3 The Pad Chamber System

The Pad Chamber (PC) system [89, 173] consists of several layers of multiwire proportional chambers, with three layers (PC1, PC2, PC3) in the West arm spectrometer, and only two (PC1, PC3) in the East arm, as shown in Fig 6.4. The PC1 is located just outside the drift chamber, at a radius of 2.49 m, while PC2 and PC3 are found between the RICH and the EMCal at a radius of 4.19 m and 4.89 m, respectively. The PCs play several important roles, both in tracking and false track rejection. For example, it is PC1 that measures the z coordinate of tracks as they exit the drift chamber; additionally, hits in the PC can be correlated with information from the drift chamber, RICH, and EMCal to reject contamination in the outer detectors arising from conversions and particle decays.

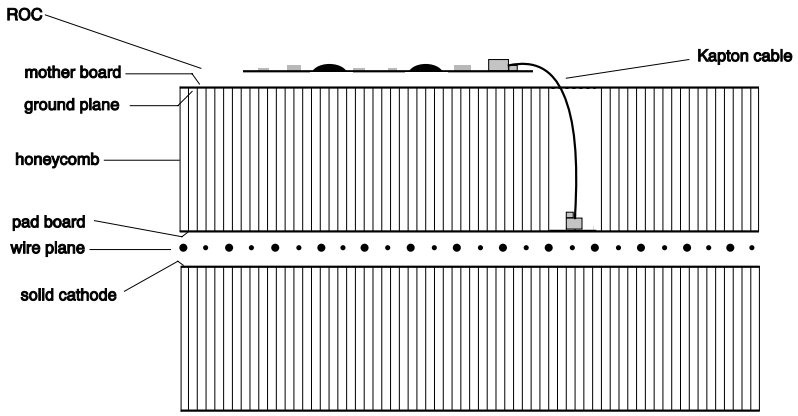

Figure 6.11: Cross-sectional view of a Pad Chamber layer. Figure reproduced from [89, 173].

Each PC layer is made up of a number of independent chambers, each composed of a plane of anode and field wires, strung between cathode planes, as shown in Fig. 6.11. One of the cathode planes is segmented into pixels, while the other is an unsegmented sheet of copper. Cathode pixels are grouped into 9×9 pixel arrays with a common readout. Unlike the drift chamber, which determines track position from drift time measurements, the PCs determine 2D track positions by sensing electron avalanches in the vicinity of a given anode wire and a 3×3 pixel cell. The PC1

is divided into 8 azimuthal chambers, or sectors, of dimensions 49.5 cm $\times$ 197.5 cm ($\phi \times z$), each with 58 anode wires. The PC3, in turn, is divided into 4×2 chambers in ϕ and z. Each chamber is filled, like the drift chamber, with a gas mixture of equal parts Ar and C_2H_6. The gas-filled detector has a material budget corresponding to 1.2% of a radiation length.

6.2.3.4 The Electromagnetic Calorimeter

The electromagnetic calorimeter (EMCal) is the outermost detector of the central arm spectrometers [92]. Its main purpose is to measure the energy of electrons and photons, but it also plays a role in particle identification and event triggering. The PHENIX EMCal was constructed using two distinct detector technologies: a sampling calorimeter using lead-scintillator towers (PbSc), and a Cherenkov calorimeter called using lead-glass crystals (PbGl). All four calorimeter sectors in the West Arm are PbSc, while the East arm has two sectors of each type. The use of different calorimeter technologies allows for cross checks on the calorimeter's energy scale.

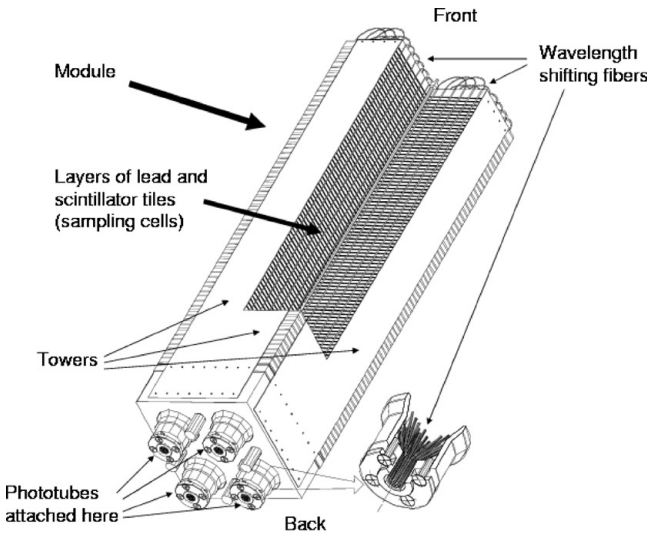

Figure 6.12: Cutaway view of a PbSc calorimeter module, comprising four individual towers. Figure reproduced from [92].

The PbSc calorimeter consists of 15522 towers, each made up of 66 interleaved tiles of lead

and plastic scintillator material, amounting to 18 radiation lengths. The light from each tower is collected by 36 wavelength-shifting fibers running perpendicularly to the tiles, and amplified by a photomultiplier tube. A set of four calorimeter towers—each read out individually—is called a module, as shown in Fig. 6.12. A collection of 36 modules is called a supermodule, and 18 supermodules form a calorimeter sector, covering an area of 2×4 m^2. The energy resolution of the PbSc calorimeter is

$$\frac{\sigma_E}{E} = \frac{8.1\%}{\sqrt{E[\text{GeV}]}} \oplus 2.1\%, \tag{6.1}$$

where the first term accounts for stochastic effects, and the second for intrinsic non-uniformity in the detector [92].

The PHENIX PbGl calorimeter was repurposed from CERN's fixed-target experiment WA98. It is composed of individual modules of lead glass (i.e., a combination of glass and lead oxide), of dimensions $4 \times 4 \times 40$ cm. Each module is individually wrapped in mylar and shrink tube, and read out by a PMT. Twenty-four modules are arranged into 6×4 structures glued with expoxy resin, to form a supermodule. In turn, a PbGl calorimeter sector is composed of 192 supermodules, arranged into a 16×12 structure. The PbSc energy resolution is

$$\frac{\sigma_E}{E} = \frac{5.9\%}{\sqrt{E[\text{GeV}]}} \oplus 0.8\%. \tag{6.2}$$

The PbGl Cherenkov momentum threshold for muons, pions, and protons is $p_{\text{min}}^{(\mu)} = 81$, $p_{\text{min}}^{(\pi)} = 106$, and $p_{\text{min}}^{(p)} = 715$ MeV/c, respectively, thus allowing the PbGl to be used for electron identification based on the mismatch between a given track's momentum and its energy deposition in the calorimeter. Fig. 6.13 shows a PbGl calorimeter supermodule, where the array of individual modules is visible, along with the PMT readouts and supporting structure.

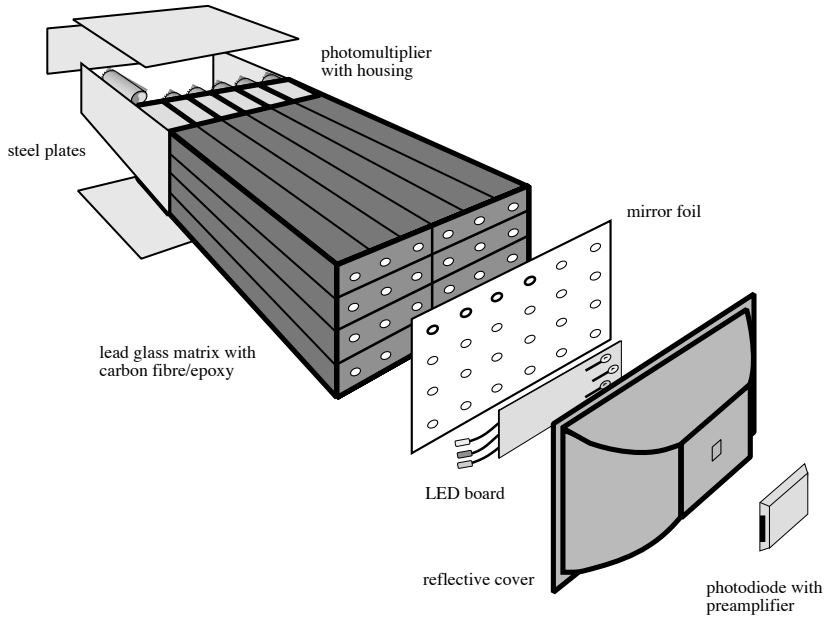

Figure 6.13: Cutaway view of a PbGl calorimeter supermodule. Figure reproduced from [92].

6.2.4 Global Event Characterization: The Beam-Beam Counter

The BBC [95] consists of two identical arms, called BBC-North and BBC-South, located symmetrically along the beam axis, 1.44 m away from the interaction point, and surrounding the beam pipe. Each arm covers $3.1 < |\eta| < 3.9$ in pseudorapidity and 2π in azimuth. Each consists of 64 mesh-dynode photomultiplier tubes (PMT), one inch in diameter, attached to 3 cm quartz crystals which act as Cherenkov radiators. The PMTs are arranged in a ring of inner radius 10 cm, and outer radius 30 cm, as shown in Fig. 6.14(a). A single PMT-radiator element is shown in Fig. 6.14(b). Each BBC arm is powered by 8 high voltage channels. An interlock mechanism disables the high voltage when temperature exceeds 50°C or no airflow is detected. The main functions of the BBC include providing signals for the PHENIX LVL1 trigger, for the determination of the longitudinal collision vertex, and for TOF timing.

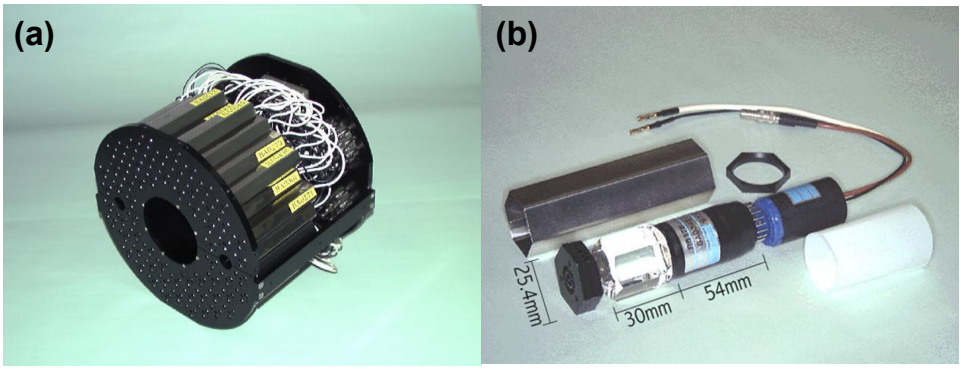

Figure 6.14: (a) Photograph of a single arm of the PHENIX BBC subsystem. (b) Photograph of one of the BBC's constituent quartz Cherenkov radiators and photomultiplier tubes.

6.2.5 Precision Tracking: The Silicon Vertex Detector

The Silicon Vertex Tracker (VTX), installed in 2011, was designed to provide charged particle tracking capabilities near the interaction point, such that the primary vertex can be reconstructed with a resolution of the order of 100 μm. The VTX consists of two arms, each comprising four layers, covering an acceptance of $|\eta| < 1.2$ (for collisions within $|z| < 10$ cm) in pseudorapidity and $140^\circ \times 2$ in azimuth, constructed using two different detector technologies. The two innermost layers, called B0 and B1, were constructed using silicon pixel technology, developed at CERN. The outermost layers, called B1 and B2, were constructed using a silicon strip-pixel hybrid technology, developed at BNL. Each layer consists of a series of ladders running parallel to the beam axis at various radii, as shown in Fig. 6.15. Notice from the figure that ladders are staggered in an overlapping configuration to minimize gaps between the sensitive areas in each sensor. Table 6.2 provides a summary of the hardware specifications of each layer.

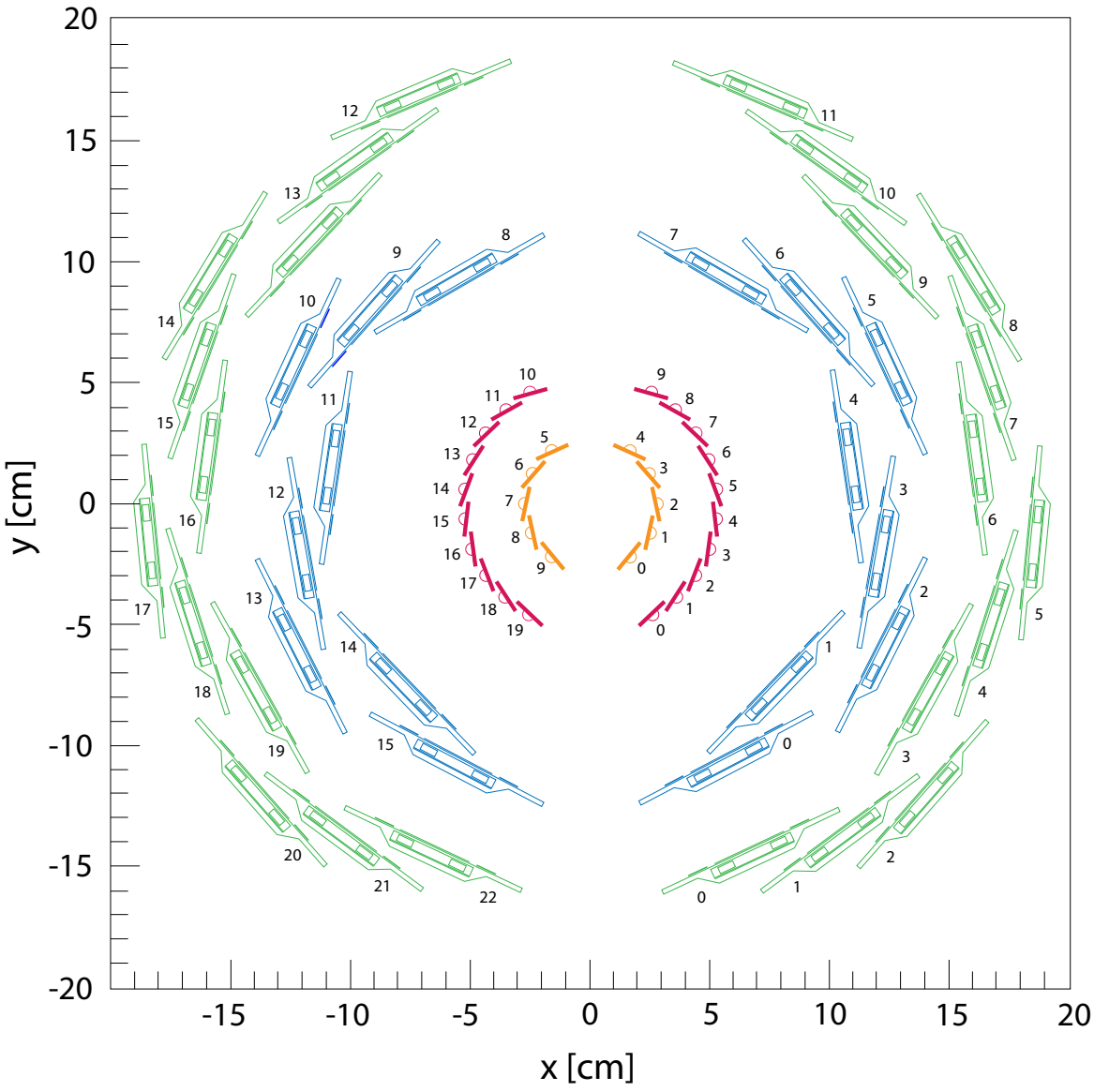

Figure 6.15: Cross sectional view of the VTX detector along the beam axis, showing the radial arrangement and numbering scheme of ladders in each layer. The innermost layers, B0 and B1, consist of silicon pixel ladders, while the outermost layers B2 and B3 consist of stripixel ladders in a staggered configuration.

Table 6.2: VTX hardware specifications for every detector layer

Layer	B0	B1	B2	B3
Type	Pixel	Pixel	Stripixel	Stripixel
Radius [cm]	2.63	5.13	11.77	16.69
Radiation Length	1.28%	1.28%	5.43%	5.43%
Ladders	10	20	16	24
Sensors per Ladder	4	4	5	6
Sensor Size $\phi \times z \times d$ [cm × cm × μm]	1.5 × 5.672 × 200	1.5 × 5.672 × 200	3.49 × 6.37 × 625	3.49 × 6.37 × 625
Active Area $\phi \times z$ [cm × cm]	1.28 × 5.56	1.28 × 5.56	3.072 × 6.0	3.072 × 6.0
Ladder Length [cm]	22.8	22.8	31.8	38.2
Chips per Sensor	4	4	12	12
Channels per Chip	8192	8192	128 ×8 bits	128 ×8 bits
Pixel/Chip or Strip/Sensor	256 × 32	256 × 32	384 × 2(X/U) × 2	384 × 2(X/U) × 2
Pixel/Strip Size [μm×μm]	50 × 425	50 × 425	80 × 30000	80 × 3000

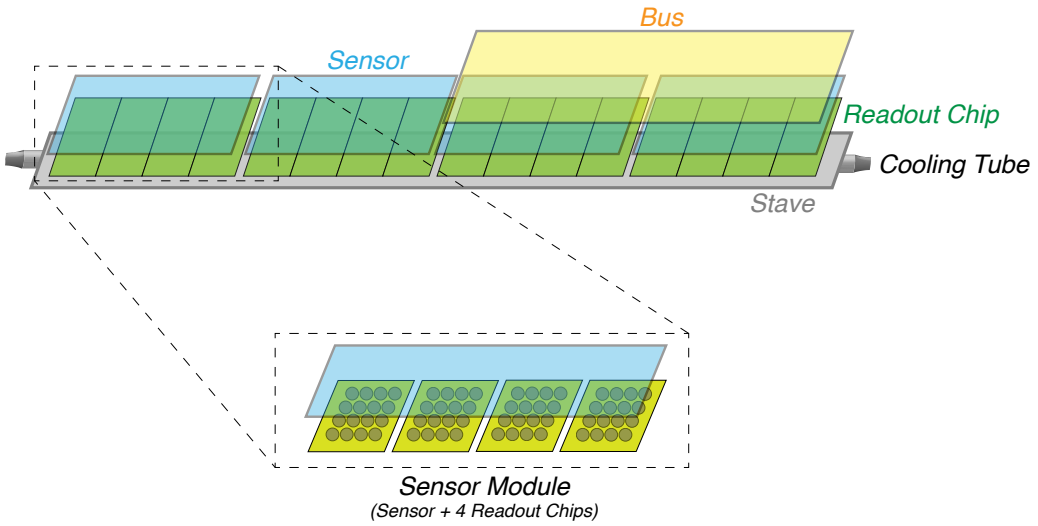

Figure 6.16: Schematic configuration of a hybrid pixel detector ladder, showing the arrangement of the support, sensing, and readout elements.

The two innermost layers B0 and B1, with 10 and 20 ladders, respectively, form the silicon pixel detector. Ladders in these layers are divided into two independent half-ladders, each consisting of two sensor modules. Each module comprises a sensing silicon pixel chip bump-bonded to four readout chips. Each pixel in the chip has dimensions 50 μm $\times$ 425 μm, and consists of n-type silicon with p^+ implants on one side. The pixels are arranged into lattices of 256 $\times$ 32 pixels, 200 μm in thickness. The readout chip, known as the ALICE1LHCb chip [185] (originally designed for the ALICE and LHCb experiments at the LHC), consists of an array of pixels which mirror those in the sensor chip both in size and layout. The readout chip provides a binary signal for every pixel, corresponding to the passage of charged particles. A pair of sensor modules is wire-bonded to a single readout bus. The bus readout is controlled by a Silicon Pixel Readout (SPIRO) module which transmits data to a front-end module (FEM), which in turn interfaces with the PHENIX data acquisition (DAQ) system. The entire arrangement is mounted on a carbon composite support stave which provides cooling and mechanical support, as shown in Fig. 6.16.

The silicon strip detector, comprising the outermost layers, consists of 18 and 26 ladders in B2 and B3, respectively. Ladders in B2 comprise 5 stripixel sensor modules, while those in B3 comprise 6 modules. Individual sensors, of size 3.43$\times$6.46 cm, consist of single-sided pnn-type silicon 625 μm in width, segmented into stripixels of dimensions 80μm $\times$ 1000μm. Individual stripixels consist of of two serpentine metal strips which collect charge liberated in the silicon from the passage of charged particles, as depicted in red and blue in Fig. 6.17, where two stripixels are shown. The blue strip in a given stripixel is electrically connected with blue strips in adjacent stripixels, whereas the red strip is connected with other red strips in stripixels located diagonally, at an angle of 4.6°. Such an arrangement defines two readout directions, called X and U, respectively, which allow for the two-dimensional location of hits to be determined. Each sensor module has 1536 channels, with 768 in each readout direction. The stripixel sensor modules are read out by the SVX4 readout chip, developed by a collaboration between FermiLab and Lawrence Berkeley Lab [131]. Each radiation-hard chip provides readout capabilities for 128 stripixels with 8-bit ADCs, 46-deep pipeline buffering, and 4-deep multi-event buffering. Readout control is carried out by a readout

card (ROC), comprising 12 SVX4 chips, a custom readout control chip (RCC) designed at Oak Rigde National Lab, as well as control buses, power, and ground. The mechanical assembly of a stripixel ladder is shown in Fig. 6.18 Further information on the design, performance and testing of the various components of the VTX detector and electronics can be found in Refs. [131, 42, 143, 43].

The final mechanical assembly of the VTX in the experimental hall is shown in Fig. 6.19. The ladders are mounted on a space frame which provides mechanical support, inside an air-tight gas enclosure filled with dry nitrogen to prevent condensation. Two circular structures, called 'big wheels' house the detector's readout electronics.

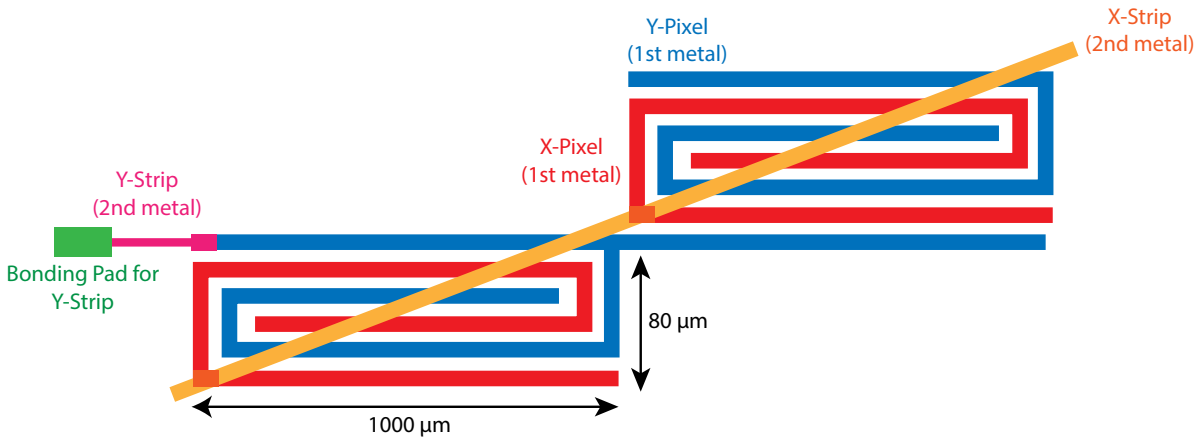

Figure 6.17: Schematic configuration of two individual diagonal stripixels. Blue strips are connected to blue strips in adjacent stripixels, defining the X readout direction, while red strips are connected to red strips in stripixels located diagonally, defining the U readout direction.

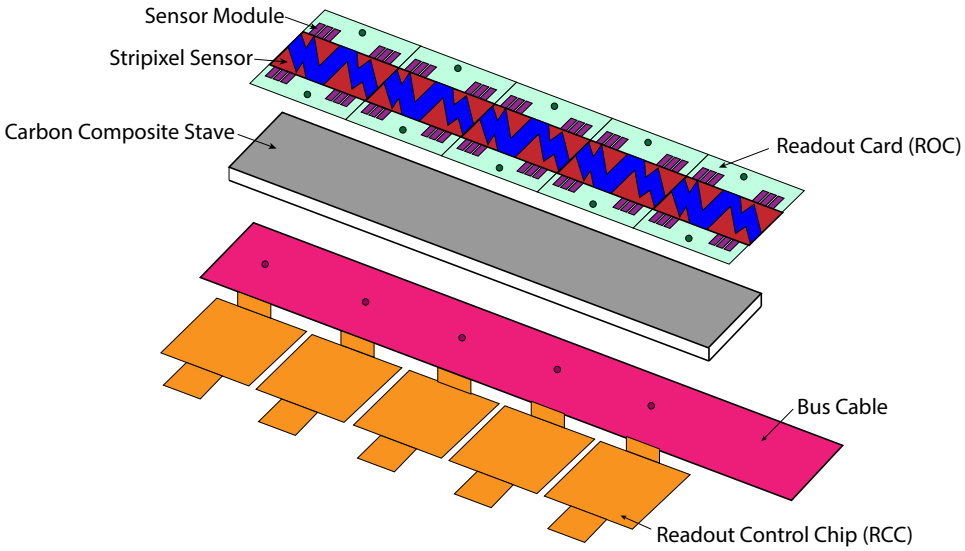

Figure 6.18: Schematic view of a strpixel ladder.

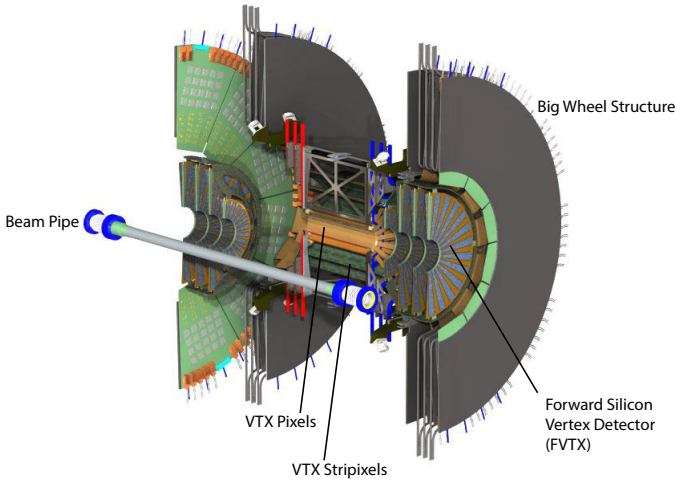

Figure 6.19: Assembly view of the VTX detector in its supporting frame, where the beam pipe has been displaced for clarity. Also shown is the unrelated Forward Silicon Vertex (FVTX) detector.

Chapter 7

Open Heavy Flavor Separation in $p+p$ Collisions

7.1 Analysis Overview and Roadmap

The ultimate goal of the analysis presented here, as motivated in Chapter 1 and Chapter 5, is to differentially measure the production of hadrons with open charm and bottom quark content in $p+p$ collisions at a center-of-mass energy of $\sqrt{s_{NN}} = 200$ GeV. These hadrons decay through the action of the weak force, and their decay modes can be well approximated by the decays of their heavy valence quark, with the lighter quark in the hadron being considered a spectator [179]. For instance, in the case of B mesons, the bottom quark decays as $b \to c + W^{*-}$ and, in turn, the virtual W can decay hadronically or through a process involving leptons in the final state, $W^- \to l\bar{\nu}$. The latter case corresponds to the *semileptonic* decay mode of the heavy flavor meson.

This analysis seeks to measure heavy flavor hadrons by reconstructing their semileptonic decay electron tracks in the PHENIX VTX and central arm subsystems. The provenance, either from a B or a D meson, of electrons can be determined based on the distance between the primary collision vertex and the track's displaced vertex; that is, the point where the parent hadron decay took place. On average, the decay kinematics of the B states are such that the mesons will travel a longer distance than D mesons before decaying, as shown in Table 7.1. This can be quantified through the *distance of closest approach* (DCA) of a given track projection to the point relative to which all tracks are reconstructed. Thus, B mesons will exhibit a broader DCA distribution than D mesons.

Table 7.1: Characteristic distance traveled before decaying by B and D mesons states

State	Flight Distance $c\tau_0$
D^0	129.9 μm
D^+	311.8 μm
B^0	457.2 μm
B^+	491.1 μm

However, measuring the DCA distribution alone of inclusive heavy flavor electrons is not sufficient to determine their origin, and an additional independent experimental observable is needed. In this analysis, such additional observable corresponds to the inclusive spectrum of heavy flavor electrons. Thus, with two independent quantities, one can construct a statistical model to infer D and B production separately. Conceptually, this procedure is akin to solving a system of independent simultaneous equations.

Fig. 7.1 provides a schematic roadmap of the various stages of this analysis. The leftmost column corresponds to the processing of experimental data: first, the raw data is examined and pruned to ensure a high-quality dataset. Then, electron tracks—consisting of heavy flavor electrons plus background electrons—are identified in data, and their DCA distribution is measured. The second column then corresponds to the use of simulations to model the electron background in data, and to determine the DCA distribution of every source of background electrons. That way, the DCA distribution of inclusive heavy flavor electrons in data can be isolated. The third column corresponds to the inclusive heavy flavor electron spectrum, which is taken from existing PHENIX publications. The results of all three columns then come together as input to a deconvolution procedure, known here as *unfolding*, which uses Bayes' Theorem and a PYTHIA-based model of heavy flavor decay, resulting in the separated yields of charm and bottom hadrons.

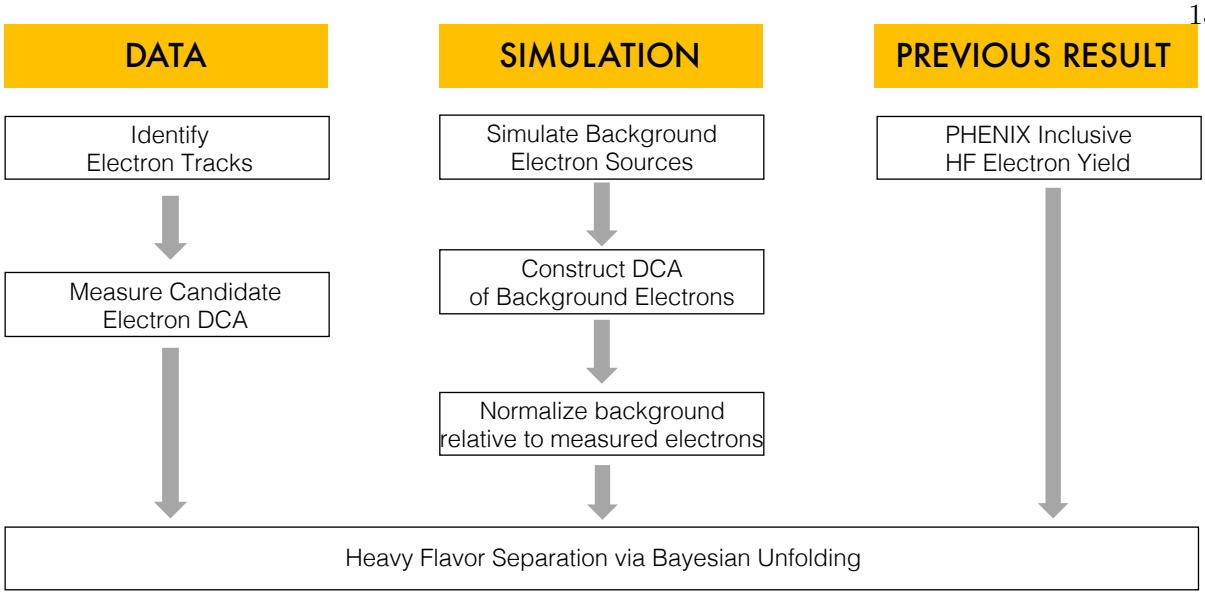

Figure 7.1: Analysis roadmap for heavy flavor separation. Electron tracks are measured in data, and their DCA distribution is constructed. Separately, simulations are used to construct the DCA distribution of background electron sources. Finally, a Bayesian deconvolution method, called *unfolding*, takes these DCA distributions as well as a previosuly published measurement of the inclusive heavy flavor electron spectrum as input, to calculate the individual yield of electrons from charm and bottom mesons.

7.2 Definition of Track Objects and Variables

This section defines and describes the relevant software objects used in this analysis, where reconstructed particle tracks are the central object of study. Tracking is carried out in the central arms, as well as in the VTX detector, defining three distinct types of track objects. Central arm tracking, using the drift and pad chambers discussed in Section 6.2.3, is done via a combinatorial Hough transform, as described in Refs. [121, 123]. The result of this reconstruction is called a `PHCentralTrack`, which most notably encapsulates the momentum of the particle, and the information required for its identification as an electron.

Regarding the VTX, the passage of charged particles through the detector results in hits consisting of individual fired pixels (in B0 and B1), or stripixels (in B2 and B3). The software object

associated with such hits is called an `SvxRawHit`. These hits are reconstructed into `SvxCluster` objects by grouping neighboring hit readout pixels, with the location of the cluster being determined as the centroid of the constituent pixels (or strips). Once clusters have been reconstructed, VTX tracking can proceed via two distinct approaches:

- **Standalone Tracking:** In this approach, tracks are reconstructed using VTX hits alone, with no central arm information. The tracking algorithm begins by linearly projecting pairs of hits different VTX layers towards the beam center, allowing for a rough collision vertex to be calculated along the longitudinal direction; if not enough pairs are available, the z-vertex provided by the BBC is used. In a second step, a recursive algorithm links the vertex with hits in the innermost layer, and then with succesive layers by propagating a helical projection outward. Poor quality tracks are then discarded, leaving a sample of good standalone tracks. The corresponding software object is called an `SvxSegment`. These are not only useful for physics analysis in their own right, but also because standalone tracks are used to calculate the seed vertex for the primary event vertex determination. Full details on the algorithms associated with standalone tracking can be found in Ref. [43].

- **VTX-CNT Tracking:** Of greater interest for the analysis described in this dissertation are the track objects reconstructed by matching `PHCentralTracks` to hits in the VTX detector. In this manner, the location of the track near the vertex can be determined with a resolution of around 100 μm, while preserving the information associated with the track provided by the central arm detectors, such as the momentum, calorimeter energy deposit, etc. The software object representing these VTX-associated tracks is called an `SvxCentralTrack`. The algorithm to reconstruct these tracks proceeds by associating a `PHCentralTrack` with hits in the outer VTX layer, and then projecting a helical trajectory inward, with the diameter of the helix determined by the track's momentum. If several reconstructed `SvxCentralTrack` are associated with the same `PHCentralTrack`, the one providing the best fit to the VTX hits is selected, and the rest are discarded. Again, see

Ref. [43] for full details.

In order to carry out VTX-level tracking with the desired resolution level, it is imperative for the reconstruction software to precisely know where each detector element is located. While the VTX detector has a reference engineering design, according to which it was built, the actual installation of the detector in the experimental hall does not perfectly reflect this geometry. Therefore, an alignment procedure has to be carried out to precisely determine the actual geometry of the detector elements relative to each other, and of the detector as a whole relative to the rest of the PHENIX apparatus. This is a large-scale least-squares minimization problem, solved using the Millepede[1] alignment software [64], and is documented in detail in Appendix B.

7.3 Event Triggers

This section provides a brief description of the triggers used in this analysis to collect "interesting" events while rejecting those that are not. The PHENIX experiment counts with a suite of high-level triggers for various physics objectives, of which the minimim bias (MB) and EMCal-RICH (ERT) triggers are of interest for electron analyses.

7.3.1 The Minimum Bias Trigger

The minimum bias trigger in PHENIX is defined as a coincidence between signals from both arms of the BBC subsystem. The trigger requires that at least one photomultiplier tube fire in each arm of the BBC in a given crossing for it to be recorded. Additionally, since timing information from the BBC can be used to compute an event vertex in the longitudinal direction, it is required that the determined vertex be $|z_{\rm vtx}| < 30$ cm. The MB trigger cross section has been determined to be $\sigma = 23 \pm 2.2$ mb through a van der Meer scan in $p+p$ collisions at $\sqrt{s_{NN}} = 200$ GeV, which means that the trigger effectively captures only $54 \pm 6\%$ of the total inelastic cross section of $\sigma = 42$ mb. In this analysis, the MB event sample is used for quality assurance and run selection, as detailed in Section 7.4.

[1] http://www.desy.de/ kleinwrt/MP2/doc/html/index.html

7.3.2 The ERT Trigger

The EMCal-RICH (ERT) trigger family is designed to maximize the sample size of electrons by identifying large localized energy deposits in the EMCal. Additionally, if those calorimeter deposits can be spatially matched to RICH hits, the trigger can be used to select events where electrons are likely to be reconstructed in the central arms. Fig. 7.2 shows the logic behind the ERT trigger: the EMCal and RICH are segmented into tiles, such that photons can be identified by a large EMCal deposit, while electrons—in addition to the EMCal signal—require a matching RICH tile hit.

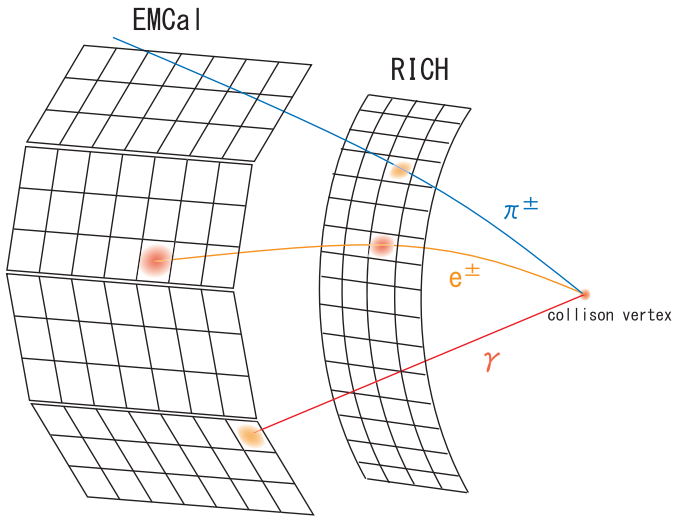

Figure 7.2: Schematic diagram of the EMCal and RHIC subsystems illustrating the electron ERT trigger. Figure reproduced from Ref. [129].

For triggering purposes, the EMCal is segmented into tiles consisting of 144 (12×12) calorimeter towers, while the RICH is segmented into tiles consisting of 20 ($5[\phi]\times4[z]$) photomultiplier tubes, corresponding to units which are read out by common electronics. The first type of ERT trigger considered, namely the `ERT4×4` measures the summed energy in neighboring 4×4 calorimeter towers within a given tile, such that the trigger fires if the energy exceeds a given threshold. Three different thresholds are defined, giving rise to the `ERT4×4a`, `ERT4×4b` and `ERT4×4c` triggers. Addi-

tionally, the ERT-E trigger, for electron identification, measures the summed energy in neighboring 2×2 calorimeter towers, requiring a minimum deposited energy of 400 MeV. A lookup table is then used to spatially match the calorimeter deposit to a hit in a RICH tile. The turn-on curves for the 4 ERT triggers used in the analysis at hand are shown in Fig. 7.3. These correspond to the ratio of the electron spectrum in each ERT trigger sample to that in the minimum bias trigger.

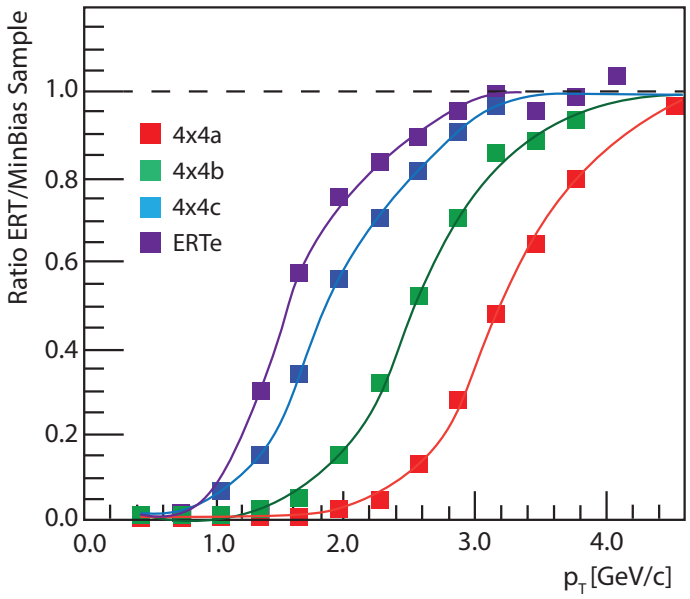

Figure 7.3: Turn-on curves for each ERT trigger used in the analysis.

7.4 Dataset and Run Selection

The RHIC collider typically operates during the first half of a given calendar year. In 2015, during the so-called Run15, it operated from early February to late June, colliding p+p, p+Au, and p+Al at $\sqrt{s_{NN}} = 200$ GeV. The $p+p$ data-taking period ran from February 10 to April 27, during which 110 pb^{-1} of wide-vertex integrated luminosity were sampled by the PHENIX experiment. Fig. 7.4 shows the integrated luminosity as a function of time for various event vertex selections.

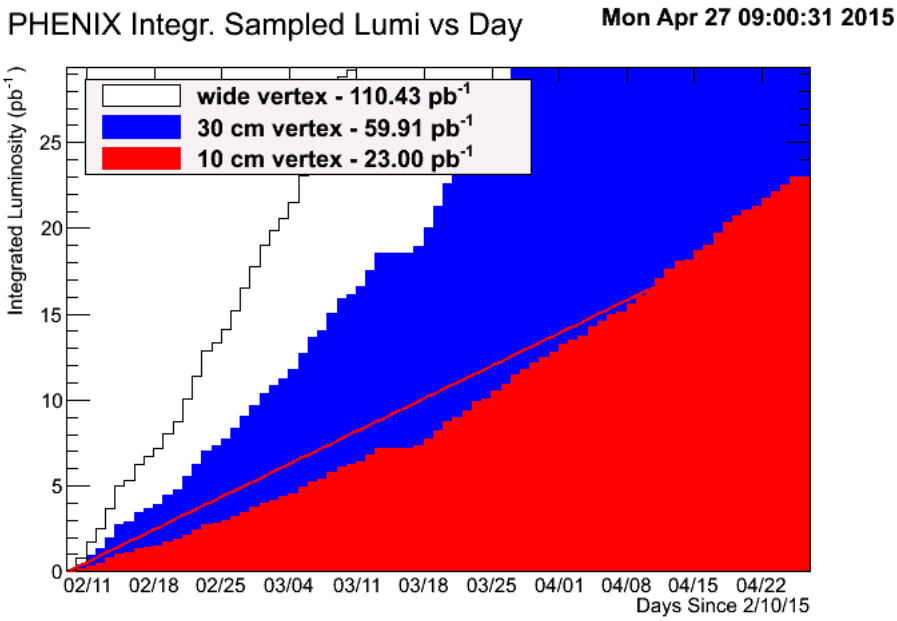

Figure 7.4: Integrated luminosity recorded, within various collison vertex selections, by the PHENIX experiment during the 2015 $p+p$ data-taking period.

During data-taking, the PHENIX experiment collects data in approximately 90-minute intervals known as 'runs'. Overall, 844 $p+p$ runs suitable for physics analysis were recorded. However, it is necessary to closely inspect certain variables of interest for the present analysis on a run-by-run basis to exclude any anomalous runs for which these variable deviate from the mean in a statistically significant manner. In particular, the following variables were examined in minimum bias events, subject to the cuts in Table 7.2.

(a) **Event Level Variables**

- Fraction of events with a primary vertex determined with the VTX detector

(b) **Cluster Variables**

- VTX Clusters per event

(c) **PHCentralTrack Variables**

- Hadron tracks per event
- Electron tracks per event

- Electron-hadron ratio

(d) **SvxCentralTrack Variables**

- Hadron tracks per event
- Electron tracks per event
- Electron-hadron ratio
- Mean of the distribution of the distance of closest approach to beam center (DCA; see Section 7.6) for hadron tracks
- Width of the hadron track DCA distribution

(e) **SvxStandalone Variables**

- Standalone tracks per event

Table 7.2: Cuts defining the variables used for quality assurance and run selection

VARIABLE	CUTS
MinBias Events	• Trigger: `BBCLL1(>0 tubes) narrowvtx` • `pmtbbcs > 0 && pmtbbcn > 0` • |BBC-z vertex| < 10 cm • Tick Cut
Electron PHCentralTrack	• `Quality = 31 or 63` • $p_T > 0.5$ GeV/c • $\chi^2/\text{ndf} < 6$ • `n0 >= 1` • `disp < 5`
Hadron PHCentralTrack	• `Quality = 31 or 63` • $p_T > 0.5$ GeV/c • $\chi^2/\text{ndf} < 6$ • `n0 < 0`
Electron SVXCentralTrack	• `Quality = 31 or 63` • $p_T > 0.5$ GeV/c • $\chi^2/\text{ndf} < 6$ • `n0 >= 1` • `disp < 5` • Require B0, B1 hits
Hadron SVXCentralTrack	• `Quality = 31 or 63` • $p_T > 0.5$ GeV/c • $\chi^2/\text{ndf} < 6$ • `n0 < 0` • Require B0, B1 hits
SvxStandaloneTrack	• $p_T > 0.5$ GeV/c • $\chi^2/\text{ndf} < 6$

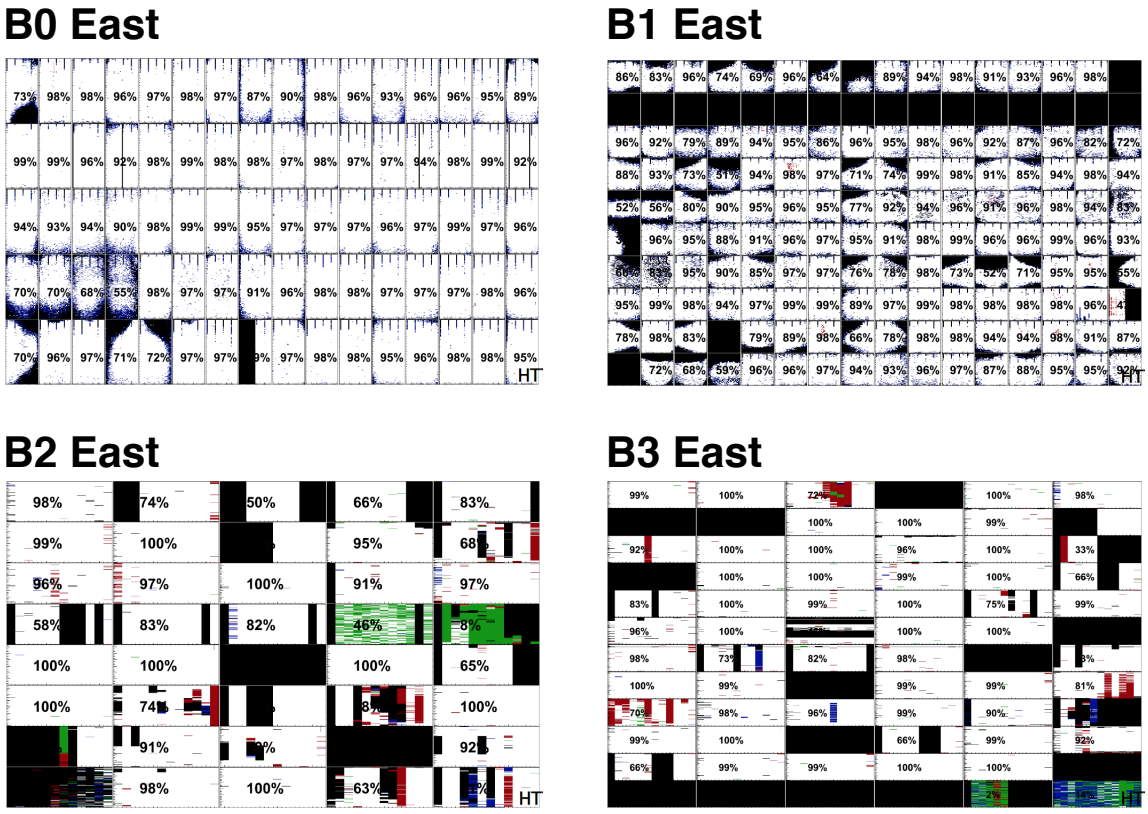

Figure 7.5: Map showing the anomalous pixels(strips) in each layer of the East arm of the VTX detector for a given Run15 $p+p$ run. Red indicates hot pixels; blue, cold; black, dead; and green, unstable. Horizontal rows correspond to individual ladders, with boxes corresponding to chips in the ladder. The number in each chip indicates the fraction normal live area.

It is a known fact that the acceptance of the VTX detector is not uniform, with a number of silicon pixels(strips) in each layer exhibiting anomalous behavior. Fig. 7.5 shows a visual representation, called a "dead map", of the status of individual pixels(strips) during a given $p+p$ run. Rows in the map correspond to detector ladders, which are further divided into individual chips. The color of pixels(strips) in each chip indicates their status. In this manner, white pixels are normal; red are hot; blue, cold; and green, unstable. The number quoted in each chip corresponds to the percentage of normal live area. It is possible to see from the dead map that substantial dead areas exist in the VTX, and that they are not correlated between detector layers. Furthermore,

instabilities in detector performace result in the dead area changing over time, such that the dead map for every other run will differ from the one presented here. A significant consequence of this state of affairs is that it becomes impossible to calculate a correction for acceptance and efficiency of the VTX detector, limiting the ability to measure fully corrected track yields.

Fig. 7.6 shows the number of clusters per event in every VTX layer as a function of run number. Notice that this quantity is not constant over time in any layer, consistent with the time-dependent changes in the VTX acceptance described above. Since the behavior is different in every layer, it is of interest to examine track-level quantities to determine the impact of the changing acceptance on track reconstruction. Along these lines, Fig. 7.7 shows the number of standalone tracks reconstructed per event. The quantity is not constant, with large run-to-run variations arising from the time-changing acceptance. It is of interest then to detect extreme outliers, where severe detector malfunction may have ocurred.

An *ad hoc* procedure was devised for this purpose, dividing the entire run range into four distinct blocks which can be identified by eye, marked by sharp changes in the number of tracks per event. In Fig. 7.7, they are labeled as 'run periods'. Each run period is fit independently with a constant, as shown by the red line. The colored band around the line corresponds to a 3-standard deviation cut on the distribution of residuals—that is, the difference between the number of tracks for a given run and the fit value. Runs for which the number of standalone tracks per event falls outside the limit of the band are marked as potentially unsuitable and set aside for closer examination. Although not shown here, a similar variation in the number of tracks per event was also observed for SvxCentralTracks.

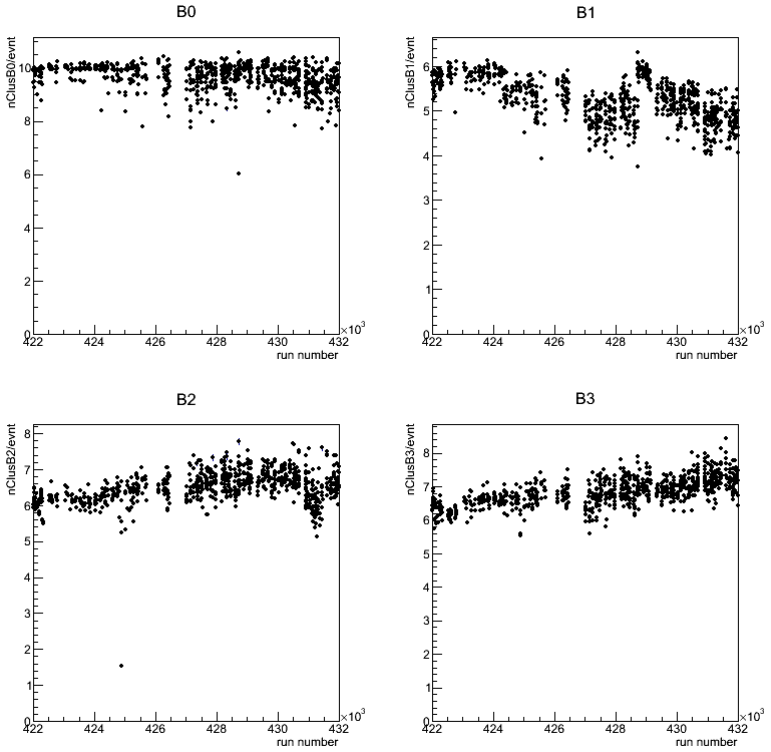

Figure 7.6: Clusters per event in each layer of the VTX as a function of run number.

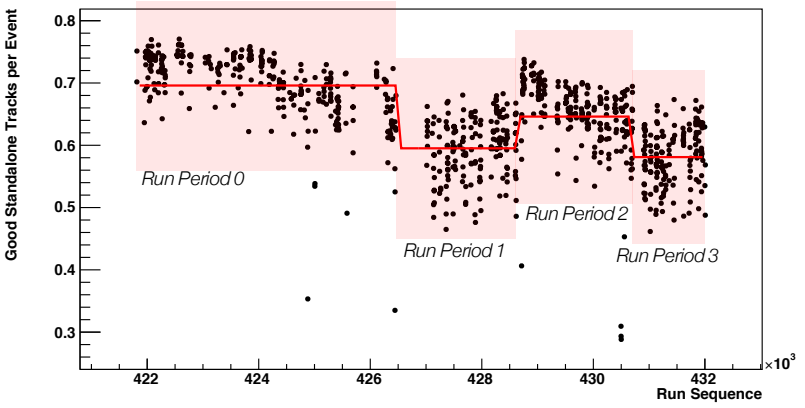

Figure 7.7: Number of good standalone tracks per event as a function of run number.

While the substantial time-dependent variation in the number of reconstructed tracks would present difficulties for measurements of absolutely normalized track yields, the key variables to examine for the analysis at hand are the ratio of electron to hadron tracks, and the shape of

hadron DCA distributions. The electron-hadron ratio is shown in Fig. 7.8 for PHCentralTracks and SVXCentralTracks, appearing to be remarkably flat with run number. This demonstrates that the changes in acceptance, as well as other effects impacting the number of reconstructed tracks, affect both electrons and hadrons equally.

Fig. 7.9 and Fig. 7.10 show the mean and the width of Gaussian fits to the DCA distributions calculated relative to the primary event vertex and the beam center, respectively. In all cases, the distributions appear to be of reasonably constant width and mean. A further check on the uniformity of the DCA distribution *shape* can be obtained by examining the integral in the peak region of the Gaussian fit relative to the tails, as shown in Fig. 7.11, which is again reasonably constant.

The outlier runs, identified from fitting the variables of interest as discussed above, were examined individually, attempting to ascertain the fundamental cause of the anomalous behavior observed. In most cases it was possible to trace the observation to faulty VTX performance. Overall, 73 runs were flagged as unsuitable for analysis, out of a total of 844.

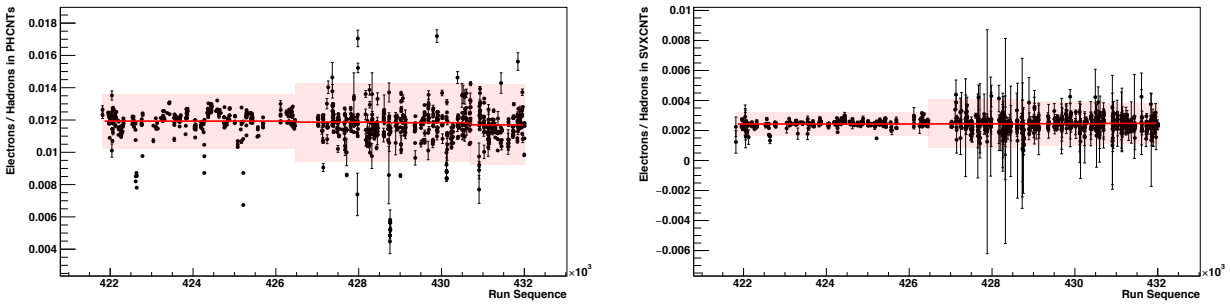

Figure 7.8: Electron-to-hadron ratio in PHCentralTracks (left) and SVXCentralTracks (right) as a function of run number.

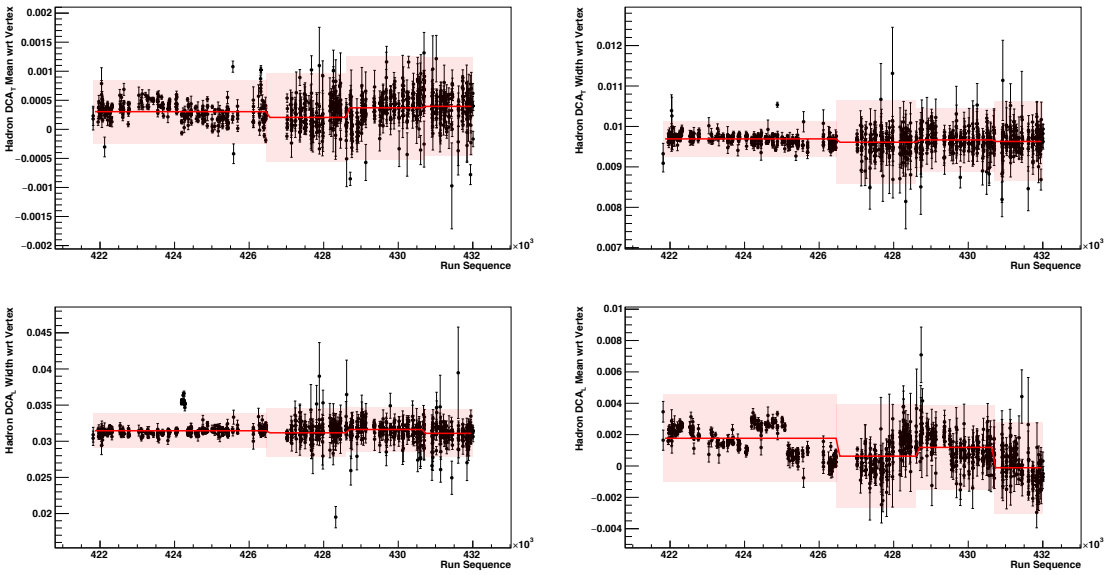

Figure 7.9: Mean and width of the hadron (top) transverse DCA and (bottom) longitudinal DCA distributions, calculated relative to the primary event vertex, as a function of run number.

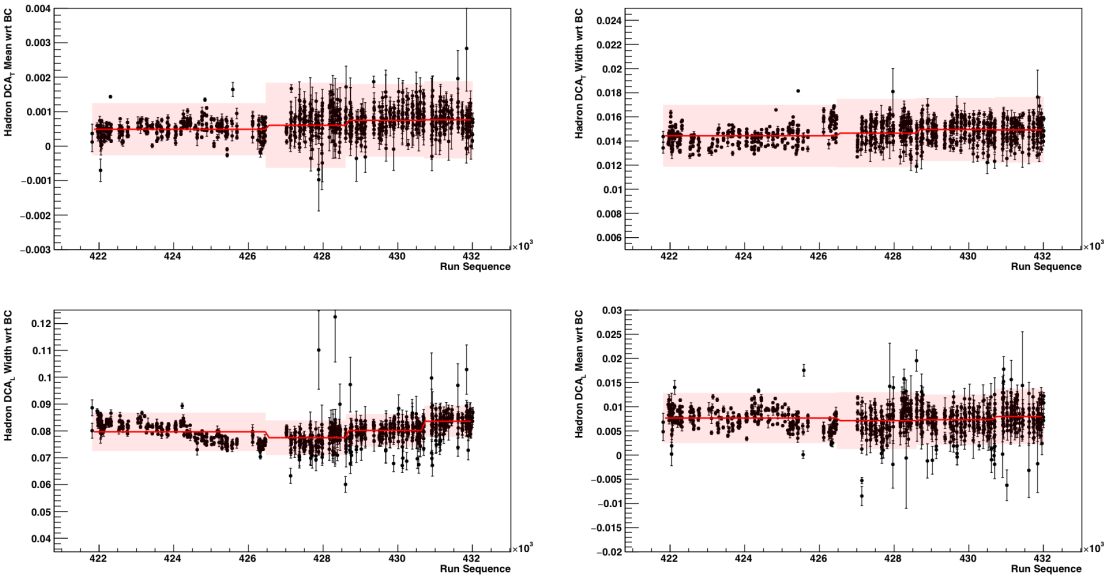

Figure 7.10: Mean and width of hadron (top) longitudinal DCA and (bottom) transverse DCA distributions, calculated relative to the beam center as a function of run number.

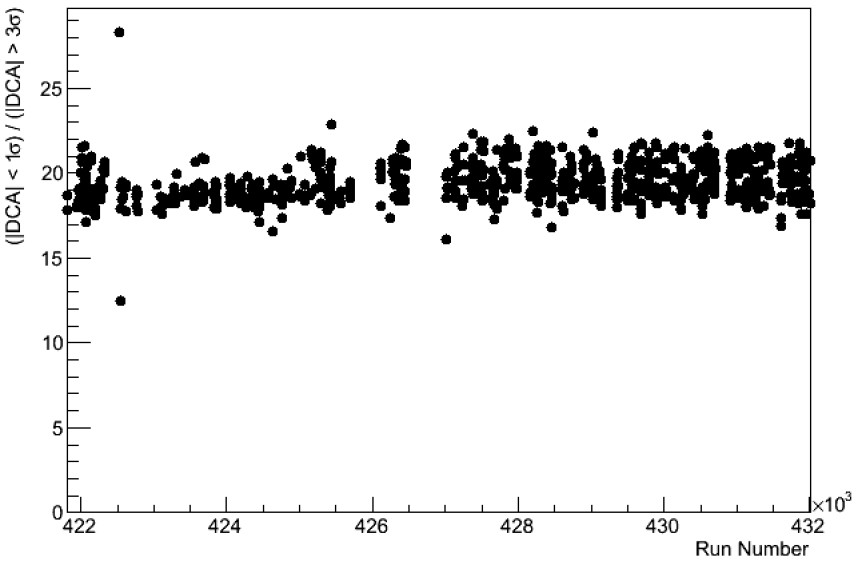

Figure 7.11: Ratio of the integral of a Gaussian fit to the hadron DCA_T distribution in the peak ($|DCA_T| < 1\sigma$) region to the tail ($|DCA_T| > 3\sigma$) region.

7.5 The Conversion Veto Cut

As stated in Section 6.2.5, the pixel and stripixel layers of the VTX have a material budget corresponding to 1.28% and 5.43% of a radiation length, respectively. Consequently, the VTX is a source of considerable conversion electrons $\gamma \to e^+e^-$ from the interaction of photons with the detector material. For comparison, the beam pipe has a material budget of $X_0(\%) = 0.22$. It is desirable to reject as much of this electron background as possible, with several options available. For instance, reconstructed tracks are required to have hits in the two innermost layers of the VTX, thus eliminating electrons originating from conversions in the outer layers. However, it is possible to construct a more general solution to reject conversion in the beam pipe and B0 by exploiting the fact that conversion electron pairs have a very narrow opening angle, as shown in Fig. 7.12. As a function of photon energy, this angle (in radians) is given by $\theta_{\text{opening}} = 8 \times 10^{-4}/E$, with E in GeV [160][2] , which is much smaller than the typical opening angle of hadronic decay products. Thus, if a given VTX track has a hit in its vicinity, within a given window of size $\Delta\phi \times \Delta z$, then

[2] This originates from the calculation, in the Born approximation, of the cross section for high-energy pair production, summed over the polarization of the electrons, and averaged over the the photon polarization.

the track can be rejected as a conversion electron.

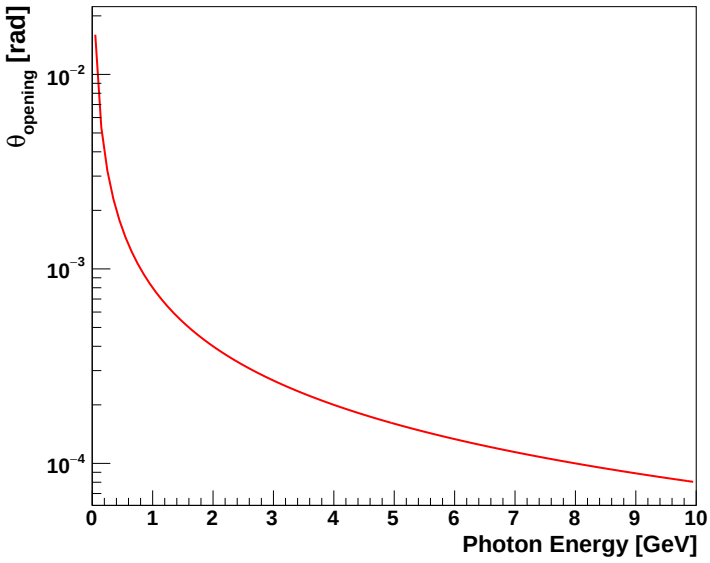

Figure 7.12: Opening angle of an e^+e^- pair from the conversion of a photon of energy E.

This procedure to reject conversions is referred to as the *conversion veto cut*. A track is said to be rejected by the conversion veto cut if a nearby hit is found within the window in *any* layer of the VTX. The window sizes are different in every layer, as shown in Table 7.3. In azimuth, the window is defined with the quantity labeled $c\Delta\phi$, corresponding to the azimuthal separation between the track and cluster $\Delta\phi$, multiplied by the charge c of the track. Notice that the window size depends on the sign of $c\Delta\phi$, being p_T-dependent for $c\Delta\phi > 0$. The p_T dependence is given in Table 7.4. Fig. 7.13 shows the azimuthal windows in p_T and $c\Delta\phi$ for every layer.

Table 7.3: Azimuthal and longitudinal conversion veto cut windows. The $\star$ indicates that the upper limit of the window is p_T-dependent. The quantity $c\Delta\phi$ corresponds to the azimuthal distance between a cluster and a track, $\Delta\phi$, multiplied by the track's charge.

VTX Layer	Window for $c\Delta\phi < 0$ [rad]	Window for $c\Delta\phi > 0$ [rad]	Window in $\lvert\Delta z\rvert$ [cm]
B0	$-0.04 < c\Delta\phi < -0.001$	$0.001 < c\Delta\phi < \star$	0.1
B1	$-0.04 < c\Delta\phi < -0.001$	$0.001 < c\Delta\phi < \star$	0.1
B3	$-0.08 < c\Delta\phi < -0.002$	$0.002 < c\Delta\phi < \star$	0.2
B4	$-0.04 < c\Delta\phi < -0.001$	$0.001 < c\Delta\phi < \star$	0.2

The size of the conversion veto windows has been tuned to maximize the rejection of photonic electron background while minimizing the rejection of tracks from random uncorrelated particles falling within the window. Previous PHENIX analyses in Au+Au [29] have used conversion veto windows narrower than the ones presented here by a factor of two, owing to the higher multiplicity environment in these collisions. The rejection power of the conversion veto cut can be quantified through the *survival rate* ε, or the fraction of tracks that pass the cut, of electrons and hadrons as shown in Fig. 7.14. The figure shows the survival rate for hadrons in data, which deviates from 100% due to the underlying uncorrelated background, and can thus be taken as a proxy for the survival rate of non-photonic electrons, such as those from heavy flavor decays. The figure also shows the survival rate of electrons from simulated direct photon conversions and π^0 decays. Notice that conversion electrons from the direct photons have a very low survival rate, as expected, while the survival rate for π^0 electrons is higher since they consists of a mixture of Dalitz ($\pi^0 \to e^+ + e^- + \gamma$) and conversion electrons.

Table 7.4: Upper limit of the p_T-dependent azimuthal conversion veto windows for $c\Delta\phi > 0$, as used in the Run11 Au+Au heavy flavor separation analysis.

VTX Layer	p_T Range [GeV]	Upper $c\Delta\phi$ Window Limit [rad]
B0	$p_T < 1.72857$	0.08
	$1.72857 < p_T < 3.63333$	$0.01 + 0.1/(p_T - 0.3)$
	$p_T > 3.63333$	0.04
B1	$p_T < 1.20909$	0.12
	$1.20909 < p_T < 3.63333$	$0.01 + 0.1/(p_T - 0.3)$
	$p_T > 3.63333$	0.04
B2	$p_T < 1.44286$	0.16
	$1.44286 < p_T < 2.96667$	$0.02 + 0.16/(p_T - 0.3)$
	$p_T > 2.96667$	0.08
B3	$p_T < 1.59032$	0.16
	$1.59032 < p_T < 40.3$	$0.036 + 0.16/(p_T - 0.3)$
	$p_T > 40.3$	0.04

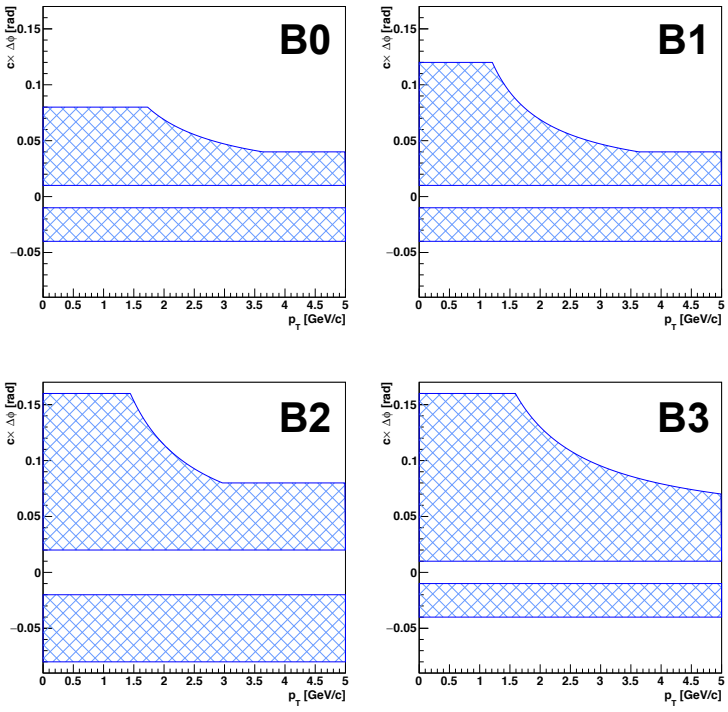

Figure 7.13: Conversion veto windows in track p_T and charge×$\Delta\phi$ in every VTX layer.

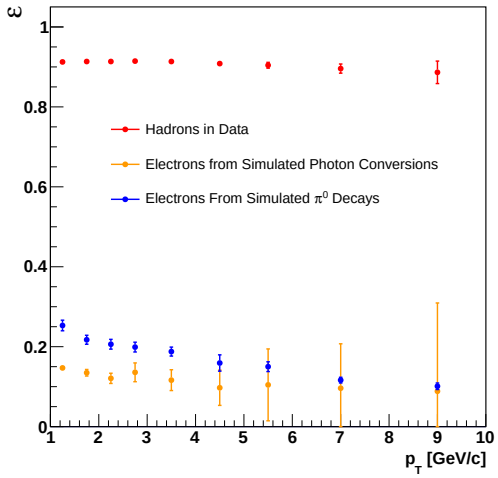

Figure 7.14: Conversion veto cut survival rate for hadrons in data, and electrons from simulated π^0 decays and photon conversions.

7.6 Measuring Track DCA in Data

A central component of this analysis is the measurement of the DCA distributions of tracks—both hadrons and identified electrons—in data. Fig. 7.15 shows a useful diagram to understand the definition of the DCA quantity used in this analysis. A track is shown in the transverse plane, bending in the magnetic field—which is assumed to be constant over the region filled by the VTX detector. The track projection is circular, with the center of the projection depicted by the black dot. Notice that the track originates from a displaced vertex, since it does not point back to the primary vertex of the collision, depicted by the red dot. The transverse DCA is then defined as

$$\mathrm{DCA}_T = L - R, \tag{7.1}$$

where, as shown, L is the distance between the primary vertex and the center of the projection, and R is the projection radius.

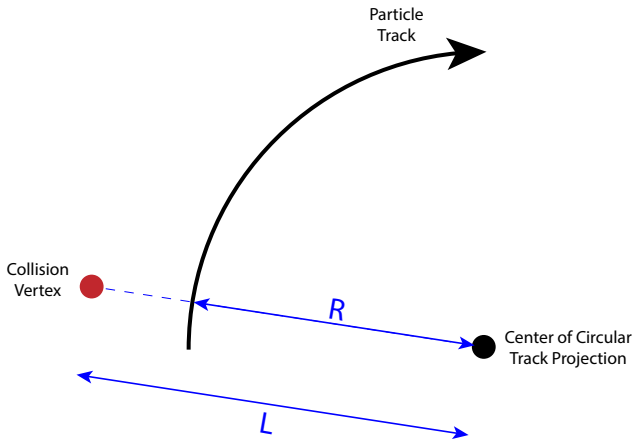

Figure 7.15: Diagram illustrating the definition of the distance of closest approach of a track in the transverse plane, DCA_T.

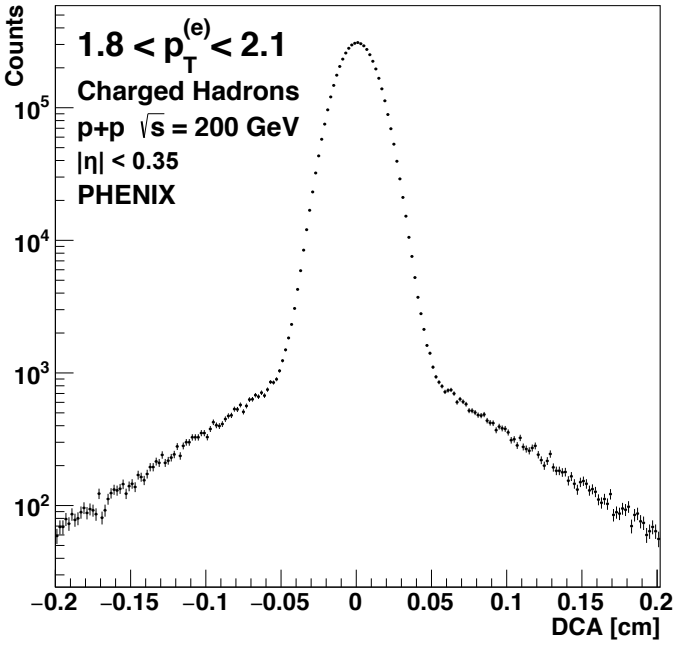

Figure 7.16: DCA distribution of hadron tracks within $1.8 < p_T$ [GeV/c] < 2.1 relative to the beam center.

According to this definition, DCA_T is a signed quantity, which is useful since the distribution is not, in general, necessarily symmetric about zero. The definition can be generalized for the DCA_T to be calculated about any abitrary point, not just the primary collision vertex. For instance, Fig. 7.16 shows the DCA_T distribution of charged hadron tracks within $1.8 < p_T$ [GeV/c] < 2.1, as calculated relative to the beam center. This consideration is of particular importance in this analysis, since the resolution of the point relative to which the measurement is made necessarily impacts the resolution of the DCA_T itself. When using DCA_T for displaced vertex analysis, it is important to ensure that its resolution be comparable to the length scale of the displaced vertices of interest. Otherwise, the discriminating power afforded by the method is lost. The following subsection deals with just this question.

7.6.1 Determination of the Beam Spread and Primary Vertex Resolution

The primary event vertex can be calculated from reconstructed VTX standalone tracks, with the algorithm described in Ref. [43]. When the primary vertex is measured for many events, the width of the resulting distribution is in reality a convolution of the beam spot size and the intrinsic primary vertex resolution. It is of interest to determine these two quantities separately, since their resolution directly impacts the resolution of the DCA_T distributions that can be measured. In order to separate them, one carries out two independent measurements of the primary vertex using only tracks in the east and west arms of the VTX detector. Assuming a beam spot and primary vertex distribution with transverse Gaussian profiles, let σ_b be the width of the beam spot; σ_{res} be the the true intrinsic resolution of the primary vertex when measured using tracks in both arms; and $\sigma_{res,E}$ and $\sigma_{res,W}$ be the intrinsic primary vertex resolutions for just the east and west arms, respectively. Under the assumption above, it is possible to use these variables to write down expressions for the width of the measured primary vertex resolution, as measured with inclusive tracks and also in each detector arm independently, as shown in Table 7.5.

Eqns. (D) and (E) in Table 7.5 can be solved for the beam spot size as a function of measured quantities, obtaining

$$\sigma_b^2 = \sigma^2_{\left(\frac{E+W}{2}\right)} - \frac{1}{4}\sigma^2_{(E-W)}. \tag{7.2}$$

The expression above can be applied to events with N and M standalone tracks in the east and west arms, respectively. Fig. 7.17 shows the determined beam spot size (in the x and y directions) as a function of the number of tracks. As expected, a roughly constant value for the beam spot size is found, broader in the x direction. The label 'ANY' corresponds to events with at least two tracks in either arm.

Having determined the beam spot size, Eqn. (A) in Table. 7.5 can be used to obtain the true resolution of the primary vertex,

$$\sigma_{res} = \sqrt{\sigma^2 - \sigma_b^2}. \tag{7.3}$$

Fig. 7.18 shows the resolution of the primary vertex, in the x and y direction, as determined from the

Table 7.5: Expressions for various measured quantities related to the primary vertex, as a function of the beam spot size and intrinsic primary vertex resolution.

Quantity	Expression
A. Inclusive primary vertex distribution	$\sigma = \sqrt{\sigma_b^2 + \sigma_{res}^2}$
B. Primary vertex distribution measured in east arm	$\sigma_E = \sqrt{\sigma_b^2 + \sigma_{res,E}^2}$
C. Primary vertex distribution measured in west arm	$\sigma_W = \sqrt{\sigma_b^2 + \sigma_{res,W}^2}$
D. Difference between the E and W primary vertices	$\sigma_{(E-W)} = \sqrt{\sigma_{res,E}^2 + \sigma_{res,W}^2}$
E. Average of the E and W vertices	$\sigma_{(\frac{E+W}{2})} = \sqrt{\sigma_b^2 + \left(\frac{\sigma_{res,E}^2 + \sigma_{res,W}^2}{4}\right)}$

equation above, as a function of the total number of standalone tracks used in its determination.[3]

As expected, the resolution improves as more tracks are available to calculate the vertex, with values ranging from $\sigma_x \approx 300$ μm for events with two tracks, to $\sigma_x \approx 100$ μm when 8 tracks are available. However, approximately 50% of all events do not have enough tracks to determine a primary vertex at all, owing to the low multiplicity of $p+p$ collisons at RHIC as well as the limited coverage and tracking efficiency of the VTX. Of the events for which a vertex can be determined, only 20% have 5 tracks or more.

[3] Recall that the primary vertex is calculated using reconstructed SvxStandalone tracks that pass a specific set of quality cuts. Thus, the number of tracks available to calculate the vertex is different from the total number of reconstructed tracks in the event.

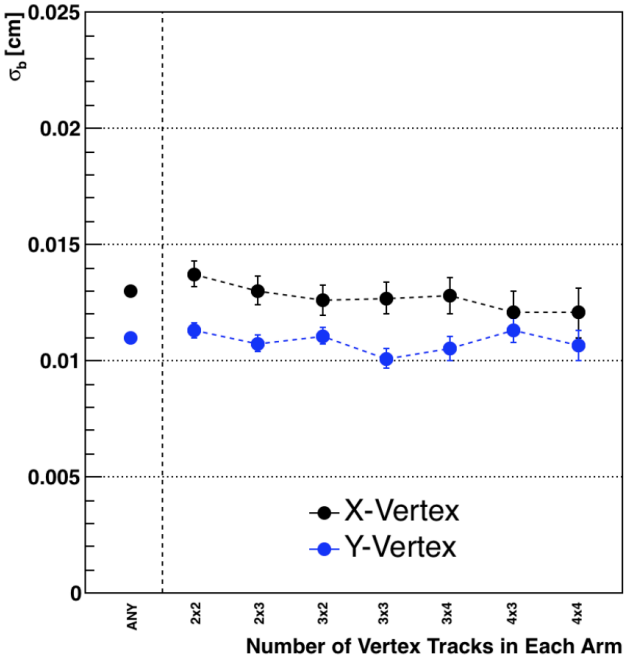

Figure 7.17: Beam spot size as calculated through independent measurements of the event vertex in the east and west arm of the detector, as a function of the number of tracks in the $E \times W$ arms.

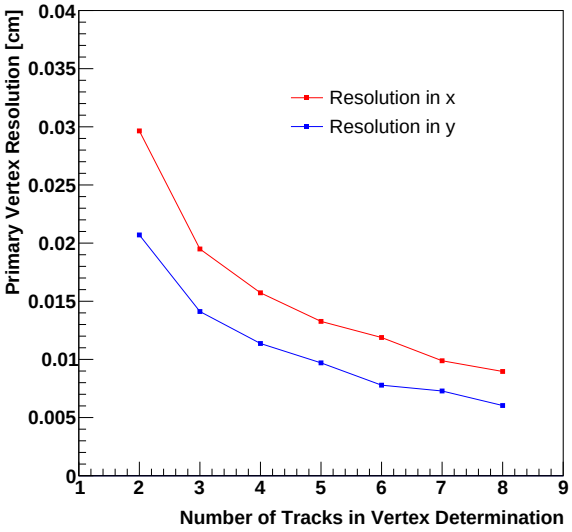

Figure 7.18: Intrinsic precise vertex resolution, in the x and y directions, as a function of the number of standalone tracks used in its determination.

In addition to limiting the resolution of the primary vertex, having only a small number of tracks available for vertex determination results in a biased DCA_T distribution. By construction, any track used to calculate the primary vertex has a DCA_T value of—or very close to—zero. If the VTX hits of such a track are matched to, say, an identified electron in the central arms coming from a heavy flavor decay, then the DCA_T of the electron will be biased towards a smaller value. In order to overcome this issue, and in consideration of the fact that the beam spread and the primary vertex have resolutions of comparable magnitude, the analysis proceeds by always calculating DCA_T relative to the beam center. The beam spread, in the x and y directions, as a function of run number is shown in Fig. 7.19, demonstrating the stability of the transverse beam size as a function of time.

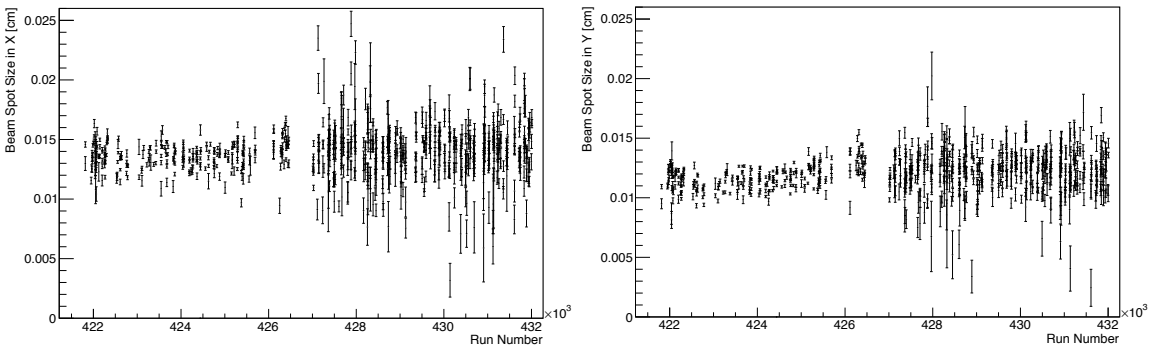

Figure 7.19: Beam spot size in the x and y coordinate as a function of run number.

7.6.2 Electron Identification

Table 7.6 lists the set of track cuts used for electron identification (using central arm variables), as well as those used to ensure a high quality track reconstruction. Electron identification in the central arm proceeds primarily through the use of the RICH and electromagnetic calorimeter. The `dep` variable quantifies, in standard deviations away from the mean, the ratio of energy deposited by a particle in the calorimeter to its track momentum. It is possible to use this variable to discriminate electrons, since they have a low mass and lose most of their energy in the calorimeter,

unlike hadrons which deposit only a fraction of their energy. The `emcdphi` and `emcdz` variables correspond to the displacement of a shower in the calorimeter relative to the track projection, and are constructed in such a way that their distribution is a standard Gaussian. The 3σ cut on these variables guarantees a match between a track and calorimeter deposit corresponding to a given electron.

Table 7.6: Electron identification and quality cuts.

Electron Identification Cuts	• $\lvert$`dep`$\rvert < 2$ • $\lvert$`emcsdphi`$\rvert < 3$ • $\lvert$`emcsdz`$\rvert < 3$ • `disp` < 5 • Require that track pass conversion veto **If Track $p_T < 5$ GeV** • `prob` > 0.1 • `n0` > 1 **If Track $p_T \geq 5$ GeV** • `prob` > 0.2 • `n0` > 3
Tracking Cuts	• χ^2/`ndf` < 3 • `quality = 31` or `quality = 63` • Require at least one hit in layers B0 and B1 • Require at least three hits in track • $\lvert$`zed`$\rvert < 75$

Regarding the RICH subsystem, only electrons fire it below $p_T \approx 5$ GeV/c. Above that threshold, charged hadrons—particularly pions—also emit Cherenkov light, which explains the p_T-dependent cut on RICH variables. The `n0` variable corresponds to the number of fired PMTs in

a Cherenkov ring associated with a given track. The `disp` variable measures, in centimeters, the displacement of the center of a Cherenkov ring from a given track projection. Finally, `prob` is related to the shape of a calorimeter shower, as quantified by

$$\chi^2 = \sum_i \frac{(E_i^{\rm pred} - E_i^{\rm meas})^2}{\sigma_i^2}, \tag{7.4}$$

normalized between zero and unity. In the above equation, $E_i^{\rm pred}$ and $E_i^{\rm meas}$ are the predicted and measured energy in the $i^{\rm th}$ calorimeter tower for a particle of energy $E = \sum_i E_i^{\rm meas}$.

Finally, a set of cuts are imposed to guarantee good track reconstruction. Of these, the χ^2/`ndf` cut corresponds to the SvxCentralTrack fit, and the `quality` cut corresponds to the associated PHCentralTrack. The particular values that `quality` takes on correspond to tracks reconstructed in the drift chamber using the X1 and X2 sections, with unique hits in U and V wires, and with a matching hit in the PC1.

7.6.3 Hadron Contamination in Electron Sample

The cuts of the previous subsection do not fully eliminate hadron contamination in the identified electron track sample. There are two sources of hadron contamination; (*i*) it can originate from the association of an electron PHCentralTrack with unrelated random hits in the VTX, leading to the reconstruction of a spurious SvxCentralTrack, or (*ii*) from legitimate hadron SvxCentralTracks that are misidentified as electrons in the central arms. The former category contributes a negligible amount of background due to the low multiplicity of $p + p$ collisions which makes it unlikely for tracks to be associated with random VTX hits. On the other hand, misidentified hadrons do contribute significantly to the identified electron candidate sample. At low track p_T, misidentified hadrons are associated with occupancy effects in which distinct tracks share hits in the RICH; at high p_T, this background is mostly asssociated with charged pions firing the RICH.

One way to quantify the fraction of candidate electron tracks attributable to hadron contamination using EMCal information exploits the difference in the shape of the `dep` distribution of electrons and hadrons. While, for real electrons, the distribution closely resembles a standard

Gaussian, it strongly deviates from a Gaussian shape in the case of hadrons. Fig. 7.20 shows the `dep` distribution of hadron tracks in various p_T categories. Each distribution was fit separately, as shown, to obtain templates describing the shape of the hadron `dep`. The `dep` distributions of *electron* candidate tracks, in various p_T bins, were subsequently fit with a function consisting of a Gaussian plus the previously determined hadron templates, with the normalization of the hadron template as the only free parameter. The results of the fit are shown in Fig. 7.21. The fraction of hadron contamination then follows straightforwardly as the ratio of integrals of the normalized template and the electron `dep` distribution, as shown by the blue dots in Fig. 7.23.

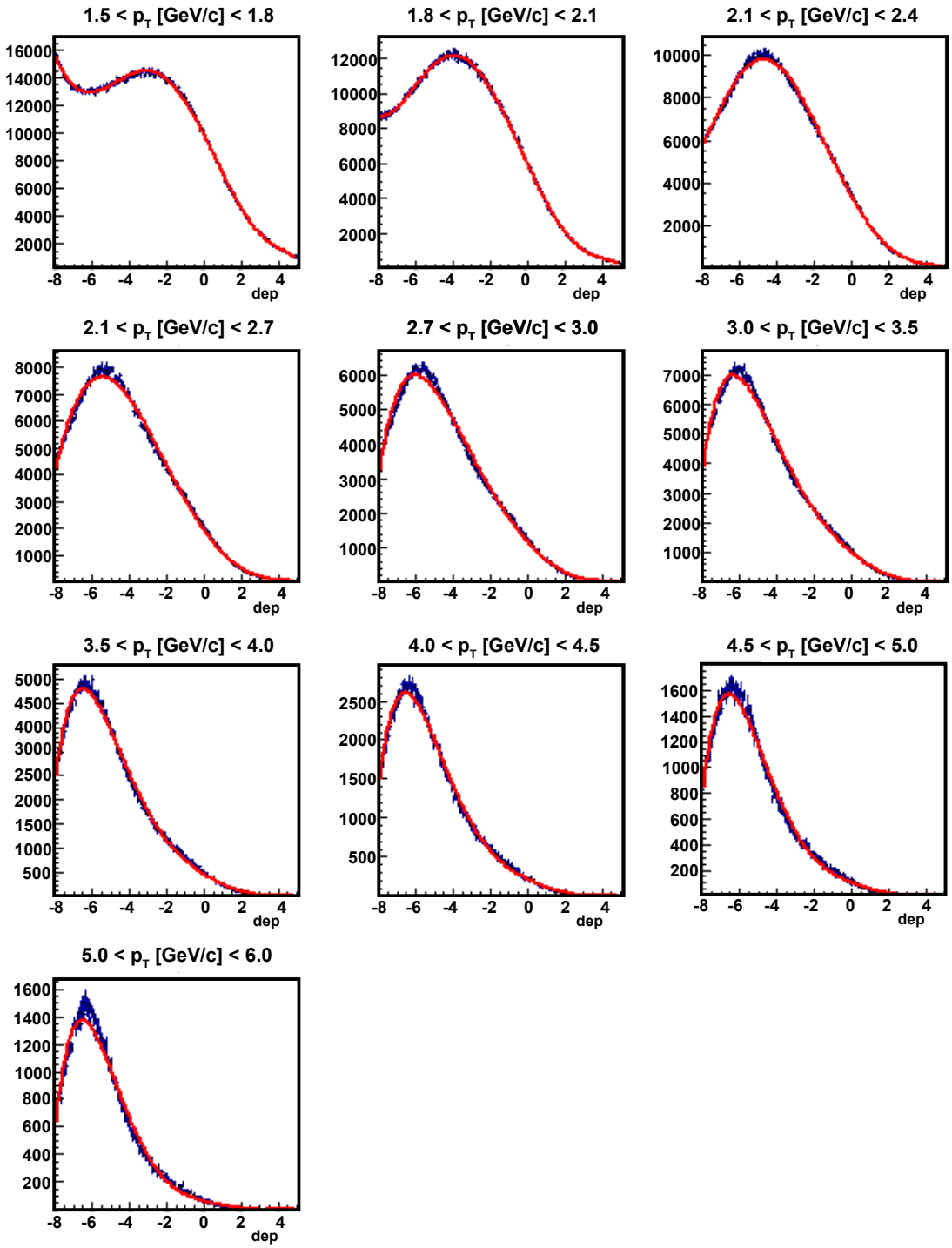

Figure 7.20: Distribution of the `dep` variable for hadron tracks. The distributions are fit to obtain a template describing the `dep` shape.

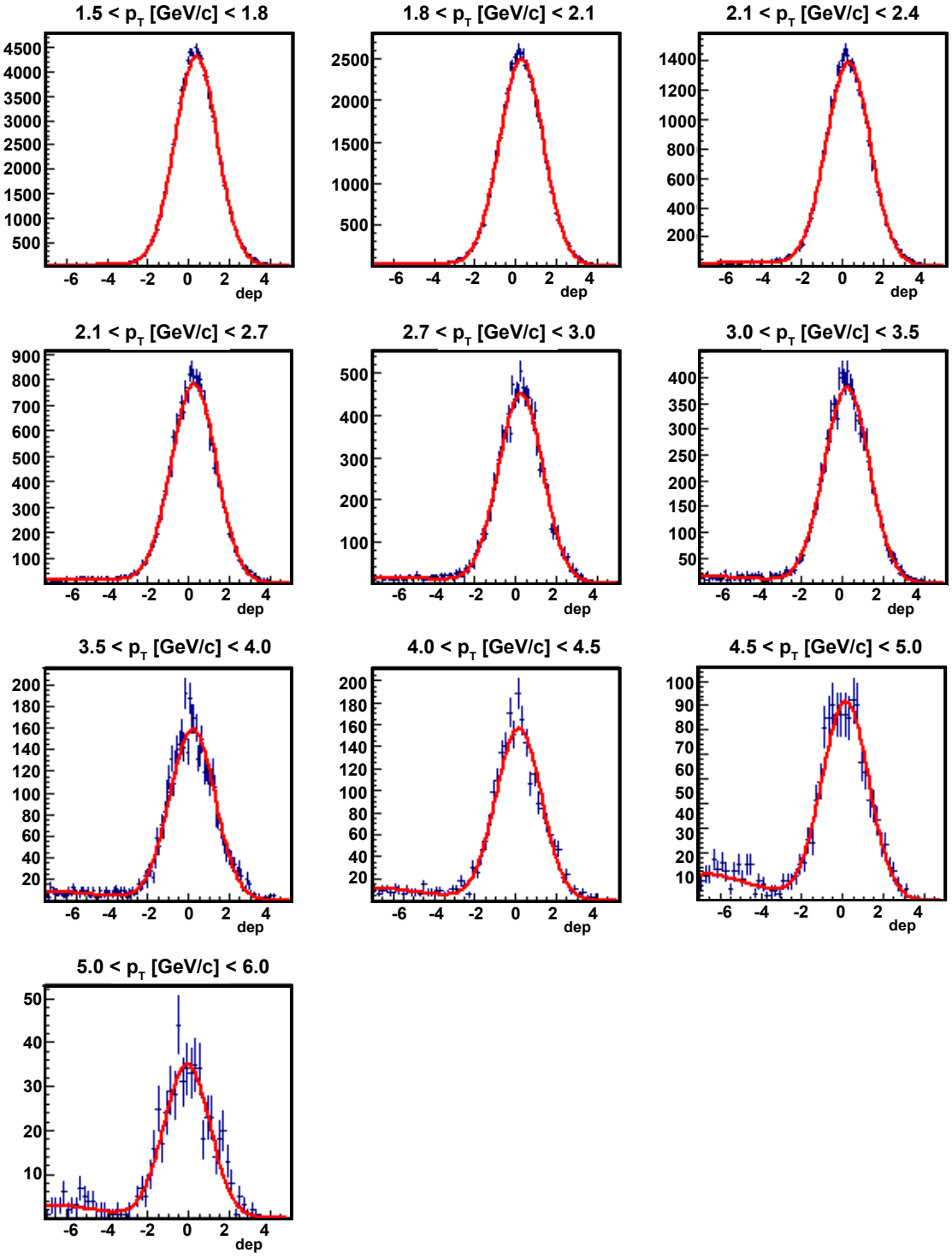

Figure 7.21: Distribution of the `dep` variable for electron tracks. The distributions are fit with a Gaussian plus a template describing the shape of hadron `dep`. See text for details.

The hadron contamination in the candidate electron sample can also be estimated independently using RICH information, exploiting the differences in RICH signals when the detector is triggered by electrons and hadrons. In particular, the cut on `n0`—used to identify electron tracks—will reject substantially more hadron than electron tracks, since only electrons fire the RICH at low p_T. Let ε_e and ε_h be the fraction of electron and hadron tracks, respectively, that pass a cut on the `n0` variable, as shown in Fig. 7.22 for `n0` > 1 and `n0` > 3, determined from a GEANT simulation of electrons, and from hadrons in data with `dep` < -6. Two different cuts are shown because the `n0` cut is p_T-dependent, as shown in Table 7.6.

Let N_t be the number of measured electron candidate tracks (which include both electrons and hadron contamination), and N_e and N_h be the 'true' number of electrons and hadrons in the sample. Also, let $\tilde{N}_t$ be the number of measured electron candidate tracks that pass the cut on `n0`. The following system of equations expresses N_t and $\tilde{N}_t$ in terms of the true number of hadrons and electrons:

$$\begin{cases} N_t = N_e + N_h \\ \tilde{N}_t = \varepsilon_e N_e + \varepsilon_h N_h. \end{cases} \tag{7.5}$$

The system can be solved for N_e and N_h,

$$N_h = \frac{\tilde{N}_t - \varepsilon_e N_t}{\varepsilon_h - \varepsilon_e} \tag{7.6}$$

$$N_e = \frac{N_t \varepsilon_h - \tilde{N}_t}{\varepsilon_h - \varepsilon_e}, \tag{7.7}$$

from which the fraction of hadrons $N_h/\tilde{N}_t$ can be obtained, as shown by the green points in Fig. 7.23. The figure shows how the two independent measurements of hadron contamination differ from each other. Therefore, the weighted average of two is taken as the final estimate of the hadron contamination, as shown in Fig. 7.24. The systematic uncertainties on the points correspond to the difference between the two independent estimates.

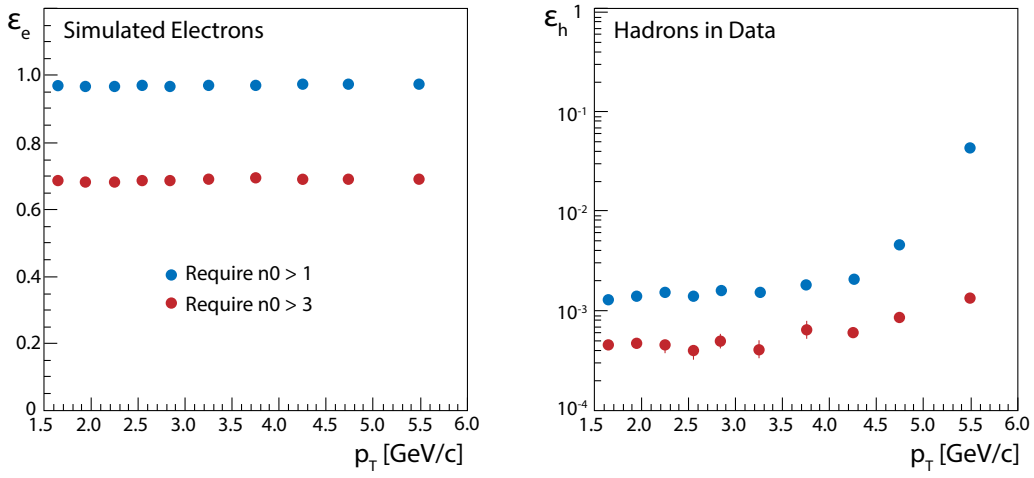

Figure 7.22: Fraction of tracks passing a cut on `n0`, for (left) simulated electrons and (right) hadron tracks in data.

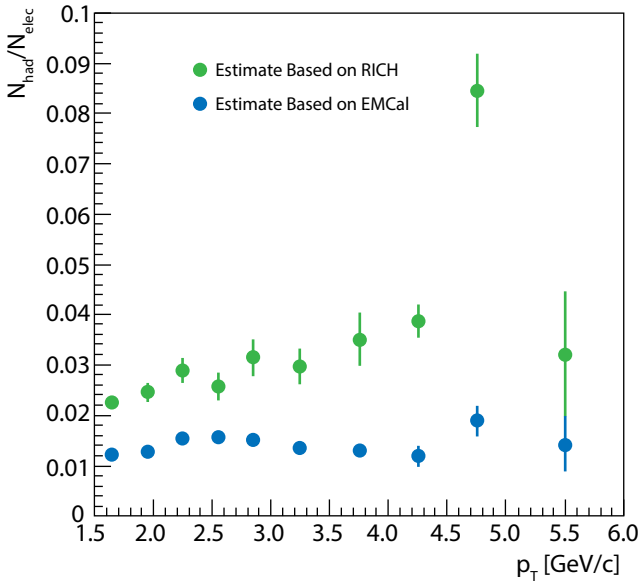

Figure 7.23: Hadron contamination in candidate electron sample, determined independently using EMCal and RICH information.

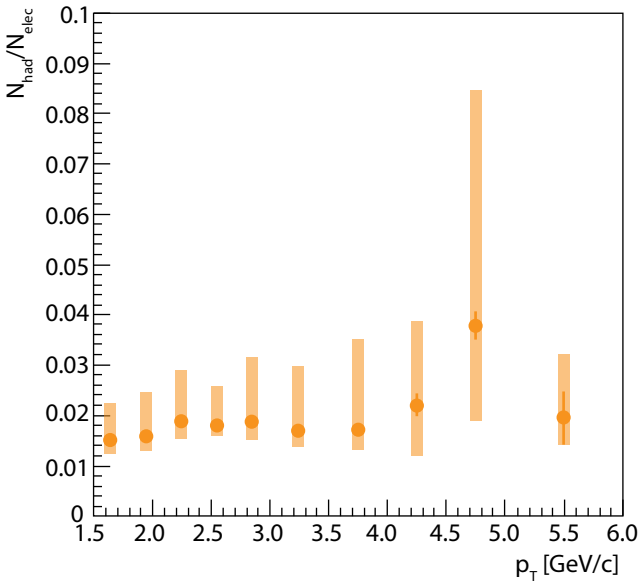

Figure 7.24: Hadron contamination as weighted average of independent estimates using EMCal and RICH information. See text for details.

7.7 Accounting for Electron Background

The previous section dealt with the identification and measurement of electron candidate tracks and their associated DCA_T. It was shown that the sample contains, in addition to electrons, misidentified hadron tracks whose relative contribution to the total sample size was estimated in two independent ways. The remaining *true* electrons can be described as belonging to one of two groups, based on their provenance. We identify *photonic* electrons as those originating from the Dalitz decay of pseudoscalar mesons, namely the π^0 and η mesons[4] , and from the conversion of photons upon interacting with detector material; on the other hand, *non-photonic* electrons originate from the decay of the J/ψ meson, and from the three-body decay of $K^{\pm}$ and K^0_s—referred to as K_e3 electrons—as well as the semileptonic decay of open heavy flavor hadrons. The desired open heavy flavor electron signal can only be isolated by correctly accounting, via simulations, for

[4] Light vector mesons, such the ρ, ω, ϕ, contribute negligibly to the candidate electron sample and are thus ignored in this analysis. This was determined from a detailed electron cocktail constructed for an earlier electron analysis in PHENIX [20], where the contribution of the light vector mesons was found to be several orders of magnitude smaller than that of J/ψ decays.

the electrons produced by all other sources, both photonic and non-photonic.

7.7.1 Constructing a Background Electron Cocktail

We account for electron background by constructing a simulated particle cocktail comprising π^0, η, direct photons, J/ψ, $K^{\pm}$, and K_0^s as primary particles. The first step is to produce these particles using a Pythia-based single-particle event generator, in which the spatial and momentum distribution of the particles can be specified. All primary particles were generated uniformly in transverse momentum, within $0 < p_T$ [GeV/c] < 20, and—with the exception of the J/ψ— uniformly in pseudorapidity $|\eta| < 0.5$. The J/ψ meson is an exception due to its decay kinematics. In order for its decay electrons to fully populate the acceptance of the central arms, it was necessary to distribute the primary particles within $|y| < 2$ following a Gaussian distribution of width $\sigma_y = 1.8$. In all cases, particles were simulated as originating from a region in the transverse plane centered on $\vec{x}_0 = (0.1612, 0.07232)$ cm with a Gaussian profile of width $\vec{\sigma} = (0.0129, 0.0109)$ cm, simulating the parameters of the beam spot in data, as described in Section 7.6.1. Longitudinally, the origin of primary particles is uniformly distributed within $|z| < 15$ cm.

As a second step in creating the electron cocktail, primary particles—with the exception of the direct photons—are forced to decay.[5] . Since the objective is to construct an *electron* cocktail, only decay modes involving electrons and photons were enabled in the decayer class, as listed in Table 7.7 along with their corresponding branching ratios. The resulting decay particles are then provided as input to a GEANT simulation of the PHENIX detector, in order to properly model the interactions with the detector material and to reconstruct particle tracks with the identical code used in PHENIX data reconstruction. As a digression, photon simulations can be used to obtain a tomographic image reconstruction of the VTX detector by tracing conversion electron tracks back to their point of origin, as shown in Fig. 7.25. This technique was used to quantify the material budget of the detector's GEANT description, ensuring that it accurately corresponds to that of the

[5] ROOT's `TPythia6Decayer` class was used for this purpose, with documentation available in `https://root.cern.ch/doc/v608/classTPythia6Decayer.html`

actual VTX.

Table 7.7: Decay modes for the primary hadron species included in the background electron cocktail. Notice that not all decay modes were considered in this analysis, and hence the branching ratios in the table do not add up to unity.

PRIMARY PARTICLE	SIMULATED DECAY MODES	BRANCHING RATIO
π^0	$\pi^0 \to \gamma\gamma$	0.988
	$\pi^0 \to \gamma e^+ e^-$	0.012
η	$\eta \to \gamma\gamma$	0.3923
	$\eta \to \pi^0\gamma\gamma$	0.0007
	$\eta \to \gamma e^+ e^-$	0.0049
	$\eta \to \gamma\pi^+\pi^-$	0.0478
	$\eta \to \pi^+\pi^- e^+ e^-$	0.0013
J/ψ	$J/\psi \to e^+ e^-$	0.0602
$K^\pm$	$K^\pm \to e^\pm \nu_e \pi^0$	0.0482
K_s^0	$K_s^0 \to \pi^0\pi^0$	0.3139

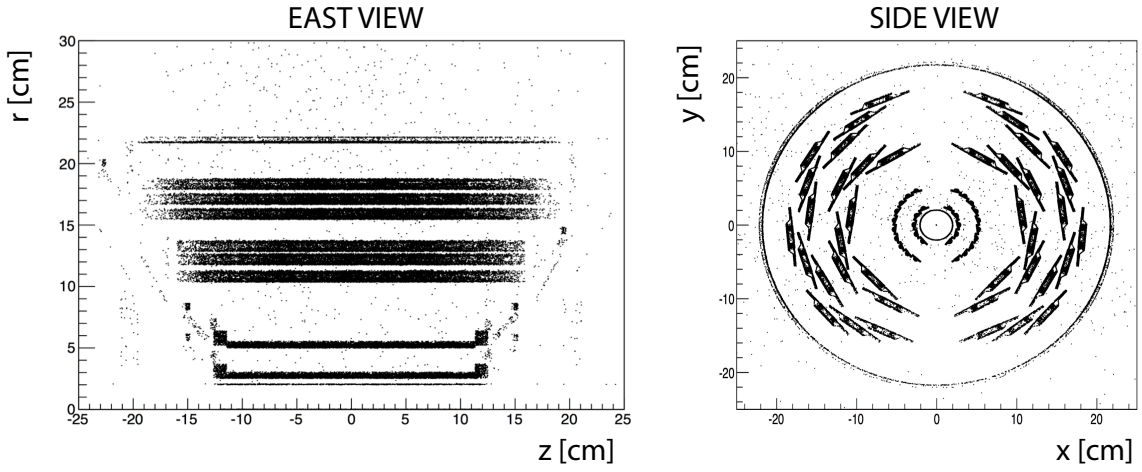

Figure 7.25: Tomographic reconstruction of the VTX detector material from GEANT photon simulations.

As a third, and final, step in creating the electron cocktail, the standard electron identification and track quality cuts (described in Subsection 7.6.2) are applied to the simulated tracks. Since the transverse momentum of primary particles is uniformly distributed, it is necessary to reweight the reconstructed electron tracks to restore their appropriate p_T spectrum. This is done by tracing the ancestry of a given electron track back to its original primary particle, whether a hadron or a photon. The weight assigned to the electron is thus the production cross section for the primary particle species at hand, evaluated at the particular p_T of the original parent particle. To facilitate this evaluation, the published cross section of π^0 [16], η [19], direct γ [34, 18], $K^{\pm}$ [21], and K^0_s [22], previously measured by PHENIX, were fit with a modified Hagedorn functional form,

$$E\frac{d^3\sigma}{dp^3} = \frac{p_0}{[\exp(-p_1 \times p_T - p_2 \times p_T^2) + p_T/p_3]^{p_4}}, \tag{7.8}$$

while the J/ψ cross section [23] was fit with a power law functional form,

$$E\frac{d^3\sigma}{dp^3} = p_0 \times \left(1 + \frac{p_T^2}{p_1^2}\right)^{-p_2}. \tag{7.9}$$

All fits are shown in Figs. 7.26 to 7.28. It is notable that the fit to the K^+ spectrum is very "hard", as the high p_T behavior is unconstrained by experimental data. Nevertheless, the high-p_T behavior

of the fit does not affect the analysis, and systematic uncertainties associated with the quality of the fit are assigned.

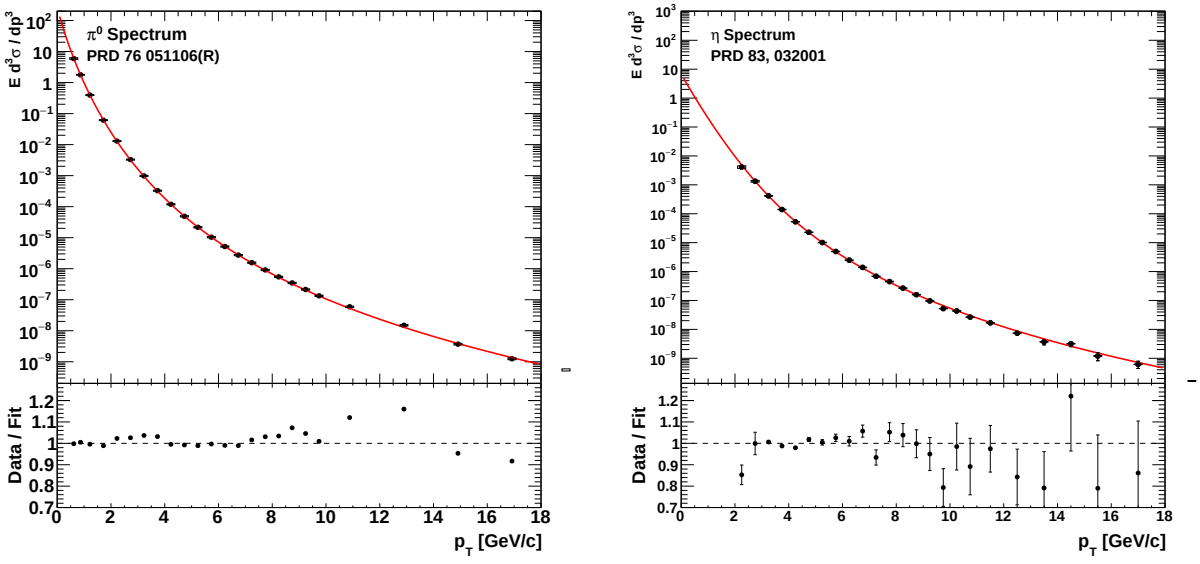

Figure 7.26: Modified Hagedorn fit to published yield of π^0 and η mesons in $p+p$ collisions at $\sqrt{s_{NN}} = 200$ GeV.

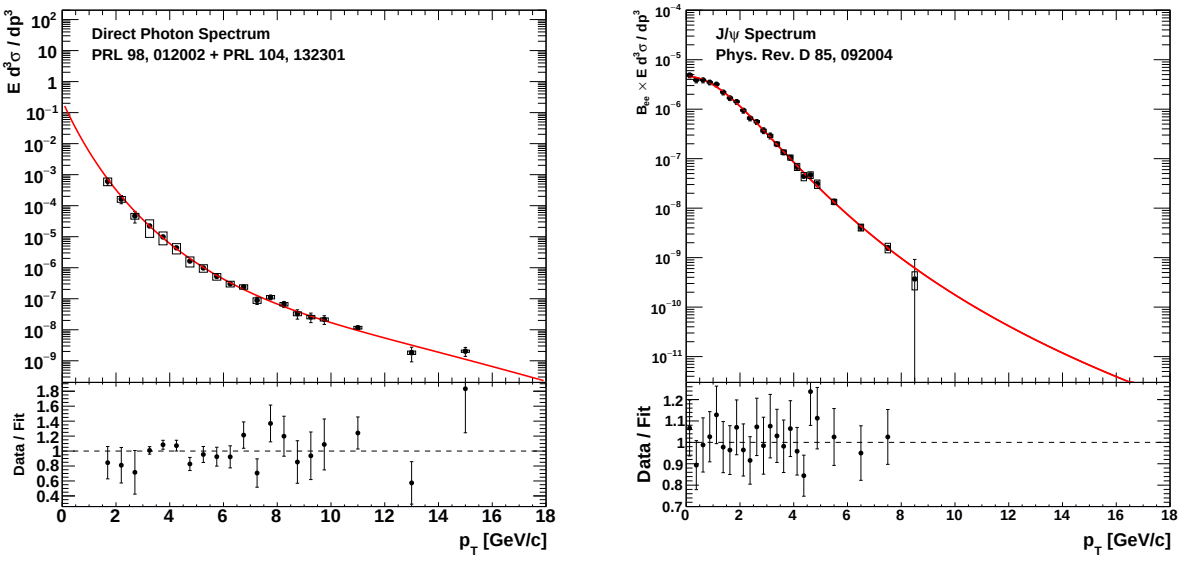

Figure 7.27: Modified Hagedorn fit to published yield of direct photons, and power law fit to yield of J/ψ in $p+p$ collisions at $\sqrt{s_{NN}} = 200$ GeV.

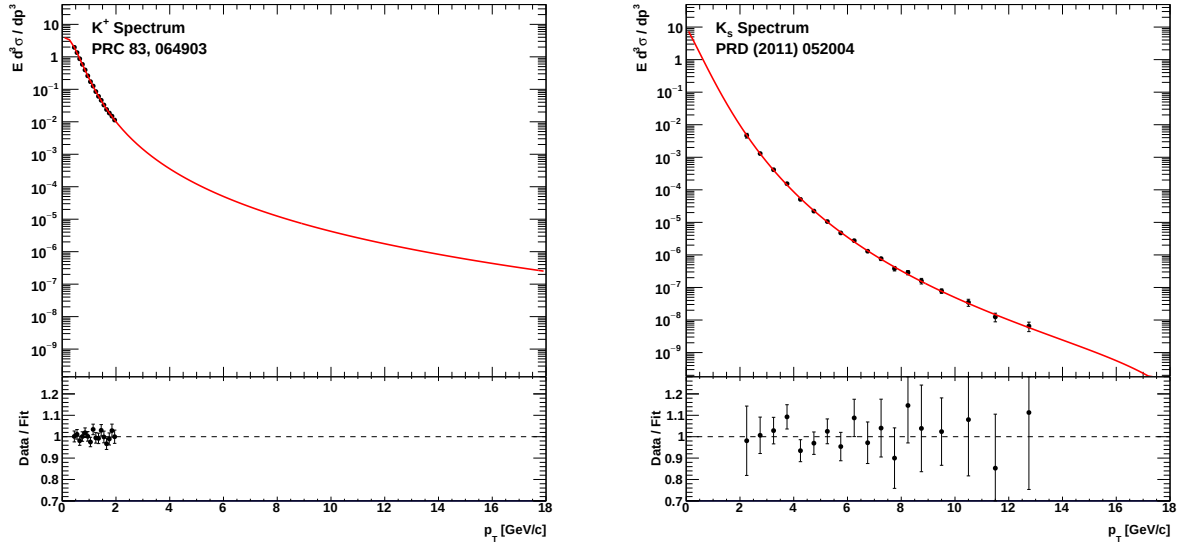

Figure 7.28: Modified Hagedorn fit to published yield of K^+ and K_s in $p+p$ collisions at $\sqrt{s_{NN}} = 200$ GeV.

Fig. 7.29 shows, for every primary particle species in the cocktail, the correlation between

parent hadron (or photon) momentum and reconstructed electron momentum, whose particular features change depending on the decay kinematics of each particle. Finally, the cocktail is normalized relative to the total photonic background, obtaining the result shown in Fig. 7.30.

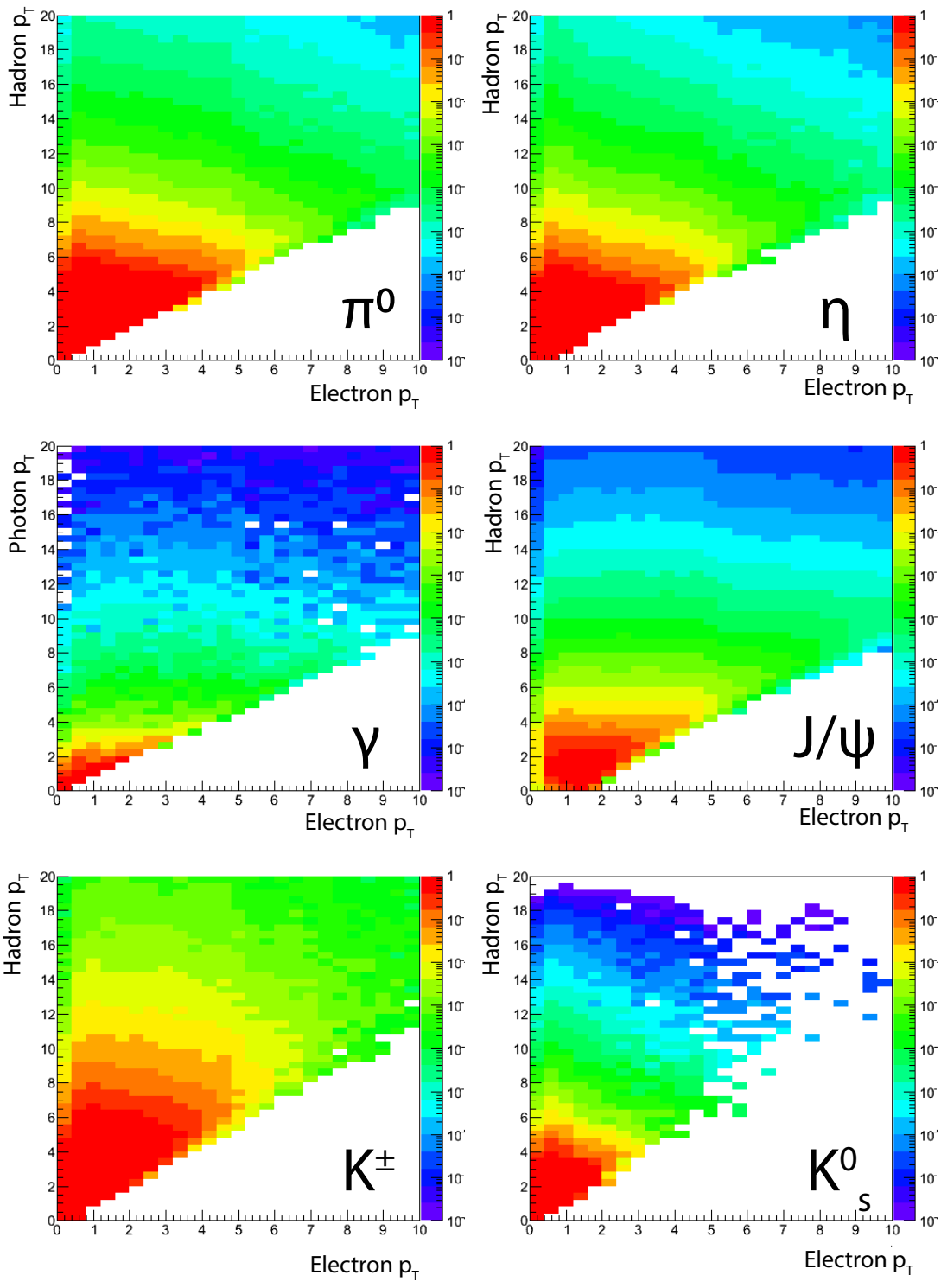

Figure 7.29: Relation between the transverse momentum of primary particles and their reconstructed decay electrons, for every species in the electron cocktail.

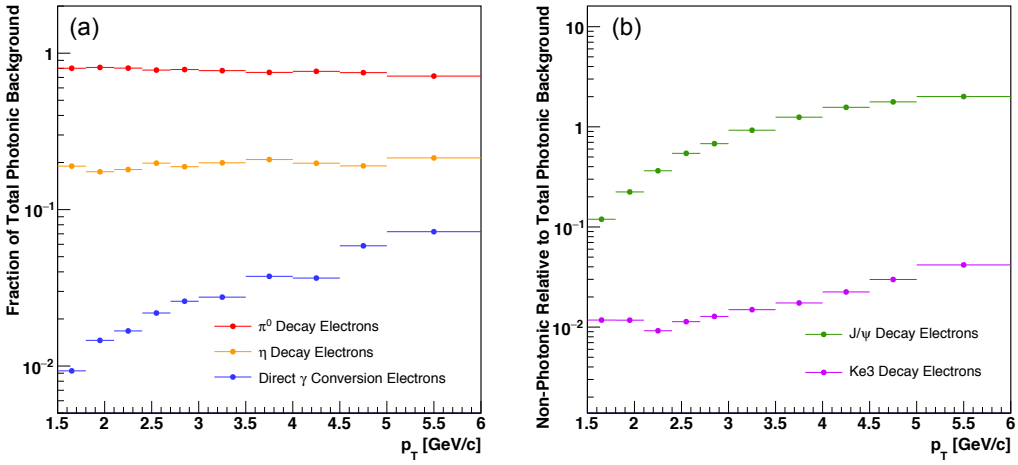

Figure 7.30: Fraction of electrons from (a) photonic and (b) non-photonic sources, relative to total photonic electron background, as determined from the electron cocktail.

7.8 Normalizing Electron Background Relative to Electron Candidate Sample

The previous subsection dealt with the construction of an electron cocktail, with the goal of determining the relative contribution of each primary particle species to the total *electron background*. Unfortunately, the cocktail does not provide information regarding the fraction of the total electron candidate sample in data that consitutes the background. The present section will discuss a data-driven approach to determine this fraction and, by extension, determine the number of electron candidate tracks attributable to each electron background source.

7.8.1 Measuring the Fraction of Non-Photonic Electrons

Let us define the quantity F_{NP} as the ratio of non-photonic electrons to inclusive electrons (i.e., both photonic and non-photonic),

$$F_{NP} = \frac{N_{NP}}{N_P + N_{NP}}, \tag{7.10}$$

where N_P and N_{NP} are the number of photonic and non-photonic electrons in the electron candidate sample, respectively. While these are not directly observable quantities, we can determine them

by measuring the number of electrons candidates N_e, and the number of electron candidates which pass the conversion veto cut $\tilde{N}_e$, as previously discussed in Section 7.5. Given that the conversion veto cut affects photonic and non-photonic electrons differently, with the latter having a lower probability of passing the cut, it is possible to write a system of equations involving the above quantities, as follows:

$$\begin{cases} N_e = N_P + N_{NP} \\ \tilde{N}_e = \varepsilon_P \times \varepsilon_{UC} \times N_P + \varepsilon_{UC} \times N_{NP}. \end{cases} \tag{7.11}$$

In the above system, ε_P and ε_{UC} are the veto cut survival rates of photonic and non-photonic electrons, respectively. The survival rate of photonic electrons, ε_P is calculated as the weighted average of the survival rates for electrons from each individual photonic source; in the case of non-photonic electrons, the survival rate of hadrons in data is taken as a proxy for ε_{UC}, as shown in Fig. 7.31. More generally, ε_{UC} accounts for the fact that uncorrelated hits in the conversion veto window can cause any track, not just non-photonic electrons, to be rejected by the conversion veto cut. Hence, N_P is multiplied by $\varepsilon_P \times \varepsilon_{UC}$ in the second line of Eqn. 7.11. Solving for N_P and N_{NP}, we obtain

$$N_P = \frac{N_e \varepsilon_{UC} - \tilde{N}_e}{\varepsilon_{UC} - \varepsilon_P}, \tag{7.12}$$

and

$$N_{NP} = \frac{\tilde{N}_e - N_e \varepsilon_P}{\varepsilon_{UC} - \varepsilon_P}. \tag{7.13}$$

In the derivation presented, the survival rates are calculational tools to arrive at N_P and N_{NP}, which correspond to electron yields unaffected by the conversion veto cut. However, since the measured electron candidate sample consists of tracks that survive the veto cut, we redefine the quantity F_{NP} to reflect this fact by setting $N_P \to \varepsilon_P \varepsilon_{UC} N_P$ and $N_{NP} \to \varepsilon_{UC} N_{NP}$. In that case, we obtain F_{NP} as shown in Fig. 7.32 as a function of p_T. It is of interest to notice the dominance, at over 90% of the total electron candidate sample, of non-photonic electrons at high p_T.

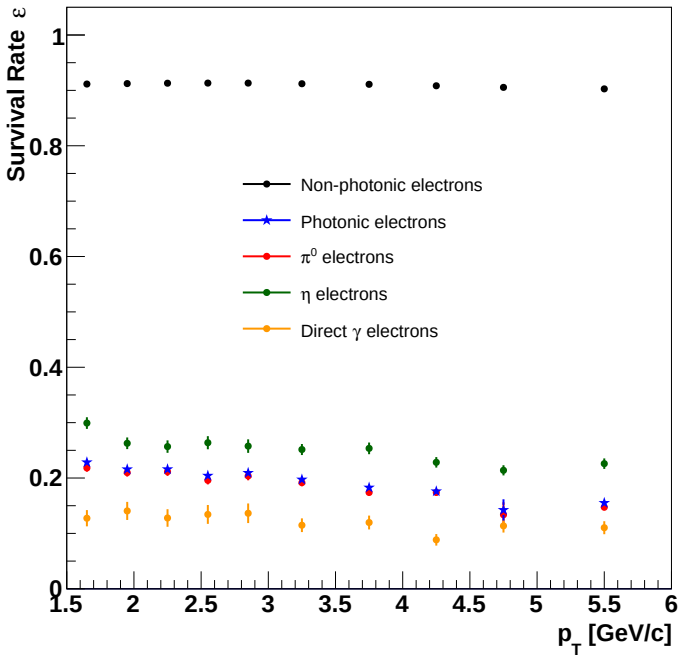

Figure 7.31: Conversion veto cut survival rate for non-photonic and photonic electrons. In the case of photonic electrons, the survival rates for electrons from individual sources are shown, as well as their weighted average.

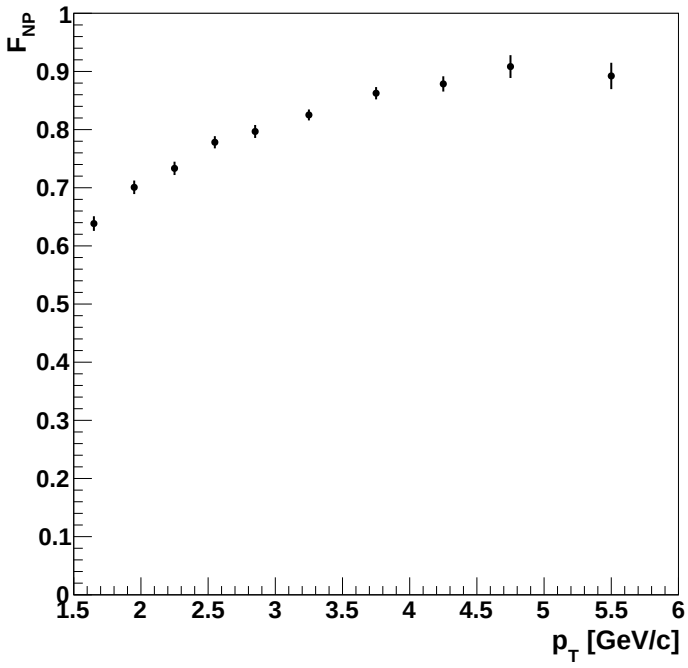

Figure 7.32: Fraction of non-photonic to inclusive electrons in the measured candidate electron sample as a function of p_T.

Given the central importance of the F_{NP} quantity in the isolation of the inclusive heavy flavor electron sample, as described in the next subsection, it is of interest to validate the calculation by comparing it to previous measurements. As described in Section 5.1.1, the PHENIX experiment measured inclusive heavy flavor electron production using 2005 data [20] using a combination of the cocktail and the converter method for background subtraction. Each of these methods was used to calculate F_{NP}, yet they cannot be directly compared to the same quantity obtained using 2015 data because of changes to the material budget over the years. If the changes to the material budget in the central arm acceptance can be quantified, then the 2005 F_{NP} can be scaled to be directly comparable to the most recent result, as shown in Fig. 7.33. In this case, an excellent agreement is seen. The full details of how the comparison was made can be found in Appendix C. Another independent way of estimating F_{NP} relies on exploiting the differences in azimuthal track-cluster correlations between photonic and non-photonic electron tracks. Appendix C describes how this

calculation was carried out, and found to be in excellent agreement with Fig. 7.32.

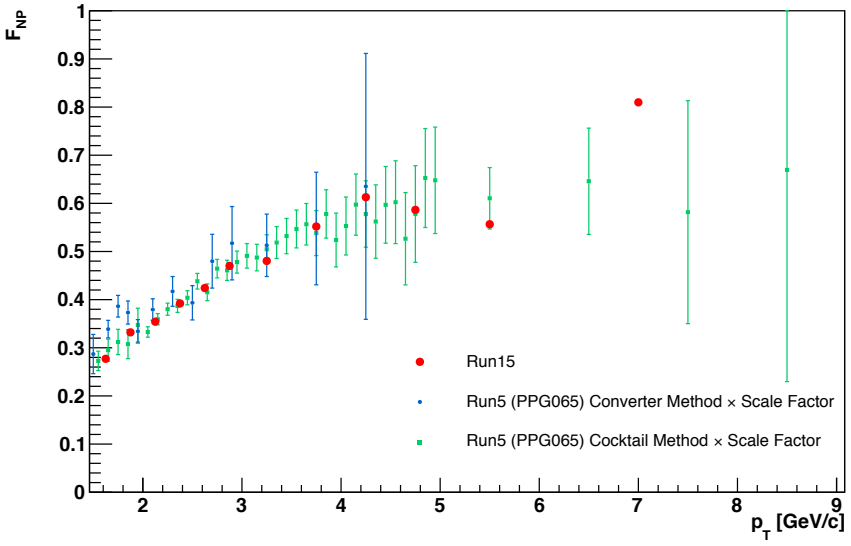

Figure 7.33: Comparison of F_{NP} in the PHENIX 2005 and 2015 heavy flavor electron analyses. The 2005 measurement has been scaled to account for changes in the material budget of the detector.

7.8.2 Normalization of Background DCA Distributions

The electron cocktail, as shown in Fig. 7.30, specifies the relative contribution of each type of primary particle to the total photonic electron background. Additonally, $1 - F_{NP}$ measures the fraction of electron candidate tracks in data that correspond to this photonic background. Therefore, by combining these two pieces of information, it is possible to absolutely determine the fraction of candidate electrons that can be attributed to each background source. For photonic electrons from the i^{th} source, such fraction is given by

$$f_i^{\text{phot}} = (1 - F_{\text{contam}})(1 - F_{NP})\frac{\tilde{N}_i}{\tilde{N}_{\pi^0} + \tilde{N}_\eta + \tilde{N}_\gamma}, \tag{7.14}$$

where $i = \pi^0\eta, \gamma$; $\tilde{N}_i$ is the number of electrons from the i^{th} source that pass the conversion veto cut in simulations, and F_{contam} is the fraction of electron candidates attributed to hadron contamination, shown in Fig. 7.24.

A similar expression cannot be constructed for the fraction of electrons from non-photonic sources, given that the background cocktail does not include heavy flavor electrons. Instead, non-photonic electrons are normalized relative to the simulated π^0 electrons, as follows

$$f_i^{\text{non-phot}} = f_{\pi^0}^{\text{phot}} \frac{\tilde{N}_i}{\tilde{N}_{\pi^0}}, \tag{7.15}$$

with $i = J/\psi, Ke3$.

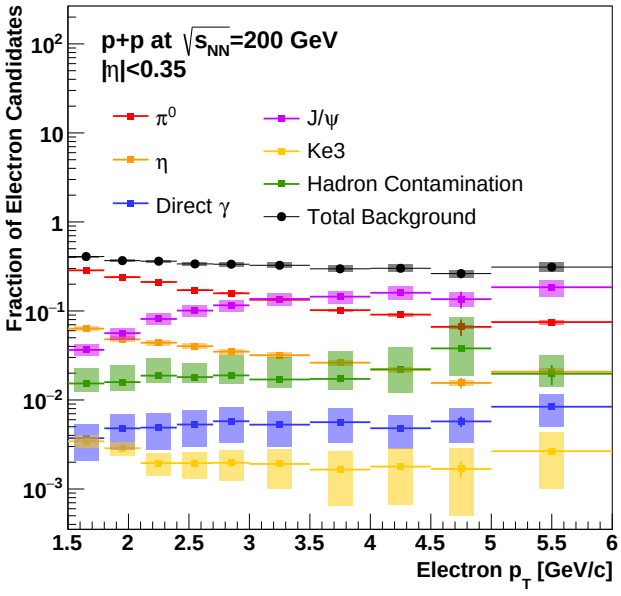

Figure 7.34: Fraction of electron candidate sample attributed to each source of background electrons, as a function of p_T.

Fig. 7.34 shows the fraction of electron candidates attributable to each background source, photonic and non-photonic, as a function of p_T. At low p_T, pions are the dominant source of electron background, giving way to J/ψ at high p_T. These fractions can be used to normalize the DCA_T distributions of the various background electrons relative to the total measured electron candidates, as shown in Fig. 7.35, where the background distributions shown are constructed by fitting the DCA_T distributions to obtain a smooth template.

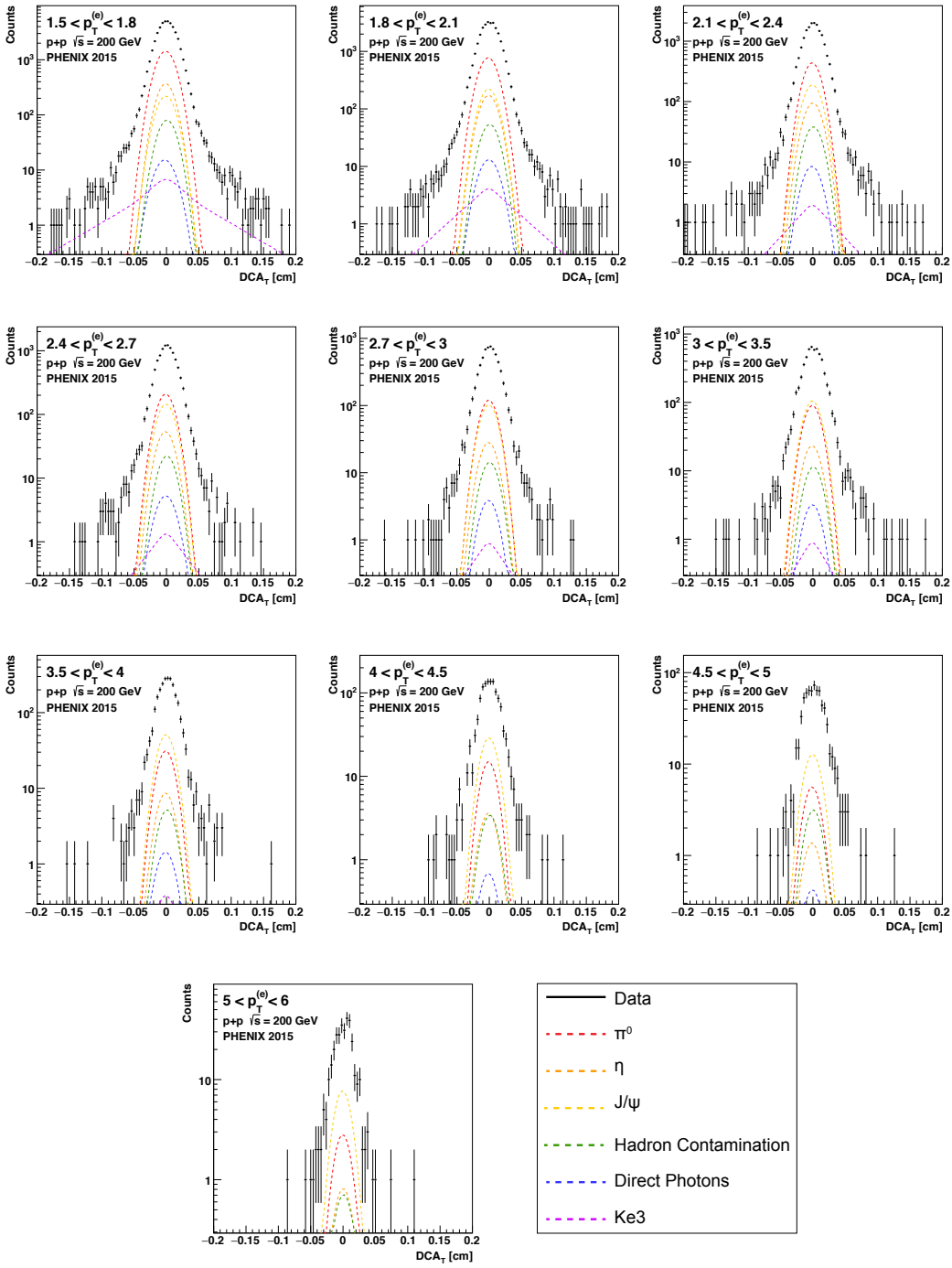

Figure 7.35: DCA_T distributions of electron candidate tracks in data, in several track p_T selections, along with the normalized contributions from individual background electron sources.

7.9 Separation of Heavy Flavor Electron Yields

One of the main goals of the present analysis is to measure the fraction of heavy flavor electrons arising from bottom quark decays. The previous section concluded by presenting the DCA_T distributions of electron candidate tracks, along with the corresponding normalized distributions of background electrons; implicitly, this defines the DCA_T distributions of inclusive heavy flavor electrons. Now, if the *shapes* of the parent D and B meson spectra were known—but not necessarily their total cross section—it would be possible to constrain the desired bottom electron fraction from the inclusive electron DCA_T distributions alone. Given that the decay kinematics are well understood, it would be straightforward to determine the decay electron DCA_T shape from each heavy quark separately, and thus fit the measured inclusive distribution with these two components to solve for the fraction of bottom electrons. Unfortunately, neither the spectral shape nor the total cross section of D and B mesons are known.

However, the PHENIX collaboration has previously measured the invariant yield of inclusive heavy flavor electrons in p+p collisions at $\sqrt{s_{NN}} = 200$ GeV, and when combined with our measured inclusive heavy flavor DCA_T distributions, it becomes possible to separate the contribution of each flavor to the electron sample. This is, in essence, an *inverse problem* in which model parameters (i.e., the spectrum of charm and bottom mesons) are deduced from data observations (i.e., the DCA_T and spectrum of inclusive heavy flavor electrons). The key to solving an inverse problem is being able to construct a mapping from the model parameters to the observed data; in this case, knowing the heavy flavor decay kinematics allows us to assign a probability to the p_T and DCA_T of a decay electron given the parent's p_T. Therefore, it is possible to determine how likely a given set of parent hadron spectra are, based on how well the calculated electron spectrum and DCA_T match the data. In this thesis, and more broadly in the context of high energy physics, the procedure to find the most likely set of model parameters is called *unfolding*.

Mathematically, inverse problems arise in a variety of fields, and numerous methods exist to solve them. Many such problems, for which the mapping can be expressed as a linear transfor-

mation, are commonly solved using matrix techniques such as singular value decompositon (SVD). Nevertheless, the unfolding problem at hand is best solved through probabilistic methods. Here, we briefly outline the solution strategy, providing a detailed description in the following subsections.

The probabilistic unfolding explores a wide range of possible spectra for D and B mesons. A given set of trial spectra are multiplied by a matrix modeling the decay process, which encodes the probability of a hadron, based on its p_T, to decay to an electron at a given p_T and DCA_T value. The result of applying the decay model to the trial spectra is then compared with the electron data provided as input using a likelihood function, and the probability that the data come from the set of trial parameters is calculated using Bayes' theorem. An exhaustive exploration of the possible parameter space using a Markov Chain Monte Carlo (MCMC) algorithm thus yields, not point estimates for the desired D and B spectra, but rather full *probability distributions*. As a result, the values that maximize the probability distributions are taken as the desired solution, with the width of the distribution providing a natural metric of the uncertainty in the estimation.

7.9.1 Bayesian Inference in a Nutshell

Bayes' theorem, a corollary of the the basic algebra of probability theory, reads as follows

$$P(\boldsymbol{\theta} \mid \boldsymbol{x}) = \frac{P(\boldsymbol{x} \mid \boldsymbol{\theta})\pi(\boldsymbol{\theta})}{P(\boldsymbol{x})}. \tag{7.16}$$

The $P(\boldsymbol{\theta}|\boldsymbol{x})$ term is called the posterior, $P(\boldsymbol{x}|\boldsymbol{\theta})$ is the likelihood, and $\pi(\boldsymbol{\theta})$ is called the prior; although less common, $P(\boldsymbol{x})$, is sometimes called the evidence. The importance of Bayes' theorem for statistical inference can be made evident if it cast as

$$P(\text{model parameters} \mid \text{data}) \propto P(\text{data} \mid \text{model parameters}) \times P(\text{model parameters}). \tag{7.17}$$

In this form, we see that the probability that the model parameters are true given the data—which is the quantity of interest—is related to the probability that the data follow from some assumed set of model parameters, which is admittedly an easier quantity to compute. In this analysis, that information is provided by the decay model of heavy flavor hadrons. In Bayesian inference, the prior

quantifies the knowledge of the true set of model parameters *prior* to the data being analyzed. On the other hand, the likelihood modifies—or, in some sense, refines—the prior through the inclusion of data to yield the desired posterior. In Eq. 7.17, the denominator $P(\text{data})$ is excluded, as it only serves as a normalization for the posterior. In this case, that normalization is unncessary since we are interested in finding the parameters which maximize the posterior.

In this analysis, the vector of model parameters $\boldsymbol{\theta} = (\boldsymbol{\theta}_c, \boldsymbol{\theta}_b)$ corresponds to the yield of D and B mesons in 17 p_T bins for each flavor. The data $\boldsymbol{x}$ corresponds to the combination of the inclusive heavy flavor electron yield in 21 data points, $\boldsymbol{Y}^{\text{data}}$, along with the electron DCA_T distributions in nine track p_T bins, $\boldsymbol{D}_i^{\text{data}}$, previously shown in Fig. 7.35. All of this information is arranged in a vector

$$\boldsymbol{x} = (\boldsymbol{Y}^{\text{data}}, \boldsymbol{D}_0^{\text{data}}, \boldsymbol{D}_1^{\text{data}}, \ldots, \boldsymbol{D}_9^{\text{data}}). \tag{7.18}$$

The 17 bins of the heavy flavor hadron spectra define a 34-dimensional parameter space, such that each point in the space corresponds to a full spectrum for both charm and bottom hadrons. The prior $\boldsymbol{\theta}_{\text{prior}}$—set in this case to be the spectrum of charm and bottom as calculated with the PYTHIA generator—provides a starting point for the sampling algorithm. The unfolding procedure then consists in a systematic drawing of trial sets of charm and bottom yields $\boldsymbol{\theta}_{\text{trial}}$ from the parameter space. For each $\boldsymbol{\theta}_{\text{trial}}$, the decay electron p_T spectrum $\boldsymbol{Y}(\boldsymbol{\theta})$ and DCA distributions $\boldsymbol{D}_j(\boldsymbol{\theta})$ are calculated as

$$\boldsymbol{Y}(\boldsymbol{\theta}) = \boldsymbol{M}^{(\boldsymbol{Y})}\boldsymbol{\theta_c} + \boldsymbol{M}^{(\boldsymbol{Y})}\boldsymbol{\theta_b}, \tag{7.19}$$

$$\boldsymbol{D}_j(\boldsymbol{\theta}) = \boldsymbol{M}_j^{(\boldsymbol{D})}\boldsymbol{\theta_c} + \boldsymbol{M}_j^{(\boldsymbol{D})}\boldsymbol{\theta_b}, \tag{7.20}$$

where $\boldsymbol{M}^{(\boldsymbol{Y})} : p_T^h \to p_T^{(e)}$ is a decay matrix encoding the probability that a hadron of p_T^h decays to an electron of $p_T^{(e)}$. Similarly, $\boldsymbol{M}_j^{(\boldsymbol{D})} : p_T^h \to \text{DCA}^{(e)}$ encodes the probability that the decay electron will have a given $\text{DCA}^{(e)}$ value. In this analysis, an additional matrix was introduced to model the detector response, by mapping the true p_T and DCA values with which $\boldsymbol{M}^{(\boldsymbol{Y})}$ were constructed, to their reconstructed counterparts. This allows for a direct comparison between the data and the

predicted electron distributions calculated from the trial parameters. The construction of these matrices is described in detail in Section 7.9.2.

With the prediction corresponding to a given set of trial parameters, the likelihood $P(\boldsymbol{x} \mid \boldsymbol{\theta})$ is constructed using the data, as follows

$$\ln P(\boldsymbol{x} \mid \boldsymbol{\theta}) = \ln P(\boldsymbol{Y}^{\text{data}} \mid \boldsymbol{Y}(\boldsymbol{\theta})) + \sum_{j=0}^{8} \ln P(\boldsymbol{D}_j^{\text{data}} \mid \boldsymbol{D}_j(\boldsymbol{\theta})). \tag{7.21}$$

In reality, the expression above corresponds to the log-likelihood function, which is more convenient to work with. Since the data $\boldsymbol{Y}^{\text{data}}$, corresponding to the inclusive heavy flavor spectrum, are assumed to have normally distributed and uncorrelated statistical uncertainties, the term $\ln P(\boldsymbol{Y}^{\text{data}} \mid \boldsymbol{Y}(\boldsymbol{\theta}))$ is modeled as a multivariate Gaussian distribution with diagonal covariance. On the other hand, since the DCA distributions $\boldsymbol{D}_j^{\text{data}}$ correspond to individual counts, the associated terms in the likelihod function are modeled by a Poisson distribution.

Since the $\boldsymbol{\theta}_{\text{trial}}$ consist of *invariant* yields of charm and bottom hadrons, the predicted electron DCA distributions will not match the corresponding measurements in normalization, since they are not corrected for acceptance and efficiency. Thus, while the predicted inclusive electron spectrum can be directly compared to data, the DCA distributions must be normalized to be compared in shape only.

7.9.2 Construction of the Heavy Flavor Decay Model

The decay matrices $\boldsymbol{M}^{(\boldsymbol{Y})}$ and $\boldsymbol{M}_j^{(\boldsymbol{D})}$, introduced in the previous subsection, were constructed by examining heavy flavor decays using the PYTHIA-6 event generator. Quark-antiquark production was forced with with the `MSEL=4` and `MSEL=5` options for charm and bottom, respectively. Decay electrons within the PHENIX central arm acceptance, $|\eta| < 0.35$, originating from the decay of open charm $(D^{\pm}, D^0, D_s, \Lambda_c)$ and open bottom $(B^{\pm}, B^0, B_s, \Lambda_b)$ hadrons were used to populate the matrices. Fig. 7.36 shows the charm hadron matrices $\boldsymbol{M}^{(\boldsymbol{Y})}$, and $\boldsymbol{M}_j^{(\boldsymbol{D})}$ for the $1.5 < p_T^{(e)}[\text{GeV}/c < 2.0$ bin in electron p_T.

The marginal probability distributions can be obtained by projecting the decay matrices, as

shown for charm (top panel) and bottom (bottom panel) hadrons in Fig. 7.37. The figure shows the probability that hadrons in five different $p_T^{(h)}$ selections decay to electrons with $p_T^{(e)}$. Here, the probabilities are integrated over all rapidities and decay channels. It is important to notice that the construction of these matrices relies exclusively on the PYTHIA generator, and thus introduces a model dependence in the final result.

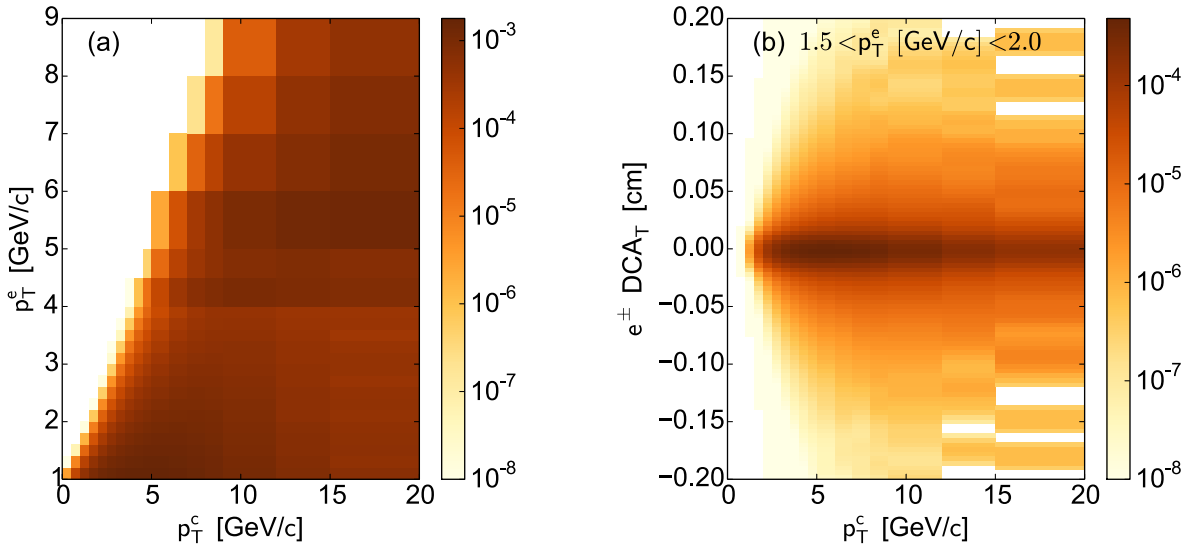

Figure 7.36: Decay matrices (left) $\boldsymbol{M}^{(\boldsymbol{Y})} : p_T^{(c)} \rightarrow p_T^{(e)}$ and (right) $\boldsymbol{M}^{(\boldsymbol{D})} : p_T^{(c)} \rightarrow \mathrm{DCA}^{(e)}$ for electrons from the decay of open charm hadrons. The intensity of the color scale corresponds to the probability that a charmed hadron at $p_T^{(c)}$ will decay to an electron of $p_T^{(e)}$ and $\mathrm{DCA}^{(e)}$. Figure reproduced from [29].

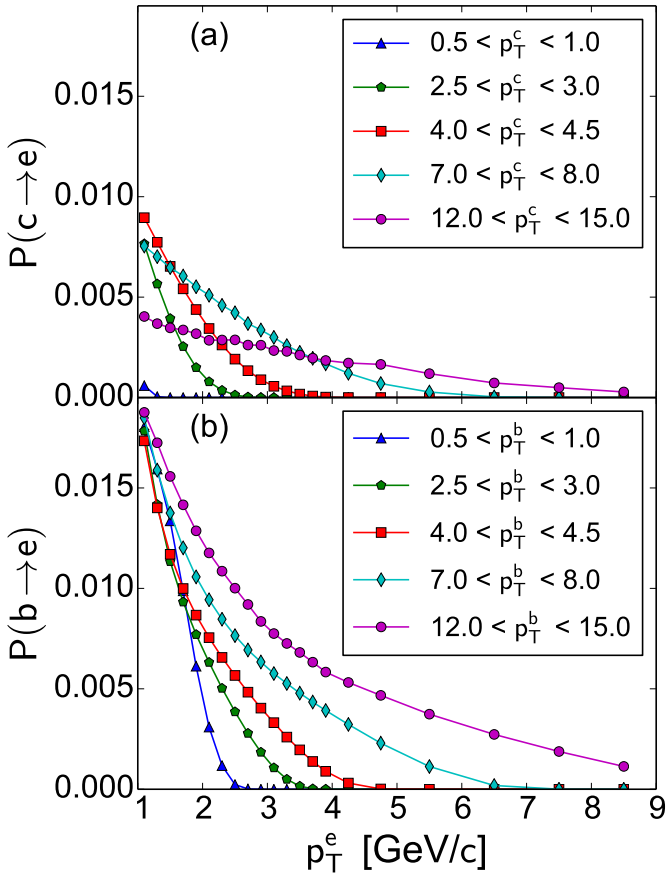

Figure 7.37: Probability of a charm (top) and bottom (bottom) hadron in a given $p_T^{(h)}$ bin to decay to an electron with a given $p_T^{(e)}$ at midrapidity $|\eta| < 0.35$. Figure reproduced from [29].

7.9.3 Sampling the Posterior Probability Distribution

As previously stated, the posterior $P(\boldsymbol{x} \mid \boldsymbol{\theta})$ is a distribution encoding the probability that the data $\boldsymbol{x}$ are explained by a set of model parameters $\boldsymbol{\theta}$. Although the prior and likelihood are well known, it is impossible to determine the shape of the distribution a priori. A naïve way of determining its (multidimensonal) shape is to randomly draw samples *uniformly* from the parameter space, evaluating the posterior at each point; ideally, one should arrive at a good approximation of the shape after enough samples have been drawn. This Monte Carlo approach, while straightforward, is extremely inefficient and impractical due to the very large dimensionality of the parameter space. Thus, the problem of estimating the shape of the posterior becomes that of finding a way of

sampling elements in the parameter space, such that the probability of drawing $\boldsymbol{\theta}$ is *proportional* to $P(\boldsymbol{x} \mid \boldsymbol{\theta})$. A random walk on the parameter space, guided by a Markov chain (i.e., using Markov chain Monte Carlo methods) provides a way of doing just that.

In this section, we will provide an intuitive explanation of what Markov chain Monte Carlo methods are, and how they relate to the problem at hand. More formal treatments can be found in [142]. In general terms, a Markov chain describes transitions between a series of states, where the probability of transitioning to the next state depends exclusively on the present state. If the Markov chain satisfies certain conditions (namely, if it is possible to transition from a given state to any other state), then the chain is said to have a unique stationary (or equilibrium) distribution. This means that, if left to "run" for a large enough number of steps, there will be a unique probability for the chain to arrive at any given state, regardless of its starting point. We thus seek a way of constructing a Markov chain whose stationary distribution corresponds to the posterior $P(\boldsymbol{x} \mid \boldsymbol{\theta})$. In this manner, after convergence, the output of the random walk will correspond to samples drawn from the desired distribution function.

In the unfolding problem at hand, the individual points in the 34-dimensional parameter space correspond to the states of the Markov chain. In order to approximate the posterior, it is required that successive random draws, or transitions, be "good" in the sense that they be more likely than the current state to explain the data given the prior, as quantified by evaluating the posterior. Thus, the Markov chain will, most of the time, move in the direction of more probable points, while seldom moving towards those that are unlikely. As a result, the random walk will return many more samples from high-density regions of the posterior, where the parameter that maximizes the distribution is more likely to be found. This sampling scheme will result in correlated samples, particularly if the step size is small.

The above sampling method corresponds to a qualitative description of the Metropolis-Hastings (MH) algorithm, and serves to illustrate the logic behind Markov chain Monte Carlo techniques. For the present analysis, we used a publicly available[6] variation of the conventional

[6] `http://dfm.io/emcee/current/`

MH sampler, called `emcee`. This particular sampler is special in that it is an *emsemble sampler* and it is *affine-invariant*. The word "ensemble" refers to the fact that the sampler consists of N "walkers" which explore the parameter space, allowing for more than one set of model parameters to be updated at a given step, thus introducing parallelization to the problem. On the other hand, "affine-invariant" means that the sampler is particularly good at sampling highly anisotropic distributions with a minimal number of free parameters. In general, if a distribution is significantly skewed, its associated difference of scales in different directions makes it hard to sample from unless a detailed tuning of the sampler's hyperparameters is carried out. An affine, or linear, transformation can be used to scale the distribution to make it more symmetric and thus easier to sample from. The `emcee` sampler thus uses affine transformations to generate update proposals for the Markov chain, combining information from various walkers. The result is that relevant scale differences are automatically adjusted, in a manner entirely transparent to the user. This is just a cursory description of the affine invariance of the sampler, and the reader is referred to [101] for further details.

7.9.4 Regularizing the Unfolded Solution

The Markov chain sampler described in the previous subsection looks for trial spectra driven exclusively by the maximization of the posterior probability distribution. However, this can sometimes lead to unphysical, yet mathematically valid, solutions. It is therefore necessary to introduce additional constraints on the solution, in a procedure known as *regularization*. In the analysis at hand, it is desirable to favor smoothness in the unfolded spectra. To that end, an additional term is added to the log-likelihood, as follows

$$\ln \pi(\boldsymbol{\theta}) = -\alpha^2(|\boldsymbol{L}\boldsymbol{R}_c|^2 + |\boldsymbol{L}\boldsymbol{R}_b|^2), \tag{7.22}$$

where $\boldsymbol{R}_{c,b}$ are the bin-by-bin ratios of the trial charm and bottom spectra to those in the prior, and $\boldsymbol{L}$ is a 17×17 second-order finite-difference matrix, representing a discretized version of the

second derivative operator:

$$\boldsymbol{L} = \frac{17}{2}\begin{bmatrix} -1 & 1 & & & & & & & \\ 1 & -2 & 1 & & & & & & \\ & 1 & -2 & 1 & & & & & \\ & & \ddots & \ddots & \ddots & & & & \\ & & & \ddots & \ddots & \ddots & & & \\ & & & & 1 & -2 & 1 & & \\ & & & & & 2 & -2 & 1 & \\ & & & & & & 1 & -1 \end{bmatrix}. \tag{7.23}$$

From the form of the regularization term it is clear that excessive curvature, as quantified by the second derivative of the spectra, is penalized by enhancing the log-likelihood such that the Markov chain sampler will interpret transitions to such states as unfavorable, even if the likelihood would otherwise be maximized in their direction.

The parameter α corresponds to the strength of the regularization penalty, and is a free parameter of the model. It is possible to determine the optimal value of this parameter by carrying out a scan of different values, running the unfolding procedure and calculating $\ln \pi(\boldsymbol{\theta}) - (|\boldsymbol{L}\boldsymbol{R}_c|^2 + |\boldsymbol{L}\boldsymbol{R}_b|^2)$ in each case. This quantity corresponds to the difference between the regularization penalty for a given value of alpha and that for $\alpha = 1$. Fig. 7.38 shows the result of such a scan plotted as a function of α. A maximum is reached at $\alpha = 1.0$, indicating the optimal value of the parameter. Admittedly, there is a systematic uncertainty associated with this choice of α, which is discussed further in Section 7.11.

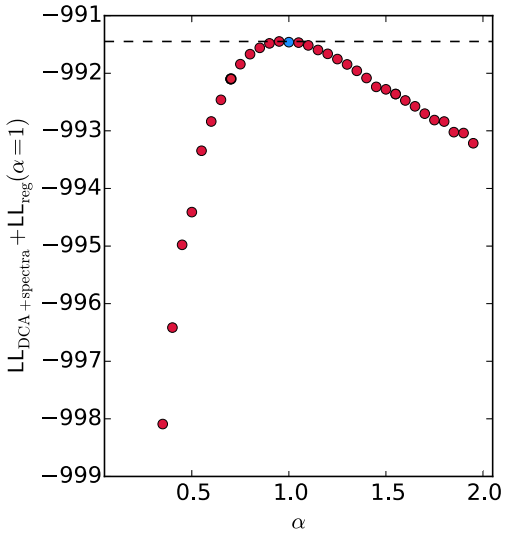

Figure 7.38: Total log-likelihood of the unfold solution as a function of the regularization strength α. The optimal value is that for which the function is maximized.

7.10 Output of the Unfolding Procedure

The result of the unfolding procedure, consisting in a large joint probability distribution for the desired model parameters, is shown in Fig. 7.39. The green (blue) area of the triangle shows the joint probability distribution for pairs of p_T bins in the same charm (bottom) heavy flavor spectrum, indicating the correlation between the two. In general, a strong positive correlation—as indicated by the positive slope of the elliptical shape—is seen between pairs of adjacent bins as a consequence of the regularization requirement of smoothness. Non-adjacent bins at intermediate p_T exhibit a modest anti-correlation. The orange region of the triangle, on the other hand, shows the corresponding correlations between pairs of p_T bins in *different* spectra. We can see that the two spectra, of charm and bottom, are largely uncorrelated except at intermediate p_T, where a strong anti-correlation is observed, reflecting how hadrons of each flavor can compensate for each other in the production of electrons in this p_T region. The zoomed distribution shows such anti-correlation, along with the individual distribution of charm and bottom yield in the $2.5 < p_T$ [GeV/c] < 3.0 bin.

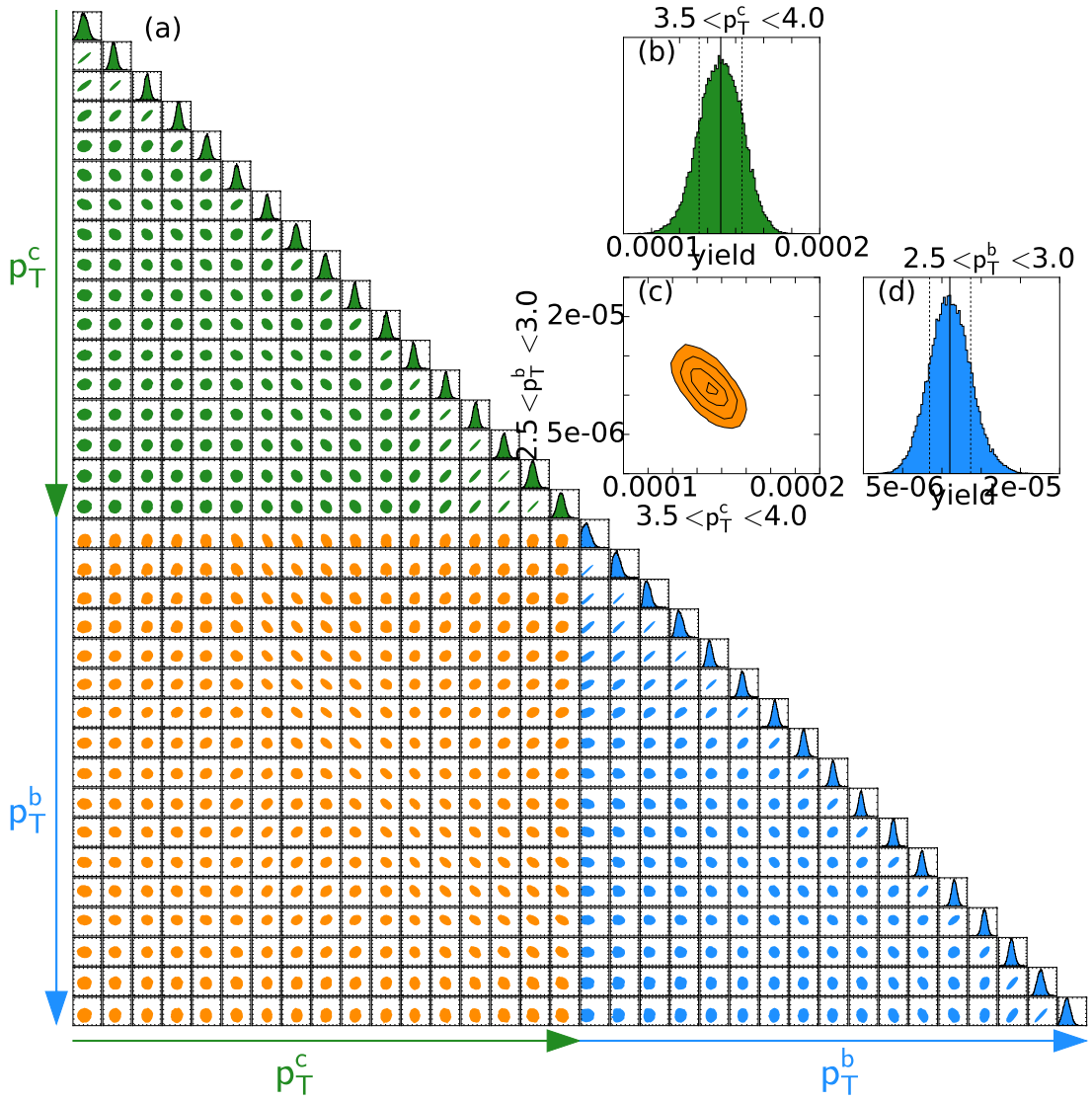

Figure 7.39: Joint probability distributions of heavy flavor hadron yields, with the marginalized distributions shown in the diagonal. The blue and green areas in the triangle display the correlation between pairs of p_T bins within the same hadron spectrum (bottom and charm, respectively). On the other hand, the orange area displays the correlations between pair of p_T bins is different spectra. The zoomed plot shows the correlations in the $2.5 < p_T$ [GeV/c] < 3.0 bin.

In order to estimate the desired model parameters it is necessary to marginalize the joint probability distribution, as shown along the diagonal of the triangle. There, an individual one-dimensional distribution is obtained for each p_T bin in the charm and bottom spectra. The value

for which a given distribution is maximized is taken as the point estimate for the yield of hadrons at that p_T bin, with the width of the distribution providing a natural metric for the associated 1σ uncertainty. Notice that some of the distributions appear truncated in the tails, particularly for bottom hadrons, as a consequence of unsampled regions in the parameter space. This poses no problem as long as the maximum of the distribution can be located. The unfolded invariant yield of charm and bottom hadrons obtained in this manner is shown in Fig. 7.40. It is important to notice that this invariant yield is not normalized per unit rapidity, but is rather reported as integrated over all rapidities as a consequence of how the decay matrix was constructed. It also follows that, like the decay matrix, these hadron invariant yields are model-dependent. Chapter 8 will discuss and interpret these results further.

Ordinarily, errors on a measurement are classified as either statistical or systematic. However, in this case, a qualification must be made: it is better to speak of "unfolding uncertainties" rather than statistical uncertainties. The data provided as input to the unfolding procedure, consisting of the measured electron track DCA_T distributions and the inclusive heavy flavor yield, carry statistical uncertainties. These are propagated through the unfolding procedure, contributing to the errors in the final result. However, the final uncertainty also has contributions from the sampling procedure itself. Due to the nature of the unfold, these uncertainties are correlated and therefore shown as a band in Fig. 7.40. The figure also contains systematic errors added in quadrature, which will be discussed in section 7.11.

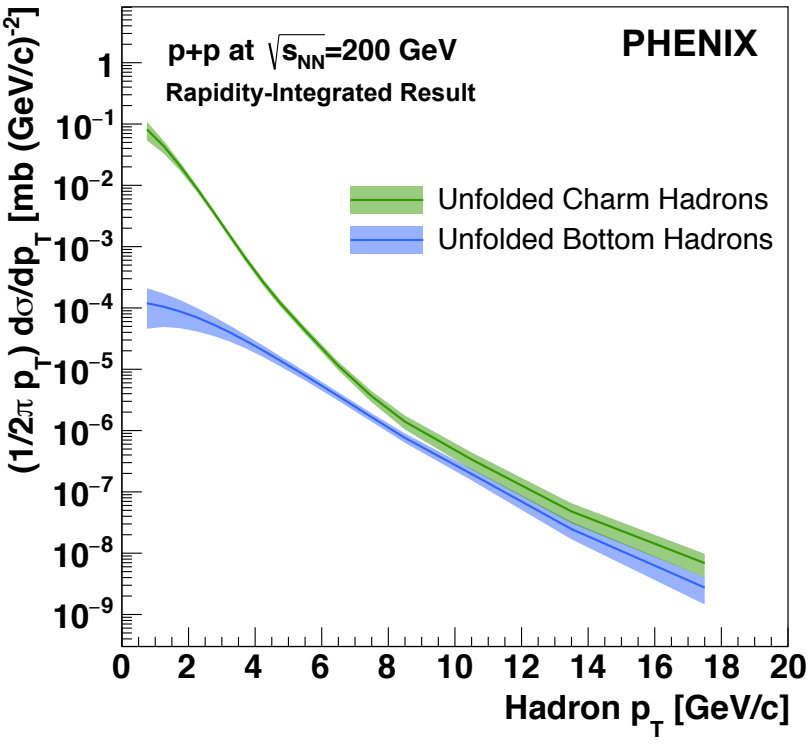

Figure 7.40: Unfolded charm and bottom hadron cross section, integrated over all rapidities, as a function of p_T. The bands represent the 1σ unfolding uncertainty, added in quadrature with systematic uncertainties. See text for details.

The quality of the unfolding procedure can be assessed by multiplying the resulting charm and bottom hadron spectra by the decay matrices, arriving at the spectra of separated heavy flavor electrons, and their DCA_T distributions. These "refolded" distributions can be directly compared to the input data used to constrain the unfolding. Fig. 7.41 shows the refolded electron spectra from charm and bottom decays. Their sum can be compared to the published inclusive spectrum. A very good agreement is observed between the two, as evidenced by the ratio plot in the bottom panel.

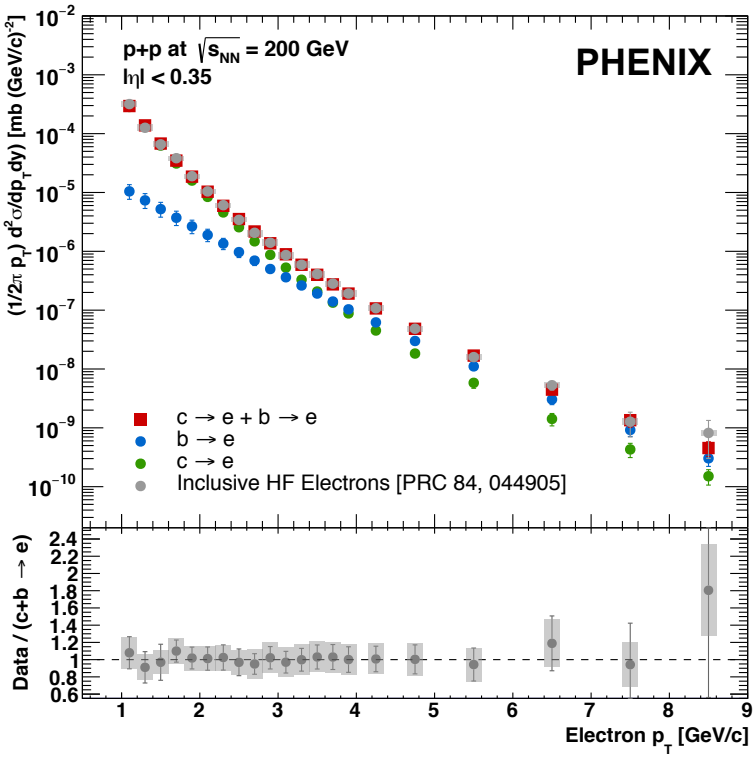

Figure 7.41: Invariant cross section of inclusive heavy flavor electrons from a previously published PHENIX result (gray) compared to the refolded charm and bottom hadron yields (shown individually in green and blue, and red when combined). The bottom panel shows the ratio of the previously published to the unfolded result.

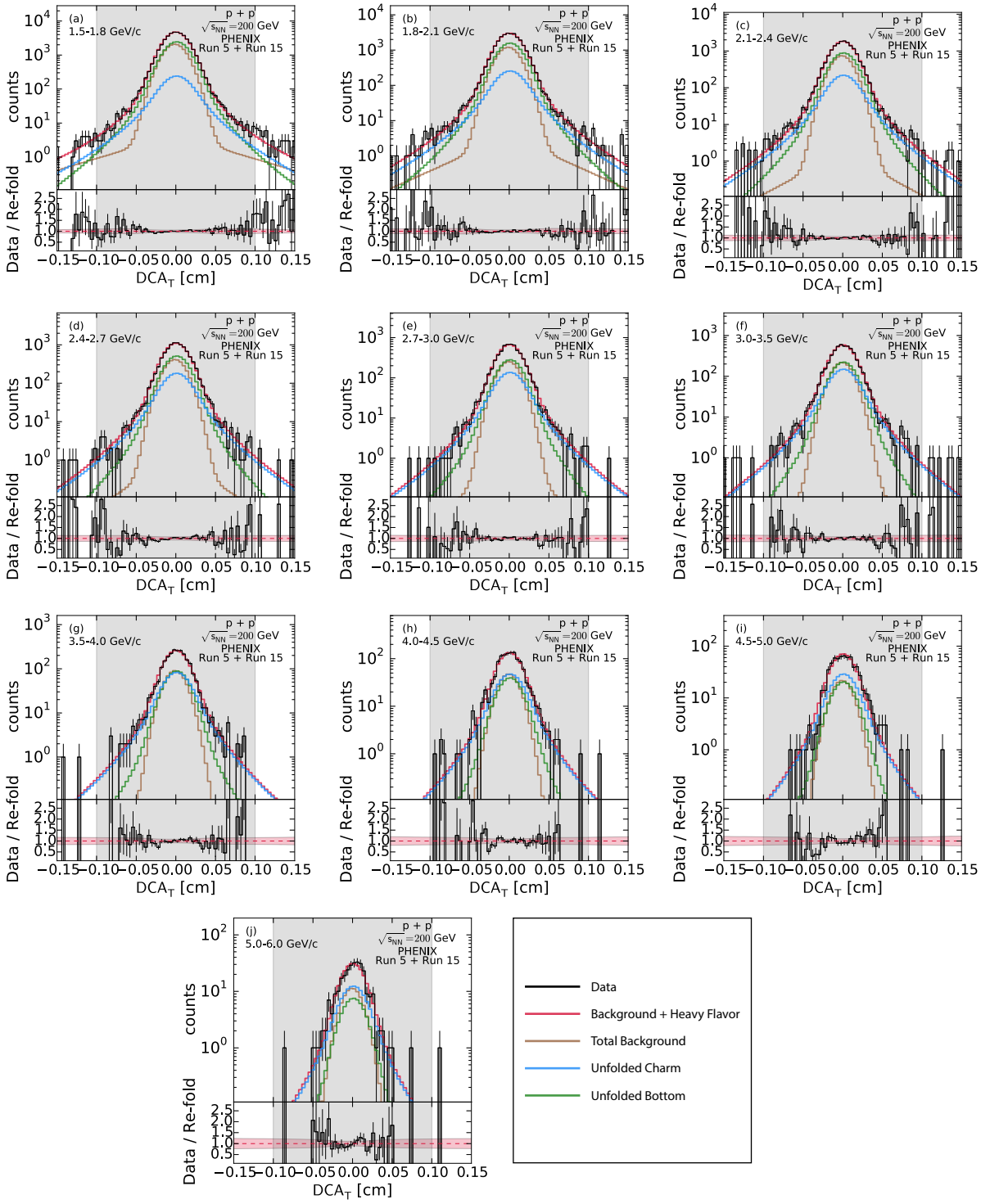

Figure 7.42: DCA_T distributions for inclusive electrons in data (black), with normalized background contributions (brown). The refolded heavy flavor DCA_T are shown for inclusive heavy flavor electrons (red), as well as separated charm (green) and bottom (blue).

Similarly, the refolded DCA_T distributions for 10 electron p_T bins between $1.5 < p_T < [\mathrm{GeV}/c] < 6.0$ are shown in Fig. 7.42. The brown curves represent to the sum of the individually normalized background sources, as calculated in section 7.8. The green and blue curves correspond to the charm and bottom contribution, respectively. Notice that the DCA_T for bottom electrons is broader than that of charm, as expected. This implies that it is the tails of the distributions, many orders of magnitude lower than the peaks, which provide the most discriminating power in the unfolding procedure. The agreement between the refolded and the measured distributions is quite good in all p_T bins, as demonstrated by the ratio in the lower panel. The gray box within $|\mathrm{DCA}_T| < 0.1$ cm indicates the region over which the DCA_T is used to constrain the unfold.

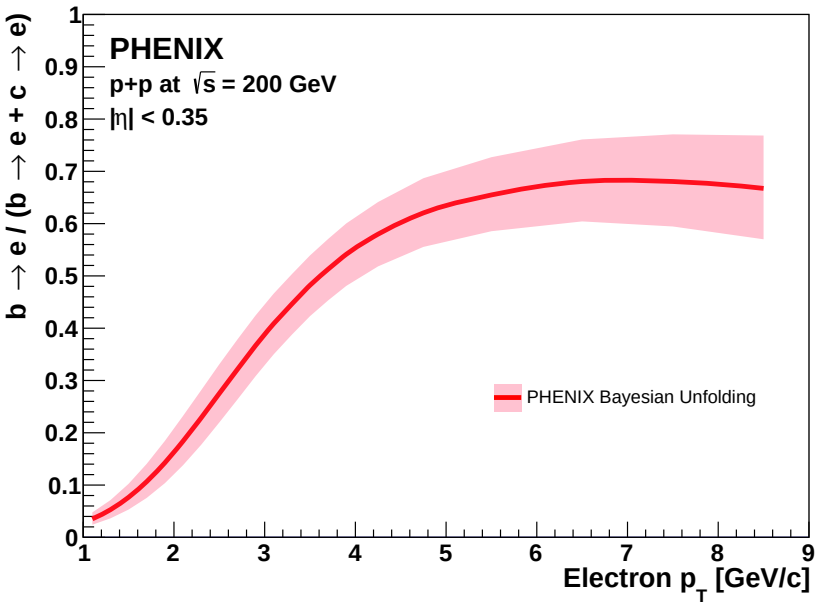

Figure 7.43: Fraction of electrons from bottom hadron decays to inclusive heavy flavor electrons at midrapidity $|\eta| < 0.35$. The band represents the total uncertainty, which includes the 1σ unfold uncertainty, as well as systematic uncertainties.

The refolded electrons can be used to compute the fraction of electrons from bottom relative to inclusive heavy flavor decays at midrapidity $|\eta| < 0.35$, where electrons from the feed-down

decay $b \to c \to e$ are treated as part of the bottom electron sample. The bottom fraction is shown as a red curve in Fig. 7.43, with systematic and non-systematic uncertainties added in quadrature. The contribution of bottom decay electrons rises quickly with p_T from approximately 5% at $p_T = 1$ GeV, to dominate over charm electrons above $p_T \approx 4$ GeV. Again, a full discussion of these results is presented in Chapter 8.

7.11 Systematic Uncertainties

The systematic uncertainties on the unfolded result originate from the following sources:

(1) The normalization of electrons from individual background sources in the construction of the electron cocktail.

(2) The choice of the regularization strength α in the unfolding procedure.

(3) The propagation of the systematic uncertainty on the inclusive heavy flavor electron yield.

(4) The choice of prior used in the unfolding.

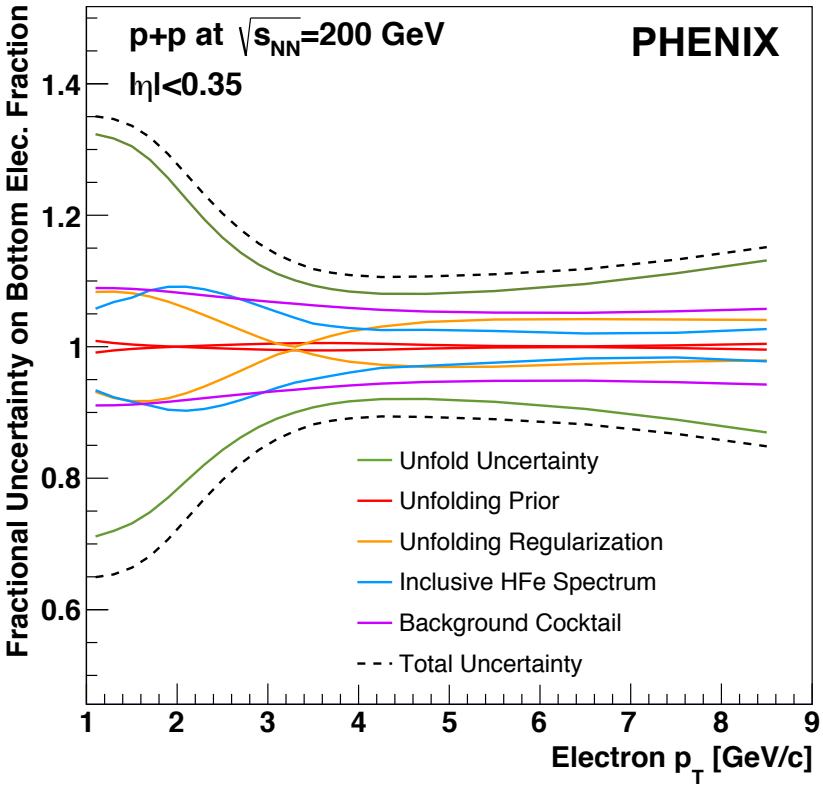

Figure 7.44: Fractional uncertainty from each source of errors on the unfolded bottom electron fraction.

The fractional contributions of each of these sources to the total error on the unfolded bottom fraction, along with that of the unfolding uncertainty, are shown in Fig. 7.44. Notice how the unfolding uncertainty dominates the total uncertainty across p_T, being significantly larger below $p_T \approx 3$ GeV/c. Such large contribution at low p_T has been identified as arising from the uncertainty on the heavy flavor invariant yield used as input for the unfolding procedure. The unfolding uncertainty also increases at high p_T owing to the lack of electron DCA_T constraint for $p_T > 6$ GeV/c. We now turn our attention to each individual source of systematic uncertainty.

7.11.1 Uncertainty from Background Electron Normalization

The dominant source of systematic uncertainty originates from the fits used to parameterize the production cross section of primary particles in the background electron cocktail. To estimate

it, individual points in the published primary particle cross section were randomly varied within the bounds of their own statistical and systematic uncertainties. The procedure was carried out 1000 times, fitting the deformed cross section at each step. As illustration, Fig. 7.45 shows the "nominal" fit to the J/ψ cross section (in red), along with the family of fits (in blue) obtained when carrying out the randomization procedure. The spread of the family of fits around the nominal value was quantified by their RMS value. As a function of p_T, Fig. 7.46 shows the extent of the RMS deviation for every primary particle species in the cocktail, except for direct photons. As expected, the uncertainties are observed to be significant in regions where the fit is not constrained by data, particularly at low p_T for all species, and at high p_T for species—such as J/ψ and $K^{\pm}$— whose cross section measurements have a limited reach in p_T. The case of the direct photon cross section is special; no randomization of the data points was carried out in that case. Instead, a constant systematic uncertainty of 50% was assigned to the parameterization of that particular primary particle cross section.

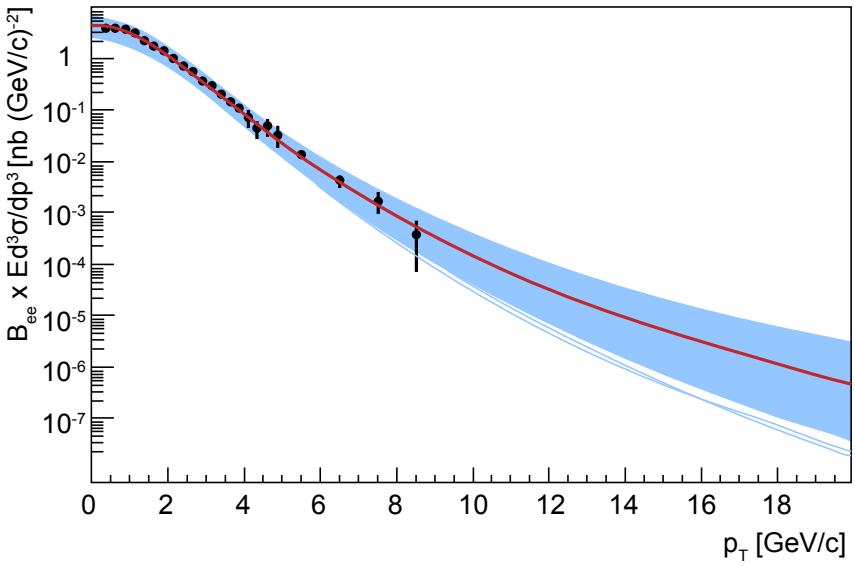

Figure 7.45: Nominal parameterization of the J/ψ cross section (red), along with 1000 variations (blue) obtained by fitting the spectrum when randomizing the data points within the bounds of their respective statistical and systematic uncertainties.

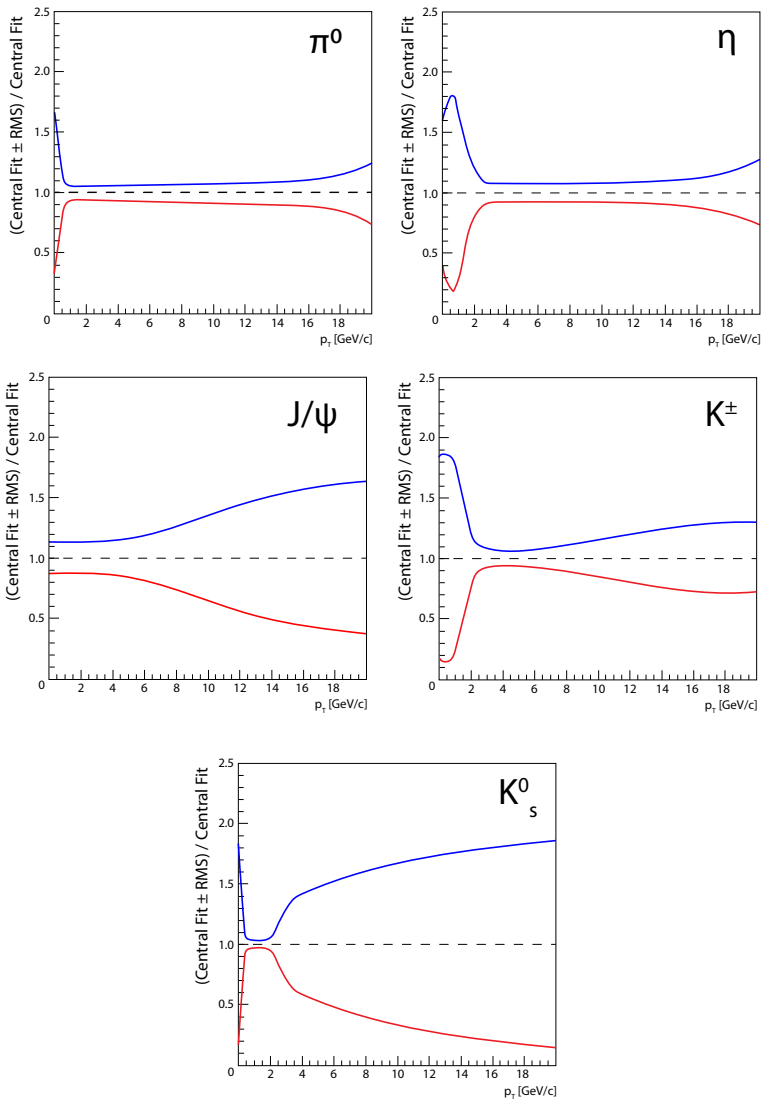

Figure 7.46: Systematic uncertainty associated with the parameterization of each primary particle production cross section. See text for details on how this quantity is calculated.

7.11.2 Uncertainty from Choice of Regularization Strength

Section 7.9.4 discussed how the strength α of the regularization term in the log-likelihood is tuned by running the unfolding procedure repeatedly, scanning over a wide range of parameter values in search of the one that maximizes the difference between the regularization penalty for a given value of alpha and that of $\alpha = 1$. The result of the scan is shown in Fig. 7.38. We assign a

systematic uncertainty to this determination of the optimal parameter by selecting the two values of α for which there is a reduction of 0.5 in the total log-likelihood. It can be shown that a change of half a unit in the log-likelihood corresponds to a 1σ variation in the underlying variable.

7.11.3 Uncertainty from Inclusive Heavy Flavor Electron Yield

The systematic uncertainty on the published spectrum of heavy flavor electrons is point-to-point correlated in p_T. Since the covariance matrix describing such correlations is not available and cannot be constructed for a previously published measurement, we carry out a series of operations to deform the spectrum by the extent allowed by its systematics. First, the spectrum is tilted (counter)clockwise by 1σ about pivot points at $p_T = 1.8$ GeV/c and $p_T = 5$ GeV/c, such that points on opposite sides of the pivot go (up)down by a fraction of their systematic uncertainty. Then, in another operation, the spectrum is folded, or "kinked", about those same points to introduce a wedge-shaped deformation. Fig. 7.47 shows an example of the resulting spectrum when it is tilted about $p_T = 5$ GeV/c; the bottom panel shows the ratio of the modified to the nominal spectrum. Various combinations of these tilting and kinking operations yield 8 different variations of the spectrum. The two that deviate the most from the nominal spectrum are selected and propagated through the unfolding, where the change in the refolded electrons constitutes the estimate of the systematic uncertainty.

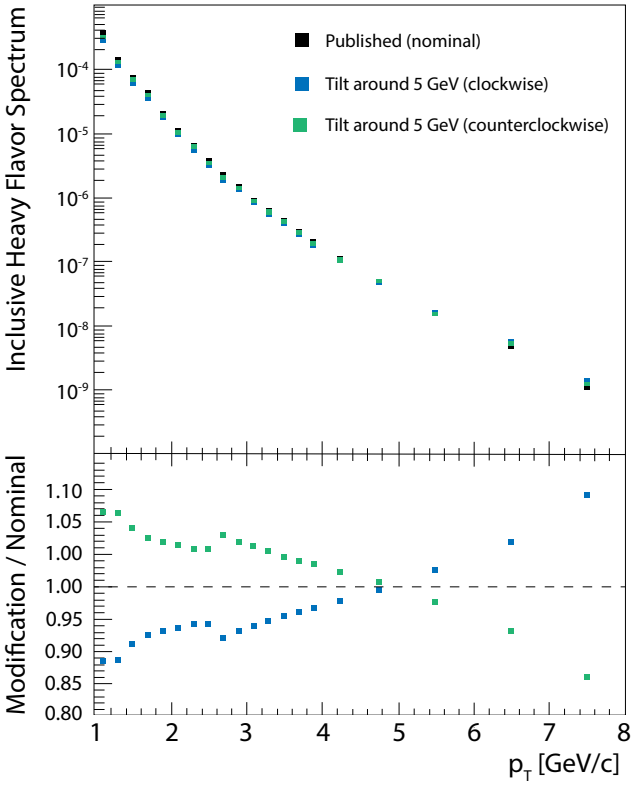

Figure 7.47: Deformation of the inclusive heavy flavor electron spectrum by tilting about a given pivot point. The ratio of the deformations to the unmodified spectrum are shown in the bottom panel.

7.11.4 Uncertainty from Choice of Unfolding Prior

In Bayesian statistics, the prior quantifies the analyzer's belief about the true model parameters before taking any actual data into consideration. In this analysis, the choice of prior serves two purposes. First, the shape of the posterior in Bayes' theorem, while driven largely by the likelihood, depends also on the prior. Second, the prior serves as the starting point of the Markov chain Monte Carlo sampler. In order for the unfolding procedure to converge correctly, it is important that the prior be well-motivated in terms of its physical content. Therefore, by default, it is taken to be the yield of charm and bottom hadrons as predicted by the PYTHIA generator. To evaluate the systematic associated with selecting a different prior, we scale the PYTHIA yields by a modified blast

wave function, as described in Ref. [30]. Admittedly, the hydrodynamics-inspired blast wave model is meant to be applied in A+A collisions; however, here we are not interested in physics it may encapsulate, but in examining the change in the unfolded result when changing the prior. From Fig. 7.44 it is seen that the choice of prior has the smallest effect of all systematic uncertainties, as expected.

Chapter 8

Results of the Heavy Flavor Separation Analysis

Chapter 7 described in detail the analysis carried out to separately measure the production of electrons from charm and bottom hadron decays in $p+p$ collisions. In brief, the distance of closest approach to the beam center was measured for candidate electron tracks using the PHENIX silicon tracker. This observable, along with the published invariant yield of heavy flavor electrons, was used to constrain an unfolding procedure based on a decay model of heavy flavor hadrons, allowing the independent production of charm and bottom to be statistically inferred. The current chapter will summarize and discuss the results of this analysis.

8.1 Separated Heavy Flavor Hadron Cross Sections

As discussed in Section 7.9, the unfolding procedure explores a 34-dimensional parameter space to find the most likely charm and bottom hadron spectra that explain the measured heavy flavor electron data, constructing the associated probability distribution in the process. The joint and marginal probability distributions shown in Fig. 7.39 (i.e., the large "triangle plot") encapsulate all the knowledge gained from the unfolding, providing a distribution for the value of each bin in the heavy flavor spectra, as well as the correlations among them.

Fig. 8.1 distills the triangle plot, showing the spectra of charm and bottom hadrons, corresponding to the values which maximize the probability distributions for each p_T bin. The decay matrix used in the unfolding procedure is normalized in such a way that a given bin contains the probability that a heavy flavor hadron at any rapidity produce an electron within the PHENIX

central arm acceptance. As a result, the spectra in Fig. 8.1 correspond by construction to the production of heavy flavor hadrons integrated over all rapidites. Given that the decay matrix was constructed using the PYTHIA generator, the unfolded heavy flavor hadron spectra are necessarily model-dependent quantities. In particular, they follow the rapidity distribution of heavy flavor in PYTHIA, as arising from the LO+LL QCD processes and the parton distribution functions implemented in the generator.

Additionally, the PYTHIA generator makes assumptions concerning the relative production of various heavy flavor species, as quantified by the ratios of mesons to baryons—which, in any case, are not fully constrained by data in $p + p$ collisions. In the heavy flavor electron separation analysis in Au+Au [29]—where clear baryon-to-meson enhancements arise as a final-state effect—the baryon-to-meson ratios in PYTHIA were systematically varied, leading to small changes within uncertainties in the final result.

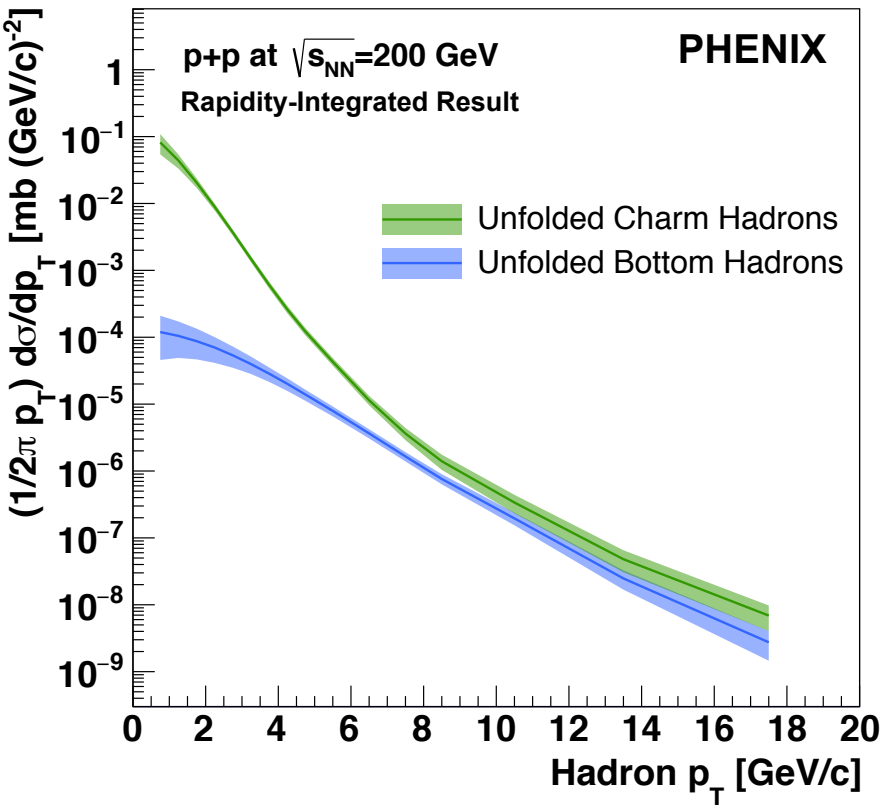

Figure 8.1: Unfolded charm and bottom hadron cross sections, integrated over all rapidities, as a function of p_T. The bands correspond to the correlated 1σ uncertainties from the unfolding procedure, added in quadrature with the systematic uncertainties.

As a check on the unfolding procedure, it is possible to use PYTHIA to derive the spectra of individual hadron species at midrapidity from the unfolded result. For instance, the ratio of the D^0 at midrapidity $|y| < 1$ to inclusive charm production can be calculated in PYTHIA as a function of p_T. Multiplying the charm spectrum in Fig. 8.1 by this ratio yields a *model-dependent* measurement of the D^0 spectrum, as shown in Fig. 8.2, compared to a corresponding measurement by the STAR collaboration [13]. The PHENIX result is fit with a modified Hagedorn functional form, with the ratios of the points to the fit shown in the bottom panel, demonstrating good agreement between the two measurements within uncertainties.

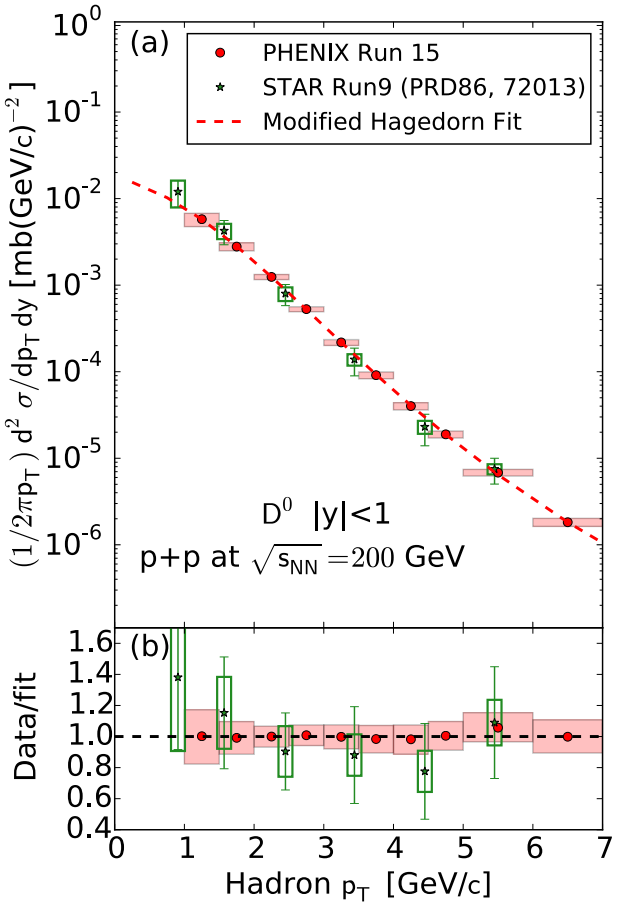

Figure 8.2: Invariant yield of D^0 mesons at midrapidity $|y| < 1$, as calculated from the rapidity-integrated charm yield in Fig. 8.1. The result is fit with a modified Hagedorn function and compared to a measurement made by the STAR collaboration [13]. The STAR measurement includes both statistical (lines) and systematic (boxes) errors. The unfolded PHENIX points include the uncertainties arising from the unfolding procedure, as well as systematic uncertainties.

It is important to notice, however, that the comparison in Fig. 8.2 is model-dependent, and that the errors shown on the D^0 spectrum do not account for this dependence. Instead, rather than provide a measurement of D^0 production, the comparison with the STAR result is intended to serve as a check on the unfolding procedure at the hadron level. Had the comparison been unsuccessful, a closer investigation of the model dependence of the unfolding decay matrix would have been warranted.

8.2 Separated Heavy Flavor Electron Cross Sections

Fig. 8.3 shows the invariant cross sections of charm and bottom decay electrons at midrapidity, which follow directly from the rapidity-integrated hadron yields through an application of the decay matrix. For ease of visualization, the bottom electron cross section has been scaled down by a factor of 10^2. The cross sections are compared to a FONLL pQCD calculation [71, 68], shown as bands reflecting uncertainties in the quark masses and renormalization scales. The charm electron spectrum is consistent with FONLL within uncertainties. The observation that, at low p_T, the measurement seems close to the upper edge of the FONLL band is consistent with other charm production measurements (see, for example, Fig. 5.7). The bottom electron spectrum, however, is undepredicted by the calculation, particularly for $p_T < 5$ GeV/c. Above that point, the measurement and calculation agree within uncertainties. Notice also that agreement with FONLL improves with increasing p_T, particularly for charm electrons. This is to be expected, as the calculation is less sensitive to the quark masses in this kinematic region.

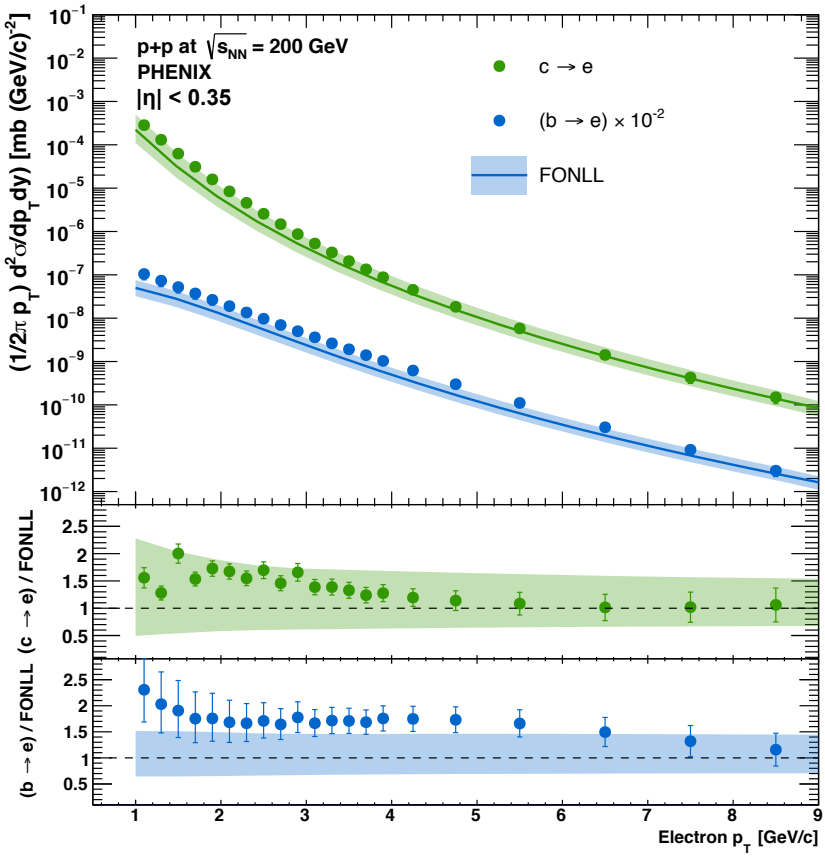

Figure 8.3: Refolded cross section of charm and bottom electrons compared to FONLL calculations. Notice that the bottom electron curves have been scaled down by a factor of 100 for ease of visualization. FONLL uncertainties account for uncertainties in the quark masses and renormalization scales.

Having obtained the individual charm and bottom electron spectra, it is of interest to examine their relative contribution to the total heavy flavor electron production. To that end, the bottom electron fraction $b \to e/(c \to e + b \to e)$ is calculated, as shown in Fig. 8.4. At low p_T, it is possible to see that heavy flavor electron production is dominated by charm decays, with the contribution of bottom decays rising sharply with p_T. Eventually, at $p_T \approx 4$ GeV/c, both flavors contribute equally to electron production, with bottom electrons dominating at higher p_T. The figure also shows that the unfolded bottom fraction is consistent with FONLL [71, 68] within the large uncertainties of the calculation, with particularly good agreement observed below $p_T = 3$ GeV/c.

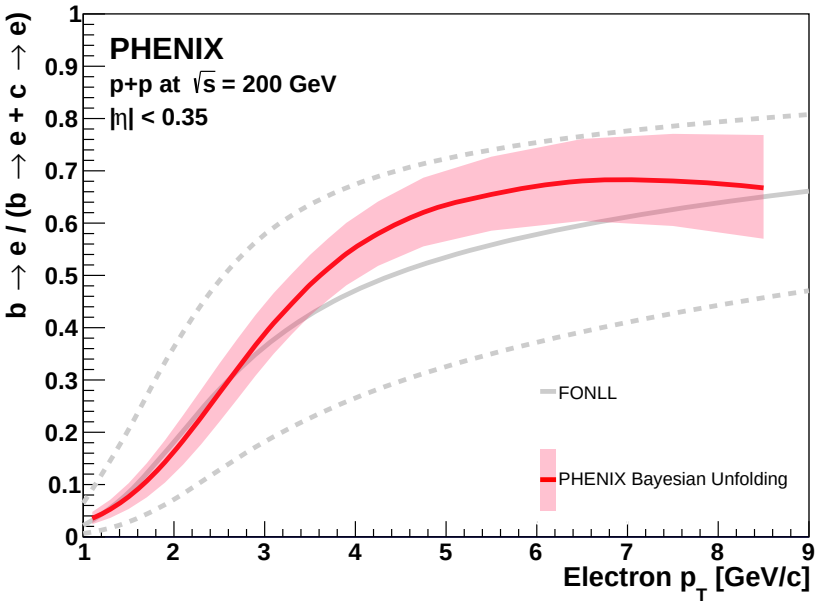

Figure 8.4: Fraction of electrons from bottom hadron decays to inclusive heavy flavor electrons at midrapidity $|\eta| < 0.35$. The red curve corresponds to the bottom fraction obtained from the unfolding procedure, with the surrounding band indicating the total uncertainty, accounting for intrinsic unfolding and systematic errors. A comparison is made to a FONLL pQCD calculation, where the outer bands represent the uncertainty on the central value from uncertainties on the quark masses and renormalization scales.

Since the principal motivation behind the analysis at hand is to provide an updated baseline of charm and bottom electron production in $p+p$ to be used in measurements made in nucleus-nucleus collisions, it is appropriate to quantify the extent to which the results at hand constitute an improvement over the baseline used in obtaining the heavy flavor R_{AA} shown in Fig. 5.15. Prior to the displaced vertex analysis presented in this dissertation, the only comparable measurements available in $p+p$ at RHIC energies were the electron-hadron correlation results described in section 5.1.1, from both PHENIX [17] and STAR [37]. Fig. 8.5 shows a comparison of those results with the bottom fraction obtained via unfolding. It is immediately striking that the unfolded result has significantly smaller total uncertainties than the correlation measurements. Furthermore, while

the correlation measurements provide a limited number of data points between $3 < p_T$ [GeV/c] < 8, the unfolded result has an extended kinematic reach covering $1 < p_T$ [GeV/c] < 8.5. It is therefore apparent that this new measurement provides not only an improved baseline for heavy-ion measurements, but also a valuable benchmark for pQCD calculations, which is another motivation to carry out precision heavy flavor measurements in elementary $p + p$ collisions.

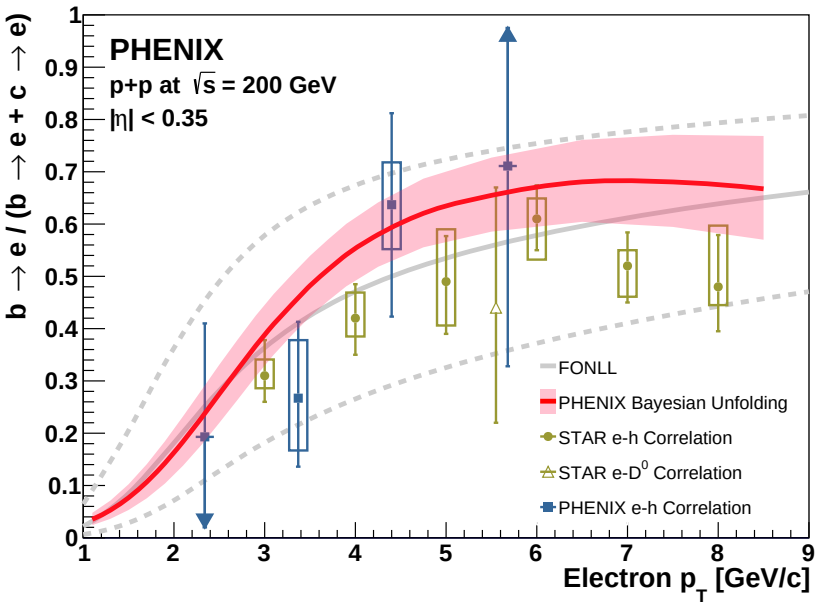

Figure 8.5: Fraction of electrons from bottom hadron decays to inclusive heavy flavor electrons at midrapidity $|\eta| < 0.35$. The red curve corresponds to the bottom fraction obtained from the unfolding procedure, with the surrounding band indicating the total uncertainty, accouting for intrinsic unfolding and systematic errors. A comparison is made to a FONLL pQCD calculation, where the outer bands represent the uncertainty on the central value from uncertainties on the quark masses and renormalization scales. Also shown are previous electron-hadron correlation measurements by PHENIX [17] and STAR [37].

Of the correlation measurements, the PHENIX result exhibits the largest uncertainties which cover the new unfolded bottom electron fraction. On the other hand, the two STAR measurements,

from electron-hadron and electron-D^0 correlations, agree with the unfolded result within their own large total uncertainties, with central values that visually appear to be distinctly lower. In order to quantify the statistical consistency of the unfolded curve and the STAR electron-hadron points, a hypothesis test was carried out under the null hypothesis that the two results are identical. Assuming Gaussian errors on both results, the following modified two-sample chi-square statistic was constructed

$$\tilde{\chi}^2 = \sigma_\epsilon + \sum_{i=1}^{N} \frac{(A_i - B_i')^2}{\sigma_{A_i}^2}. \tag{8.1}$$

In the above equation, the sum runs over the number of points in the STAR measurement. A_i is a sample drawn from a Gaussian centered on the i^{th} STAR point, of width equal to the point's *statistical* error; B_i' is the value of the unfolded bottom fraction at the p_T of the i^{th} STAR point, modified by a fixed fraction σ_ϵ of the curve's total uncertainty. This fraction is the same for all i, since the errors on the unfold result are correlated. The modified statistic is sampled repeatedly to construct its distribution. The p-value for the observed difference between the two measurements is then found to be 0.003. Under this conservative estimate, using only the statistical error on the STAR result, the null hypothesis must be rejected. However, when the systematic errors are considered, the p-value increases to 0.15, such that the null hypothesis can no longer be rejected. The conclusion is that the two measurements are indeed consistent owing to the large systematic uncertainty on the STAR result.

In terms of physics impact, the unfolded bottom electron fraction in $p+p$ shown in Fig. 8.5 demonstrates conclusively, with small uncertainties, that at high p_T open heavy flavor production is dominated by bottom quarks. Being more massive than charm quarks, their energy loss from gluon radiation is strongly suppressed due to the dead cone effect [86], as previously discussed in Section 5.2. Under the resulting mass hierarchy of radiative energy loss, the comparable suppression of heavy flavor electrons and light hadrons at high p_T, shown in Fig. 8.6, is reaffirmed as a puzzling observation.

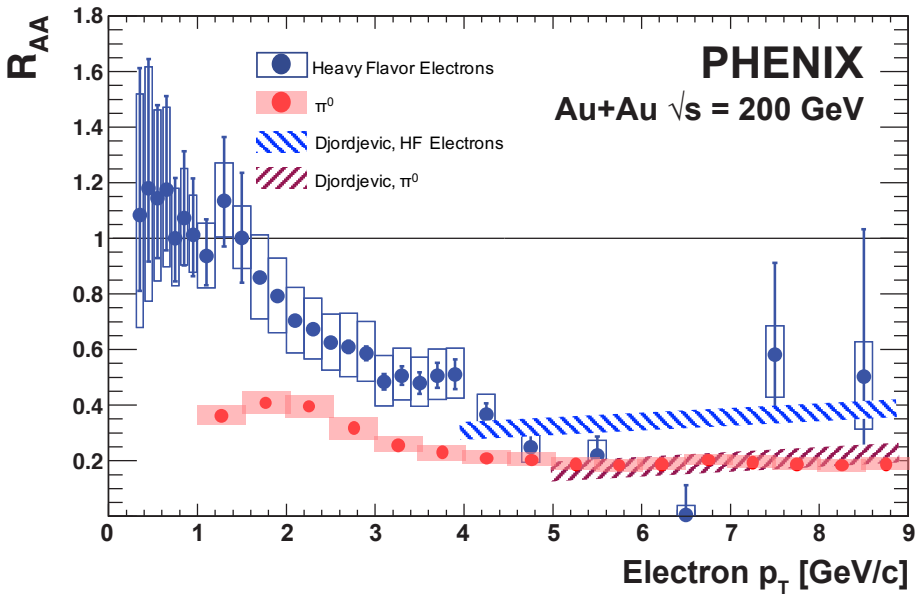

Figure 8.6: Nuclear modification factor R_{AA} of combined heavy flavor electrons and neutral pions, as measured by PHENIX in Au+Au collisions. The theory calculation by M. Djordjevic incorporates both collisional and radiative energy loss mechanisms in the context of a dynamical picture of scattering center [85].

It has been known for some time that radiative energy loss alone is insufficient to account for the comparable suppression of light and heavy quarks. In fact, the contribution of collisional mechanisms to total energy loss has been shown to be about as large as that of gluon radiation [149], with modern models of energy loss incorporating both mechanisms [84, 199]. However, problems exist with traditional models of radiative energy loss which assume static scattering centers, since this assumption necessarily leads to vanishing energy loss through collisional mechanisms. State-of-the-art calculations [85] reconcile both energy loss mechanisms in the context of a finite-size dynamical picture, where the constituents of the QGP medium are modeled as moving particles. Fig. 8.6 shows R_{AA} calculations by M. Djordjevic using such an approach with a number of further refinements including the effects of finite magnetic mass and a running coupling. This unified framework leads to a good description of the strong suppression of light hadrons, as well as of

heavy flavor electrons within the large uncertainties of the data points at high p_T.

Further insight and constraint for future theoretical calculations can be gained by separating the inclusive heavy flavor R_{AA} into independent measurements for charm and bottom electrons, since the mass difference between the two quark flavors can be leveraged to provide insight into the interplay of radiative and collisional energy loss. The first such measurement of separated charm and bottom electron R_{AA}, carried out by the PHENIX experiment, was done with the Au+Au data set recorded in the RHIC 2011 run period, with the results shown in Fig. 5.15. The large uncertainties, which prevent drawing strong conclusions, can be alleviated by (i) repeating the measurement with a larger Au+Au dataset, and (ii) using the result presented in this dissertation as a baseline. The PHENIX collaboration has made progress towards an updated separated heavy flavor electron R_{AA} [150, 100] using the Au+Au dataset recorded in 2014, which is 20 times larger than that of 2011, allowing for the centrality dependence of the R_{AA} to be measured. Forthcoming results will additionally incorporate the updated baseline measurement, promising to shed light on the relative suppression of bottom and charm quarks in the QGP.

Bibliography

[1] Morad Aaboud et al. Measurements of long-range azimuthal anisotropies and associated Fourier coefficients for *pp* collisions at $\sqrt{s} = 5.02$ and 13 TeV and p+Pb collisions at $\sqrt{s_{\rm NN}} =$ 5.02 TeV with the ATLAS detector. Phys. Rev., C96(2):024908, 2017.

[2] Georges Aad et al. Measurements of the electron and muon inclusive cross-sections in proton-proton collisions at $\sqrt{s} = 7$ TeV with the ATLAS detector. Phys. Lett., B707:438–458, 2012.

[3] Georges Aad et al. Measurement of the differential cross-section of B^+ meson production in pp collisions at $\sqrt{s} = 7$ TeV at ATLAS. JHEP, 10:042, 2013.

[4] Georges Aad et al. Observation of Associated Near-Side and Away-Side Long-Range Correlations in $\sqrt{s_{NN}}$=5.02TeV Proton-Lead Collisions with the ATLAS Detector. Phys. Rev. Lett., 110(18):182302, 2013.

[5] Georges Aad et al. Observation of Long-Range Elliptic Azimuthal Anisotropies in $\sqrt{s}$ =13 and 2.76 TeV *pp* Collisions with the ATLAS Detector. Phys. Rev. Lett., 116(17):172301, 2016.

[6] G. Abbiendi et al. Scaling violations of quark and gluon jet fragmentation functions in e+ e- annihilations at $\sqrt{s} = 91.2$ GeV and 183 GeV to 209-GeV. Eur. Phys. J., C37(1):25–47, 2004.

[7] Betty Abelev et al. Heavy flavour decay muon production at forward rapidity in protonproton collisions at $\sqrt{s} = 7$ TeV. Phys. Lett., B708:265–275, 2012.

[8] Betty Abelev et al. Measurement of electrons from semileptonic heavy-flavour hadron decays in pp collisions at $\sqrt{s} = 7$ TeV. Phys. Rev., D86:112007, 2012.

[9] Betty Abelev et al. Long-range angular correlations on the near and away side in p-Pb collisions at $\sqrt{s_{NN}} = 5.02$ TeV. Phys. Lett., B719:29–41, 2013.

[10] Betty Bezverkhny Abelev et al. Measurement of electrons from semileptonic heavy-flavor hadron decays in *pp* collisions at $\sqrt{s} = 2.76$ TeV. Phys. Rev., D91(1):012001, 2015.

[11] Jaroslav Adam et al. Centrality dependence of particle production in p-Pb collisions at $\sqrt{s_{\rm NN}}$= 5.02 TeV. Phys. Rev., C91(6):064905, 2015.

[12] L. Adamczyk et al. Inclusive charged hadron elliptic flow in Au + Au collisions at $\sqrt{s_{NN}} =$ 7.7 - 39 GeV. Phys. Rev., C86:054908, 2012.

[13] L. Adamczyk et al. Measurements of D^0 and D^* Production in $p+p$ Collisions at $\sqrt{s} = 200$ GeV. Phys. Rev., D86:072013, 2012.

[14] L. Adamczyk et al. Observation of D^0 Meson Nuclear Modifications in Au+Au Collisions at $\sqrt{s_{NN}} = 200$GeV. Phys. Rev. Lett., 113(14):142301, 2014.

[15] A. Adare et al. Energy Loss and Flow of Heavy Quarks in Au+Au Collisions at $\sqrt{s_{NN}} =$ 200-GeV. Phys. Rev. Lett., 98:172301, 2007.

[16] A. Adare et al. Inclusive cross-section and double helicity asymmetry for pi0 production in p + p collisions at $\sqrt{s_{NN}} = 200$-GeV: Implications for the polarized gluon distribution in the proton. Phys. Rev., D76:051106, 2007.

[17] A. Adare et al. Measurement of Bottom versus Charm as a Function of Transverse Momentum with Electron-Hadron Correlations in p^+p Collisions at $\sqrt{s} = 200$ GeV. Phys. Rev. Lett., 103:082002, 2009.

[18] A. Adare et al. Enhanced production of direct photons in Au+Au collisions at $\sqrt{s_{NN}} = 200$ GeV and implications for the initial temperature. Phys. Rev. Lett., 104:132301, 2010.

[19] A. Adare et al. Cross section and double helicity asymmetry for η mesons and their comparison to neutral pion production in p+p collisions at $\sqrt{s} = 200$ GeV. Phys. Rev., D83:032001, 2011.

[20] A. Adare et al. Heavy Quark Production in $p+p$ and Energy Loss and Flow of Heavy Quarks in Au+Au Collisions at $\sqrt{s_{NN}} = 200$ GeV. Phys. Rev., C84:044905, 2011.

[21] A. Adare et al. Identified charged hadron production in $p+p$ collisions at $\sqrt{s} = 200$ and 62.4 GeV. Phys. Rev., C83:064903, 2011.

[22] A. Adare et al. Measurement of neutral mesons in $p + p$ collisions at $\sqrt{s}$= 200 GeV and scaling properties of hadron production. Phys. Rev., D83:052004, 2011.

[23] A. Adare et al. Ground and excited charmonium state production in $p + p$ collisions at $\sqrt{s} = 200$ GeV. Phys. Rev., D85:092004, 2012.

[24] A. Adare et al. Quadrupole Anisotropy in Dihadron Azimuthal Correlations in Central d+Au Collisions at $\sqrt{s_{NN}}$=200 GeV. Phys. Rev. Lett., 111(21):212301, 2013.

[25] A. Adare et al. Centrality categorization for $R_{p(d)+A}$ in high-energy collisions. Phys. Rev., C90(3):034902, 2014.

[26] A. Adare et al. Measurement of long-range angular correlation and quadrupole anisotropy of pions and (anti)protons in central d+Au collisions at $\sqrt{s_{NN}}$=200 GeV. Phys. Rev. Lett., 114(19):192301, 2015.

[27] A. Adare et al. Measurements of elliptic and triangular flow in high-multiplicity ^{3}He+Au collisions at $\sqrt{s_{NN}} = 200$ GeV. Phys. Rev. Lett., 115(14):142301, 2015.

[28] A. Adare et al. An Upgrade Proposal from the PHENIX Collaboration. 2015 arXiv:1501.06197.

[29] A. Adare et al. Single electron yields from semileptonic charm and bottom hadron decays in Au+Au collisions at $\sqrt{s_{NN}} = 200$ GeV. Phys. Rev., C93(3):034904, 2016.

[30] Andrew M. Adare, Michael P. McCumber, James L. Nagle, and Paul Romatschke. Examination whether heavy quarks carry information on the early-time coupling of the quark-gluon plasma. Phys. Rev., C90(2):024911, 2014.

[31] K. Adcox et al. Flow measurements via two particle azimuthal correlations in Au+Au collisions at $\sqrt{s_{NN}}$ = 130-GeV. Phys. Rev. Lett., 89:212301, 2002.

[32] P. A. R. Ade et al. Planck 2015 results. XIII. Cosmological parameters. Astron. Astrophys., 594:A13, 2016.

[33] Ronald J. Adler, T. K. Das, and Alvaro Ferraz Filho. Analytic wave function for the deuteron d state. Phys. Rev. C, 16:1231–1234, Sep 1977.

[34] S. S. Adler et al. Measurement of direct photon production in p + p collisions at $\sqrt{s_{NN}}$ = 200-GeV. Phys. Rev. Lett., 98:012002, 2007.

[35] S. S. Adler et al. Measurement of Single Muons at Forward Rapidity in p+p Collisions at $\sqrt{s_{NN}}$ = 200-GeV and Implications for Charm Production. Phys. Rev., D76:092002, 2007.

[36] H. Agakishiev et al. High p_T non-photonic electron production in $p+p$ collisions at $\sqrt{s} = 200$ GeV. Phys. Rev., D83:052006, 2011.

[37] M. M. Aggarwal et al. Measurement of the Bottom contribution to non-photonic electron production in $p + p$ collisions at $\sqrt{s}$=200 GeV. Phys. Rev. Lett., 105:202301, 2010.

[38] C. Aidala et al. Measurement of long-range angular correlations and azimuthal anisotropies in high-multiplicity p+Au collisions at $\sqrt{s_{NN}} = 200$ GeV. Phys. Rev., C95(3):034910, 2017.

[39] C. Aidala et al. Measurements of azimuthal anisotropy and charged-particle multiplicity in d+Au collisions at $\sqrt{s_{NN}}$ =200, 62.4, 39, and 19.6 GeV. Phys. Rev., C96(6):064905, 2017.

[40] C. Aidala et al. Measurements of Multiparticle Correlations in $d+$Au Collisions at 200, 62.4, 39, and 19.6 GeV and $p+$Au Collisions at 200 GeV and Implications for Collective Behavior. Phys. Rev. Lett., 120(6):062302, 2018.

[41] C. Aidala et al. Creating small circular, elliptical, and triangular droplets of quark-gluon plasma. 2018 arXiv:1805.02973.

[42] Y. Akiba. PROPOSAL FOR A SILICON VERTEX TRACKER (VTX) FOR THE PHENIX EXPERIMENT., 2004 `https://www.bnl.gov/isd/documents/28627.pdf`.

[43] Ryohji Akimoto. Measurement of Charms and Bottoms with Semi-leptonic Decay Modes in p+p Collisions at sqrt(s) = 200 GeV. PhD thesis, University of Tokyo, 2014. Available: `https://www.{PHENIX}.bnl.gov/{PHENIX}/WWW/talk/archive/theses/2014/Akimoto_Ryohji-Dthesis_akimoto_20140214.pdf`.

[44] Mark G. Alford, Andreas Schmitt, Krishna Rajagopal, and Thomas Schfer. Color superconductivity in dense quark matter. Rev. Mod. Phys., 80:1455–1515, 2008.

[45] B. Alver, M. Baker, C. Loizides, and P. Steinberg. The PHOBOS Glauber Monte Carlo. 2008 arXiv:0805.4411.

[46] B. Alver and G. Roland. Collision geometry fluctuations and triangular flow in heavy-ion collisions. Phys. Rev., C81:054905, 2010. [Erratum: Phys. Rev.C82,039903(2010)].

[47] Massimiliano Alvioli, Brian A. Cole, Leonid Frankfurt, D. V. Perepelitsa, and Mark Strikman. Evidence for x-dependent proton color fluctuations in pA collisions at the CERN Large Hadron Collider. Phys. Rev., C93(1):011902, 2016.

[48] B. Andersson, G. Gustafson, G. Ingelman, and T. Sjstrand. Parton fragmentation and string dynamics. Physics Reports, 97(2):31 – 145, 1983.

[49] Bo Andersson. The Lund model. Camb. Monogr. Part. Phys. Nucl. Phys. Cosmol., 7:1–471, 1997.

[50] A. Andronic et al. Heavy-flavour and quarkonium production in the LHC era: from proton-proton to heavy-ion collisions. Eur. Phys. J., C76(3):107, 2016.

[51] Elke-Caroline Aschenauer et al. The RHIC SPIN Program: Achievements and Future Opportunities. 2015 arXiv:1501.01220.

[52] Maximilian Attems, Jorge Casalderrey-Solana, David Mateos, Daniel Santos-Olivn, Carlos F. Sopuerta, Miquel Triana, and Miguel Zilho. Paths to equilibrium in non-conformal collisions. JHEP, 06:154, 2017.

[53] R. Averbeck. Heavy-flavor production in heavy-ion collisions and implications for the properties of hot QCD matter. Prog. Part. Nucl. Phys., 70:159–209, 2013.

[54] Sakir Ayik. Boltzmann-Langevin Transport Model for Heavy-Ion Collisions. In Hot and Dense Nuclear Matter, NATO ASI Series, pages 579–588. Springer, Boston, MA, 1994. DOI: 10.1007/978-1-4615-2516-5_51.

[55] R. Baier, D. Schiff, and B. G. Zakharov. Energy loss in perturbative QCD. Ann. Rev. Nucl. Part. Sci., 50:37–69, 2000.

[56] S. Batsouli, S. Kelly, M. Gyulassy, and J. L. Nagle. Does the charm flow at RHIC? Phys. Lett., B557:26–32, 2003.

[57] Johannes Bellm et al. Herwig 7.0/Herwig++ 3.0 release note. Eur. Phys. J., C76(4):196, 2016.

[58] J. et al. Beringer. Review of particle physics. Phys. Rev. D, 86:010001, Jul 2012.

[59] Jonah E. Bernhard, J. Scott Moreland, Steffen A. Bass, Jia Liu, and Ulrich Heinz. Applying Bayesian parameter estimation to relativistic heavy-ion collisions: simultaneous characterization of the initial state and quark-gluon plasma medium. Phys. Rev., C94(2):024907, 2016.

[60] G.F. Bertsch and S. Das Gupta. A guide to microscopic models for intermediate energy heavy ion collisions. Physics Reports, 160(4):189 – 233, 1988.

[61] H. A. Bethe and L. C. Maximon. Theory of bremsstrahlung and pair production. i. differential cross section. Phys. Rev., 93:768–784, Feb 1954.

[62] Ante Bilandzic, Raimond Snellings, and Sergei Voloshin. Flow analysis with cumulants: Direct calculations. Phys. Rev., C83:044913, 2011.

[63] J. D. Bjorken. Highly Relativistic Nucleus-Nucleus Collisions: The Central Rapidity Region. Phys. Rev., D27:140–151, 1983.

[64] V. Blobel and E. Lohrmann. Statistische und numerische Methoden der Datenanalyse. Teubner-Studienbücher : Physik. Vieweg+Teubner Verlag, 1998.

[65] Szabolcs Borsanyi, Gergely Endrodi, Zoltan Fodor, Antal Jakovac, Sandor D. Katz, Stefan Krieg, Claudia Ratti, and Kalman K. Szabo. The QCD equation of state with dynamical quarks. JHEP, 11:077, 2010.

[66] Wim Botermans and Rudi Malfliet. Quantum transport theory of nuclear matter. Physics Reports, 198(3):115 – 194, 1990.

[67] Adam Bzdak and Guo-Liang Ma. Elliptic and triangular flow in p+Pb and peripheral Pb+Pb collisions from parton scatterings. Phys. Rev. Lett., 113(25):252301, 2014.

[68] Matteo Cacciari, Stefano Frixione, Nicolas Houdeau, Michelangelo L. Mangano, Paolo Nason, and Giovanni Ridolfi. Theoretical predictions for charm and bottom production at the LHC. JHEP, 10:137, 2012.

[69] Matteo Cacciari and Einan Gardi. Heavy quark fragmentation. Nucl. Phys., B664:299–340, 2003.

[70] Matteo Cacciari, Mario Greco, and Paolo Nason. The p_T spectrum in heavy flavor hadroproduction. JHEP, 05:007, 1998.

[71] Matteo Cacciari, Michelangelo L. Mangano, and Paolo Nason. Gluon PDF constraints from the ratio of forward heavy-quark production at the LHC at $\sqrt{S} = 7$ and 13 TeV. Eur. Phys. J., C75(12):610, 2015.

[72] S. Campbell et al. A Proposal for the Muon Piston Calorimeter Extension (MPC-EX) to the PHENIX Experiment at RHIC. 2013 arXiv:1301.1096.

[73] J. Carlson and R. Schiavilla. Structure and dynamics of few nucleon systems. Rev. Mod. Phys., 70:743–842, 1998.

[74] Serguei Chatrchyan et al. Observation of long-range near-side angular correlations in proton-lead collisions at the LHC. Phys. Lett., B718:795–814, 2013.

[75] A K Chaudhuri. A Short Course on Relativistic Heavy Ion Collisions. 2053-2563. IOP Publishing, 2014.

[76] Paul M. Chesler and Wilke van der Schee. Early thermalization, hydrodynamics and energy loss in AdS/CFT. Int. J. Mod. Phys., E24(10):1530011, 2015.

[77] Paul M. Chesler and Laurence G. Yaffe. Holography and colliding gravitational shock waves in asymptotically AdS 5 spacetime. Phys. Rev. Lett., 106:021601, 2011.

[78] Georgios Choudalakis. Fully Bayesian Unfolding. 2012 arXiv:1201.4612.

[79] Fred Cooper and Graham Frye. Single-particle distribution in the hydrodynamic and statistical thermodynamic models of multiparticle production. Phys. Rev. D, 10:186–189, Jul 1974.

[80] G. D'Agostini. Improved iterative Bayesian unfolding. In Alliance Workshop on Unfolding and Data Correction Hamburg, Germany, May 27-28, 2010, 2010.

[81] A. Dainese, C. Loizides, and G. Paic. Leading-particle suppression in high energy nucleus-nucleus collisions. Eur. Phys. J., C38:461–474, 2005.

[82] P. Danielewicz and M. Gyulassy. Dissipative Phenomena in Quark Gluon Plasmas. Phys. Rev., D31:53–62, 1985.

[83] C E DeTar, , and J F Donoghue. Bag models of hadrons. Annual Review of Nuclear and Particle Science, 33(1):235–264, 1983.

[84] Magdalena Djordjevic. Collisional energy loss in a finite size QCD matter. Phys. Rev., C74:064907, 2006.

[85] Magdalena Djordjevic. Light and heavy flavor phenomenology at RHIC and LHC. Nuclear Physics A, 932:302 – 309, 2014. Hard Probes 2013.

[86] Yuri L. Dokshitzer and D. E. Kharzeev. Heavy quark colorimetry of QCD matter. Phys. Lett., B519:199–206, 2001.

[87] R. Keith Ellis, W. James Stirling, and B. R. Webber. QCD and collider physics. Camb. Monogr. Part. Phys. Nucl. Phys. Cosmol., 8:1–435, 1996.

[88] B.B Back et al. The PHOBOS detector at RHIC. Nuclear Instruments and Methods in Physics Research Section A: Accelerators, Spectrometers, Detectors and Associated Equipment, 499(2):603 – 623, 2003. The Relativistic Heavy Ion Collider Project: RHIC and its Detectors.

[89] K. Adcox et al. PHENIX central arm tracking detectors. Nuclear Instruments and Methods in Physics Research Section A: Accelerators, Spectrometers, Detectors and Associated Equipment, 499(2):489 – 507, 2003. The Relativistic Heavy Ion Collider Project: RHIC and its Detectors.

[90] K. Adcox et al. PHENIX detector overview. Nuclear Instruments and Methods in Physics Research Section A: Accelerators, Spectrometers, Detectors and Associated Equipment, 499(2):469 – 479, 2003. The Relativistic Heavy Ion Collider Project: RHIC and its Detectors.

[91] K.H. Ackermann et al. Star detector overview. Nuclear Instruments and Methods in Physics Research Section A: Accelerators, Spectrometers, Detectors and Associated Equipment, 499(2):624 – 632, 2003. The Relativistic Heavy Ion Collider Project: RHIC and its Detectors.

[92] L Aphecetche et al. PHENIX calorimeter. Nuclear Instruments and Methods in Physics Research Section A: Accelerators, Spectrometers, Detectors and Associated Equipment, 499(2):521 – 536, 2003. The Relativistic Heavy Ion Collider Project: RHIC and its Detectors.

[93] M Adamczyk et al. The brahms experiment at RHIC. Nuclear Instruments and Methods in Physics Research Section A: Accelerators, Spectrometers, Detectors and Associated Equipment, 499(2):437 – 468, 2003. The Relativistic Heavy Ion Collider Project: RHIC and its Detectors.

[94] M. Aizawa et al. PHENIX central arm particle id detectors. Nuclear Instruments and Methods in Physics Research Section A: Accelerators, Spectrometers, Detectors and Associated Equipment, 499(2):508 – 520, 2003. The Relativistic Heavy Ion Collider Project: RHIC and its Detectors.

[95] M. Allen et al. PHENIX inner detectors. Nuclear Instruments and Methods in Physics Research Section A: Accelerators, Spectrometers, Detectors and Associated Equipment, 499(2):549 – 559, 2003. The Relativistic Heavy Ion Collider Project: RHIC and its Detectors.

[96] S.H. Aronson et al. PHENIX magnet system. Nuclear Instruments and Methods in Physics Research Section A: Accelerators, Spectrometers, Detectors and Associated Equipment, 499(2):480 – 488, 2003. The Relativistic Heavy Ion Collider Project: RHIC and its Detectors.

[97] Enrico Fermi. High Energy Nuclear Events. Progress of Theoretical Physics, 5(4):570–583, July 1950.

[98] Wojciech Florkowski. Phenomenology of Ultra-Relativistic Heavy-Ion Collisions. World Scientific, 2010.

[99] G Flucke, P Schleper, G Steinbrck, and M Stoye. Cms silicon tracker alignment strategy with the millepede ii algorithm. Journal of Instrumentation, 3(09):P09002, 2008.

[100] Takashi Hachiya for the PHENIX Collaboration. "nuclear modification factor of charm and bottom quark yields in au+au collisions at $\sqrt{s_{NN}} = 200$ gev by the PHENIX experiment" talk at the 27th international conference on ultrarelativistic heavy-ion collisions. lido di venezia, 2018.

[101] Daniel Foreman-Mackey, David W. Hogg, Dustin Lang, and Jonathan Goodman. emcee : The mcmc hammer. Publications of the Astronomical Society of the Pacific, 125(925):306, 2013.

[102] Rainer J. Fries, Vincenzo Greco, and Paul Sorensen. Coalescence Models For Hadron Formation From Quark Gluon Plasma. Ann. Rev. Nucl. Part. Sci., 58:177–205, 2008.

[103] Stefano Frixione, Fabian Stoeckli, Paolo Torrielli, Bryan R. Webber, and Chris D. White. The MC@NLO 4.0 Event Generator. 2010.

[104] Charles Gale, Sangyong Jeon, Bjrn Schenke, Prithwish Tribedy, and Raju Venugopalan. Event-by-event anisotropic flow in heavy-ion collisions from combined Yang-Mills and viscous fluid dynamics. Phys. Rev. Lett., 110(1):012302, 2013.

[105] Klaus Geiger and Dinesh Kumar Srivastava. Parton cascade description of relativistic heavy ion collisions at the cern super proton synchrotron at 158A gev? Phys. Rev. C, 56:2718–2725, Nov 1997.

[106] Klaus Geiger and Berndt Muller. Dynamics of parton cascades in highly relativistic nuclear collisions. Nucl. Phys., B369:600–654, 1992.

[107] F. Gelis. Color Glass Condensate and Glasma. Int. J. Mod. Phys., A28:1330001, 2013.

[108] Francois Gelis, Edmond Iancu, Jamal Jalilian-Marian, and Raju Venugopalan. The Color Glass Condensate. Ann. Rev. Nucl. Part. Sci., 60:463–489, 2010.

[109] Murray Gell-Mann. Symmetries of baryons and mesons. Phys. Rev., 125:1067–1084, Feb 1962.

[110] Roy J. Glauber. Quantum Optics and Heavy Ion Physics. Nucl. Phys., A774:3–13, 2006.

[111] David J Griffiths. Introduction to elementary particles; 2nd rev. version. Physics textbook. Wiley, New York, NY, 2008.

[112] Miklos Gyulassy and Michael Plumer. Jet Quenching in Dense Matter. Phys. Lett., B243:432–438, 1990.

[113] M. Habich, G. A. Miller, P. Romatschke, and W. Xiang. Testing hydrodynamic descriptions of $p + p$ collisions at $\sqrt{s} = 7$ TeV. Eur. Phys. J., C76(7):408, 2016.

[114] R. Hagedorn. Statistical thermodynamics of strong interactions at high-energies. Nuovo Cim. Suppl., 3:147–186, 1965.

[115] H. Hahn, E. Forsyth, H. Foelsche, M. Harrison, J. Kewisch, G. Parzen, S. Peggs, E. Raka, A. Ruggiero, A. Stevens, S. Tepikian, P. Thieberger, D. Trbojevic, J. Wei, E. Willen, S. Ozaki, and S.Y. Lee. The rhic design overview. Nuclear Instruments and Methods in Physics Research Section A: Accelerators, Spectrometers, Detectors and Associated Equipment, 499(2):245 – 263, 2003. The Relativistic Heavy Ion Collider Project: RHIC and its Detectors.

[116] M. Harrison, T. Ludlam, and S. Ozaki. RHIC project overview. Nuclear Instruments and Methods in Physics Research Section A: Accelerators, Spectrometers, Detectors and Associated Equipment, 499(2):235 – 244, 2003. The Relativistic Heavy Ion Collider Project: RHIC and its Detectors.

[117] Liang He, Terrence Edmonds, Zi-Wei Lin, Feng Liu, Denes Molnar, and Fuqiang Wang. Anisotropic parton escape is the dominant source of azimuthal anisotropy in transport models. Physics Letters B, 753:506 – 510, 2016.

[118] Min He, Rainer J. Fries, and Ralf Rapp. Heavy Flavor at the Large Hadron Collider in a Strong Coupling Approach. Phys. Lett., B735:445–450, 2014.

[119] Ulrich Heinz and Raimond Snellings. Collective flow and viscosity in relativistic heavy-ion collisions. Ann. Rev. Nucl. Part. Sci., 63:123–151, 2013.

[120] W. A. Horowitz. Testing pQCD and AdS/CFT Energy Loss at RHIC and LHC. AIP Conf. Proc., 1441:889–891, 2012.

[121] Ronald John Belmont III. Measurements of Identified Hadrons in Au+Au and d+Au Collisions at $\sqrt(s) = 200$ GeV. PhD thesis, Vanderbilt University, 2012. Available: `https://www.{PHENIX}.bnl.gov/{PHENIX}/WWW/talk/archive/theses/2012/Belmont_Ron-belmont.pdf`.

[122] Barbara V. Jacak and Berndt Müller. The exploration of hot nuclear matter. Science, 337(6092):310–314, 2012.

[123] Stephen C. Johnson, John W. No, Federica Ceretto, Axel Drees, Thomas K. Hemmick, Barbara Jacak, and For The PHENIX Collaboration. Three-Dimensional Track Finding in the PHENIX Drift Chamber by a Combinatorial Hough Transform Method, 1998 `https://pdfs.semanticscholar.org/754b/6a1b4bc328fcfcc2749b0b5bfc3561fb8cbe.pdf`.

[124] Vardan Khachatryan et al. Observation of Long-Range Near-Side Angular Correlations in Proton-Proton Collisions at the LHC. JHEP, 09:091, 2010.

[125] Vardan Khachatryan et al. Measurement of the B^+ Production Cross Section in pp Collisions at $\sqrt{s} = 7$ TeV. Phys. Rev. Lett., 106:112001, 2011.

[126] Vardan Khachatryan et al. Measurement of long-range near-side two-particle angular correlations in pp collisions at $\sqrt{s}$ =13 TeV. Phys. Rev. Lett., 116(17):172302, 2016.

[127] Vardan Khachatryan et al. Evidence for collectivity in *pp* collisions at the LHC. Phys. Lett., B765:193–220, 2017.

[128] P. F. Kolb, P. Huovinen, Ulrich W. Heinz, and H. Heiselberg. Elliptic flow at SPS and RHIC: From kinetic transport to hydrodynamics. Phys. Lett., B500:232–240, 2001.

[129] Kijima Kotaro. First measurement of ω and ϕ mesons via di-electron decay channels in proton+proton collisions at $\sqrt{s_{NN}} = 200$ GeV. PhD thesis, Kijima Kotaro, Hiroshima University, 2012.

[130] P. Kovtun, Dan T. Son, and Andrei O. Starinets. Viscosity in strongly interacting quantum field theories from black hole physics. Phys. Rev. Lett., 94:111601, 2005.

[131] B. Krieger, S. Alfonsi, N. Bacchetta, S. Centro, L. Christofek, M. Garcia-Sciveres, C. Haber, K. Hanagaki, J. Hoff, M. Johnson, H. von der Lippe, P. Lujan, E. Mandelli, G. Meng, A. Nomerotski, D. Pellet, P. Rapidis, M. Utes, J. P. Walder, M. Weber, W. Wester, T. Wilkes, R. Yarema, W. Yao, and T. Zimmerman. Svx4: a new deep-submicron readout IC for the Tevatron collider at Fermilab. IEEE Transactions on Nuclear Science, 51(5):1968–1973, Oct 2004.

[132] Aleksi Kurkela and Urs Achim Wiedemann. Picturing perturbative parton cascades in QCD matter. Physics Letters B, 740:172 – 178, 2015.

[133] L. D. Landau. On the multiparticle production in high-energy collisions. Izv. Akad. Nauk Ser. Fiz., 17:51–64, 1953.

[134] D. J. Lange. The EvtGen particle decay simulation package. Nucl. Instrum. Meth., A462:152–155, 2001.

[135] Yen-Jie Lee. Long-range angular correlations of charged particles in high multiplicity e+e- collisions using archived data from the ALEPH detector at LEP. 2018. Presented at the 27th International Conference on Ultrarelativistic Nucleus-Nucleus Collisions. Venice, Italy.

[136] Bao-An Li and Che Ming Ko. Formation of superdense hadronic matter in high energy heavy-ion collisions. Phys. Rev. C, 52:2037–2063, Oct 1995.

[137] Zi-Wei Lin and C M Ko. Kaon interferometry at RHIC from the AMPT model. Journal of Physics G: Nuclear and Particle Physics, 30(1):S263, 2004.

[138] Zi-Wei Lin, Che Ming Ko, Bao-An Li, Bin Zhang, and Subrata Pal. A Multi-phase transport model for relativistic heavy ion collisions. Phys. Rev., C72:064901, 2005.

[139] C. Loizides, J. Nagle, and P. Steinberg. Improved version of the PHOBOS Glauber Monte Carlo. SoftwareX, 1-2:13–18, 2015.

[140] Constantin Loizides. Experimental overview on small collision systems at the LHC. Nucl. Phys., A956:200–207, 2016.

[141] Guo-Liang Ma and Adam Bzdak. Long-range azimuthal correlations in proton proton and proton nucleus collisions from the incoherent scattering of partons. Phys. Lett., B739:209–213, 2014.

[142] David MacKay. Information Theory, Inference and Learning Algorithms. Cambridge University Press, 2003.

[143] E. J. Mannel. System electronics and DAQ for the silicon vertex detector upgrade for PHENIX. In 2007 15th IEEE-NPSS Real-Time Conference, pages 1–6, April 2007.

[144] Wang Mei-Juan, Chen Gang, and Wu Yuan-Fang. Eccentricity and elliptic flow at fixed centrality in Au+Au collisions at $\sqrt{s_{NN} = 200}$ gev in an AMPT model. Chinese Physics C, 37(1):014104, 2013.

[145] Frank Meier, Supervised By, Hans-Christian Kstli, Roland Horisberger, and Urs Langenegger. Track based alignment of the cms pixel barrel detector using the Millepede-II alignment algorithm. 09 2008.

[146] Michael L. Miller, Klaus Reygers, Stephen J. Sanders, and Peter Steinberg. Glauber modeling in high energy nuclear collisions. Ann. Rev. Nucl. Part. Sci., 57:205–243, 2007.

[147] J. T. Mitchell, D. V. Perepelitsa, M. J. Tannenbaum, and P. W. Stankus. Tests of constituent-quark generation methods which maintain both the nucleon center of mass and the desired radial distribution in Monte Carlo Glauber models. Phys. Rev., C93(5):054910, 2016.

[148] Stanislaw Mrowczynski. Quark - gluon plasma. Acta Phys. Polon., B29:3711, 1998.

[149] Munshi G. Mustafa. Energy loss of charm quarks in the quark-gluon plasma: Collisional versus radiative. Phys. Rev., C72:014905, 2005.

[150] Kazuya Nagashima. PHENIX measurements of single electrons from charm and bottom decays at midrapidity in Au+Au collisions. Nucl. Phys., A967:644–647, 2017.

[151] J. L. Nagle, A. Adare, S. Beckman, T. Koblesky, J. Orjuela Koop, D. McGlinchey, P. Romatschke, J. Carlson, J. E. Lynn, and M. McCumber. Exploiting Intrinsic Triangular Geometry in Relativistic ^{3}He+Au Collisions to Disentangle Medium Properties. Phys. Rev. Lett., 113(11):112301, 2014.

[152] J. L. Nagle, Ron Belmont, Kurt Hill, Javier Orjuela Koop, Dennis V. Perepelitsa, Pengqi Yin, Zi-Wei Lin, and Darren McGlinchey. Minimal conditions for collectivity in e^+e^- and $p + p$ collisions. Phys. Rev., C97(2):024909, 2018.

[153] J. L. Nagle and J. Orjuela Koop. A Quasiparticle Transport Explanation for Collectivity in the Smallest of Collision Systems ($p + p$ and e^+e^-). In Quark Matter 2018., 2018.

[154] James L. Nagle and William A. Zajc. Small System Collectivity in Relativistic Hadron and Nuclear Collisions. 2018.

[155] H. Niemi and G. S. Denicol. How large is the Knudsen number reached in fluid dynamical simulations of ultrarelativistic heavy ion collisions? 2014.

[156] Jacquelyn Noronha-Hostler, Li Yan, Fernando G. Gardim, and Jean-Yves Ollitrault. Linear and cubic response to the initial eccentricity in heavy-ion collisions. Phys. Rev., C93(1):014909, 2016.

[157] Carlo Oleari. The POWHEG-BOX. Nucl. Phys. Proc. Suppl., 205-206:36–41, 2010.

[158] Jean-Yves Ollitrault. Relativistic hydrodynamics for heavy-ion collisions. Eur. J. Phys., 29:275–302, 2008.

[159] Jean-Yves Ollitrault, Arthur M. Poskanzer, and Sergei A. Voloshin. Effect of flow fluctuations and nonflow on elliptic flow methods. Phys. Rev. C, 80:014904, Jul 2009.

[160] Haakon Olsen. Opening angles of electron-positron pairs. Phys. Rev., 131:406–415, Jul 1963.

[161] J. D. Orjuela Koop, A. Adare, D. McGlinchey, and J. L. Nagle. Azimuthal anisotropy relative to the participant plane from a multiphase transport model in central p + Au , d + Au , and ^{3}He + Au collisions at $\sqrt{s_{NN}} = 200$ GeV. Phys. Rev., C92(5):054903, 2015.

[162] J. D. Orjuela Koop, R. Belmont, P. Yin, and J. L. Nagle. Exploring the Beam Energy Dependence of Flow-Like Signatures in Small System d+Au Collisions. Phys. Rev., C93(4):044910, 2016.

[163] M.E. Peskin and D.V. Schroeder. An Introduction to Quantum Field Theory. Advanced book classics. Avalon Publishing, 1995.

[164] Michael E. Peskin and Daniel V. Schroeder. An Introduction to quantum field theory. Addison-Wesley, Reading, USA, 1995.

[165] A Pikin, J G Alessi, E N Beebe, A Kponou, R Lambiase, R Lockey, D Raparia, J Ritter, L Snydstrup, and Y Tan. RHIC EBIS: basics of design and status of commissioning. Journal of Instrumentation, 5(09):C09003, 2010.

[166] Johann Rafelski and Jeremiah Birrell. Traveling Through the Universe: Back in Time to the Quark-Gluon Plasma Era. J. Phys. Conf. Ser., 509:012014, 2014.

[167] Paul Romatschke. Collective flow without hydrodynamics: simulation results for relativistic ion collisions. Eur. Phys. J., C75(9):429, 2015.

[168] Paul Romatschke. Light-Heavy Ion Collisions: A window into pre-equilibrium QCD dynamics? Eur. Phys. J., C75(7):305, 2015.

[169] Paul Romatschke. Azimuthal Anisotropies at High Momentum from Purely Non-Hydrodynamic Transport. Eur. Phys. J., C78(8):636, 2018.

[170] Paul Romatschke. Relativistic Fluid Dynamics Far From Local Equilibrium. Phys. Rev. Lett., 120(1):012301, 2018.

[171] Paul Romatschke and Ulrike Romatschke. Viscosity Information from Relativistic Nuclear Collisions: How Perfect is the Fluid Observed at RHIC? Phys. Rev. Lett., 99:172301, 2007.

[172] Paul Romatschke and Ulrike Romatschke. Relativistic Fluid Dynamics In and Out of Equilibrium – Ten Years of Progress in Theory and Numerical Simulations of Nuclear Collisions. 2017.

[173] V. G. Ryabov. Drift chambers for the PHENIX central tracking system. Nucl. Instrum. Meth., A419:363–369, 1998.

[174] Carlos A. Salgado and Urs Achim Wiedemann. Calculating quenching weights. Phys. Rev., D68:014008, 2003.

[175] Helmut Satz. The Thermodynamics of Quarks and Gluons. In Sarkar Sourav, Helmut Satz, and Bikash Sinha, editors, The Physics of the Quark-Gluon Plasma, pages 1–21. 2010.

[176] Bjoern Schenke, Prithwish Tribedy, and Raju Venugopalan. Fluctuating Glasma initial conditions and flow in heavy ion collisions. Phys. Rev. Lett., 108:252301, 2012.

[177] Bjrn Schenke. Origins of collectivity in small systems. Nucl. Phys., A967:105–112, 2017.

[178] Soeren Schlichting and Prithwish Tribedy. Collectivity in Small Collision Systems: An Initial-State Perspective. Adv. High Energy Phys., 2016:8460349, 2016.

[179] H Schroder. Physics of b mesons. Reports on Progress in Physics, 52(7):765, 1989.

[180] Michael H. Seymour and Andrzej Siodmok. Constraining MPI models using σ_{eff} and recent Tevatron and LHC Underlying Event data. JHEP, 10:113, 2013.

[181] Chun Shen and Ulrich Heinz. The road to precision: Extraction of the specific shear viscosity of the quark-gluon plasma. Nucl. Phys. News, 25(2):6–11, 2015.

[182] Ghi R. Shin and Berndt Muller. A Relativistic parton cascade with radiation. J. Phys., G28:2643–2656, 2002.

[183] Torbjrn Sjstrand, Stefan Ask, Jesper R. Christiansen, Richard Corke, Nishita Desai, Philip Ilten, Stephen Mrenna, Stefan Prestel, Christine O. Rasmussen, and Peter Z. Skands. An Introduction to PYTHIA 8.2. Comput. Phys. Commun., 191:159–177, 2015.

[184] Raimond Snellings. Elliptic Flow: A Brief Review. New J. Phys., 13:055008, 2011.

[185] W. Snoeys et al. Pixel readout electronics development for the ALICE pixel vertex and LHCb RICH detector. Nucl. Instrum. Meth., A465:176–189, 2000.

[186] Paul Sorensen. Elliptic Flow: A Study of Space-Momentum Correlations in Relativistic Nuclear Collisions. In Rudolph C. Hwa and Xin-Nian Wang, editors, Quark-gluon plasma 4, pages 323–374. 2010.

[187] Reinhard Stock. Ultra-relativistic nucleus-nucleus collisions. Proceedings, 17th International Conference, Quark Matter 2004, Oakland, USA, January 11-17, 2004. J. Phys., G30:S633–S648, 2004.

[188] Derek A. Teaney. Viscous Hydrodynamics and the Quark Gluon Plasma. In Rudolph C. Hwa and Xin-Nian Wang, editors, Quark-gluon plasma 4, pages 207–266. 2010.

[189] R. Thomas, Burkhard Kampfer, and G. Soff. Gluon emission of heavy quarks: Dead cone effect. Acta Phys. Hung., A22:83–91, 2005.

[190] R. S. Thorne and R. G. Roberts. A Variable number flavor scheme for charged current heavy flavor structure functions. Eur. Phys. J., C19:339–349, 2001.

[191] Juan M. Torres-Rincon. Boltzmann-Uehling-Uhlenbeck Equation. In Hadronic Transport Coefficients from Effective Field Theories, Springer Theses, pages 33–45. Springer, Cham, 2014. DOI: 10.1007/978-3-319-00425-9_2.

[192] Giorgio Torrieri, Barbara Betz, Jorge Noronha, and Miklos Gyulassy. Mach cones in heavy ion collisions. Acta Phys. Polon., B39:3281–3308, 2008.

[193] Raju Venugopalan. The Color glass condensate: An Overview. Eur. Phys. J., C43:337–344, 2005.

[194] R. Vogt. Cold Nuclear Matter Effects on Open and Hidden Heavy Flavor Production at the LHC. In Proceedings, 7th Int. Workshop on Charm Physics, Detroit, USA, May 18-22, 2015, 2015.

[195] Ramona Vogt. Ultra-Relativistic Heavy-Ion Collisions. Elsevier, 2007.

[196] S. Voloshin and Y. Zhang. Flow study in relativistic nuclear collisions by Fourier expansion of Azimuthal particle distributions. Z. Phys., C70:665–672, 1996.

[197] Xin-Nian Wang and Miklos Gyulassy. HIJING: A Monte Carlo model for multiple jet production in p p, p A and A A collisions. Phys. Rev., D44:3501–3516, 1991.

[198] Ryan D. Weller and Paul Romatschke. One fluid to rule them all: viscous hydrodynamic description of event-by-event central p+p, p+Pb and Pb+Pb collisions at $\sqrt{s} = 5.02$ TeV. Phys. Lett., B774:351–356, 2017.

[199] Simon Wicks, William Horowitz, Magdalena Djordjevic, and Miklos Gyulassy. Elastic, inelastic, and path length fluctuations in jet tomography. Nucl. Phys., A784:426–442, 2007.

[200] Urs Achim Wiedemann. Jet Quenching in Heavy Ion Collisions. pages 521–562, 2010. [Landolt-Bornstein23,521(2010)].

[201] Frank Wilczek. QCD made simple. Phys. Today, 53N8:22–28, 2000.

[202] Zhe Xu and Carsten Greiner. Thermalization of gluons in ultrarelativistic heavy ion collisions by including three-body interactions in a parton cascade. Phys. Rev., C71:064901, 2005.

[203] Zhe Xu and Carsten Greiner. Transport rates and momentum isotropization of gluon matter in ultrarelativistic heavy-ion collisions. Phys. Rev., C76:024911, 2007.

[204] K. Yagi, T. Hatsuda, and Y. Miake. Quark-Gluon Plasma: From Big Bang to Little Bang. Cambridge Monographs on Particle Physics, Nuclear Physics and Cosmology. Cambridge University Press, 2005.

[205] Bin Zhang. ZPC 1.0.1: A Parton cascade for ultrarelativistic heavy ion collisions. Comput. Phys. Commun., 109:193–206, 1998.

[206] Hanzhong Zhang, J. F. Owens, Enke Wang, and Xin-Nian Wang. Dihadron tomography of high-energy nuclear collisions in NLO pQCD. Phys. Rev. Lett., 98:212301, 2007.

Appendix A

Centrality Categorization in $p(d)$+A Collisions

A.1 Categorizing Centrality with Monte Carlo Glauber Calculations

Characterizing event geometry by correlating centrality with particle production in small asymmetric systems presents a number of challenges not encountered in large A+A collisions. For starters, the identification of "centrality" with the size of the overlap area between the colliding nuclei is no longer necessarily meaningful given the much smaller size of the projectile relative to the target, such that other factors—like the separation between partons—have a greater bearing on event multiplicity. In general, a collision with small impact parameter where the projectile goes through the thickest part of the target, will result in higher particle multiplicity. However, certain effects such as fluctuations in parton configurations within individual nucleons [47] can significantly affect the interaction cross-section, resulting in deviations from the Glauber model assumptions. This appendix presents the methodology used by the PHENIX experiment to categorize centrality in d+Au—which is equally applicable to p+Au and ^{3}He+Au collisions—and to correct for biases in the measurement of centrality-dependent particle yields arising from auto-correlations between multiplicity measured at forward and central rapidity. This work was published, including contributions from the author of this dissertation regarding the p_T dependence of the above auto-correlations, in Ref. [25].

The PHENIX experiment uses a standard Monte Carlo Glauber approach to centrality categorization in d+Au collisions. The nuclear density profile for the Au nucleus is taken to be the Woods-Saxon distribution, from which individual nucleon positions are sampled. For the deuteron,

the Hulthén wavefunction is used to model the internucleon separation of the proton and neutron constituents. The inelastic nucleon interaction cross section is taken to be $\sigma_{NN} = 42 \pm 3$ mb, from measurements. A nucleon-nucleon interaction is said to have occured if two given nucleons lie within a distance $\sqrt{\sigma_{NN}/\pi}$ of each other. A sample event is shown in Fig. A.1. The event-by-event random sampling of nucleon positions, along with the criterion to identify wounded nucleons, yields immediately the number of participants, binary collisions, and eccentricity of the event.

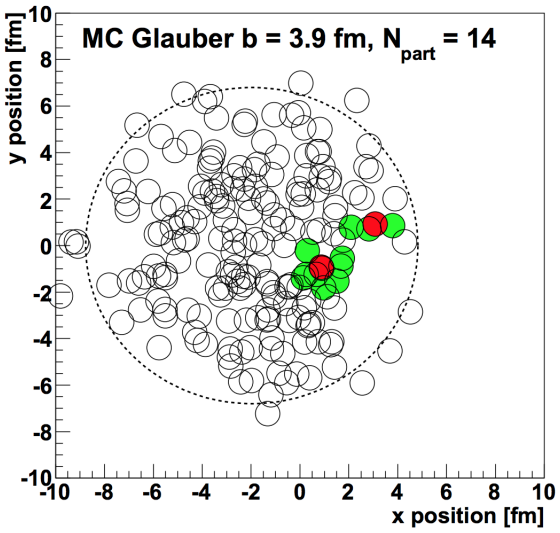

Figure A.1: Initial geometry of a d+Au event in MC Glauber. The black circles represent spectator nucleons; the red and green filled circles represent participant nucleons in the projectile and target, respectively. Figure reproduced from [25].

In order to relate the geometric quantities above with measured charge at backward rapidity ($-3.9 < \eta < -3.1$), as measured by the BBC-South detector (henceforth referred to simply as "BBC"), we posit that the charge in the BBC is proportional to the number of binary collisions N_{coll} with fluctuations from each individual collision modeled by a negative binomial distribution (NBD).

$$\mathrm{NBD}(x;\mu,\kappa) = \left(1+\frac{\mu}{\kappa}\right)^{-\kappa} \frac{(\kappa+x-1)!}{x!(\kappa-1)!} \left(\frac{\mu}{\mu+\kappa}\right)^{x}. \tag{A.1}$$

If one then convolves the distribution of the number of binary collisions Gl(n) as determined using

the Monte Carlo Glauber model with negative binomial fluctuations, one obtains

$$P(q) = \sum_{n=1}^{N_{\rm coll}^{max}} \mathrm{Gl}(n) \times \mathrm{NDB}(q; n\mu; n\kappa), \tag{A.2}$$

where q is the charge in the BBC. As it stands, the equation above can be fit to the experimentally measured distribution of charge in the BBC to determine the parameters of the negative binomial distribution, $\mu = 3.03$ and $\kappa = 0.46$. Fig. A.3 shows, in the upper panel, the distribution of summed BBC charge (open circles) from experiment, along with the best Glauber+NBD fit (histogram). The histogram is then sliced into quantiles, shown as colored bands, which correspond to individual centrality classes. Events corresponding to centrality selections at high multiplicity are called "central", while those at low multiplicity are called "peripheral". We observe a very good fit of the experimental data, except at very low summed charge values due to the minimum-bias trigger inefficiency in this region, as is shown in the lower panel of the figure. In fact, the minimum-bias trigger condition of recording at least one particle in each arm of the BBC detector, was measured to capture $88 \pm 4\%$ of the total inelastic cross section.

Having fit the data, the model provides distributions of the number of participants and binary collisions in each centrality class, $N_{\rm part}$ and $N_{\rm coll}$, as well as other geometric quantities such as the eccentricity ε_n and the spatial overlap area S. We will not reproduce these values here, but rather refer the reader to Table I in Ref. [25], where the details of the calculation are also presented along with a discussion on the sources of systematic uncertainty in the Glauber+NBD model.

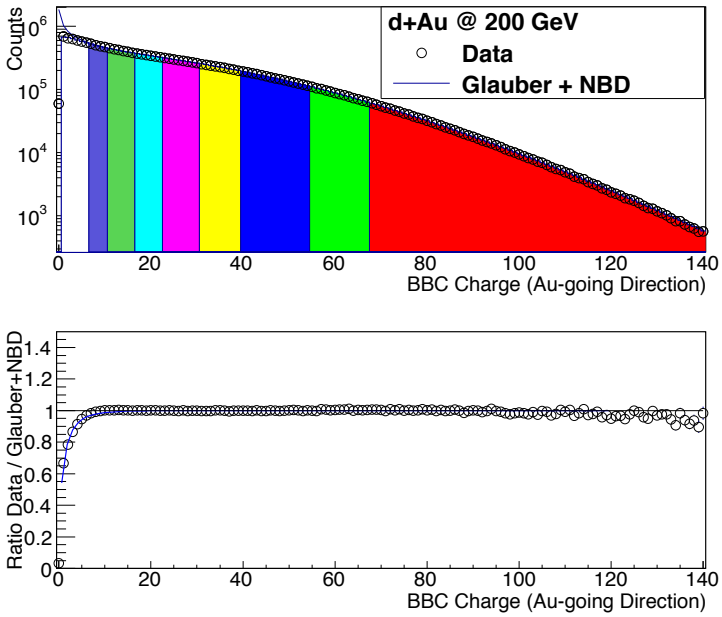

Figure A.2: (top) The open points show the distribution of charge measured in the BBC in $d+Au$ collisions at $\sqrt{s_{NN}} = 200$ GeV. The histogram shows the results of the Glauber+NBD calculation, where the colored bands correspond to the centrality classes 0%-5%, 5%-10%, 10%-20%, 20%-30%, 30%-40%, 40%-50%, 50%-60%, 60%-70%, and 70%-88%. (bottom) Ratio of measured BBC charge to that calculated with Glauber. The line is a fit to the trigger efficiency turn-on curve. Figure reproduced from [25].

A.2 Centrality Bias Effects in Small System Collisions

The procedure outlined in the previous section provides a means of classifying a given d+Au event into a geometrical category based *exclusively* on the charge recorded in the BBC detector. Therefore, any effect with the potential to alter the multiplicity in the acceptance of the BBC, without affecting the true geometry of the event (e.g., a hard scattering between partons), can lead to a miscategorization of centrality. In this section, we describe a framework to model and account for autocorrelation bias effects between particle production at forward rapidity and mid-rapidity,

deriving correction factors for measured centrality-dependent particle yields. First, we will describe how p_T-independent bias correction factors can be calculated from the Glauber+NBD formalism previously presented, and then we will extend the calculation to p_T-dependent factors using the HIJING event generator. The significance of this calculation is well motivated, since any bias in the measurement of centrality-dependent particle yields will necessarily affect the calculation of nuclear modification factors, R_{xA}, a central quantity for the study of a variety of physics, including energy loss and cold nuclear matter effects in small systems.

Let's begin by considering the elementary case of $p + p$ collisions. At $\sqrt{s_{NN}} = 200$ GeV, the PHENIX minimum-bias trigger captures $52 \pm 4\%$ of the total inelastic measured cross section $\sigma_{NN} = 42$ mb. However, when considering events with hadrons detected at mid-rapidity ($|\eta| < 0.35$), the same trigger will fire $75 \pm 3\%$ of the time. Since particle production at midrapidity can be ascribed predominantly to non-diffractive (i.e., non-grazing, or head-on) collisions, which account for only part of the total inelastic cross section, then the minimum-bias trigger can be said to be biased towards this class of events. As a result, any invariant yield measured in $p+p$ collisions will be biased towards a larger value. The same argument holds for peripheral d+Au collisions.

Now, for our purposes, d+Au events can be thought of a superposition of many individual $p + p$ collisions. Thus, if some of those individual nucleon-nucleon collisions produce particles at midrapidity, there will be greater charge deposition in the BBC, as explained above, and thus a bias towards a more central categorization of the event. If one then attempted to measure particle production at midrapidity in peripheral events, one would obtain a lower value than expected, since some peripheral events would have been misclassified as more central. Therefore, the yield would need to be corrected up. Following the same logic, the migration of events from a peripheral to a more central categorization implies that measured yields in central events would be artificially inflated, and would need to be corrected down. We call these corrections *bias factors*.

The Glauber+NBD framework can be used to calculate the bias factors based on the observations that (i) the minimum-bias trigger fires 75% of the time when a particle is detected at midrapidity in $p + p$ collisions, and (ii) that BBC charge deposition increases by 55% when par-

Table A.1: Bias factor correction and selected geometric quantities for different centrality bins in d+Au collisions at $\sqrt{s_{NN}} = 200$ GeV, as calculated using a Monte Carlo Glauber approach.

	0-20%	20-40%	40-60%	60-88%
Bias Factor	0.94 ± 0.01	1.00 ± 0.01	1.03 ± 0.02	1.03 ± 0.06
$\langle N_{\rm coll} \rangle$	15.1 ± 1.0	10.2 ± 0.7	6.6 ± 0.4	3.2 ± 0.2
$\langle N_{\rm part} \rangle$	15.2 ± 0.6	11.1 ± 0.6	7.8 ± 0.4	4.3 ± 0.2

ticles are detected at midrapidity in minimum-bias events, as determined from data. Therefore, in a Monte Carlo Glauber d+Au event with N binary collisions, we select one of them to have an increased contribution to particle production, as modeled by multiplying the NBD parameters μ and κ by 1.55, leaving the other $N - 1$ collisions unaffected. Thus, the invariant yield can be calculated using the above prescription, and divided by that calculated in the standard formulation, obtaining the desired bias factor for each centrality class, as summarized in Table along with other geometric quantities of interest.

The bias factor calculation, as presented above, does not account for their pT dependence, which can be accounted for under certain assumptions by changing the input values corresponding to the trigger efficiency and the increase in forward multiplicity when particles are detected at midrapidity. However, in order to fully understand the p_T dependence of the various effects that contribute to the bias factors, it is of interest to carry out the calculation using a model where the true event information is accessible, such as the HIJING event generator to simulate $p + p$ and d+Au collisions at $\sqrt{s_{NN}}$. In order to provide a comparison as close as possible to experimental results—yet without requiring a full GEANT simulation of the PHENIX subsystems—we define a set of selection cuts: charge deposition in the BBC detectors, and the central arm detectors is taken to be the number of final-state charged particles from HIJING within the corresponding acceptance ($3.1 < |\eta| < 3.9$ and $|\eta| < 0.35$, respectively). The minimum-bias trigger is modeled by requiring at least one charged particle in each of the BBC acceptance regions. Table A.2 compares the minimum-bias trigger efficiency of simulated events against the measured values in real data. Also displayed is the minimum bias efficiency in the presence of at least one high-p_T (i.e., $p_T > 1$ GeV)

particle in the central arm region. While the results from simulation fail to agree quantitatively with the data, they do qualitatively reproduce the expected trend. We now check the increase in BBC multiplicity when a particle is detected at midrapidity; in data, it has been measured to be 1.55, while in HIJING it is 1.62, as shown in Table A.3. The p_T dependence of the increase is shown in Fig A.3. Even though the HIJING results do not agree quantitatively with the reference values measured in $p+p$ data, the qualitative agreement does confirm the existence of the desired correlation effects. We can thus proceed to calculate the bias factor corrections for d+Au collisions, bearing in mind that the lack of agreement might stem from the specific handling of single- and double-diffractive events in the HIJING generator.

Table A.2: Minimum bias trigger efficiency in HIJING simulations of $p+p$ collisions

Method	MinBias Efficiency	MinBias Efficiency w/ Particle in $\|\eta\| < 0.35$	Ratio
HIJING	0.48	0.62	1.29
$p+p$ Data	0.51	0.75	1.47

Table A.3: Change in mean charged particle multiplicity in the BBC-South acceptance when a high p_T particle is detected at midrapidity.

Method	$\langle$BBC-S Charge$\rangle$	$\langle$BBC-S Charge$\rangle$ with High p_T Particle	Ratio
HIJING	1.40	2.27	1.62
$p+p$ Data	–	–	1.55

We begin by determining the distribution of BBC charge deposition in HIJING d+Au collisions, as shown in Fig. A.4. We compute the quantiles of the distribution, identically as in data, to define centrality classes. Once defined, we determine the true $N_{\rm coll}$ distribution for each centrality, as shown in Fig. A.5. The mean and width of the HIJING distributions compare favorably with those determined for data using Monte Carlo Glauber+NBD, as shown in Table A.2, although they are

	HIJING		Glauber + NBD	
Centrality	$\langle N_{\rm coll} \rangle$	RMS	$\langle N_{\rm coll} \rangle$	RMS
0-20%	15.0	4.1	15.06 ± 1.01	4.87
20-40%	10.1	3.5	10.25 ± 0.70	4.25
40-60%	6.3	3.0	6.58 ± 0.44	3.59
60-88%	2.8	2.0	3.12 ± 0.19	2.31

somewhat narrower.

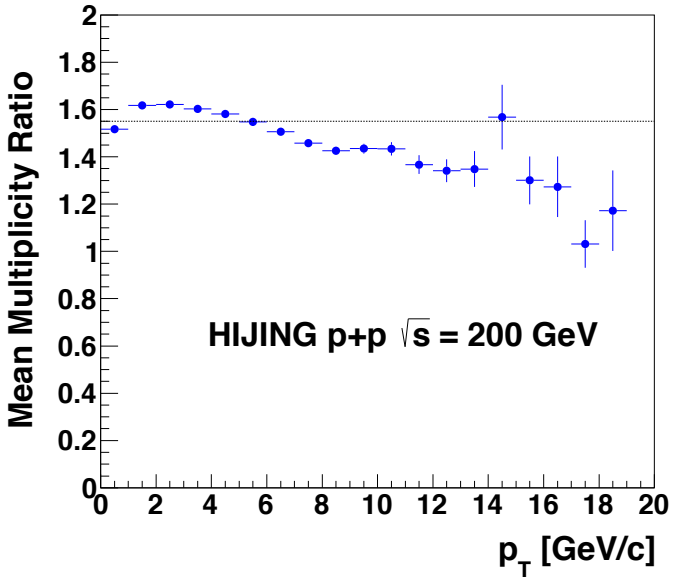

Figure A.3: The p_T dependence of the ratio of mean multiplicity in the BBC-South in triggered events with particle production at midrapidity, to all inelastic $p+p$ collisions in HIJING simulations. The dashed line indicates the reference inclusive mean multiplicity ratio of 1.55. Figure reproduced from [25].

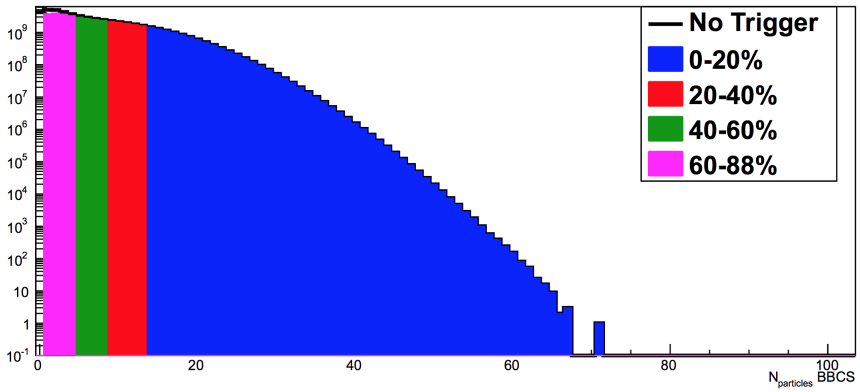

Figure A.4: Distribution of BBC charge deposition in HIJING d+Au events. The quantiles of this distribution, as shown, correspond to centrality categories.

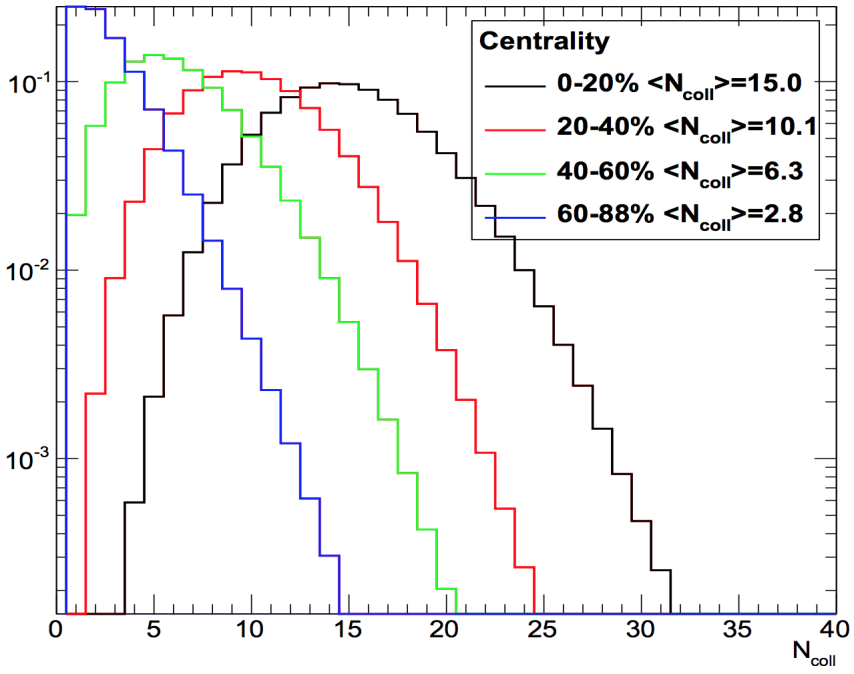

Figure A.5: Distribution of the number of binary collisions N_{coll} for HIJING d+Au, in various centrality classes.

We then proceed to calculate the bias factors. This requires determining, for each centrality, the *measured* particle yield at midrapidity (which is affected by the autocorrelation bias with forward multiplicity), and the *true* particle yield (which, unlike in data, can be determined in

simulations). The measured yield is straightforward to obtain, as one simply needs to count the number of particles in the central arm acceptance. On the other hand, determining the true yield requires sorting all events into centrality classes to match the $N_{\rm coll}$ distributions determined from the measured selections. In other words, in this approach it is the $N_{\rm coll}$ distribution that determines the centrality class. Computationally, this amounts to convolving, for each desired p_T bin, the $N_{\rm coll}$ distribution of the centrality of interest with the yield per event of particles in the given p_T range as a function of $N_{\rm coll}$. This procedure is summarized schematically for the 0-20% centrality class in Fig. A.6. The bias factor is then simply

$$C(p_T) = \frac{\text{True Yield}(p_T)}{\text{Measured Yield}(p_T)}. \tag{A.3}$$

The d+Au bias factors, as a function of p_T, for each centrality class are shown in Fig. A.7. In the 0-20% centrality class, we observe a slight rise in the bias factor with increasing p_T. In peripheral events we observe no discernible p_T dependence. The same results are summarized in Table A.4 and compared to the values from the Glauber+NBD calculation, with which a good agreement is observed.

Finally, we can apply the method we have developed to calculate bias factor corrections for p+Pb collisions at $\sqrt{s_{NN}} = 5.02$ TeV, as occur at the LHC. The results are shown in Fig A.8. In this case, we observe the same qualitative behavior—namely, bias factors are less than unity in central collisions, consistent with unity for mid-central, and greater than unity in peripheral. However, quantitatively, we observe these bias factors to be quite large, about an order of magnitude higher than the bias factors at RHIC energy, and strongly p_T-dependent. The large magnitude of bias factors at LHC energies can be understood from the autocorrelation between the particles production at midrapidity and the multiplicity of the event. Whereas at RHIC energies the multiplicity at backward rapidity—used to determine centrality—depends only modestly on the particle p_T at midrapidity, it exhibits a strong p_T dependence at LHC energies [25]. Such increase in multiplicity with particle p_T has been investigated, and is well described by multi-parton interactions [180], particularly within the range $1 < p_T < 10$ GeV/c. We verified that HIJING accounts for the increase

in multiparton activity with collision energy by examining the average number of hard scatterings per nucleon-nucleon interaction, which goes from 0.24 in the case of d+Au at $\sqrt{s_{NN}} = 200$ GeV, to 1.36 for p+Pb at $\sqrt{s_{NN}} = 5.02$ TeV.

The large magnitude of these bias factors is certainly a matter of concern, since any centrality-dependent measurement of particle yields at LHC energies will be substantially affected. The ALICE collaboration has investigated the bias [11] using various centrality estimators, and has quantified its magnitude in p+Pb collisions at $\sqrt{s_{NN}} = 5.02$ TeV through a quantity called $Q_{p+\mathrm{Pb}}$, akin to a nuclear modification factor $R_{p+\mathrm{Pb}}$, whose deviations from unity at high p_T are inversely proportional to the bias factors as defined in this dissertation. Fig. A.9 shows $Q_{p+\mathrm{Pb}}$ calculated using four different centrality estimators used by ALICE, which show a good qualitative agreement, and a reasonable quantitative agreement with the HIJING bias factors.

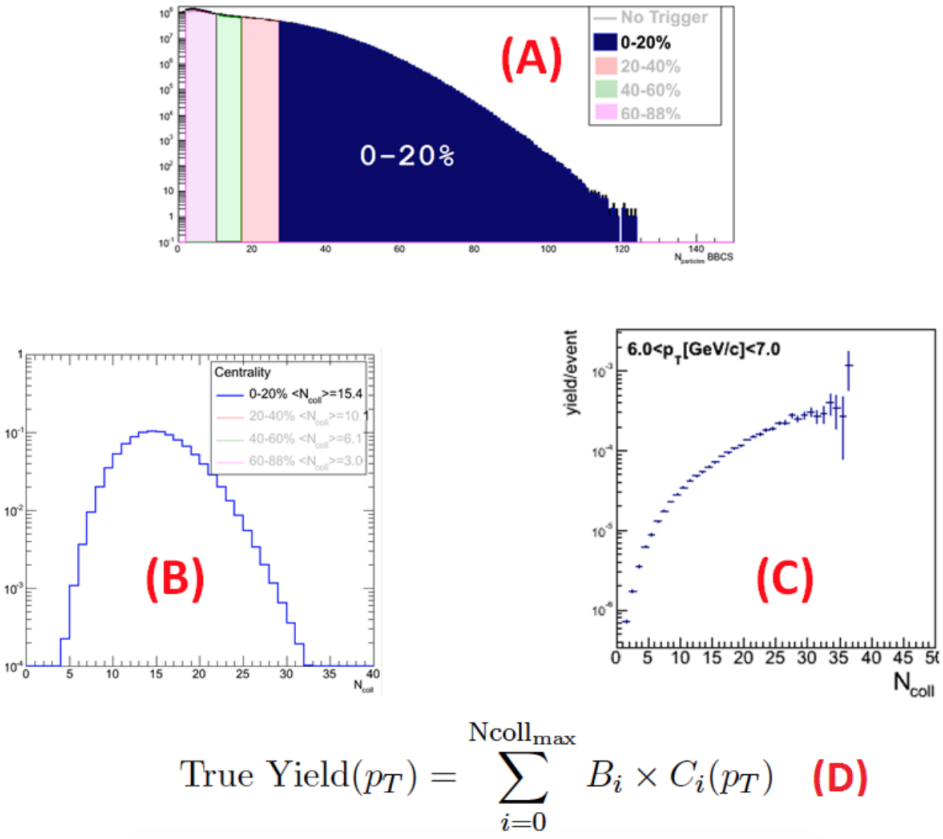

Figure A.6: Histogram (A) is the BBC charge distribution used to define centrality categories as one would experimentally. Once the range of BBC charge for a given centrality is known, we extract histogram (B) correspondin to the N_{coll} distribution for events in a given centrality. This histogram defines the event category of interest. Histogram (C) is the yield per event of particles in a given p_T range as a function of N_{coll}. Is is independent of event centrality. Finally, Equation (D) shows the calculation of the true particle yield as a function of p_T. It is calculated by summing, for each bin, the product of the normalized N_{coll} and the particle yield per event.

Table A.4: Mean bias factors as a function of p_T for each centrality class in HIJING d+Au collisions, compared to reference values from a Glauber+NBD calculation.

Centrality	Glauber+NBD	HIJING $1 \leq p_T < 5$	HIJING $5 \leq p_T < 10$	HIJING $10 \leq p_T < 15$	HIJING $15 \leq p_T < 20$
0-20%	0.94 ± 0.01	0.951 ± 0.001	0.962 ± 0.001	1.000 ± 0.005	1.038 ± 0.020
20-40%	1.00 ± 0.01	0.996 ± 0.001	1.008 ± 0.001	1.010 ± 0.006	0.996 ± 0.021
40-60%	1.03 ± 0.02	1.010 ± 0.001	1.022 ± 0.001	1.019 ± 0.007	1.005 ± 0.025
60-88%	1.03 ± 0.06	1.030 ± 0.001	1.026 ± 0.001	0.999 ± 0.008	0.991 ± 0.030

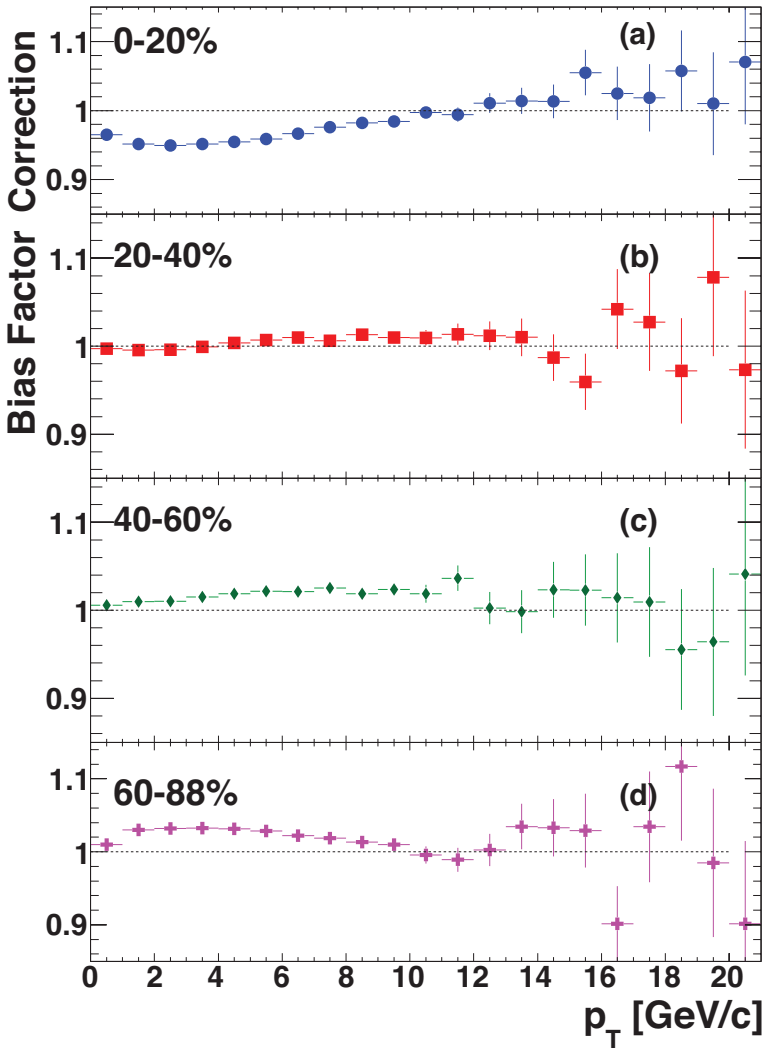

Figure A.7: Bias factor corrections for four different centrality classes in d+Au collisions at $\sqrt{s_{NN}} =$ 200 GeV. Figure reproduced from [25].

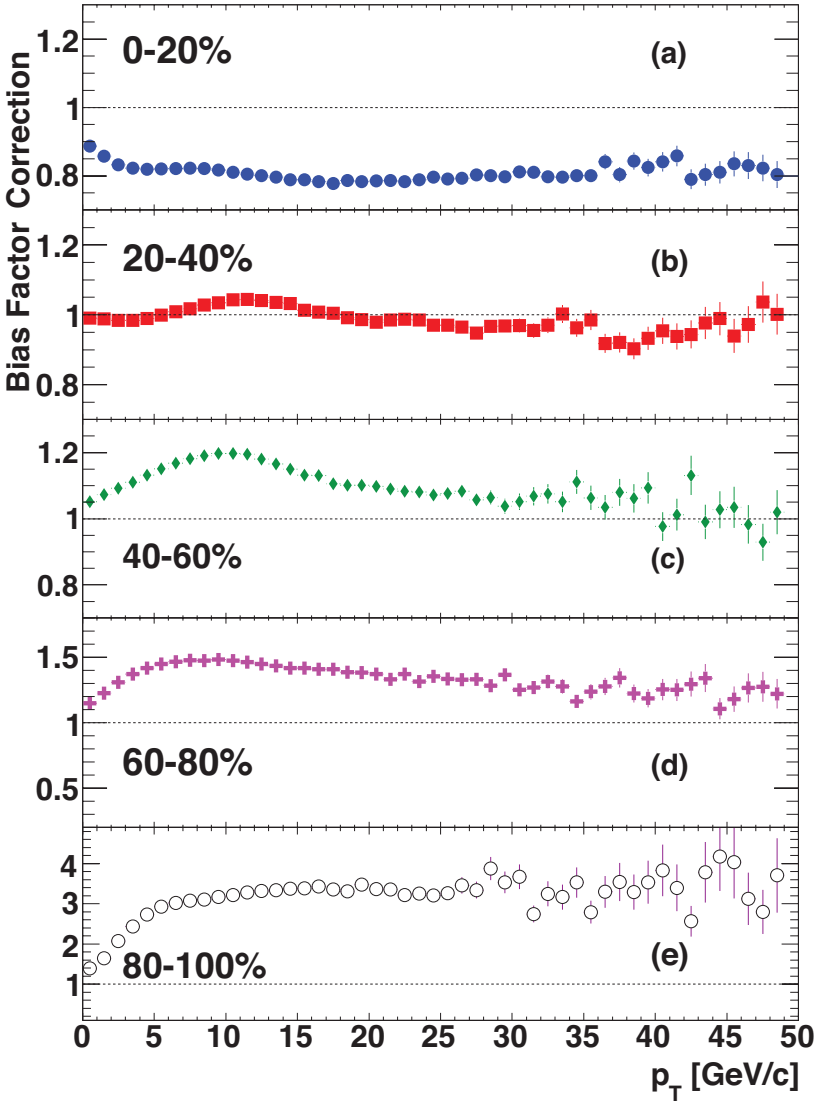

Figure A.8: Bias factor corrections for five different centrality classes in p+Pb collisions at $\sqrt{s_{NN}} =$ 5.02 TeV. Figure reproduced from [25].

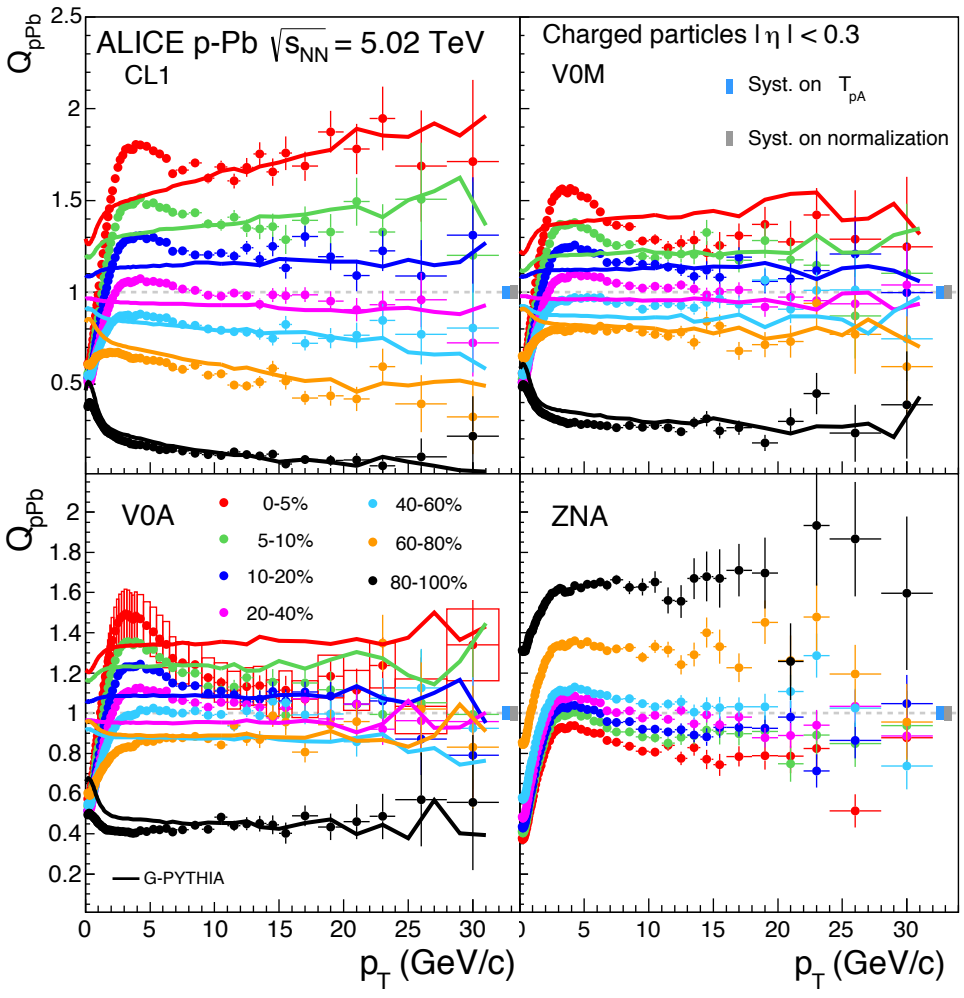

Figure A.9: The centrality-dependence of the $Q_{p+\mathrm{Pb}}$ quantity, as defined by the ALICE collaboration, in p+Pb collisions at $\sqrt{s_{NN}} = 5.02$ TeV, using various centrality estimators. See text for details. Figure reproduced from [11].

Appendix B

Alignment of the PHENIX Silicon Vertex Detector

The VTX detector, as described in Chapter 6, was constructed and installed following design specifications for the spatial layout and arrangement of the various detector elements relative to each other in the PHENIX coordinate system. This design-level description of the coordinates and orientation of each VTX ladder is known as the detector's *ideal geometry*, as shown in Fig. 6.15 in the transverse plane. Nevertheless, the placement of detector elements in the PHENIX experimental hall necessarily differs from the ideal geometry due to mounting uncertainty. It is thus crucial to quantitatively reconcile the extent of these differences since track reconstruction is carried out with a software model of the VTX geometry, such that achieving the desired tracking resolution depends on the software accurately describing the spatial coordinates of detector hits in space.

This appendix describes in detail the procedure—known as detector alignment—followed to construct an accurate representation of the VTX geometry as installed in the experimental hall in 2015. Two types of alignment are discussed, namely the *self-alignment*, in which VTX ladders are aligned relative to each other, and the *global alignment*, in which the orientation of the VTX as a whole is aligned relative to the PHENIX central arms. The self-alignment procedure was carried out a single time at the beginning of the 2015 data-taking period, while the alignment relative to the central arms was carried out every time the carriage carrying the central arm subsystems was moved for maintenance access.

The self-alignment procedure was carried out with the Millepede II software, version 04-01-01, developed by V. Blobel to solve linear least squares optimization problems consisting of hundreds

or thousands of parameters.[1] While many software packages implement linear least squares, Millepede is special in that it distinguishes between *global* and *local* parameters, eliminating local parameters to reduce the dimensionality of the associated matrix inversion problem, which would otherwise be intractable or would require an inordinate amount of processing time and resources. While the implementation of the method in Millepede is perfectly general, it was developed for and has been applied particularly to the problem of aligning large detectors in high-energy physics experiments. For instance, see Ref. [99] for a description of the alignment of the CMS silicon tracker. In particular, for tracking detectors, the alignment proceeds through the minimization of residuals between track projections and the detector hits from which tracks are reconstructed.

B.1 Dimensionality Reduction in Global Least Squares Minimization

Before delving into the details of how Millepede was used to align the PHENIX VTX detector, it is perhaps useful to first consider a generic example of how Millepede reduces the dimensionality of large least squares problems [64, 145]. Consider a series of hits in a misaligned detector, which are reconstructed into a finite number of tracks. Let $\vec{y}$ be a vector with the coordinates of the detector hits, and $\vec{x}$ be a vector containing the parameters of the reconstructed tracks. Then, the residuals $\vec{r}$ are given by

$$r_i = y_i - f(x_i, \vec{\beta}), \tag{B.1}$$

where $f(x_i, \vec{\beta})$ is a linear function depending on the parameters $\vec{\beta}$, describing the geometry of the detector, as follows

$$f(x_i, \vec{\beta}) = \sum_j \beta_j X_{ij}. \tag{B.2}$$

The problem is then to find the set of parameters $\vec{\beta}_0 = \underset{\beta}{\operatorname{argmin}}(S)$ which minimize the squared sum of residuals S. If V is the covariance matrix associated with the residuals, then the sum of residuals is given by $S = \vec{r}^T V \vec{r}$. This can be differentiated with respect to the parameters $\vec{\beta}$ to arrive at a

[1] The Millepede manual, which is the primary documentation for the software, is available at `http://www.desy.de/~kleinwrt/MP2/doc/html/draftman_page.html`. The source code, as well as other useful documentation can be found under `http://www.desy.de/~blobel/mptalks.html`.

matrix equation—known as the normal equation—for $\vec{\beta}_0$, as covered in any standard reference on least squares minimization. The normal equation takes the form

$$(X^T V X)\vec{\beta} = X^T V \vec{y}. \tag{B.3}$$

Ordinarily, the normal equation could be solved through a number of standard procedures for overdetermined systems. However, the problem lies in the dimension of A, which makes the inversion a very expensive procedure, in terms of computation. Consider an alignment problem, for a detector of M modules and N degrees of freedom per module. In that case, $M \times N$ parameters are required to describe the detector. In addition to these global parameters, there will be a number of local parameters associated with the number of hits per detector element and the parameters required to describe a given track projection at each element. For example, the VTX has 70 ladders (140 half-ladders), 8 degrees of freedom per ladder (which will be discussed later), two parameters for a straight line fit per track. Thus, it is easy to see that the number of parameters becomes very large for detector alignment problems.

The key insight of the Millepede approach is that only global parameters—those describing the detector itself—are relevant. Thus, let global and local parameters be labeled with the superscripts (G) and (L), respectively. The matrix normal equation can be recast by writing the matrix $A^T V A$ in ordered form, with global parameters in the upper left corner. In that case, the matrix will take on a special block structure, and the normal equation $(A^T V A)\vec{\beta} = A^T V \vec{y}$ will read

$$\begin{bmatrix} \sum C_i & G_1 & \dots & G_i & \dots \\ G_1^T & \Gamma_1 & 0 & 0 & 0 \\ \vdots & 0 & \ddots & 0 & 0 \\ G_i^T & 0 & 0 & \Gamma_i & 0 \\ \vdots & 0 & 0 & 0 & \ddots \end{bmatrix} \cdot \begin{bmatrix} \vec{\beta}^{(G)} \\ \beta_1^{(L)} \\ \vdots \\ \beta_i^{(L)} \\ \vdots \end{bmatrix} = \begin{bmatrix} \vec{\delta}^{(G)} \\ \delta_1^{(L)} \\ \vdots \\ \delta_i^{(L)} \\ \vdots \end{bmatrix}, \tag{B.4}$$

where $\vec{\delta} = (\vec{\delta}^{(G)}, \vec{\delta}^{(L)}) = A^T V \vec{y}$. The block matrix $\sum C_i$ is a square matrix corresponding to the global parameters; the matrices Γ_i on the diagonal correspond to local parameters from a given

track; and the G_i matrices connect global and local parameters. The sparseness and block structure of $A^T V A$ considerable simplifies the problem of finding its inverse by allowing it to be reduced to a matrix problem of dimension equal to number of global parameters. With this approach, the Millepede is capable of solving alignment problems with up to 10^5 parameters in a matter of a few hours.

B.2 Self-Alignment of the PHENIX VTX

B.2.1 Track Fitting

The previous section outlined the mathematics of finding a set of global parameters (i.e., the geometry of detector elements) that minimize the squared sum of residuals between detector hits and track projections in Millepede. We now turn our attention to setting up this problem in the context of the PHENIX VTX detector.

PHENIX carries out the alignment procedure using data collected when the magnetic field in the central arms is turned off. In these zero-field runs, particle tracks in the VTX detector follow straight trajectories that are fit independently in the transverse and in the $r - z$ planes. In the transverse plane, the fit is parameterized by

$$y'(x') = m'x' + y'_0, \tag{B.5}$$

where the primed variables indicate the rotated coordinate system about the z axis by the track's azimuthal angle, such that the track is aligned with the x axis. In this way, the errors have the correct orientation required by the least squares fitting procedure, and m' and y'_0 become fit parameters. In the $r - z$ plane, the fit equation is

$$z(x') = x' \cot\theta + z_0. \tag{B.6}$$

The fit parameters of the above linear equations are determined through maximum likelihood estimation assuming a multivariate Gaussian model for errors. Just as in the previous section, we seek parameters $\vec{\beta}$ that minimize $(\vec{y} - X\vec{\beta})^T V (\vec{y} - X\vec{\beta})$, where V is the covariance matrix

containing the measurement resolutions. In this case, the normal equation is solved using singular value decompositon (SVD) since the dimensionality of the problem is small, corresponding to the number of hits in the track.

Having obtained the fits as described above, the residuals are defined as

$$\Delta s = y'_0 + m'x' - y'_{\text{measured}} \tag{B.7}$$

in the azimuthal direction, and

$$\Delta z = z_0 + x' \cot\theta - z'_{\text{measured}} \tag{B.8}$$

in the longitudinal direction.

B.2.2 Beam Center and DCA Determination

Having fit straight line tracks, it is possible to determine the collision vertex (v_x, v_y) on an event-by-event basis. This is done, again, by solving a linear system of equations through least squares estimation. In the transverse plane, the system is given by

$$y_0^{(i)} = -m^{(i)} v_x + v_y, \tag{B.9}$$

where the index i runs over the number of reconstructed straight line tracks, m is the track slope, and $y_0 = y(x = 0)$. In the longitudinal direction, the system is given by

$$z_0^i = -\cot\theta^{(i)} v_r + v_z. \tag{B.10}$$

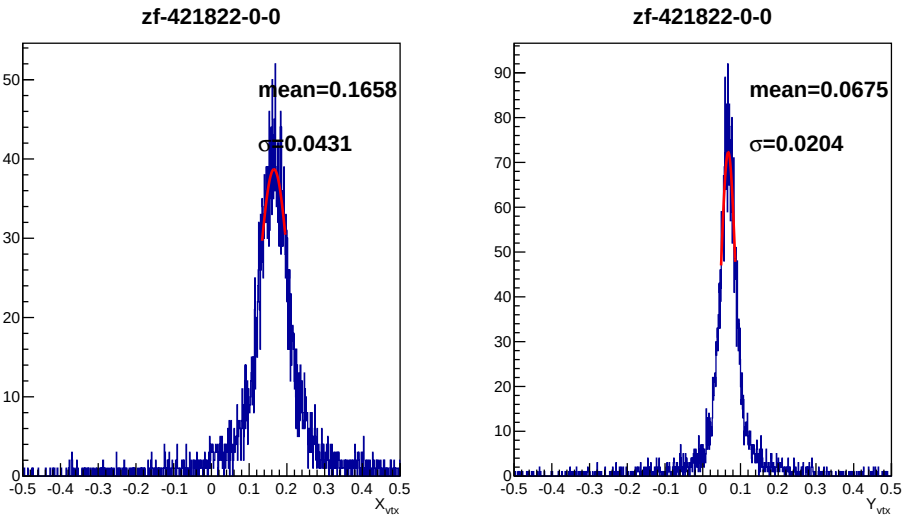

Figure B.1: Distribution of event vertices in the x and y directions prior to alignment. The position of the beam center is extracted from fits to the distributions.

The distribution of event vertices in x and y obtained for a single zero-field run prior to carrying out the Millepede alignment is shown in Fig. B.1. The location of the beam center is extracted from fits to the distributions, as shown. This value, obtained prior to alignment, is held constant and used for every iteration of the alignment procedure, as will be described in the next section.

Having determined the beam center, the distance of closest approach (DCA) of tracks relative to the beam center can be calculated, as a fundamental observable that can be used to assess the quality of the alignment. In the transverse plane, the DCA is given by

$$DCA_{xy} = \hat{n} \cdot \vec{b}, \tag{B.11}$$

where $\hat{n} = (-\sin\phi, \cos\phi)$ is the normal vector, and $\vec{b}$ is the impact parameter of the track. In the rotated frame, it is just the distance between the track projection and the rotated vertex position, $\vec{b'} = (0, y'_0 + m'v'_x - v_y y)$. In the longitudinal direction, the DCA is given by

$$DCA_z = z_0 + v'_x \cot\theta - v_z. \tag{B.12}$$

Note that the above definition of the DCA is distinct from that used in the displaced vertex analysis

described in Chapter 7.

B.2.3 Alignment Procedure

The Millepede alignment of the VTX detector can be carried out for three different detector units, corresponding to different levels of granularity. Namely, it is possible to carry out the alignment at the half-ladder, ladder, and arm level. During alignment, all units are allowed to move independently along Cartesian (x, y, z) or polar (r, s) degrees of freedom. In addition to these, the arms are allowed to rotate about their principal axes, *roll, pitch* and *yaw*. The track fits and their corresponding residuals as well as the beam center value, as described in the previous subsection, are provided as input to Millepede, which then proceeds to iteratively carry out local track fitting as the various detector elements move during alignment. Since the minimization of the objective function requires the computation of its gradient, it is necessary to provide Millepede with expressions for the derivatives, global and local. Local derivatives follow straightforwardly from the expressions for $y(x')$ and $z(x')$ in subsection B.2.1, while global derivatives—corresponding to the change in Δs and Δz when a detector element moves in a given direction—are listed in Table B.1.

Table B.1: Global derivatives of residuals relative to relevant coordinate degrees of freedom.

$d.o.f$	Δs	Δz
x	$-\sin\phi$	$\cos\phi\cot\theta$
y	$\cos\phi$	$\sin\phi\cot\theta$
z	0	1
s	1	0
r	$\Delta s/r$	$-\cot\theta$
pitch	$-z\cos\phi$	$-y + z\sin\phi\cot\theta$
yaw	$-z\sin\phi$	$x - z\cos\phi\cot\theta$
roll	1	0

The alignment was carried out in four steps, beginning with alignment at the arm level, then at the half-ladder level, and finally at the ladder level. There is no fixed prescription to determine the specific steps in which to carry out the alignment, but we find this heuristic approach from coarse to fine granularity to yield good results. Table B.2 describes the steps involved in running the Millepede alignment, specifying the detector elements that were aligned, the degrees of freedom under consideration, as well as their respective constraints. The straight line tracking, described in subsection B.2.1, which serves as input to Millepede, was carried out in between alignment steps.

Table B.2: Steps followed in the VTX self-alignment. Each step consists of a series of sub-steps where the alignment is carried out along specific coordinates for specific detector elements subject to a series of constraints on the possible degrees of freedom.

STEP	DESCRIPTION	DEGREES OF FREEDOM	CONSTRAINTS
Step 1	Arm	(x, y, z)	None
Step 2	Arm	(x, y, z, P, Y)	None
	Half-Ladder	(x, y, z, s)	(x, y, z, s) shear
Step 3	Half-Ladder	(x, y, z, s)	(x, y, z, s) shear
			(s, z) translation
	Ladder	(s, z, r)	(z, s) shear
			(z, r) contraction/expansion
Step 4	Arm	(x, y, z, P, Y)	None

The final results of the self-alignment procedure are summarized in Fig. B.2. The left(right) panel shows the overall magnitude and direction of displacement in the transverse(longitudinal) direction of individual detector elements, in units of microns.

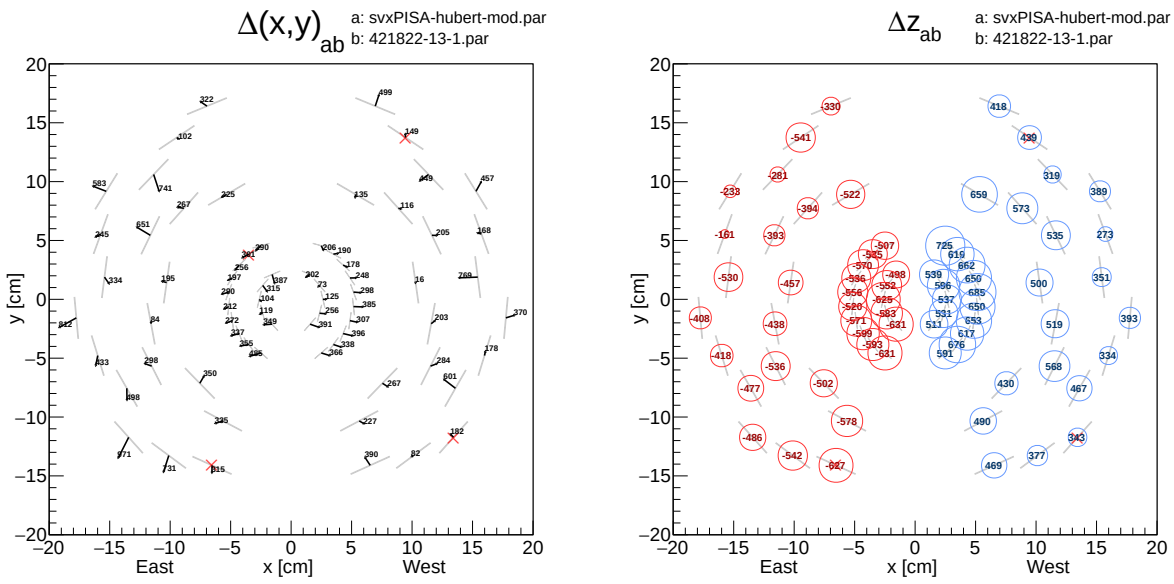

Figure B.2: Summary of coordinate changes, in microns, in the (left) transverse and (right) longitudinal direction for each ladder after the alignment procedure, relative to the ideal geometry.

On the other hand, Fig. B.3 provides an indicator of the quality of the alignment. Shown in the figure are the residuals Δs and Δz for each ladder in every layer. The residuals prior to te alignment procedure are shown in gray, appearing to be distributed around zero with large fluctuations. After the alignment, the resulting residuals are shown in red and blue, for Δs and Δz, respectively. In this case, they appear to be consistent with zero with minimal variation, as desired.

Furthermore, Fig. B.4 shows the xy vertex in the transverse plane as a function of the z vertex. Before the alignment, there is a clear linear trend with z vertex, whereas after the alignment the dependence is minimal. Fig. B.5 shows the azimuthal dependence of the DCA in the xy plane. Prior to alignment, it exhibits a clear sinusoidal modulation, becoming flat after the procedure, and centered around zero as shown in Fig. B.6. Lastly, Figs. B.10 to B.17 show the distribution of residuals in each ladder, in each layer, of the VTX before and after alignment. Prior to the procedure, the residuals are distributed normally with a non-zero mean, as shown by the gray histograms, and afterwards the distributions become centered very close to zero, as expected.

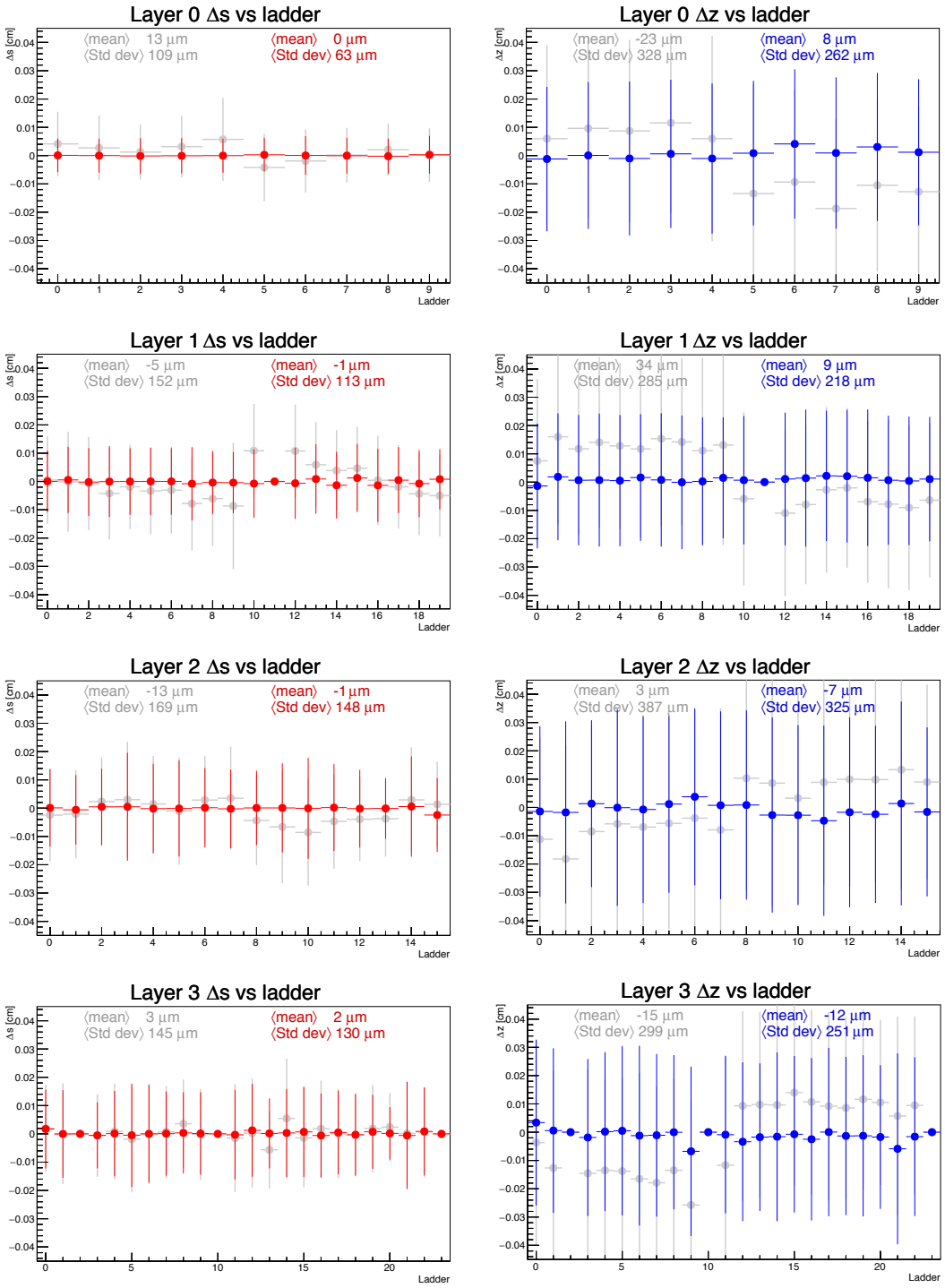

Figure B.3: Summary of residuals Δs, Δz in the azimuthal and longitudinal directions, respectively, as a function of ladder number for each layer of the VTX. The residuals prior to the alignment procedure are shown in gray, with the result after alignment shown in red and blue.

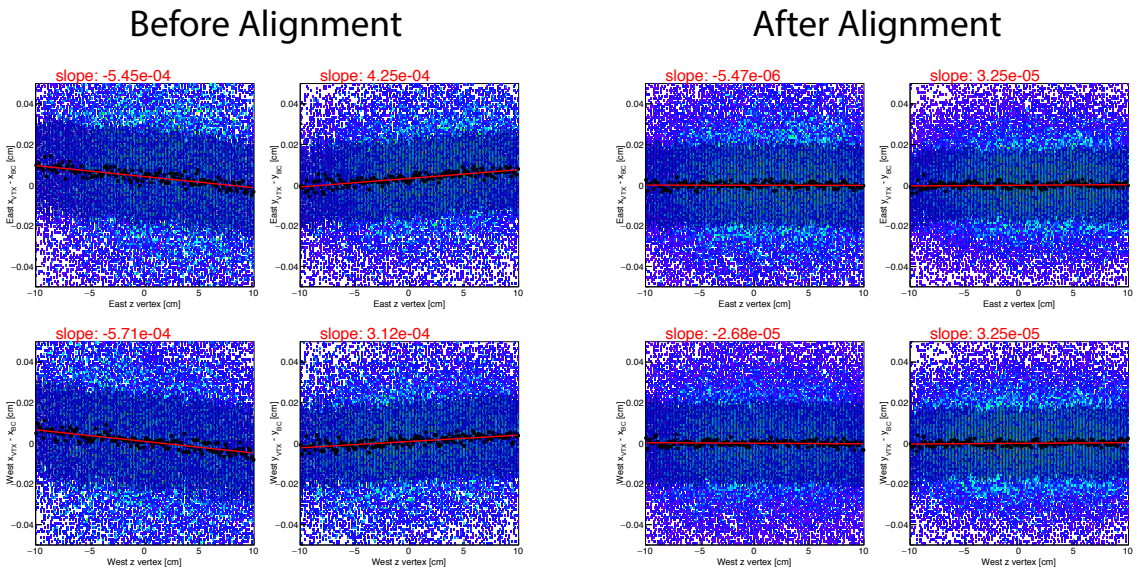

Figure B.4: Vertex in the xy plane versus z vertex before (left) and after (right) the alignment procedure. The top panels of each block show the east and west xy vertex versus the east z vertex, and the bottom panels shown the same xy vertices versus the west z vertex.

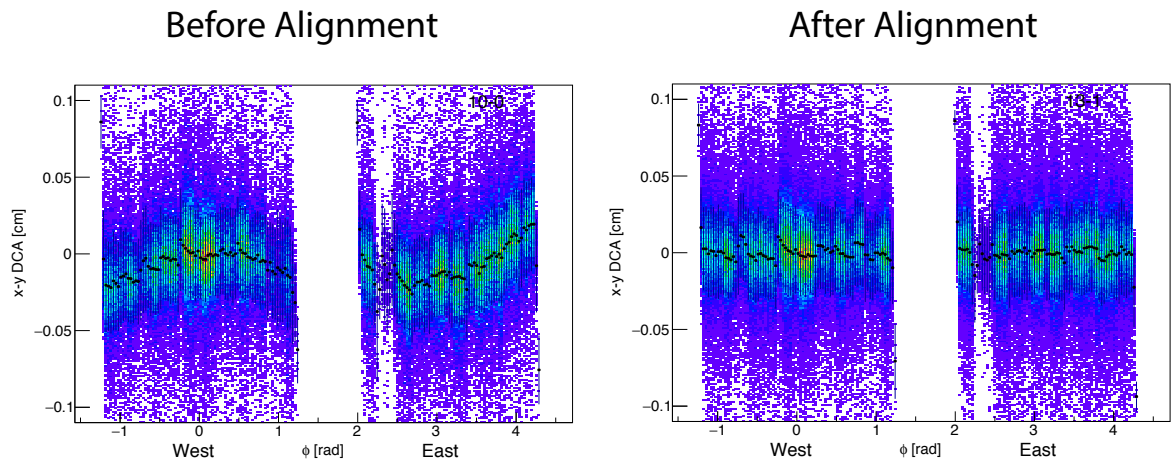

Figure B.5: Transverse DCA as a function of azimuthal angle before (left) and after (right) the alignment procedure.

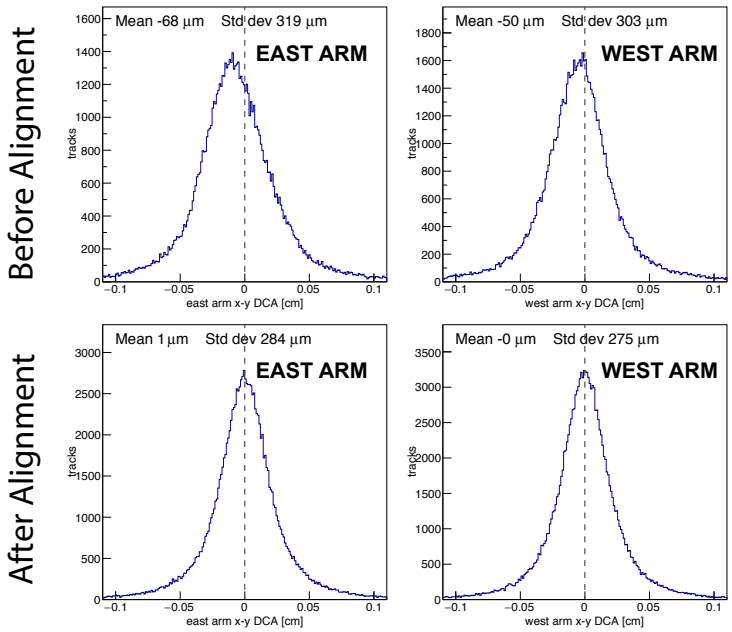

Figure B.6: Distribution of transverse DCA for tracks in the east and west detector arms before (top) and after (bottom) the alignment procedure.

B.3 Alignment of the VTX Relative to the PHENIX Central Arms

If the VTX detector were used exclusively to reconstruct particle tracks in standalone mode, the self-alignment procedure of the previous section would be sufficient. However, since the analysis described in this dissertation utilizes track objects reconstructed by matching tracks in the PHENIX central arm tracking with VTX hits, it is necessary to ensure that the VTX and the central arms are properly aligned. In this case, the entire VTX is taken as a single unit, with two degrees of freedom in azimuth ϕ and polar angle θ, assuming that the detector is properly self-aligned.

This alignment of the VTX relative to the central arms is not carried out with Millepede, and zero-field data is not necessary. The procedure begins by determining the beam center, as previously described, which is then used to reconstruct tracks in the central arms. These tracks are then matched to hits in the VTX detector, and residuals are calculated between the hits and

the track projection as follows

$$\Delta\phi = \arcsin(\Delta s / r_{\text{clus}}), \tag{B.13}$$

$$\Delta\theta = \arcsin(\Delta z / r_{\text{clus}}), \tag{B.14}$$

where r_{clus} is the radial coordinate of a given VTX hit. The distribution of residuals in each detector layer can be plotted for each detector arm, as shown in Fig. B.7 for $\Delta\phi$, and in Fig. B.8 for $\Delta\theta$. The mean of the distributions can be estimated through a Gaussian fit. The left panel of Fig. B.9 shows the mean $\Delta\phi$ and Δz in each arm prior to alignment, which are seen to be roughly constant as a function of ladder number such that they can be fit with a constant, as is also shown in the figure. The fit constant provides a set of parameters by which tracks in the central arms are rotated. This procedure can be carried out iteratively, reconstructing tracks after every rotation, until the extracted rotation parameters become arbitrarily small. The right panel of Fig. B.9 shows the resulting mean residuals after the last step of the alignment procedure.

The alignment of the VTX relative to the central arms was carried out seven times during the $p + p$ run period in 2015, immediately after a carriage move, obtaining the average residuals shown in Table. B.3.

Table B.3: Average residuals for each arm, computed after each central arm carriage move.

	Arm 1		Arm2	
Run Number	$\Delta\phi$	Δz	$\Delta\phi$	Δz
421999	0.0038	0.0056	-0.0050	-0.0020
423268	0.0043	0.0043	-0.0047	-0.0060
425171	0.0037	0.0046	-0.0047	-0.0055
427020	0.0037	0.0048	-0.0047	-0.0054
429114	0.0035	0.0044	-0.0038	-0.0062
430124	0.0041	0.0044	-0.0042	-0.0058
431022	0.0042	0.0032	-0.0040	-0.0059

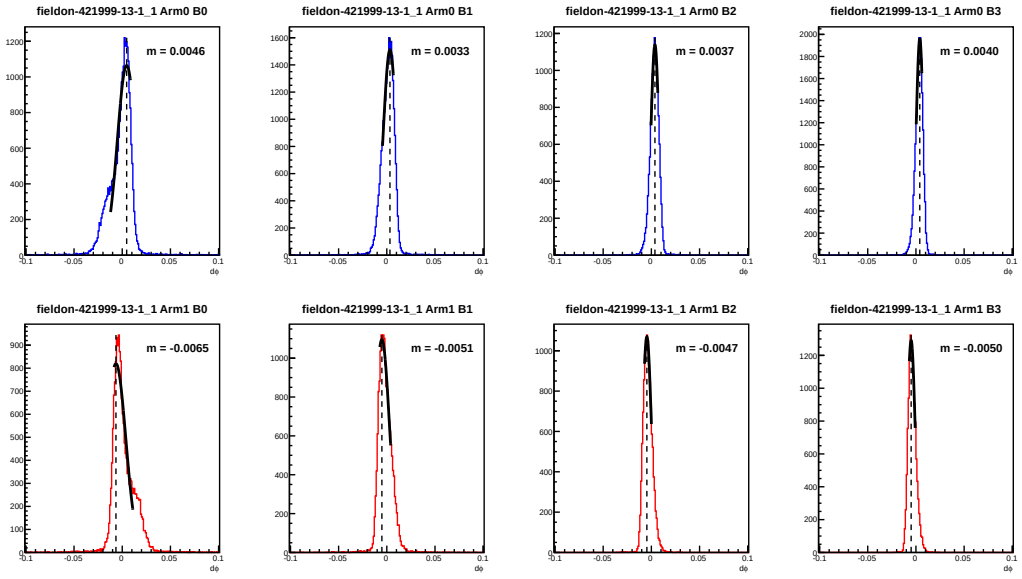

Figure B.7: Distribution of $\Delta\phi$ residuals in each layer in the East (top) and West (bottom) detector arms for the alignment procedure relative to the central arms.

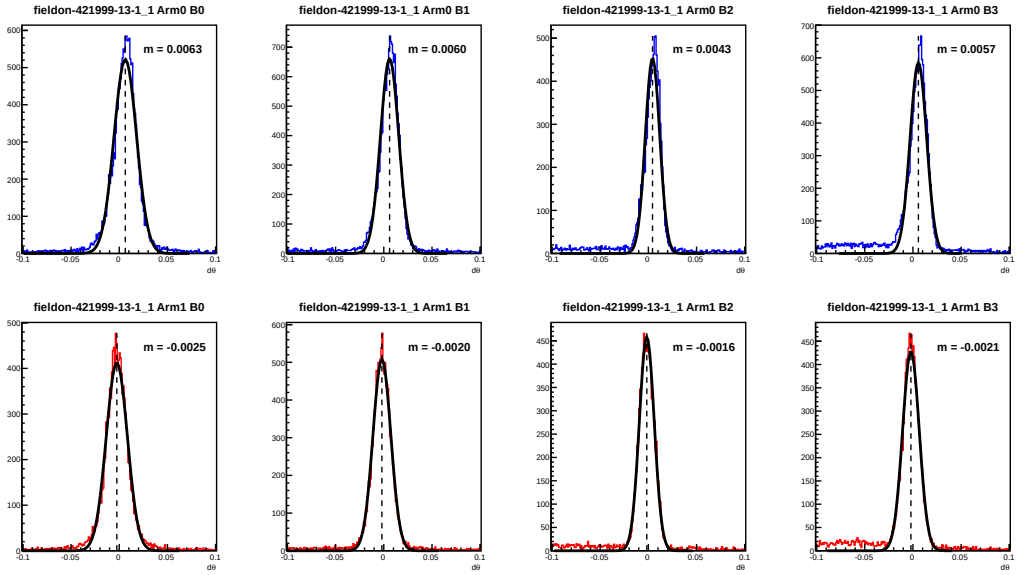

Figure B.8: Distribution of $\Delta\theta$ residuals in each layer in the East (top) and West (bottom) detector arms for the alignment procedure relative to the central arms.

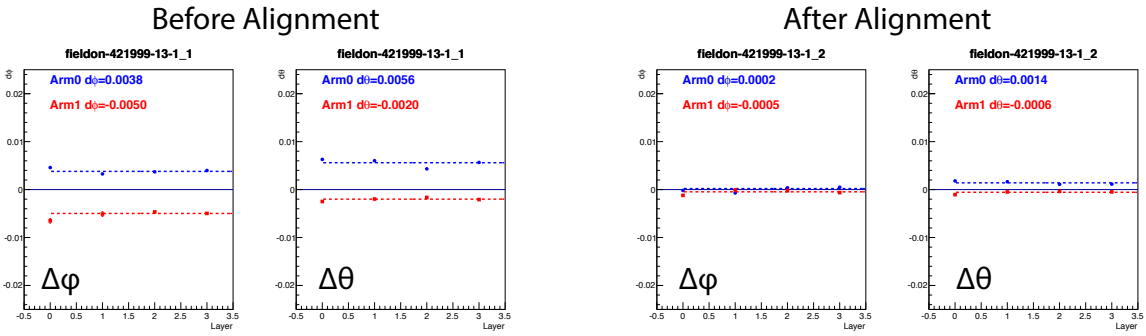

Figure B.9: Mean residuals $\Delta\phi$ and $\Delta\theta$ for every ladder in the two arms of the VTX, before (left) and after (right) the alignment with respect to the central arms.

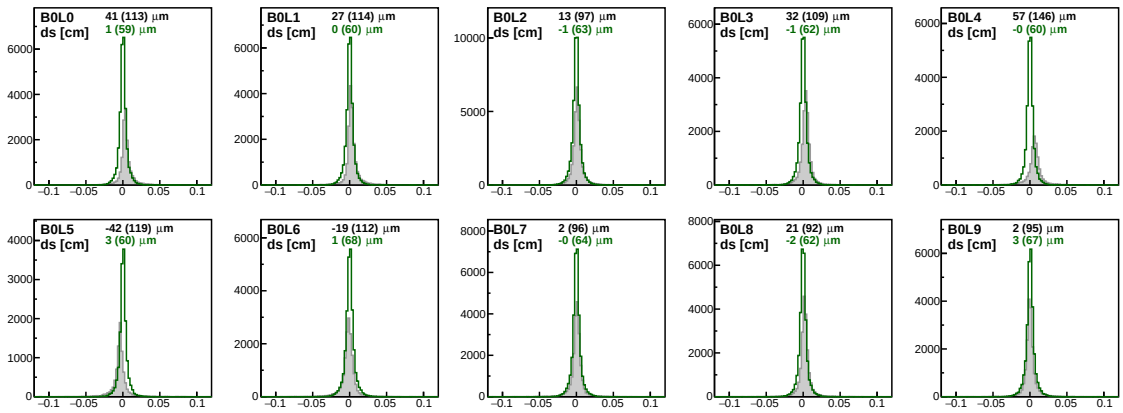

Figure B.10: Distributions of *ds* residuals for every ladder in layer B0.

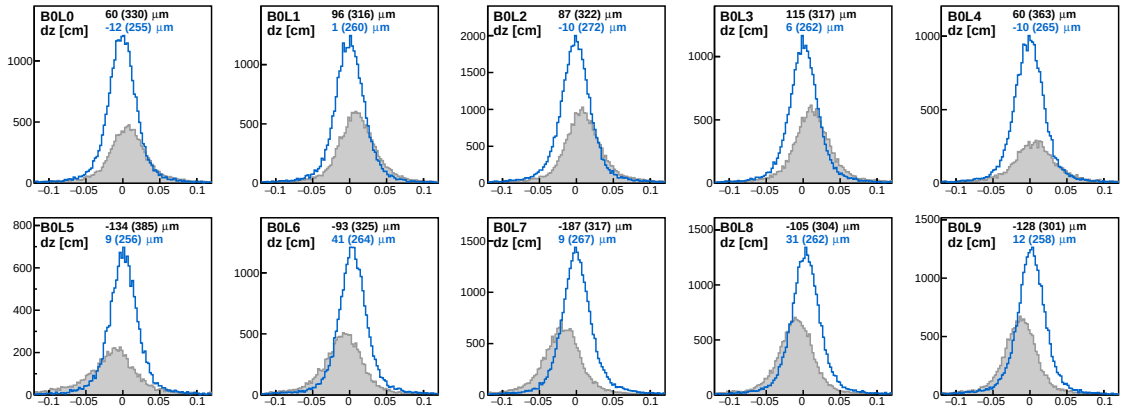

Figure B.11: Distributions of *dz* residuals for every ladder in layer B0.

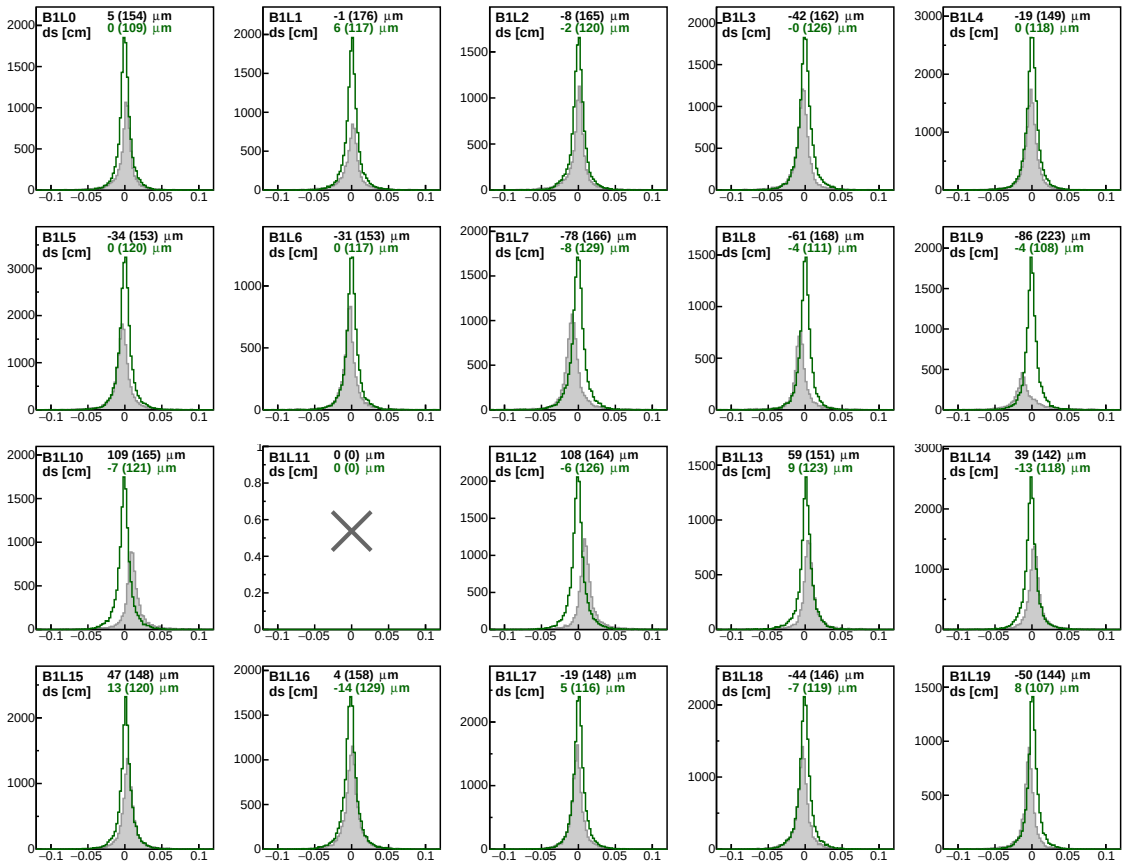

Figure B.12: Distributions of *ds* residuals for every ladder in layer B1.

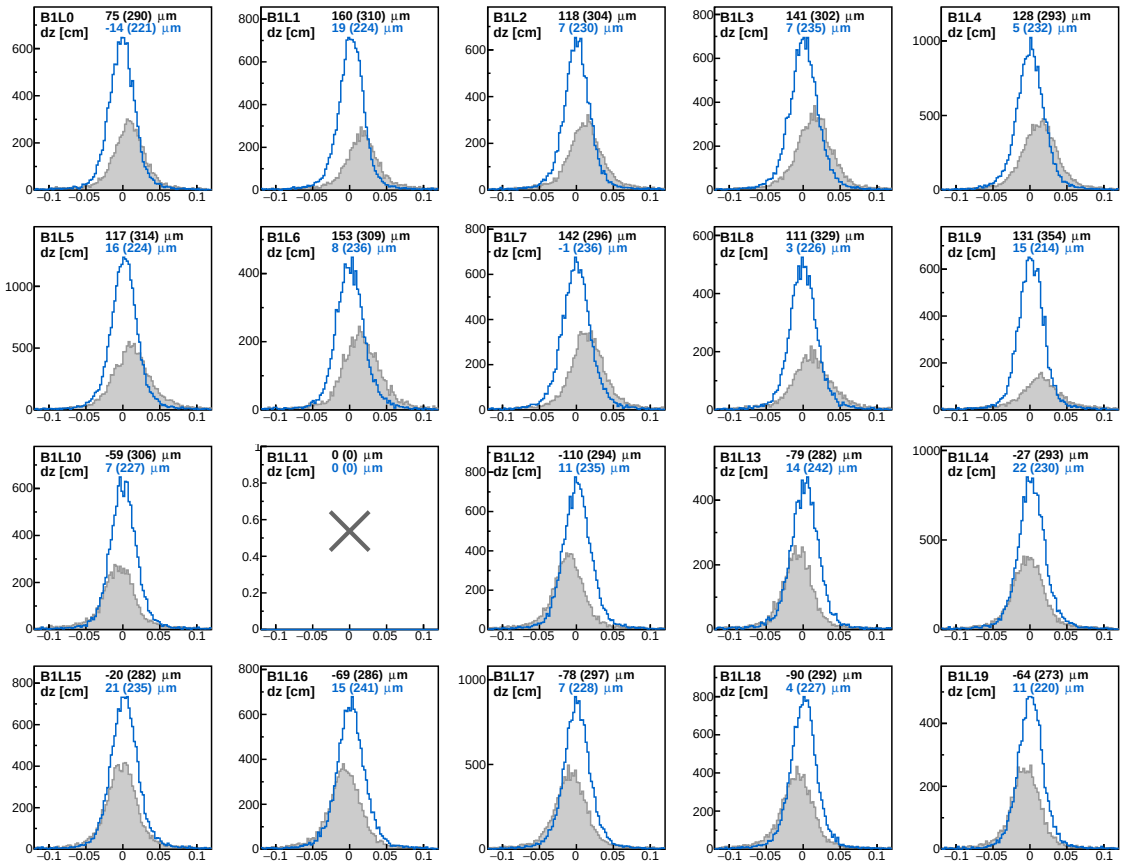

Figure B.13: Distributions of dz residuals for every ladder in layer B1.

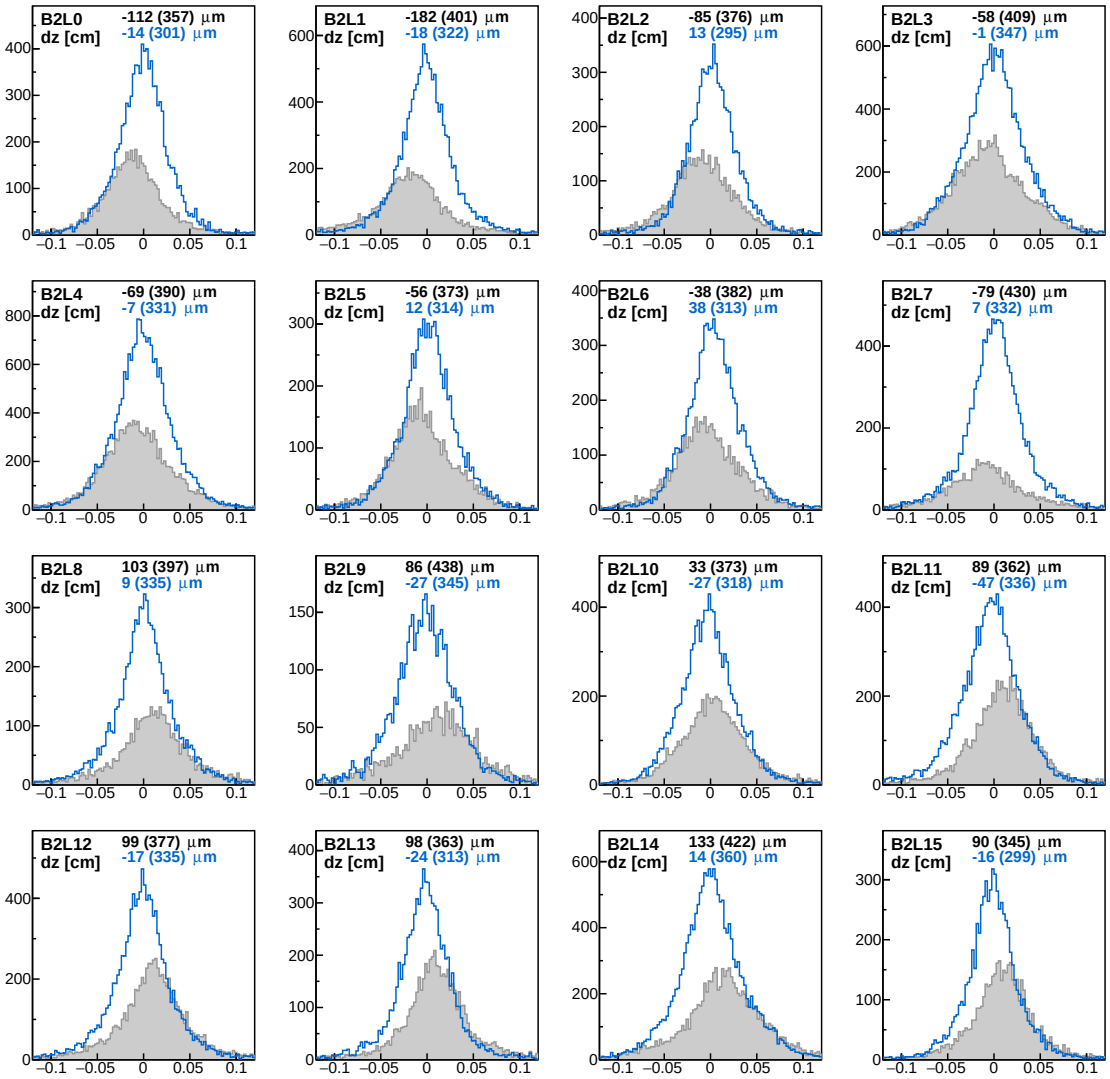

Figure B.14: Distributions of *ds* residuals for every ladder in layer B2.

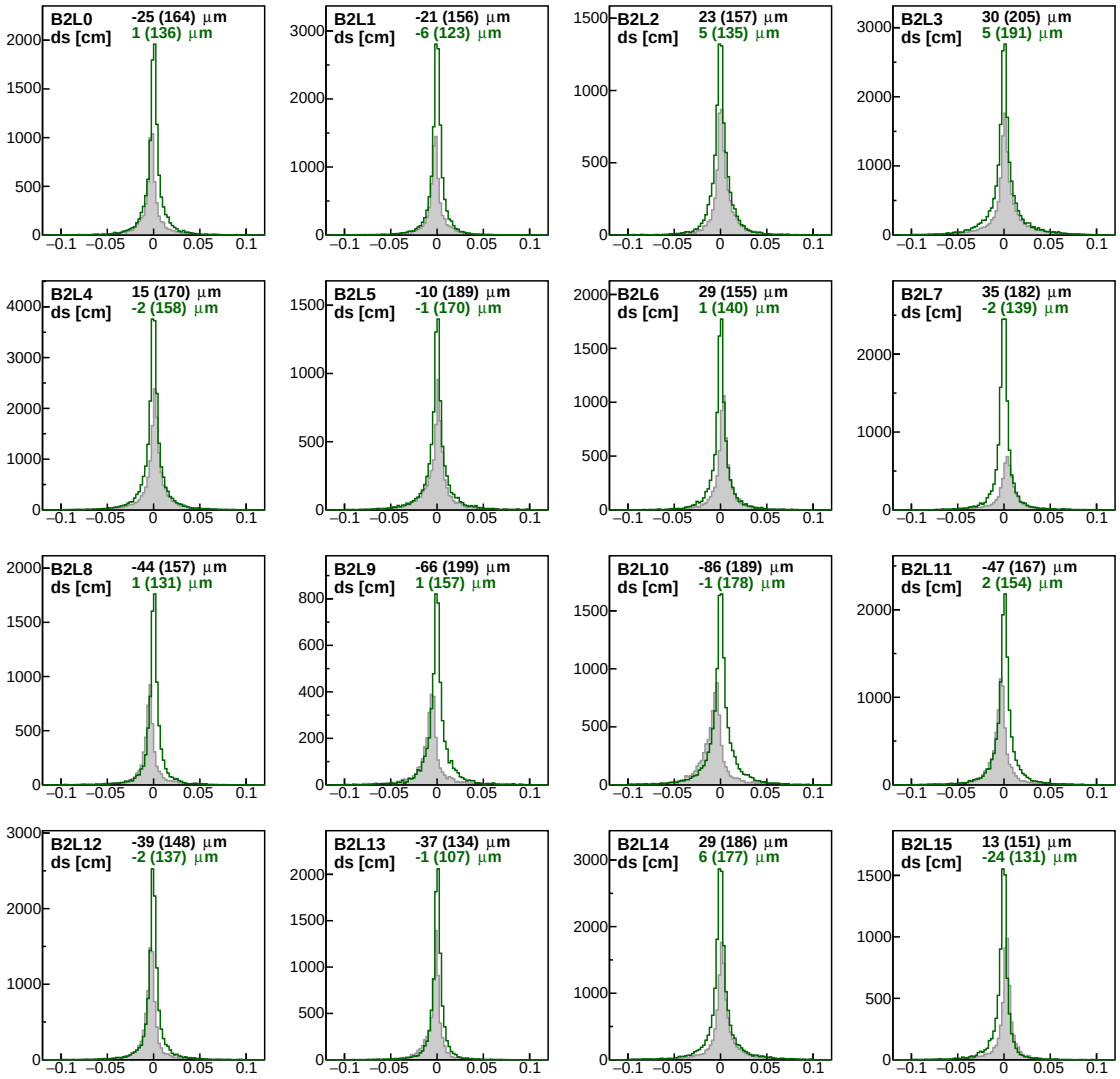

Figure B.15: Distributions of dz residuals for every ladder in layer B2.

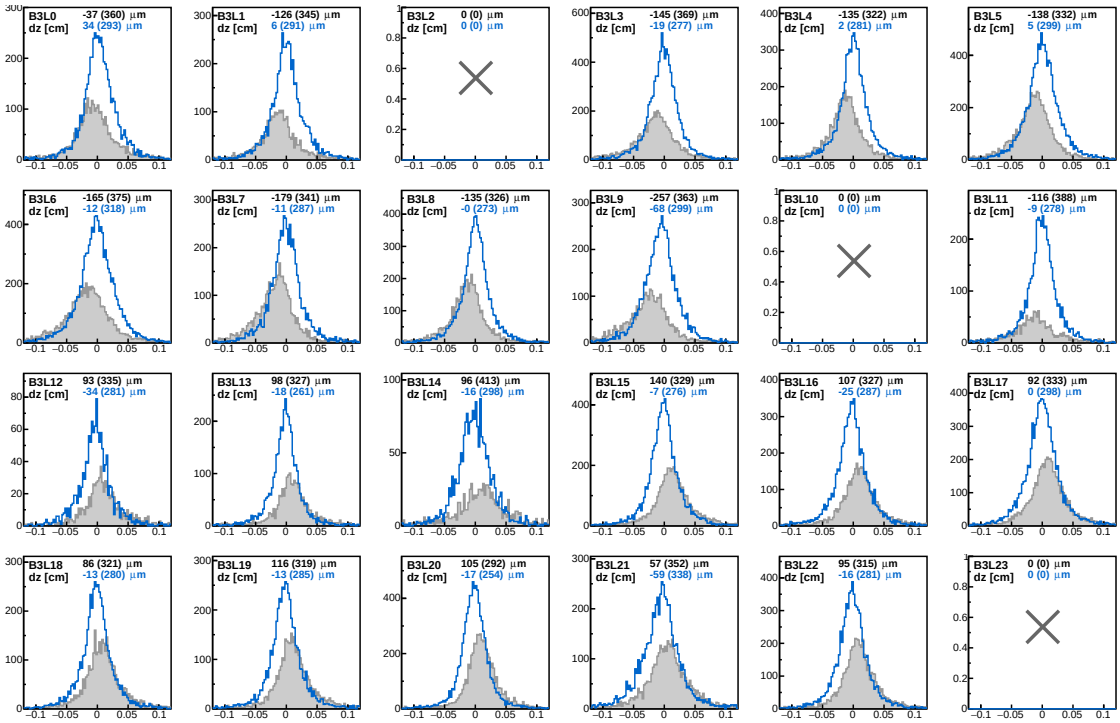

Figure B.16: Distributions of *ds* residuals for every ladder in layer B3.

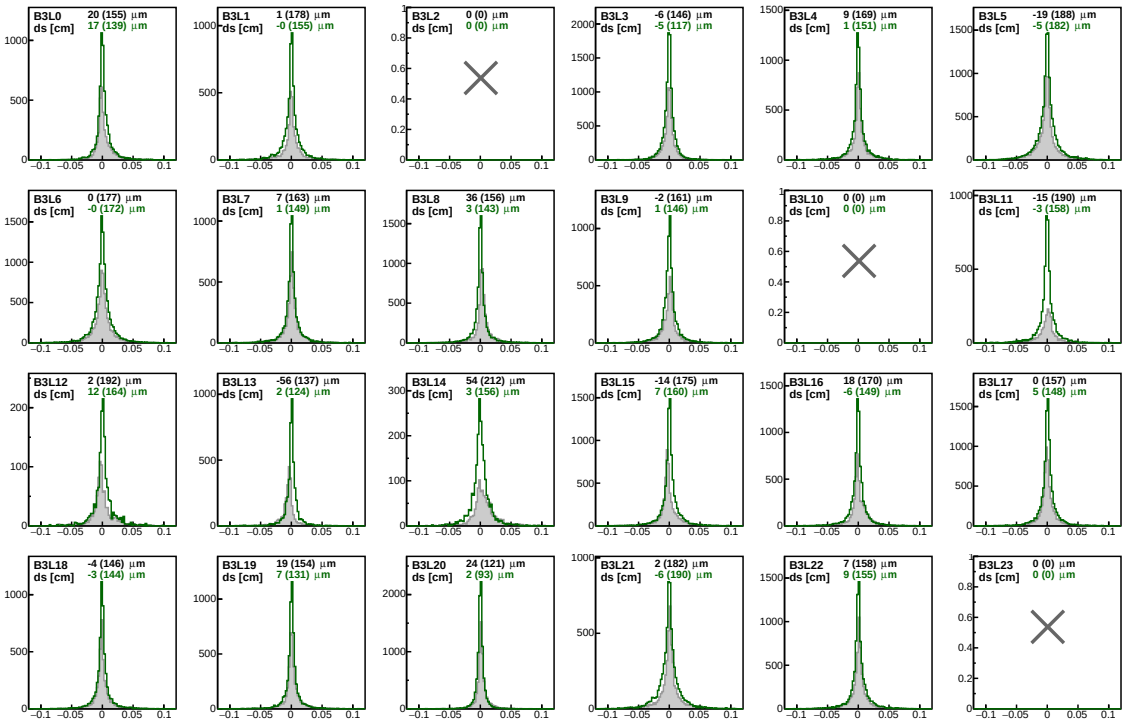

Figure B.17: Distributions of dz residuals for every ladder in layer B3.

Appendix C

Validating the Calculation of F_{NP}

Section 7.8.1 described the calculation of F_{NP}, corresponding to the fraction of electron candidates attributable to non-photonic sources as a function of electron p_T. The F_{NP} quantity is of central importance to the isolation of the inclusive heavy flavor DCA_T distributions, as it determines the normalization of all electron background sources relative to the total electron candidate sample. Therefore, it is of interest to carry out cross-checks to validate the calculation.

C.1 Comparing to Previous PHENIX Measurements

Section 5.1.1 described a previous measurement [20] of inclusive heavy flavor electrons by PHENIX, where two distinct methods—namely, the converter and cocktail methods—were used for electron background subtraction. That analysis, using data collected in the 2005 RHIC run period, reported the ratio of non-photonic to photonic electrons, $R_{NP} = N_{NP}/N_P$. Such quantity, while related to our F_{NP}, is not directly comparable to it as it depends on the material budget of the PHENIX detector, which changed significantly between 2005 and 2015. However, if the changes in the material budget can be quantified, it becomes possible to determine a scaling factor such that the two measurements can be compared.

Table C.1 summarizes the changes in the material budget—in terms of radiation lengths—in the central arm acceptance between the 2005 and 2015 run periods. In 2005, the beam pipe was thicker and constructed out of steel, and a helium-filled bag was present to reduce in-air conversions. In contrast, the 2015 beam pipe was constructed out of beryllium in an effort to

minimize conversions, and the main converter was the innermost layer of the VTX detector. Notice that succesive layers are not considered because of track hit requirements. Given the information in the table, there are 3.9 times more conversion electrons in 2015 compared to 2005. We now propagate this factor to derive a relation between the 2005 R_{NP} and the 2015 F_{NP}.

2005	**2015**
Beam Pipe $X_0(\%) = 0.29$	Beam Pipe $X_0(\%) = 0.22$
Air + Helium Bag $X_0(\%) = 0.1$	VTX Layer B0 $X_0(\%) = 1.3$
Total $X_0(\%) = 0.39$	**Total** $X_0(\%) = 1.52$

Table C.1: Changes in the PHENIX material budget between the 2005 and 2015 detector configuration.

The non-photonic and Dalitz contributions to the electron background are independent of material budget, and thus remain the same across run periods. Thus, the R_{NP} in 2005 and 2015 read, respectively,

$$R_{NP}^{(05)} = \frac{N_{NP}}{N_D + N_C^{(05)}}, \tag{C.1}$$

and

$$R_{NP}^{(15)} = \frac{N_{NP}}{N_D + N_C^{(15)}}. \tag{C.2}$$

In the above, N_{NP}, N_D and N_C are the number of non-photonic, Dalitz, and conversion electrons, respectively. We want to find a p_T-dependent function α such that $R_{NP}^{(15)} = \alpha(p_T) R_{NP}^{(05)}$. That is,

$$\frac{N_{NP}}{N_D + N_C^{(15)}} = \alpha(p_T) \frac{N_{NP}}{N_D + N_C^{(05)}}, \tag{C.3}$$

which simplifies to

$$\alpha(p_T) = \frac{N_D + N_C^{(05)}}{N_D + N_C^{(15)}}. \tag{C.4}$$

However, we know from the table how to relate $N_C^{(05)}$ and $N_C^{(15)}$, such that $\alpha(p_T)$ can be cast

all in terms of 2015 information

$$\begin{aligned}\alpha(p_T) &= \frac{N_D + \frac{1}{3.9}N_C^{(15)}}{N_D + N_C^{(15)}} \\ &= \frac{1 + \frac{1}{3.9}N_C^{(15)}/N_D}{1 + N_C^{(15)}/N_D}.\end{aligned} \tag{C.5}$$

The ratio of conversion to Dalitz electrons $N_C^{(15)}/N_D$ in the above equation can be evaluated using GEANT simulations, obtaining $\alpha(p_T)$ as shown in Fig. C.1.

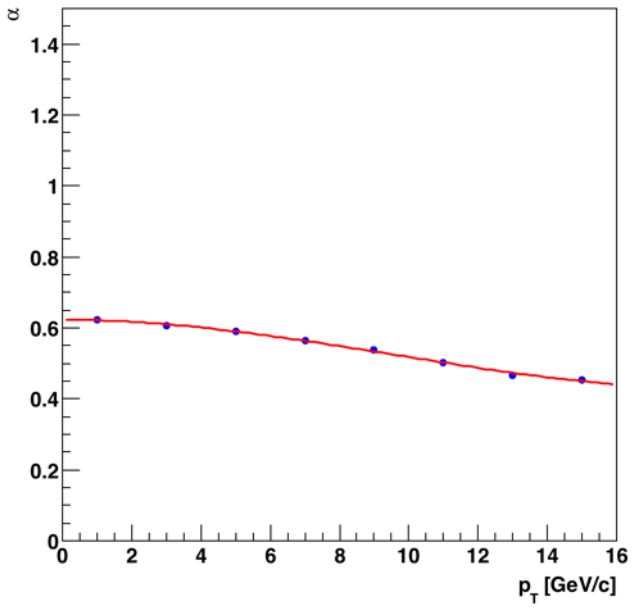

Figure C.1: p_T-dependent scaling factor to compare conversions between the 2005 and 2015 PHENIX configurations.

Finally, having obtained the desired scaling for R_{NP}, the equivalent $F_{NP} = R_{NP}/(1 + R_{NP})$ is shown in Fig. C.2. Excellent agreement is seen between the 2005 and 2015 results, thus validating our calculation.

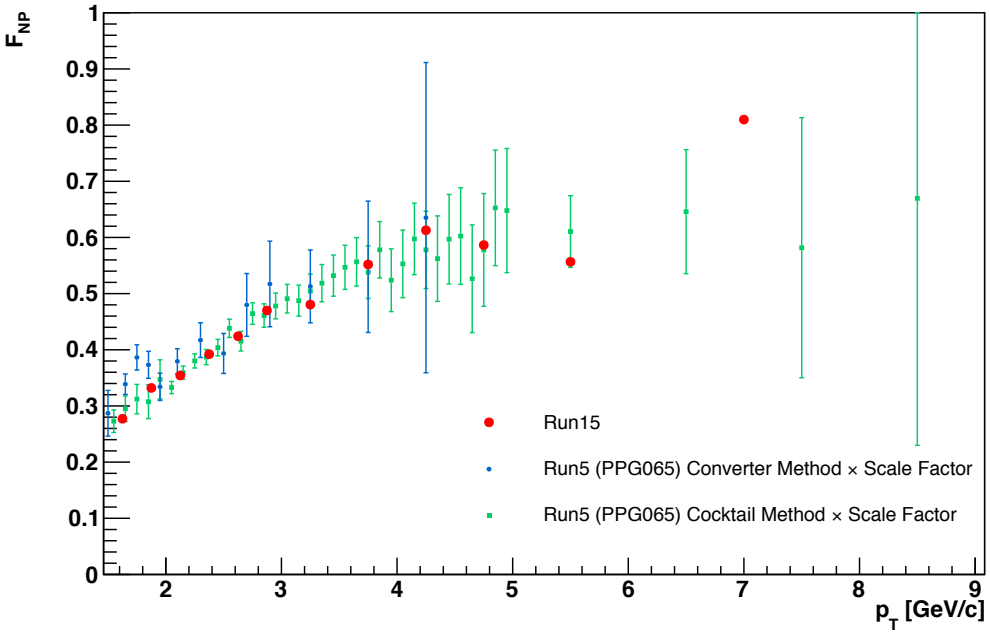

Figure C.2: Comparison of F_{NP} in the PHENIX 2005 and 2015 heavy flavor electron analyses. The 2005 measurement has been scaled to account for changes in the material budget of the detector.

C.2 Calculating F_{NP} Through Azimuthal Track-Cluster Correlations

The calculation of F_{NP} described in Section 7.8.1 relied on using the different conversion veto survival rates of photonic and non-photonic electrons to separate their contributions to the total electron candidate sample; let this be known as the "conversion veto method". However, it is also possible to estimate F_{NP} by examining the distribution of the azimuthal separation between pairs of clusters in a given VTX layer, where one of the clusters is associated with a reconstructed track. The distribution of $c\Delta\phi$ in VTX layer B1, where c is the charge of the track and $\Delta\phi$ is the azimuthal pair separation, is shown in Fig. C.3 for charged hadron tracks in data within $1 < p_T$ [GeV/c] < 1.5. In principle, *hadron* tracks should be uncorrelated with clusters such that the $c\Delta\phi$ distribution be uniform. However, the prominent correlated peak structure seen in the figure can be attributed to (i) charge deposits from a single track traversing overlapping ladders, (ii) cluster splitting within a single ladder, and (iii) secondary ionization. Of these, the last two effects

are dominant. The correlated part of the distribution can be isolated by fitting the underlying uncorrelated background, as depicted by the dotted line in the figure.

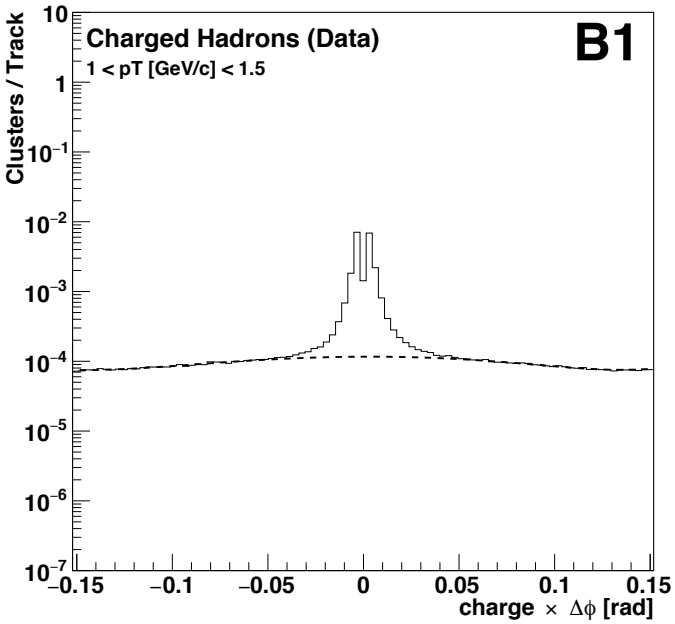

Figure C.3: Distribution of azimuthal separation of cluster pairs in VTX layer B1, where one of the clusters in the pair is associated with a reconstructed hadron SvxCentralTrack with $1 < p_T < 1.5$ GeV/c.

Now, unlike hadrons and non-photonic electrons, photonic electron tracks should exhibit a clear correlation with surrounding clusters owing to the kinematics of conversion pairs and Dalitz decays. In fact, this is the logic behind the conversion veto cut. Therefore, the $c\Delta\phi$ distribution of inclusive electrons in data should be amenable to be described as a linear combination of a non-photonic template (obtained by proxy from hadrons in data) and a photonic template (obtained from simulations) with a single free parameter, namely F_{NP}:

$$\frac{1}{N_{\text{track}}}\frac{dn^{\text{data}}}{d(c\Delta\phi)} = F_{NP}\frac{1}{N_{\text{track}}}\frac{dn^{\text{photonic}}}{d(c\Delta\phi)} + (1 - F_{NP})\frac{1}{N_{\text{track}}}\frac{dn^{\text{non-phot}}}{d(c\Delta\phi)}. \tag{C.6}$$

The photonic template is obtained by running *single-particle* GEANT simulations of π^0, η, and

photons, and constructing the corresponding $c\Delta\phi$ distribution in VTX layers B0 and B1. Since this procedure only captures the correlated signal, the underlying event is modeled by adding the uncorrelated part of the hadron $c\Delta\phi$ distribution. Because conversions are rare, the size of the statistical sample that can be collected by running single-particle simulations is very limited given the computational resources available, leading to large statistical fluctuations in the template, as shown in Fig. C.4. Therefore, the desired template is constructed by fitting the broad tails of the distribution with a double exponential function, as shown in the figure.

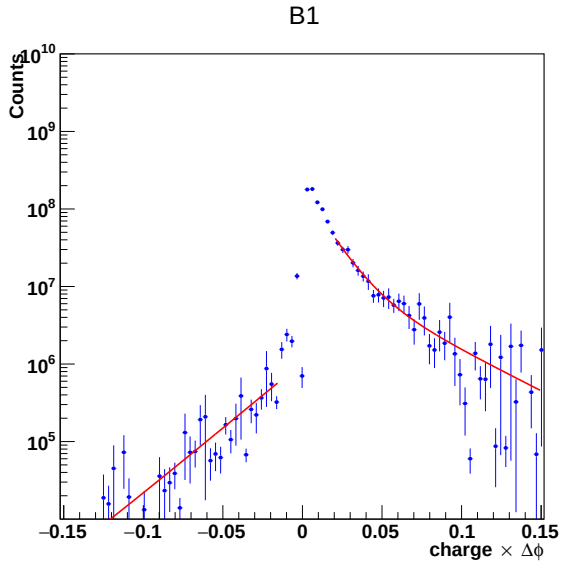

Figure C.4: Distribution of $c\Delta\phi$ for simulated photonic electrons in VTX layer B1. A template has been constructed by fitting the broad tails of the distribution with a double exponential.

Having constructed the photonic and non-photonic templates for B0 and B1 in all p_T bins of interest, the $c\Delta\phi$ distribution of inclusive electrons in data is fit as described, obtaining the results shown in Fig. C.5 for the specific bin of tracks with $1.5 < p_T$ [GeV/c] < 2.0. Three different fits are carried out, over three different $c\Delta\phi$ ranges, as shown in the figure. The average of the three fits is the reported F_{NP} value, with their standard deviation taken as an uncertainty on the measurement. Fig. C.6 compares the result obtained with the template fits, to that obtained with the conversion veto cut method. A very good agreement is seen between the two results.

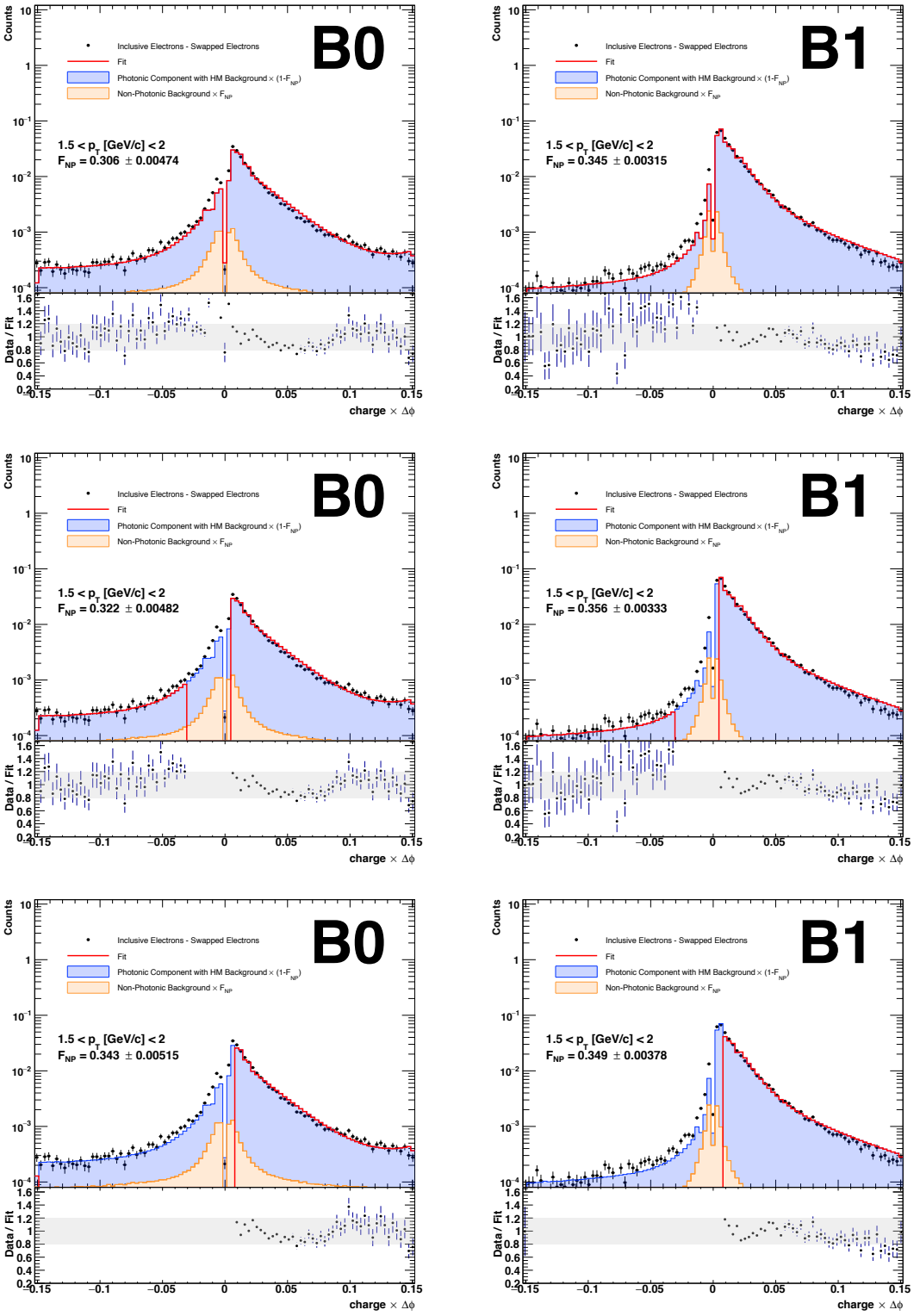

Figure C.5: Calculation of F_{NP} with the template fitting method over various $c\Delta\phi$ ranges, in both layers B0 and B1.

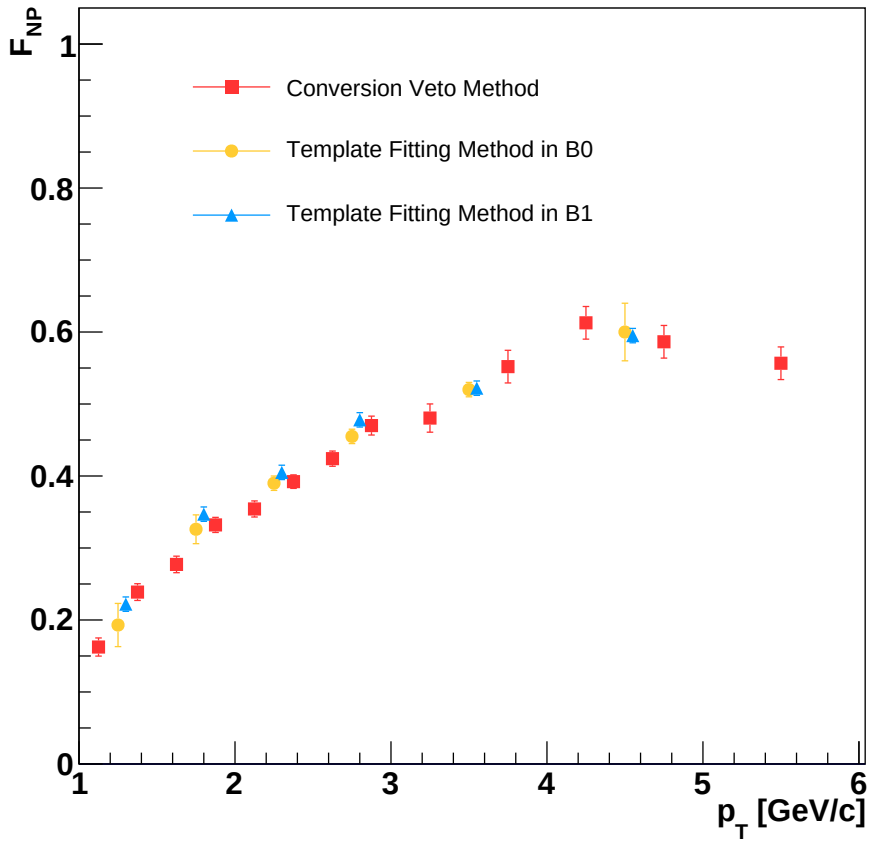

Figure C.6: Comparison of F_{NP} as obtained with the conversion veto cut method, and with the template fitting method in B0 and B1. For ease of visualization, the blue points have been displaced by a small amount in the horizontal direction.